LA-UR-12-26788
Approved for public release; distribution is unlimited.

Title:	A Multi-scale Approach to Statistical and Model-based Structural Health Monitoring with Application to Embedded Sensing for Wind Energy
Author(s):	Taylor, Stuart G.
Intended for:	PhD Dissertation in Structural Engineering at the University of California, San Diego

UNIVERSITY OF CALIFORNIA, SAN DIEGO

A Multi-scale Approach to Statistical and Model-based Structural Health Monitoring with Application to Embedded Sensing for Wind Energy

A dissertation submitted in partial satisfaction of the
requirements for the degree Doctor of Philosophy

in

Structural Engineering

by

Stuart Glynn Taylor

Committee in charge:

Professor Michael Todd, Chair
Professor Yuri Bazilevs
Professor Charles Farrar
Professor Rajesh Gupta
Professor William Hodgkiss

2013

The Dissertation of Stuart Glynn Taylor is approved, and it is acceptable in quality and form for publication on microfilm and electronically:

_____

_____

_____

_____

_____

Chair

University of California, San Diego

2013

EPIGRAPH

Trust in the LORD with all your heart and lean not on your own understanding;
in all your ways acknowledge him, and he will make your paths straight.

Proverbs 3:5,6

TABLE OF CONTENTS

LIST OF ABBREVIATIONS

°C	degrees Celsius
A	Area, Ampere
AC	Alternating Current
ADC	Analog-to-Digital Converter
AR	Auto Regressive
ARS	Agricultural Research Service
CCC	Cross Correlation Complement
COTS	Commercial-off-the-shelf
CPRL	Conservation and Production Research Laboratory
DAC	Digital-to-Analog Converter
DC	Direct Current
DOF	Degree of Freedom
DWF	Diffuse Wave Field
E	Elastic (Young's) modulus
EOM	Equations of Motion
F	Farad
FRF	Frequency Response Function
ft	Foot/feet
g	Acceleration due to gravity (~9.81 m/s^2)
GPa	Gigapascal (1×10^9 N/m^2)
GRB	Gamma-Ray Bursts
HP	High-Pressure
I	Moment of inertia

ICCC	Impulse Cross Correlation Complement
iFFT	Inverse Fast Fourier Transform
IRF	Impulse Response Function
JTAG	Joint Test Action Group (common name for IEEE 1149.1)
kW	Kilowatt
LANL	Los Alamos National Laboratory
LHS	Left Hand Side
LP	Low-Pressure
LTI	Linear Time Invariant
m	Meter
mA	Milliampere
MAC	Modal Assurance Criterion
mm	Millimeter
ms	Millisecond
mV	Millivolt
N	Newton
μW	Microwatt
MSD	Mahalanobis Squared Distance
NDE	Nondestructive Evaluation
nF	Nanofarad
NIRE	Normalized Impulse Residual Energy
NRE	Normalized Residual Energy
Pa	Pascal (N/m^2)
PoE	Power over Ethernet

PZT	Lead Zirconate Titanate
RAPTOR	RAPid Telescopes for Optical Response
RF	Radio Frequency
RHS	Right Hand Side
ROC	Receiver Operating Characteristic
s	Second
SHM	Structural Health Monitoring
SDOF	Single Degree of Freedom
SMA	SubMiniature version A (coaxial RF connector)
SNL	Sandia National Laboratory
UAV	Unmanned Aerial Vehicle
UGW	Ultrasonic Guided Wave
USDA	United States Department of Agriculture
WASP	Wireless Active Sensing Platform
WID	Wireless Impedance Device
WiDAQ	Wireless Data Acquisition module (add-on to the WID3)
WSN	Wireless Sensor Node
Ω	Ohm

LIST OF SYMBOLS

k	Linear spring stiffness
E	Modulus of elasticity
I	Area moment of inertia
L	Length
m	Mass
ρ	Density
A	Cross-sectional area
x	Displacement coordinate
b	Linear damping constant
$\mathbf{A}$	State-space system state matrix
$\mathbf{B}$	State-space system input influence matrix
$\mathbf{C}$	State-space system output matrix
$\mathbf{D}$	State-space system feed forward matrix
β , γ , α	Parameters for Newmark integration
X , Y , Z	Coordinate system directions
$Z(s)$ or $Z(\omega)$	Complex impedance
$V(s)$ or $V(\omega)$	Complex voltage
$I(s)$ or $I(\omega)$	Complex current
$Y(s)$ or $Y(\omega)$	Complex admittance
$\mathbf{x}$	Feature vector
$\boldsymbol{\mu}$	Mean of multivariate distribution
$\boldsymbol{\Sigma}$	Covariance of multivariate distribution
a	Geometric constant
s	Laplace variable
i	Imaginary unit
$\bar{\varepsilon}_{33}^{\ T}$	Complex dielectric constant
d_{3x}^2	Piezoelectric coupling constant
$\bar{Y}_{xx}^{\ E}$	Complex Young's modulus
$G(\omega)$	Complex conductance
$B(\omega)$	Complex susceptance
δ	dielectric loss factor
η	mechanical loss factor

x	Real part of mechanical impedance
y	Imaginary part of mechanical impedance
K	Measured susceptance slope
c_n	Empirical constant
Ω	frequency in cycles per admittance measurement frequency line
Φ	Phase angle in cycles per admittance measurement frequency line
$\mathbf{x}_i = \mathrm{x}_i[k]$	The i^{th} excitation signal
k	Signal index
$\mathbf{y}_i = y_i[k]$	The i^{th} measured response signal
$\mathbf{r}_i = r_i[k]$	The i^{th} residual signal
$\mathbf{v}_i = v_i[k]$	The i^{th} residual envelope
$\mathbf{w}_j = w_j[k]$	The i^{th} baseline signal envelope
$\boldsymbol{\psi}_i = \psi_i[k]$	The i^{th} estimated impulse response
$\boldsymbol{\rho}_i = \rho_i[k]$	The i^{th} impulse residual signal
$\boldsymbol{\upsilon}_i = \upsilon_i[k]$	The i^{th} residual impulse envelope signal
$\boldsymbol{\omega}_j = \omega_i[k]$	The i^{th} baseline impulse envelope signal
μ	Signal mean
σ	Signal standard deviation
t	Time variable
$\underline{x}_n$ or $\underline{x}(t)$	System state vector
$\underline{y}_n$ or $\underline{y}(t)$	System output vector
$\underline{u}_n$ or $\underline{u}(t)$	System input vector
$\mathbf{K}_e$	Observer gain matrix
$\underline{e}_n$ or $\underline{e}(t)$	Observer output error signal
$\underline{R}$	Nodal residual vector
$\mathbf{K}^{int}$	Tangent internal stiffness matrix
$\mathbf{K}^{dyn}$	Tangent inertial matrix
$\mathbb{K}$	Full system Jacobian, $\mathbf{K}^{int} + \mathbf{K}^{dyn}$
$\underline{w}_n$ or $\underline{w}(t)$	System input disturbance vector
$\mathbf{Q}$	System input disturbance covariance
$\underline{v}_n$ or $\underline{v}(t)$	Measurement noise vector
$\mathbf{R}$	Measurement noise covariance
$\mathrm{E}[\ ]$	Expectation of quantity

LIST OF FIGURES

LIST OF TABLES

ACKNOWLEDGEMENTS

First, I acknowledge my wife, Laura (Love!), for her support through this entire process. We met as I was preparing to begin my studies at UCSD, and we've now been married for over 3.5 of the 4.5 years this process has taken. This time around, I've had the "married student" experience, and I can say from experience that it's better. Laura, thank you for your love, commitment, support, and awesomeness.

Second, I acknowledge my advisor, Mike Todd. Mike brought me on as a PhD student in 2008, and since that time, he has taught and mentored me, and helped bring me to where I am today as a research engineer. Furthermore, I sincerely appreciate Mike permitting me to spend the vast majority of my PhD in Los Alamos, NM, where I enjoy the small-town life and the mountain air. Even with 900 miles between us, Mike was always available, and he never felt like more than a stone's throw away.

While at LANL, I have had the privilege of working with Chuck Farrar, Gyuhae Park, Kevin Farinholt, Eric Raby, and DJ Luscher. Chuck was my mentor in the LADSS program in 2003, and he has been an excellent mentor to me in these later years with respect to how research and business get done at LANL. I was Gyuhae's charge when I came back to LANL as a post-master's student in 2007, and he has guided my research efforts almost continuously since that time. Over these years, I have also worked closely with Kevin Farinholt, who has been an example to me of a truly outstanding engineer, and one whom I aspire to emulate. I also gratefully acknowledge my collaboration with Eric Raby and DJ Luscher, without whose expertise in their respective fields I would not have been able to complete this work. I have also received amazing support from Debra Bomar at UCSD and Kathie Womack at LANL. Debra has handled all of my university paperwork seamlessly since before I began at UCSD, and while

Kathie left LANL in 2012, she has been the one who made everything happen since I arrived in Los Alamos five years ago.

I also acknowledge the support of my fellow students (though some of these are now former students), including Eric Flynn, Greg Jarmer, and especially Erik Moro, with whom I have shared three offices and (briefly) an apartment. I sincerely appreciate Erik's friendship through the years, sharing music, coffee, ideas, and derivations. Finally, I am grateful to all the friends and family who have supported me along the way, including my family at Crossroads Bible Church in Los Alamos, and I am particularly thankful for the support, encouragement, and prayers from my dad, Ray Taylor, and my mom, Donna Chicon.

The research presented in this dissertation was funded by the National Science Foundation Graduate Research Fellowship Program, the Los Alamos National Laboratory Engineering Institute, the Department of Energy through the Laboratory Directed Research and Development program at Los Alamos National Laboratory, and the UCSD Department of Structural Engineering. This dissertation has been approved by Los Alamos National Laboratory for unlimited public release (LA-UR-12-26788).

Section 2.2 and portions of Section 3.3 have been published in part in [1] *Smart Structures and Systems,* S. G. Taylor, K. Farinholt, G. Park, M. Todd, and C. Farrar, 2010. The title of this paper is "Multi-scale wireless sensor node for health monitoring of civil infrastructure and mechanical systems." The dissertation author was the primary investigator and author of this paper.

Section 2.3 and other portions of Section 3.3 have been published in part in [2] *Measurement Science and Technology,* S. G. Taylor, K. M. Farinholt, E. B. Flynn, E. Figueiredo, D. L. Mascarenas, E. A. Moro, G. Park, M. D. Todd, and C. R. Farrar, 2009. The title of this paper is "A mobile-agent-based wireless sensing network for structural monitoring applications." The dissertation author was the primary investigator and author of this paper.

Section 2.4 has been published in part in [3] *Journal of Structural Engineering,* C. J. Stull, S. G. Taylor, J. Wren, D. L. Mascareñas, and C. R. Farrar, 2012. The title of this paper is "Real-Time Condition Assessment of RAPTOR Telescope Systems."

Other portions of Section 3.3 have been published in part in [4] *SPIE Smart Structures/NDE*, S. G. Taylor, C. J. Stull, J. Wren, E. Y. Raby, and C. R. Farrar, 2012. The title of this paper is "Embedded sensor node deployment to monitor telescope drive system components." The dissertation author was the primary investigator and author of this paper.

Section 3.4 is currently being prepared in part for publication [5]. S. G. Taylor, E. Y. Raby, G. Park, K. M. Farinholt, and M. D. Todd, 2013. The title of this paper is "Active sensing platform: development and deployment." The dissertation author was the primary investigator and author of this paper.

Portions of Section 2.5 and Chapter 4 have been recommended for publication in [6] *Smart Materials and Structures*, S. G. Taylor, G. Park, K. M. Farinholt, and M. D. Todd, 2012. The title of this paper is "Diagnostics for piezoelectric transducers under cyclic loads deployed for structural health monitoring applications." The dissertation author was the primary investigator and author of this paper.

Other portions of Section 2.5 and Chapter 5 have been accepted by [7] *Structural Health Monitoring,* S. G. Taylor, G. Park, K. M. Farinholt, and M. D. Todd, 2012. The title of this paper is "Fatigue crack detection performance comparison in a composite wind turbine rotor blade." The dissertation author was the primary investigator and author of this paper.

Other portions of Chapter 5 are intended for submission in part to [8] *Journal of Intelligent Material Systems and Structures,* S. G. Taylor, K. M. Farinholt, G. Park, C. R. Farrar, M. D. Todd, and J.-R. Lee, 2013. The title of this paper is "Incipient crack detection in composite wind turbine blades." The dissertation author was the primary investigator and author of this paper.

Portions of Section 2.6 and Chapter 6 have been submitted in part to [9] *IMAC XXXI: A Conference and Exposition on Structural Dynamics*, S. G. Taylor, D. J. Luscher, and M. D. Todd, 2013. The title of this paper is "State estimate of wind turbine blades using geometrically exact beam theory." The dissertation author was the primary investigator and author of this paper.

Other portions of Section 2.6 and Chapter 6 are currently being prepared for publication [10]. S. G. Taylor, D. J. Luscher, and M. D. Todd, 2013. The title of this paper is "Nonlinear state observer for structural monitoring of wind turbine rotor blades." The dissertation author was the primary investigator and author of this paper.

VITA

2005 Bachelor of Science, University of Houston

2007 Master of Science, University of Houston

2013 Doctor of Philosophy, University of California, San Diego

PUBLICATIONS

*Work that has been incorporated into this dissertation

Peer Reviewed Journal Articles

*S. G. Taylor, K. Farinholt, G. Park, M. Todd, and C. Farrar, "Multi-scale wireless sensor node for health monitoring of civil infrastructure and mechanical systems," Smart Structures and Systems, vol. 6, pp. 661-673, 2010.

*S. G. Taylor, K. M. Farinholt, E. B. Flynn, E. Figueiredo, D. L. Mascarenas, E. A. Moro, G. Park, M. D. Todd, and C. R. Farrar, "A mobile-agent-based wireless sensing network for structural monitoring applications," Measurement Science and Technology, p. 045201, 2009.

S. G. Taylor and D. C. Zimmerman, "Improved Experimental Ritz Vector Extraction with Application to Damage Detection," Journal of Vibration and Acoustics, vol. 132, p. 011012, 2010.

*C. J. Stull, S. G. Taylor, J. Wren, D. L. Mascareñas, and C. R. Farrar, "Real-Time Condition Assessment of RAPTOR Telescope Systems," Journal of Structural Engineering, vol. 1, p. 426, 2012.

Articles Accepted for Publication

*S. G. Taylor, G. Park, K. M. Farinholt, and M. D. Todd, "Fatigue crack detection performance comparison in a composite wind turbine rotor blade," Structural Health Monitoring, accepted 12-Nov 2012.

*S. G. Taylor, G. Park, K. M. Farinholt, and M. D. Todd, "Diagnostics for piezoelectric transducers under cyclic loads deployed for structural health monitoring applications," *Smart Materials and Structures,* accepted 11-Dec 2012.

Articles in Review

*S. G. Taylor, E. Y. Raby, G. Park, K. M. Farinholt, and M. D. Todd, "Wireless active sensing platform: development and deployment," *Sensors Journal, IEEE*, in review 2012.

Articles in Progress

*S. G. Taylor, K. M. Farinholt, G. Park, C. R. Farrar, M. D. Todd, and J.-R. Lee, "Incipient crack detection in composite wind turbine blades," *Journal of Intelligent Material Systems and Structures,* in progress 2013.

*S. G. Taylor, D. J. Luscher, and M. D. Todd, "Nonlinear state observer for structural monitoring of wind turbine rotor blades," in progress 2013.

Conference Proceedings

*S. G. Taylor, D. J. Luscher, and M. D. Todd, "State estimate of wind turbine blades using geometrically exact beam theory," in *IMAC XXXI*, Garden Grove, CA, 2013.

S. G. Taylor, G. Khoury, D. C. Zimmerman, and M. D. Todd, "Finite element-based damage detection using expanded Ritz vector residuals," in *IMAC XXXI*, Garden Grove, CA, 2013.

*S. G. Taylor, C. J. Stull, J. Wren, E. Y. Raby, and C. R. Farrar, "Embedded sensor node deployment to monitor telescope drive system components," in *SPIE Smart Structures/NDE*, San Diego, California, USA, 2012, pp. 83430C-6.

S. G. Taylor, H. Jeong, J. K. Jang, G. Park, K. M. Farinholt, M. D. Todd, and C. M. Ammerman, "Full-scale fatigue tests of CX-100 wind turbine blades. Part II: analysis," in *SPIE Smart Structures/NDE*, San Diego, California, 2012, pp. 83430Q-10.

S. G. Taylor, K. M. Farinholt, G. Park, C. R. Farrar, M. D. Todd, and J.-R. Lee, "Structural health monitoring of research-scale wind turbine blades," in *Asia-Pacific Workshop on Structural Health Monitoring*, Melbourne, Australia, 2012.

S. G. Taylor, K. M. Farinholt, G. Park, C. R. Farrar, M. D. Todd, and J.-R. Lee, "Incipient Crack Detection in Composite Wind Turbine Blades," in *Advances in Structural Health Management and Composite Structures*, Jeonju, Korea, 2012.

S. G. Taylor, K. M. Farinholt, H. Jeong, J. Jang, G. Park, M. D. Todd, C. R. Farrar, and C. M. Ammerman, "Wind turbine blade fatigue tests: lessons learned and application to SHM system development," in *European Workshop on Structural Health Monitoring*, Dresden Germany, 2012.

S. G. Taylor, J. Carroll, K. M. Farinholt, G. Park, C. R. Farrar, and M. D. Todd, "Embedded processing for SHM with integrated software control of a wireless impedance device," in *SPIE Smart Structures/NDE*, San Diego, CA, USA, 2011, p. 797904.

S. G. Taylor, C. J. Stull, J. Wren, and C. R. Farrar, "Real-time Condition Assessment of RAPTOR Telescope Systems," presented at the Asia-Pacific Structural Health Monitoring Workshop, Tokyo, Japan, 2010.

S. G. Taylor, E. B. Flynn, D. L. Mascarenas, M. D. Todd, D. Dondi, T. Rosing, S. Kpotufe, S. Dasgupta, K. Lin, and R. Gupta, "Integrated wireless powering and data interrogation for civil infrastructure monitoring," presented at the Bridge Maintenance, Safety, Management and Life-Cycle Optimization, Philadelphia, PA, 2010.

S. G. Taylor, K. M. Farinholt, G. Park, C. R. Farrar, and M. D. Todd, "Multi-scale wireless sensor node for impedance-based SHM and long-term civil infrastructure modeling," presented at the Bridge Maintenance, Safety, Management and Life-Cycle Optimization, Philadelphia, PA, 2010.

S. G. Taylor, K. M. Farinholt, G. Park, and C. R. Farrar, "Energy harvesting and wireless energy transmission for powering SHM sensor nodes," presented at the Bridge Maintenance, Safety, Management and Life-Cycle Optimization, Philadelphia, PA, 2010.

S. G. Taylor, K. M. Farinholt, G. Park, C. R. Farrar, E. B. Flynn, D. L. Mascarenas, and M. D. Todd, "Wireless impedance device for electromechanical impedance sensing and low-frequency vibration data acquisition," in *SPIE Smart Structures/NDE*, San Diego, CA, USA, 2009, pp. 729228-12.

S. G. Taylor, K. M. Farinholt, G. Park, and C. R. Farrar, "Impedance-based Wireless Sensor Node for SHM, Sensor Diagnostics, and Low-frequency Vibration Data Acquisition," in *7th International Workshop on Structural Health Monitoring*, Stanford, CA, 2009, pp. 831-838.

S. G. Taylor, K. M. Farinholt, E. B. Flynn, E. Figueiredo, D. L. Mascareñas, G. Park, M. D. Todd, and C. R. Farrar, "A Mobile-Agent Based Wireless Sensing Network for SHM – Field Study at the Alamosa Canyon Bridge," in *7th International Workshop on Structural Health Monitoring*, Stanford, CA, 2009, pp. 1731-1738.

S. G. Taylor and D. C. Zimmerman, "Structural Health Monitoring Using Ritz Vectors and Expanded Residuals," in *International Modal Analysis Conference*, Orlando, FL, 2007.

S. G. Taylor and D. C. Zimmerman, "Damage Detection in a Cargo Bay Frame Using Ritz Vectors," in *International Modal Analysis Conference*, Orlando, FL, 2005.

S. G. Taylor, C. Rupp, D. Johnson, C. Farrar, and P. Avitabile, "Failure Prediction in Composite Plates with Impact-induced Damage," in *International Modal Analysis Conference*, Dearborn, MI, 2004.

FIELDS OF STUDY

Major Field: Structural Engineering

Studies in Structural Dynamics
Professor Michael Todd

Studies in Signal Processing
Professor William Hodgkiss

Studies in Structural Health Monitoring
Professor Charles Farrar

ABSTRACT OF THE DISSERTATION

A Multi-scale Approach to Statistical and Model-based Structural Health Monitoring with Application to Embedded Sensing for Wind Energy

by

Stuart Glynn Taylor

Doctor of Philosophy in Structural Engineering

University of California, San Diego, 2013

Professor Michael Todd, Chair

This dissertation presents a systems-level approach to multi-scale structural health monitoring (SHM) with specific focus on wind turbine rotor blades, combining innovative sensing platforms for incipient damage detection with state estimation for structural performance assessment. The practical implementation of this approach rests in three areas: hardware development and deployment for embedded data acquisition; demonstration of incipient damage detection using embedded systems for active-sensing SHM, including an in-depth assessment of sensor diagnostics; and development of a nonlinear observer for state and loads estimation applied to a geometrically nonlinear beam model.

Structural Health Monitoring is generally defined as the development of an in-situ damage assessment capability, and when combined predictive loading and failure models, enables risk-informed models for decision-making. These decision models require contributions from a wide variety of technology areas. Sensing systems (in many cases, capable of providing multiple data types) must be developed specifically to provide the data necessary for structural damage detection and performance assessment. A means of sensor diagnostics is necessary to provide confidence in the recorded data. Statistical modeling and classification feed the development of optimal detectors necessary to ascertain the presence, location, and severity of damage. Methods of state estimation are needed to map kinematic measurements to physical performance metrics. A probabilistic representation of future loads applied to a structural model enables an assessment of the structure's future performance. Finally, a cost model is combined with a probabilistic risk assessment, given the detectors' output and the structure's estimated future performance, to render the risk-minimizing decision. This dissertation presents key contributions among the underpinnings of this ultimate decision model: (1) embedded sensor development and deployment; (2) sensor diagnostics for active-sensing methods; (3) an assessment of incipient damage detection performance for large-scale composite structures; and (4) the development and application of a state observer, demonstrated in the specific case of a geometrically nonlinear beam model.

Chapter 1
Introduction

1.1. Overview

1.2. Structural Health Monitoring

Structural Health Monitoring (SHM) offers the possibility of improving production quality, boosting manufacturing output, or increasing customer satisfaction, but the underlying motivation for the application for SHM systems is always and must be economic. The promise of SHM is always some combination of reduced maintenance costs, increased asset/resource availability, and improved life safety. Presentations of SHM as found in the literature often follow a process similar to that depicted in Figure 1: some data are collected, and a projection of that data onto a much smaller subspace (feature extraction) shows a change correlated with some physical change in the system (damage). However, connecting SHM research to realizable gains for asset owners requires a more comprehensive approach.

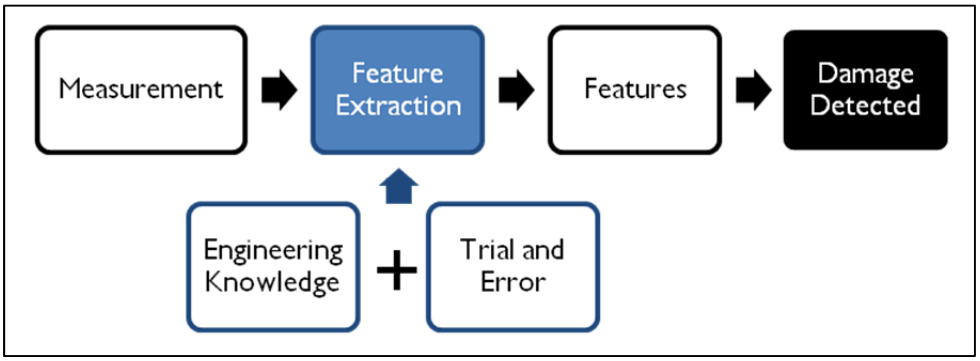

Figure 1: A simplistic view of structural health monitoring

An SHM system that delivers positive value to asset owners must ultimately provide the ability to make risk-informed decisions. Expanding the simplistic view of SHM given in Figure 1, an SHM system for risk-informed decisions requires: (1) feature extraction; (2) detection and response; and (3) planning and action. Each of these primary phases is supported by multiple processes, requiring multiple technologies. This process is shown pictorially in Figure 2. The Feature Extraction phase requires hardware to collect appropriate data, as well a sensor diagnostics system to verify that the sensors are performing correctly. In order to identify the type and extent of damage, the Detection and Response phase requires real-time measurements combined with a physics-based model to provide the "Informed Model" that informs the detection process. The Planning and Action phase requires the observations from the detection phase, as well as measurement-informed simulation results (state observer) and estimates of future performance in response to potential loads (loads model). Furthermore, in producing these estimates, known uncertainty on the various inputs must be propagated to enable quantification of the uncertainty associated with the estimates and predictions.

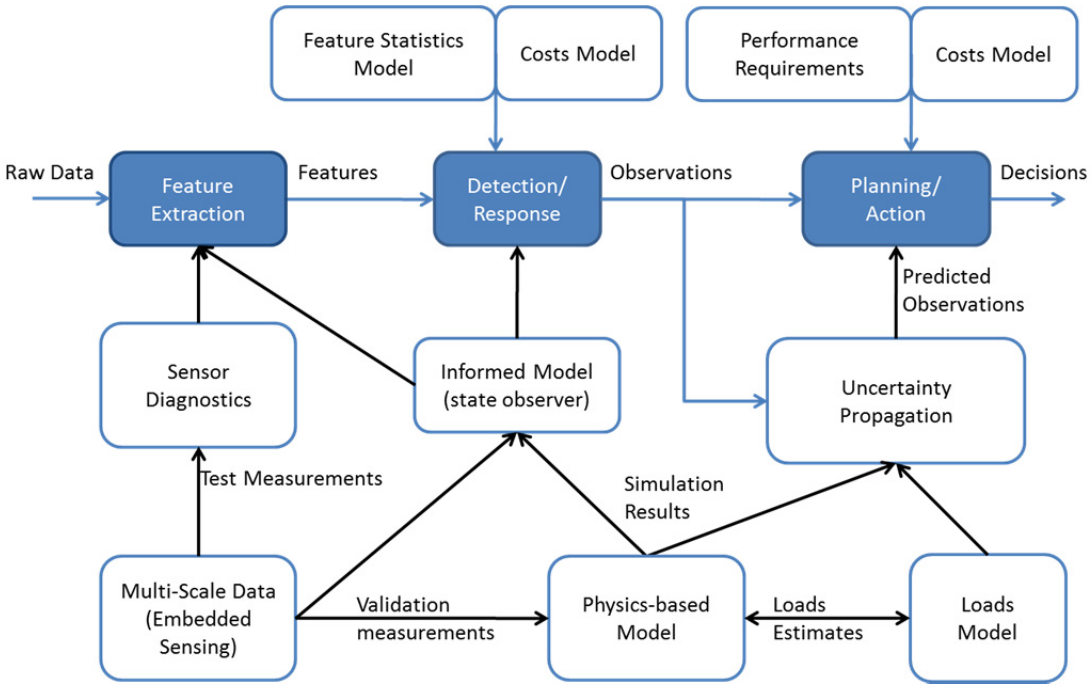

Figure 2: Applied structural health monitoring with informed decision models

1.3. Overview of the Dissertation

1.3.1. Embedded Sensing for SHM

Embedded sensing entails incorporating data acquisition hardware with processing and communications capability into the structure being monitored in such a way that the monitoring can take place while the structure is operational. The embedded sensing approach differs from most conventional sensing approaches, which are typically implemented using commercial-off-the-shelf (COTS) acquisition systems to collect data from a structure in a controlled, off-line environment. Experimental model validation (such as modal testing for test-analysis correlation) and nondestructive evaluation (NDE) are typically approached in this manner. In these cases, the sensing equipment may be too expensive to justify its permanent installation in the structure, it may be too bulky to permit ordinary operation of the structure, or its operation may require such specialized training that leaving the equipment in place in the absence of a

qualified technician would be impractical. For assets of high value or that are inaccessible following deployment, the capability to perform such "conventional" sensing may be actually embedded in the structure, but the cost justification for such cases is rare. However, continuous advances in low-power computation, communication, and sensing are enabling embedded systems for SHM to become more cost-effective and commonplace, with such systems being specifically developed for mobile structures, such as airplanes, automobiles, ships, and locomotives, as well as for static structures, such as bridges, buildings, and large pieces of industrial machinery.

Chapter 3 focuses on embedded sensing development application to SHM. The embedded systems developed and presented in this dissertation have contributed to the areas of civil infrastructure monitoring [11], wireless communication for embedded SHM [2], integrated sensing and diagnostics [12], and multi-scale sensing [1, 13].

1.3.2. Sensor Diagnostics

In permanent SHM system installations or long-duration tests, the ability to assess the condition of the sensors and actuators installed on a structure being monitored is essential. Transducer failure can be a significant source of SHM system failure, and a lack of adequate sensor diagnostics capability can lead to false positives in damage detection and also contribute to system downtime. Although a separate sensor diagnostic capability may suffice when utilizing conventional data acquisition systems, an embedded SHM system requires a seamless ability to implement sensor diagnostics in real time, so that deviations from baseline measurements can immediately and confidently be attributed to structural changes rather than sensor malfunction.

Chapter 4 focuses on diagnostics for piezoelectric sensors using impedance measurements, and in particular provides two key contributions to the SHM community in the

application of piezoelectric transducers: (1) the assessment of sensor performance and failure modes over a long-duration fatigue test in a severe loading environment, and (2) the identification and normalization of nonstationary impedance measurements collected during cyclic loading of a structure [6]. This situation is significant, because many structures commonly considered candidates for embedded SHM undergo cyclic loads while in operation, including aircraft, automobiles, bridges, and wind turbine flexible members.

1.3.3. Experimental Damage Detection Performance

In the experimental fatigue test described in Section 2.5, decisions for sensor placement, acquisition hardware type, and analysis methods applied were motivated by standard practices for active sensing SHM [14], which have been proven effective in smaller-scale experimental contexts [15]. The active sensing approach to SHM entails interrogating the structure by intentionally exciting it in some manner and measuring its subsequent response. The relative performance of the hardware systems and analysis methods implemented were then compared in terms of their ability to detect and localize incipient damage. By implementing a number of distinct SHM system possibilities and assessing their relative detection performance, this portion of the dissertation points toward a more effective approach for composite rotor blade SHM. Although this process follows established methods, it does so with a careful comparison of the actual detection performance for each permutation. This example ultimately highlights the need for a model informed by the physics of the structure and clearly defined performance metrics/requirements.

Chapter 5 focuses on experimental applications of SHM on a wind turbine rotor blade under fatigue loading, and it details two main contributions to the SHM community: (1) the publication of a large scale fatigue test with a thorough active-sensing component for SHM; and

(2) the exploration and comparison of methods commonly implemented in SHM literature to a large-scale problem [7].

1.3.4. State Estimation

Effective structural prognostics of wind turbine blades will require estimates of quantities directly related to performance metrics, such as an ultimate load limit or absolute maximum deflection. To this end, a state observer is proposed for a geometrically nonlinear beam finite element model. This model was developed as a fast-running simulation to capture the relevant dynamics of wind turbine flexible members. Although much more complicated models can be implemented to predict the behavior of such composite structures, they would not be feasible for implementation in real-time, embedded systems for SHM. The state observer enables the evaluation of structural performance in light of detected damage with respect to measureable performance metrics, such as an ultimate load or maximum deflection.

Chapter 6 focuses on observers for state and loads estimation. In a typical observer application, a reference model is used to observe the behavior of a physical system, which is commonly referred to as a ‘plant’. The observer implements a Newton-Raphson iterative scheme to drive the measured output error toward zero by updating a fictitious external force exerted on the model. By updating an external force rather than estimating the state directly, the proposed state observer is intended to produce an estimate of the state that is consistent with the structure’s behavior even in the face of model uncertainty, provided the model is sufficiently “close” to the plant. The contribution of this chapter is in the development and application of a state observer to feed the decision models described above.

1.4. Contributions of the Dissertation

1. Development and deployment of SHM-specific data acquisition hardware for multi-scale sensing with integrated capacity for impedance-based sensor diagnostics
2. Demonstrated a new design of a hybrid wireless sensor node network for civil infrastructure monitoring utilizing a network-hopping mobile-host
3. Publication of sensor diagnostics results from a large-scale experimental campaign, including an assessment of failure modes, transducer performance, and longevity
4. Proposed a normalization scheme for nonstationary impedance measurements for sensor diagnostics with piezoelectric transducers under cyclic loading
5. Publication of incipient crack detection results from a large-scale experimental campaign, including a statistical comparison of common methods and features
6. Proposed a method to adapt diffuse wave field measurements for processing using methods common to processing ultrasonic guided wave measurements for SHM
7. Derived a Newton-Raphson state observer for implementation with a nonlinear finite element code, and showed its relationship to the Kalman filter
8. Demonstrated the proposed Newton-Raphson state observer in a bench-top experiment with a vertically cantilevered beam

Chapter 2
Experimental Test Platforms

2.1. Introduction

This chapter presents six experimental test platforms referred to through the course of the dissertation. Some of the platforms utilized have multiple applications, so it is convenient to concentrate their descriptions here.

2.2. Sensor Diagnostics Demonstration Plate

An aluminum plate with 12 piezoelectric transducers bonded to its surface is shown in Figure 3. The plate measures 12x12x0.5 inches, and has 12 APC International D-0.500-0.020-851 PZT patches, fabricated using APC International's 851 material [16]. Each patch is a disc measuring 0.5 inches in diameter and 0.02 inches thick. The patches operate in the d_{3x} mode, such that strains in the planar x direction induce voltages in the out-of-plane 3 direction and vice-versa (see Figure 45). Six of the transducers were mounted according to standard procedures, bonded using a cyanoacrylate adhesive. Three of the transducers were mounted to simulate progressive debonding, with segments of wax paper placed nominally under 25%, 50%

and 75% of each patch surface, respectively. The last three transducers were mounted to simulate broken sensors; they were first mounted according to standard procedures, and then a rotary cutting tool was used to cut away 25%, 50% and 75% of each patch. This test platform was used as a laboratory demonstration of the impedance measurement capabilities of the embedded sensor nodes presented in Chapter 3. Although there were originally six healthy transducers, two of the transducers' leads have broken off, so that only four healthy transducers remain useful.

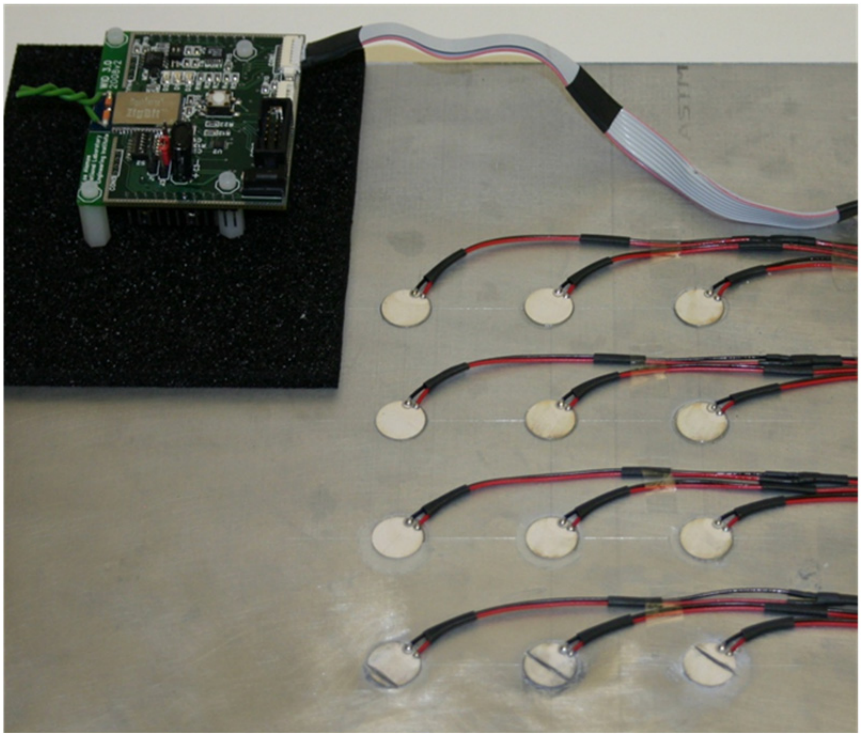

Figure 3: Sensor Diagnostics demonstration plate with healthy, debonded, and broken sensors

2.3. Alamosa Canyon Bridge

The Alamosa Canyon Bridge, located in southern New Mexico, USA, is a traditional steel girder bridge with a reinforced concrete deck 25 cm thick. This bridge has been decommissioned and is utilized by the New Mexico Department of Transportation as a test bed

for structural health monitoring systems from university and research organizations. The bridge has multiple spans, and a typical joint in the bridge is fastened with 14 bolts, making it an ideal test platform for applications related to bolted joint monitoring. A photograph of the bridge, inset with a detailed view of a joint and an instrumented washer installed with a bolt, is shown in Figure 4. These washers are used in the same manner as their conventional counterparts. When mounted in a structure, the dynamics of these washers will change as the preload is changed. Specifically, the resonant peaks of the device shift to higher frequencies and their magnitudes drop as the preload increases. For experiments conducted using the Wireless Impedance Device (WID3) described in Section 3.3, a total of 12 washers instrumented with APC International D-0.500-0.020-851 PZT transducers were installed, and these transducers could then be interrogated to monitor changes in the washers' boundary conditions caused by changes in the bolt preload.

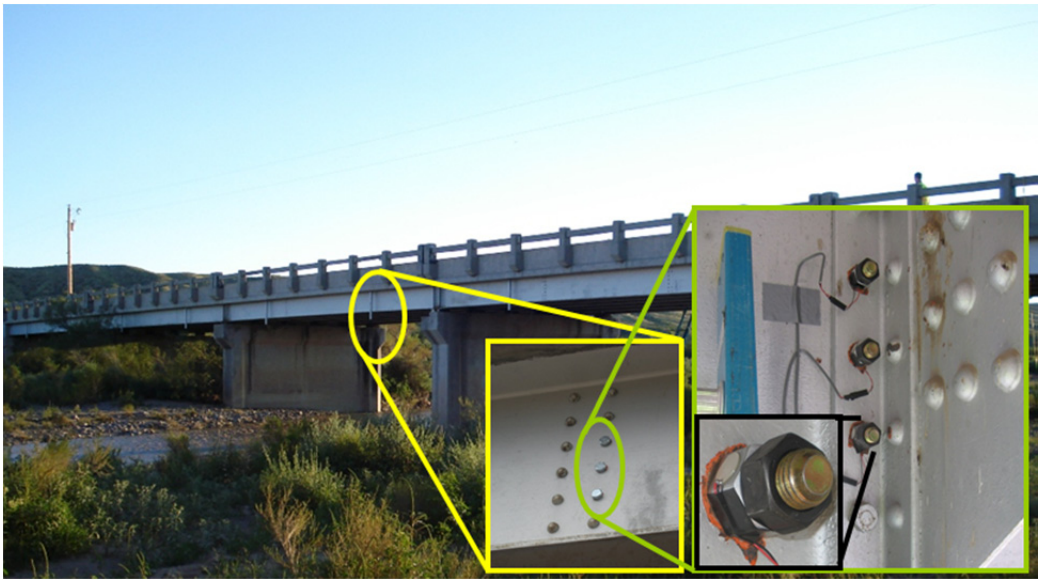

Figure 4: Alamosa Canyon Bridge with detail of bolted joint and instrumented washer

2.4. RAPTOR Telescope Drive System

Comprising the primary hardware component of the Los Alamos Thinking Telescope Project [17], the RAPid Telescopes for Optical Response (RAPTOR) observatory network is made up of several autonomous astronomical observatories designed to search for astrophysical transients, namely, gamma-ray bursts (GRBs) [18]. Although they are intrinsically bright, GRBs are difficult to detect because of their short duration. Typically, GRBs are first observed by orbiting satellites, and in conjunction with this information, the RAPTOR telescopes are able to identify and record these events using a two-step process. First, a large field-of-view telescope provides location information on potential events of interest. Once such an event is identified, narrow-field telescopes are moved quickly to perform more detailed spectroscopy and light curve measurements. Because of the large number of potential events of interest, this process must be maintained on a continual basis throughout the night at rates more than 10 times faster than that of typical astronomical mounts.

An individual RAPTOR "observatory," shown in Figure 5 (left) is a standalone structure with two main structural components: an automated enclosure and the telescope drive system. The SHM focus of this test bed is on the telescope drive system, specifically, components referred to as "capstans," which provide the friction interfaces between the motors that drive the mounts and the drive wheels for both the right ascension and declination axes. The capstan itself is a 3.38 inch (8.58 cm) long stainless steel rod, 0.25 inch (6.35 mm) in diameter, with a urethane coating. This coating wears with use, resulting in irregular travel of the drive wheel and the eventual inability to actuate the wheel. Figure 6 shows capstans at various levels of wear.

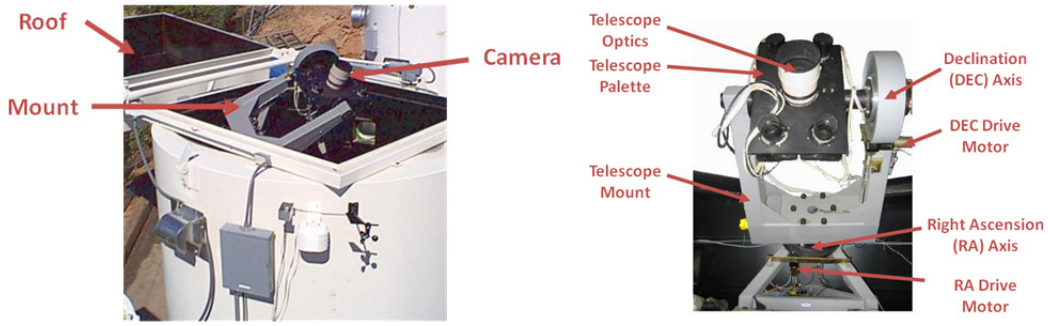

Figure 5: RAPTOR telescope and enclosure, or "observatory" (left); telescope system with mount and drive mechanisms (right)

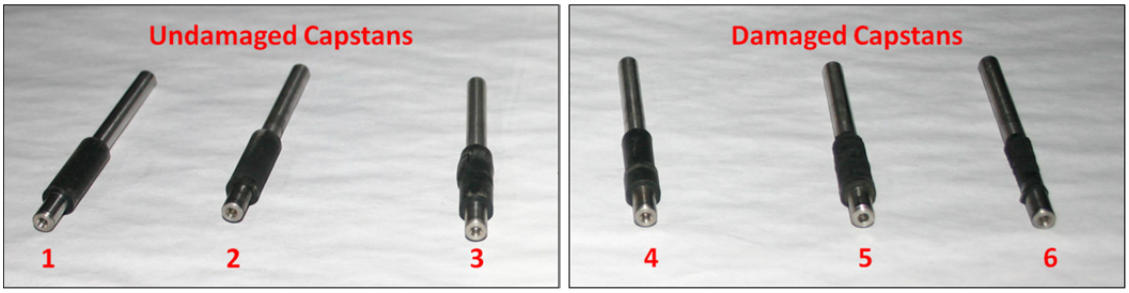

Figure 6: Capstans showing varying levels of wear

The RAPTOR telescope systems employing this capstan-based drive mechanism are currently operated in a run-to-failure mode; the capstans, which are almost invariably the first component to fail, are often replaced only after an inability to control the telescope optics is observed. Left unchecked, the inevitable wearing away of the urethane coating can eventually cause damage to other, considerably more expensive components, such as the large drive wheels. Given the variability in both the geospatial locations and the duty cycles associated with these telescope systems, the rates at which the capstans experience wear are highly inconsistent, precluding the development of a cost-effective maintenance schedule for individual telescope systems or for the network as a whole. Conversely, replacing the capstans without regard to their condition at a conservatively chosen interval is hampered by the man-hours involved in accessing the remotely-located systems. An SHM system deployed across the entire RAPTOR observatory network, which has the potential to grow into a globally distributed sensing system,

would offer a means of monitoring the condition of each observatory, enabling managers to plan maintenance schedules that adapt to the real-time needs of each installation and to make more cost-effective use of the limited maintenance resources.

2.5. CX-100 Rotor Blade Fatigue Test

2.5.1. Overview

The CX-100 wind turbine rotor blade, developed by researchers at Sandia National Laboratory (SNL) [19], was an experimental rotor blade design that included a carbon fiber spar cap, with a fiberglass shell laid over a balsa wood frame. The rotor blade was mounted to a 7-ton steel frame designed to approximate a fixed-free boundary condition. Loads were introduced to the blade using a universal resonant excitation (UREX) system, which hydraulically actuated steel masses along linear rails oriented in the flapwise direction at the rotor blade's first resonance. In the experiment described here, a 9-meter CX-100 wind turbine rotor blade was subject to fatigue loading until failure in a controlled laboratory environment [20, 21]. Drawings of the rotor blade are shown in Figure 7, and a photograph of the test setup is shown in Figure 8. The UREX system, which had a mass of 582 kg, was mounted 1.6 m from the rotor blade's root, and an additional proof mass of 145 kg was mounted to the blade 6.75 m from the root. The addition of these masses reduced the blade's resonant frequencies further below their corresponding free-free values than simply mounting it to the test stand; the first three resonant frequencies for these three configurations are given in Table 1.

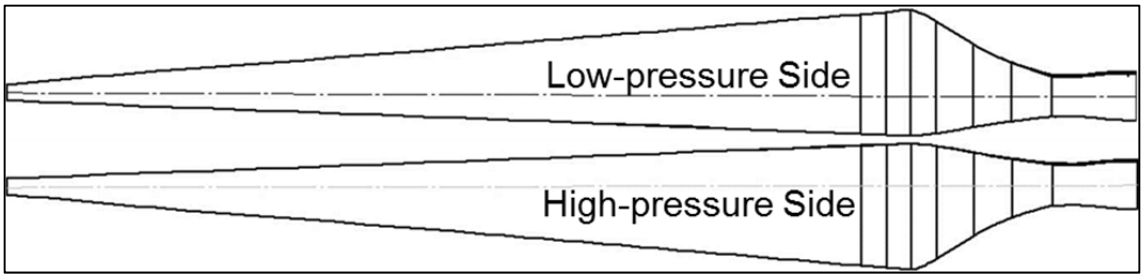

Figure 7: CX-100 rotor blade schematics: low and high-pressure side views.

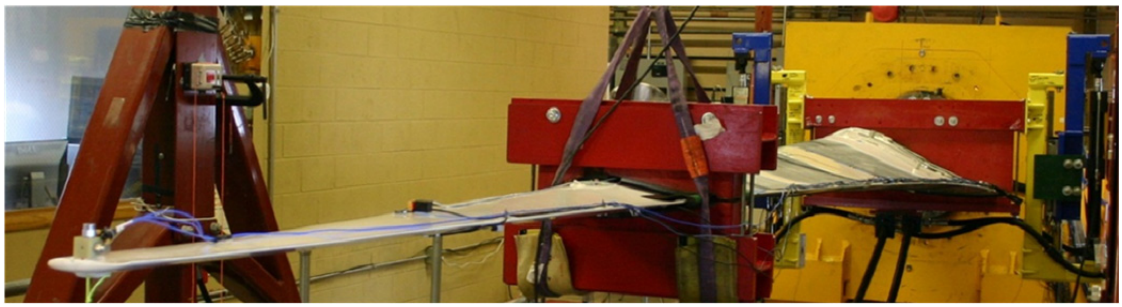

Figure 8: Fatigue test experimental setup

Table 1: CX-100 Resonant Frequencies (Hz) in three configurations

Mode	Free-Free [15]	Fixed-Free [21]	Fixed-Free with UREX [21]
1st Flapwise	7.61	4.35	1.82
1st Edgewise	18.1	6.43	2.68
2nd Flapwise	20.2	11.5	9.23

2.5.2. Instrumentation for Active Sensing

The surface of the rotor blade was instrumented with active sensing arrays composed of APC International D-0.500-0.020-851 PZT transducers, bonded to the surface of the rotor blade using Loctite 234790 cyanoacrylate adhesive. In the root area of the rotor blade, the transducers were installed in three main configurations. On the low-pressure (LP) side, arrays LP-A1, LP-A2 and LP-A3 were arranged as “inner” arrays, observing a 0.75-m diameter region centered on collocated actuators located 1 m from the rotor blade root, while array LP-A4 was arranged as an “outer” array, observing a 2-m elliptical region centered on its actuator located 1.5 m from

the rotor blade root. The “inner” and “outer” designations refer to two concentric array layouts, in which the smaller elliptical array, dubbed the “inner” array, is surrounded by the larger “outer” array. On the high-pressure (HP) side, arrays HP-A2 and HP-A3 were collocated arrays observing a 0.75-m diameter region centered on collocated actuators located 1 m from the rotor blade root. In the case of collocated sensor arrays, multiple PZT patches were installed at each location so that separate data acquisition systems could independently interrogate the same array geometries. The sensor array layout for each PZT array is summarized in Table 2 and depicted graphically in Figure 9. Each sensor path is numbered. The centrally located actuator is labeled ‘A’, and path 0 is the path from the actuator to a collocated sensor, if present.

Table 2: PZT sensor array detail for CX-100 fatigue test

Side of rotor blade	Array No.	Array Designation	Array Config.	DAQ	Collocated Actuator & Sensor	Number of Patches
Low-pressure	1	LP-A1	“Inner”	LASER	Yes	7
Low-pressure	2	LP-A2	“Inner”	Metis	Yes	7
Low-pressure	3	LP-A3	“Inner”	WASP	No	6
Low-pressure	4	LP-A4	“Outer”	LASER	Yes	8
Low-pressure	5	LP-A5	“Linear”	NI	Yes	8
High-pressure	1	HP-A2	“Inner”	Metis	Yes	7
High-pressure	2	HP-A3	“Inner”	WASP	No	6

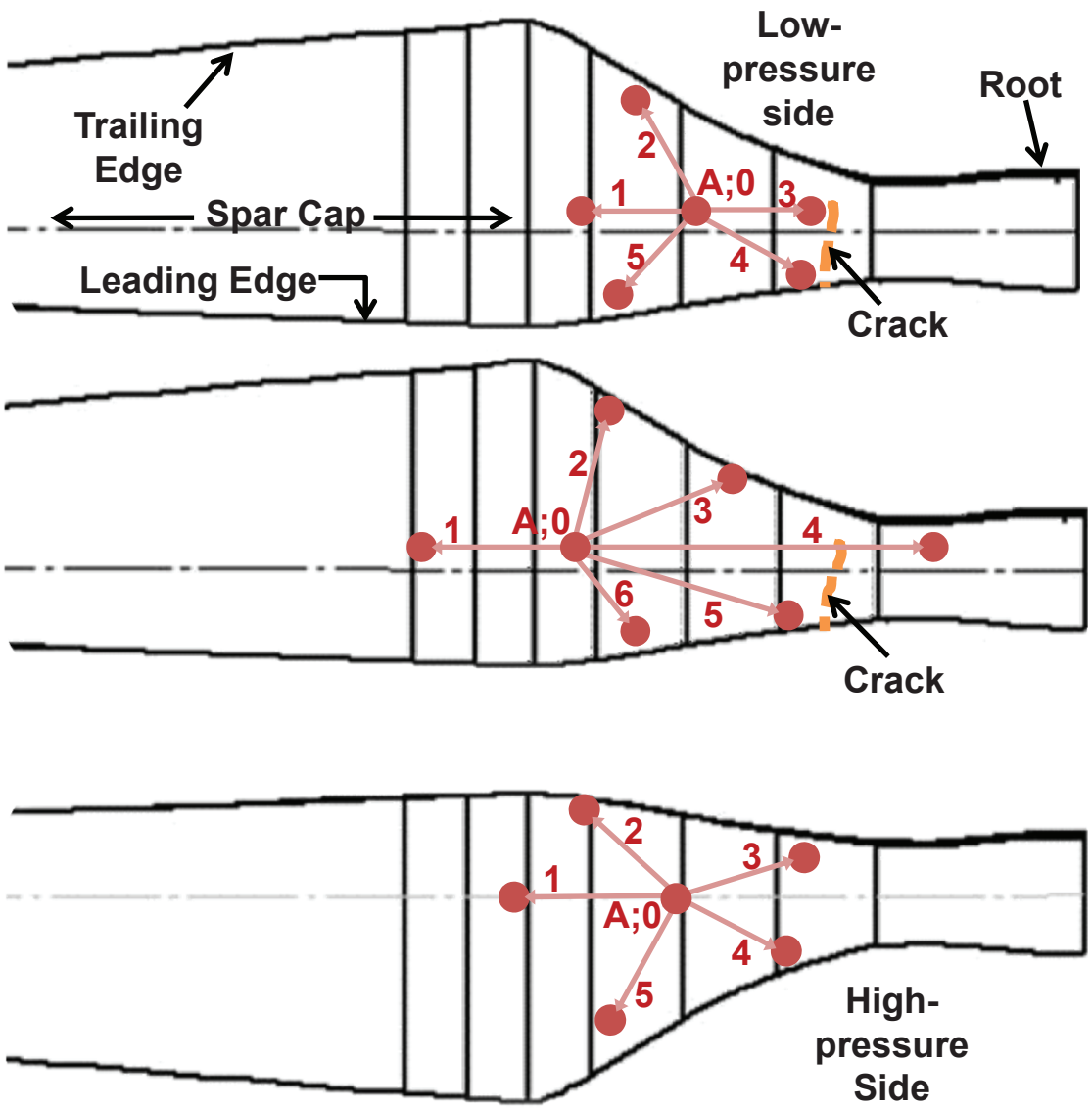

Figure 9: CX-100 root area sensor arrays with marked sensor locations: low-pressure-side inner array (top); low-pressure-side outer array (middle); and high-pressure-side array (bottom)

Arrays LP-A1 and LP-A4 were monitored by a single Bruel & Kjaer LASER data acquisition system using an electronically controlled switch box. The LASER system was employed for diffuse wave field measurements, and it excited the blade while simultaneously measuring its response (referred to as "active interrogation") with band-limited white noise from 500 Hz to 40 kHz, at a sampling rate of 96 kHz. For array LP-A1, a total of 1554 datasets were collected between 05/24/2011 and 11/16/2011. Of these, the first 120 datasets collected

through 08/31/2011 were used as baseline data, including 22 datasets collected prior to 08/11/2011, when the rotor blade first underwent fatigue loading. The remaining 1434 datasets were utilized for detection purposes. For the array LP-A4, a total of 1275 datasets were collected between 05/24/2011 and 10/30/2011. Of these, the first 125 datasets collected through 08/31/2011 were used as baseline data, including 30 datasets taken prior to 08/11/2011. The remaining 1150 datasets were utilized for detection purposes. Only datasets taken through 10/30/2011 were utilized because the actuator patch for the inner sensor array became damaged on that day.

Arrays LP-A2 and HP-A2 were monitored by the MD7 IntelliConnector [22], by Metis Design, which was employed for ultrasonic guided wave (UGW) interrogation over several transmission frequencies ranging from 50 kHz to 250 kHz at a sampling rate of 10 MHz. On the low-pressure side, a total of 709 datasets were collected between 05/24/2011 and 11/16/2011 using the IntelliConnector system. Of these, 88 were used as training data, corresponding to data collected through 08/31/2011. Of the training data, the first 20 datasets were collected prior to 08/11/2011, when the rotor blade first underwent fatigue loading. Data were collected both during fatigue loading and during rest periods. Because data collected during fatigue loading exhibited a time-varying mean, the data were high-pass filtered prior to further processing using an equiripple filter [23] with a cutoff frequency 20 kHz.

Arrays LP-A3 and HP-A3 were monitored by the Wireless Active Sensing Platform (WASP), the prototype embedded sensor node described in Section 3.4, deployed in order to assess its performance in comparison to the commercial systems employed. Because the WASP's firmware was still in development at the start of the test, it was limited for this test to a 50 kHz sampling rate.

Array LP-A5 was monitored by two four-channel National Instruments (NI) 4431 modules linked together to interrogate the 8-patch array. The excitation signal from the NI 4431 modules was band-limited white noise up to 50 kHz, with a sampling frequency of 100 kHz.

2.5.3. Fatigue Test Progression

The fatigue test began on 08/11/2011, and it ran intermittently for approximately 8.5 million cycles until a catastrophic fatigue crack became visible on 11/08/2011. Based on prior fatigue test experience with this blade design, the duration of this fatigue test exceeded three times the expected number of cycles, There is little information available concerning PZT patches in an active-sensing SHM system being subjected to such abusive conditions for this length of time. During the test, some transducers failed and required replacement or repair for various reasons, including cable connection breaks, patch de-bonding, and physical patch fracture. The dates and locations of patch failures are indicated in Figure 10, overlaying a plot of fatigue cycle counts versus date. The transducer failures are divided into three location categories: low-pressure inner array location 3 (LP-I3), low-pressure inner array location 4 (LP-I4), and all other locations. Locations LP-I3 and LP-I4, which are indicated in Figure 9 (top), were directly adjacent the crack, and they experienced the majority of the sensor failures.

Although the catastrophic crack that surfaced on 11/8/2011 was obvious under visual inspection and in terms of its impact on the blade's dynamics, the incipient damage, which beforehand was not obvious in either of those two modes, was first detectable between 10/18/2011 and 10/22/2011 using various methods [24-26], including those presented in Chapter 5. The majority of the sensor failures experienced that did not occur as the crack surfaced on 11/08/2011 were near these dates, around 10/20/2011. In hindsight, the slowly developing crack may have caused some less visibly obvious changes at the rotor blade's surface, further causing some of the sensors in close proximity to fail.

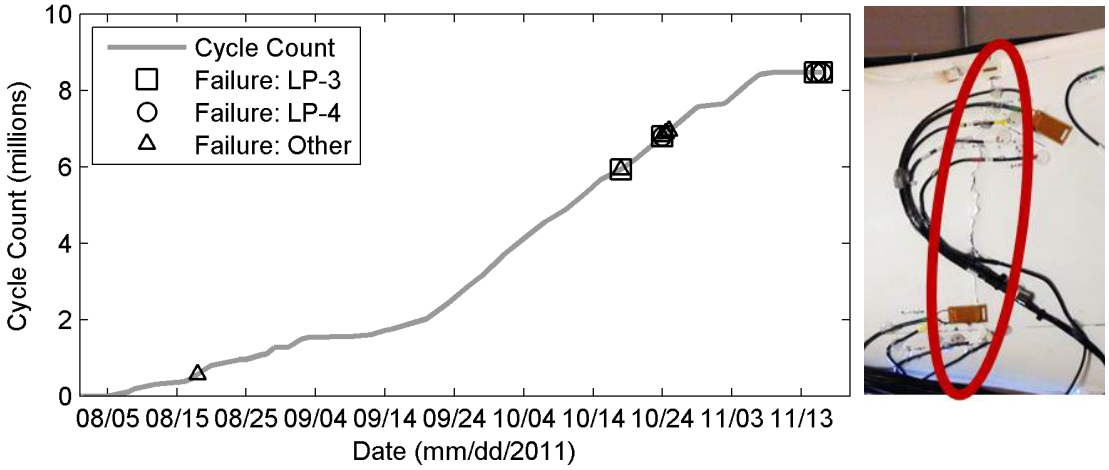

Figure 10: Fatigue cycles versus date with sensor failures indicated by group location (left) and photograph of surfaced fatigue crack (right)

2.6. Vertically Cantilevered Aluminum Beam

An aluminum cantilevered beam was utilized as a surrogate wind turbine blade to test the proposed observer for state estimation. The model parameters are given in Table 3.

Table 3: Model parameters for aluminum cantilevered beam

Parameter	Symbol	Value	Units	Source
Length	L	0. 8382	m	Measured
Density	ρ	2687	kg/m^3	Textbook
Elastic Modulus	E	68.9	GPa	Textbook
Cross Sectional Area	A	83.4	mm^2	Measured
Area Moment of Inertia	I	74.8	mm^4	Calculated from measurements

The beam is depicted in Figure 11 as: (a) the physical beam; (b) a 21-node (10-element) beam model with 3-noded quadratic elements; (c) a 5-node (2-element) beam model; and (d) an SDOF spring-mass model. The beam is vertically cantilevered to a relatively massive (6.5 kg) base that is constrained to move only in the X-direction.

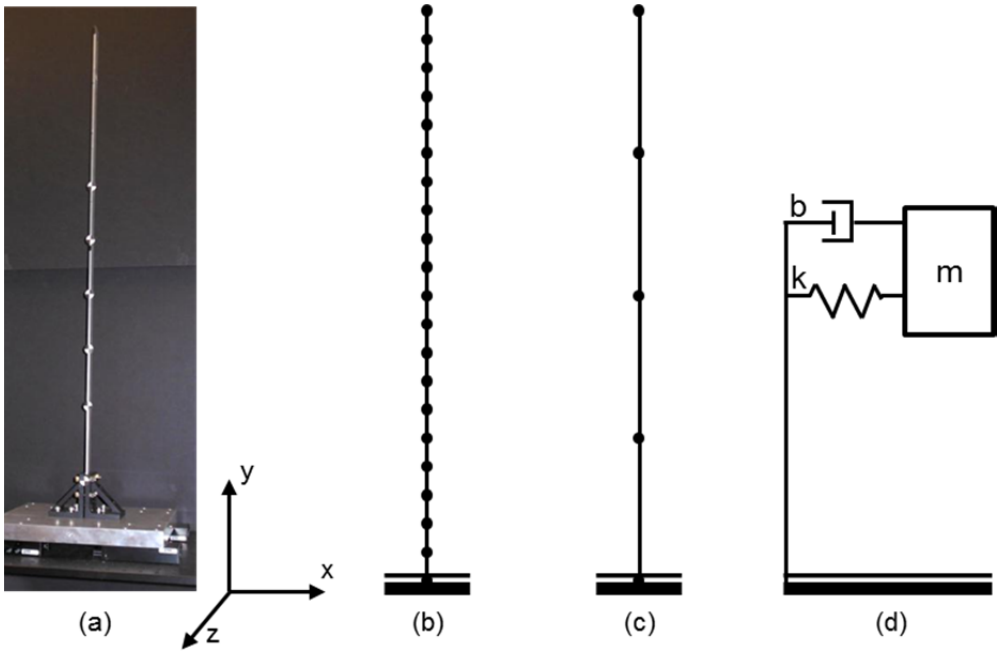

Figure 11: Diagrams of upright cantilevered beams with base excitation

2.6.1. SDOF Model

The beam was modeled as a single-degree-of-freedom (SDOF) system as shown in Figure 11. The stiffness was first computed using Euler-Bernoulli beam theory as $k = (12EI)/L^3$, and the sprung mass was taken as the mass of the beam, $m = \rho AL$. Then, the stiffness value was adjusted so that the natural frequency of the system matched the first resonance of the *NLBeam* model, 3.745 Hz. The value of the damper was selected to achieve 0.2% critical damping. Denoting the motion of the base and of the mass in the X-direction x_0 and x_1, respectively, the system EOM are

$$m\ddot{x}_1 + b\dot{x}_1 + kx_1 = b\dot{x}_0 + kx_0, \tag{2.1}$$

where m is the mass in kg, b is the damping constant in N/(m/s), and k is the stiffness in N/m. Cast in the form of Eq. (6.1), with the base displacement and velocity as the system inputs, the mass acceleration as the system output, the observer system state space matrices are

$$\mathbf{A}=\begin{bmatrix} 0 & 1 \\ -\frac{k}{m} & -\frac{b}{m} \end{bmatrix} \quad \mathbf{B}=\begin{bmatrix} 0 & 0 \\ \frac{k}{m} & \frac{b}{m} \end{bmatrix} \quad \underline{u}=\begin{bmatrix} x_0 \\ \dot{x}_0 \end{bmatrix}$$
$$\mathbf{C}=\begin{bmatrix} -\frac{k}{m} & -\frac{b}{m} \end{bmatrix} \quad \mathbf{D}=\begin{bmatrix} \frac{k}{m} & \frac{b}{m} \end{bmatrix} \quad \underline{x}=\begin{bmatrix} x_1 \\ \dot{x}_1 \end{bmatrix}. \tag{2.2}$$

2.6.2. Numerical Beam

The beam was modeled with the parameters given in Table 3 using *NLBeam*, a research finite element code developed at LANL for the purpose of modeling wind turbine flexible structural components within a multi-physics wind farm simulation code. *NLBeam* implements a geometrically nonlinear, generalized Timoshenko beam theory, capable of representing fully 3D motion as a function of a single beam reference coordinate. However, because the excitation is restricted to act in one direction, and the material for this example is isotropic, the motion is restricted to the planar case, so each node has effectively 3 degrees of freedom (DOFs): translation in X, translation in Y, and rotation about Z. The elements implemented in *NLBeam* are 3-noded elements with quadratic interpolation functions, so the 10-element model has 21 nodes. The equations of motion are solved in *NLBeam* using an implicit Newmark time integration scheme, which for the plant model was implemented with parameters $\beta = 0.5625$ and $\gamma = 1$. These values, defined in the customary manner for Newmark integration [27], were based on a numerical damping value of $\alpha = 0.5$, where α is a numerical analog to percent critical damping, and

$$\begin{aligned} \gamma &= \left(\tfrac{1}{2}+\alpha\right) \\ \beta &= \tfrac{1}{4}\left(1+\alpha\right)^2 . \end{aligned} \tag{2.3}$$

2.6.3. Experimental Beam

Simultaneous acceleration and video data were collected from the beam as it underwent base excitation at a frequency near its first resonance. The video data were captured using a Photron FASTCAM 512PCI, which recorded a 512x64 pixel image at 250 frames per second. For the distance at which the video data were collected, the camera covered the 0.8382m length of the beam in 440 pixels, or 1.9mm per pixel. The base excitation motion was visually observed to be ~3 mm peak-to-peak, so that motion could be captured by the camera using at most 3 pixels, depending on the exact location of the motion with respect to the camera's lens. Because of the low camera resolution, the measured displacement was highly quantized; the measured displacement time traces are plotted for the beam tip, midpoint, and base in Figure 12. The camera was controlled by a dedicated desktop PC, and a camera trigger signal was routed to a National Instruments PXI chassis, which also recorded the signals from accelerometers mounted on the beam. In this manner, time-synchronized acceleration and video data could be collected.

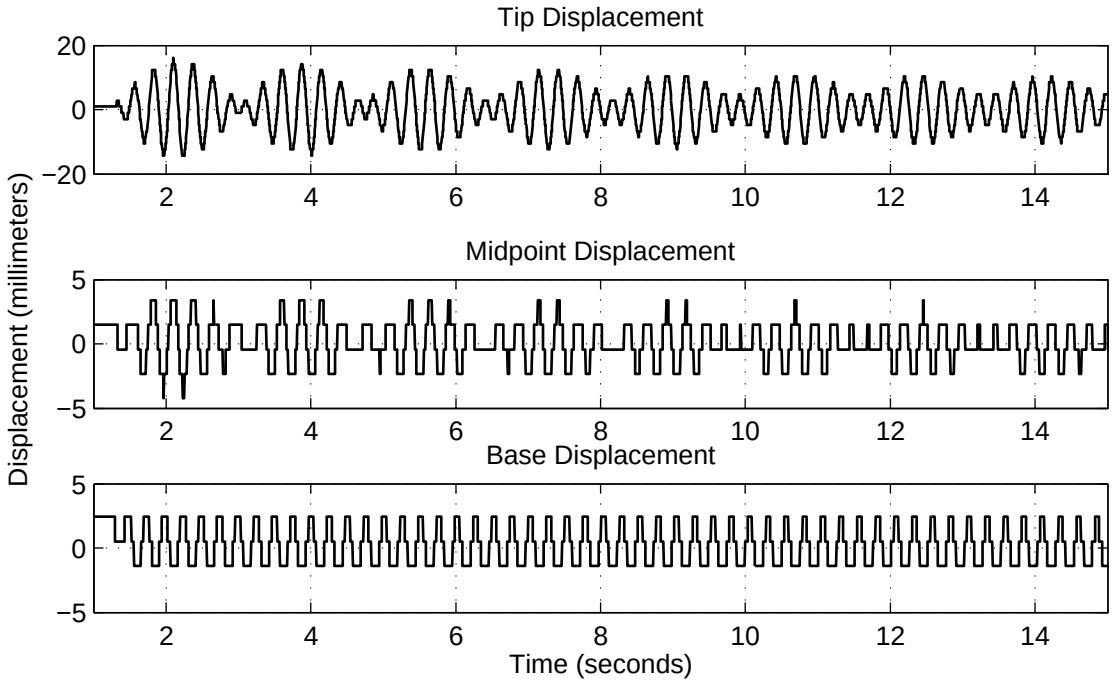

Figure 12: Measured beam displacement using high-speed, low-resolution camera

Two PCB Piezotronics 354C10 triaxial accelerometers were mounted on the beam at its tip and midpoint. Acceleration data were recorded in the x and y directions in the beam coordinate system, as defined in Figure 11. The base plate was physically excited using an Agilent 33210A arbitrary waveform generator connected to a Techron model 5530 power supply amplifier, which drove a Vibration Test Systems electrodynamic shaker. The shaker was connected to the base plate using a 0.25-inch (6.4-mm) diameter stinger through a PCB Piezotronics 208C02 force transducer, which measured the force between the shaker stinger and the aluminum base plate to which the beam was vertically cantilevered, and which was constrained along linear bearings to slide only along the x direction. On the opposite side of the aluminum base plate, a PCB Piezotronics 352C22 uniaxial accelerometer was mounted to measure the corresponding base acceleration. The accelerometers were calibrated using a handheld PCB Piezotronics 394C06 calibrator, and the values are listed in Table 4.

Table 4: Accelerometer locations and calibration values

Coordinate Direction		Accelerometer Serial Number (Location on Beam) and Calibration (mV/(m/s^2))		
Accelerometer Coordinates	Beam Coordinates	SN 3186 (Tip)	SN 2899 (Midpoint)	SN38951 (base; uniaxial)
Z	X	0.878	0.985	1.057
X	Y	0.922	0.789	

Although the input signal to the shaker was a pure sinusoid, the shaker utilized was slightly broken, and it introduced significant harmonics into the motion of the base plate. These harmonics are well-captured by the force transducer and the base plate accelerometer, and because the excitation control is open-loop only, it is more important that the input is measured than that the structure be excited with a particular waveform.

2.7. USDA/ARS CPRL LIST Turbine

A Micon 65/13 wind turbine was utilized as a test bed for operational deployment of a multi-scale sensing system. This turbine was part of the Long-Term Inflow and Structural Test (LIST) program at the US Department of Agriculture's (USDA) Conservation and Production Research Laboratory (CPRL). The LIST facility and two turbines are shown in photographs in Figure 13. Located in Bushland, TX, the CPRL is part of the USDA's Agricultural Research Service (ARS). The site was selected because it is representative of a commercial wind energy production site in the Great Plains. The Micon 65/13 model turbine at the CPRL has a 115 kW-rated generator, and while modern utility scale turbines are at least an order of magnitude larger. The Micon 65/13 model wind turbine was a popular production turbine in the 1980s, and the particular turbine utilized in this work was a used turbine that had been in production service in the Palm Springs, CA area. The LIST is described in detail by Jones, Sutherland and Neal in [28], and has been reported on extensively by Sutherland et al. [29-34]. More recently, White et

al. have utilized this Micon 65/13 wind turbine as the subject of structural monitoring investigations using inertial measurements [35-38].

In the experimental application presented in this dissertation, the Micon 65/13 was equipped with three 9-m CX-100 blades, of the same design as that utilized for the fatigue test described above. Each blade was equipped with two triaxial and two uniaxial accelerometers. The accelerometers were positioned on the side high-pressure at 2m and 8.15m from the root, with the triaxial accelerometers positioned near the leading edge, and the uniaxial accelerometers positioned near the trailing edge. The rotor blades were also instrumented with fiber Bragg grating optical strain gauges with unbounded, collocated FBGs for temperature compensation. The strain measurement points were on the HP side, aligned with the triaxial accelerometers, located at 2.2m, 4.5m, and 7m from the blade root. In addition to these sensors, one blade was manufactured with four internally embedded PZT patch arrays, monitoring the leading edge, trailing edge, spar cap, and root area of the blade.

Figure 13: USDA CPRL LIST turbine facility: control building and turbine “A” (left); turbine “B” (right)

2.8. Summary and Acknowledgements

This chapter has provided details of several experimental platforms utilized throughout the dissertation work.

Section 2.2 has been published in part in [1] *Smart Structures and Systems,* S. G. Taylor, K. Farinholt, G. Park, M. Todd, and C. Farrar, 2010. The title of this paper is "Multi-scale wireless sensor node for health monitoring of civil infrastructure and mechanical systems." The dissertation author was the primary investigator and author of this paper.

Section 2.3 has been published in part in [2] *Measurement Science and Technology,* S. G. Taylor, K. M. Farinholt, E. B. Flynn, E. Figueiredo, D. L. Mascarenas, E. A. Moro, G. Park, M. D. Todd, and C. R. Farrar, 2009. The title of this paper is "A mobile-agent-based wireless sensing network for structural monitoring applications." The dissertation author was the primary investigator and author of this paper.

Section 2.4 has been published in part in [3] *Journal of Structural Engineering,* C. J. Stull, S. G. Taylor, J. Wren, D. L. Mascareñas, and C. R. Farrar, 2012. The title of this paper is "Real-Time Condition Assessment of RAPTOR Telescope Systems."

Portions of Section 2.6 have been submitted in part to [9] *IMAC XXXI: A Conference and Exposition on Structural Dynamics*, S. G. Taylor, D. J. Luscher, and M. D. Todd, 2013. The title of this paper is "State estimate of wind turbine blades using geometrically exact beam theory." The dissertation author was the primary investigator and author of this paper.

Other portions of Section 2.6 are currently being prepared for publication [10]. S. G. Taylor, D. J. Luscher, and M. D. Todd, 2013. The title of this paper is "Nonlinear state observer for structural monitoring of wind turbine rotor blades." The dissertation author was the primary investigator and author of this paper.

Sections 2.5.1 and 2.5.3 have in part been submitted to [7] *Structural Health Monitoring,* S. G. Taylor, G. Park, K. M. Farinholt, and M. D. Todd, 2012. The title of this paper is "Fatigue crack detection performance comparison in a composite wind turbine rotor blade." The dissertation author was the primary investigator and author of this paper.

Section 2.5.2 has been published in part in [6] *Smart Materials and Structures,* S. G. Taylor, G. Park, K. M. Farinholt, and M. D. Todd, 2012. The title of this paper is "Diagnostics for piezoelectric transducers under cyclic loads deployed for structural health monitoring applications." The dissertation author was the primary investigator and author of this paper.

Chapter 3
Embedded Sensing

3.1. Introduction

This chapter focuses on embedded sensing, with a review of current research in embedded sensing, sensor nodes, and sensor networks. Section 3.2 reviews applications of sensor networks and sensor nodes found in the literature, as well as current and recently developed sensor nodes for embedded SHM, including research platforms and commercial-off-the-shelf (COTS) devices. Sections 3.3 and 3.4 present two specific sensor nodes for embedded SHM developed as part of this dissertation: the Wireless Impedance Device v3 (WID3); and the Wireless Active Sensing Platform (WASP). Their features are detailed, with specific emphasis on their innovations and unique contributions to embedded sensing for SHM. Demonstration and deployment examples are also presented for these sensor nodes.

3.2. Literature Survey

3.2.1. Networks for Embedded Sensing

Structural Health Monitoring requires the collection of measurements from a structure in operation and processing those measurements to make decisions about the ability of the structure to perform its intended function. These systems will require a communications network so that measured data can be shared and processed, whether in a centralized or decentralized manner. Some examples of communications networks for SHM systems, detailed by Farrar et al. [39], are described below.

In a wired network with central processing, any number of devices with potentially large power requirements collects and transfer data from the transducers to a central processing location, which is often a nearby PC, but may be an off-site location. The centralized approach is the most common network type for SHM systems and can be easily implemented in an ad hoc manner for small systems, but it has the disadvantage for large installations [40] that cable management and sensing infrastructure maintenance become unwieldy [41].

A wireless sensor network implementing a hopping protocol can overcome many of the disadvantages of wired systems, especially for large installations [41-43]. Wireless communication can remedy the cabling issues with the traditional monitoring system and significantly reduce the maintenance costs. With standardized communications protocols including IEEE 802.11 through 802.16 (e.g., Wi-Fi, Bluetooth, and ZigBee), data transfer is more robust, and transfer rates can approach those of wired networks. Some of the technical challenges for wireless sensor networks include the uncertain and often harsh deployment environments, the need for autonomous reconfigurability in order to maintain robustness against individual node failures or to permit network expansion, data security for sensitive information, and the potential need to integrate with both mobile and stationary network devices. A major

consideration in deploying a wireless sensor network is that of powering the nodes, leading to a trade-off between local computation and radio transmission. Zimmerman et al. developed a parallel processing algorithm using a wireless sensor network to address this very issue [44]. Ambient energy harvesting may be sufficient to operate the nodes for short periods of time, [45], but the interplay between local computation and data transmission must be carefully balanced with the amount of energy available.

A combined approach to communication and powering, first demonstrated by Mascarenas et al. [46, 47] integrates wireless energy transmission technology and remote interrogation platforms based on unmanned vehicles to assess damage in structural systems. An example of this type of network is shown in a photograph in Figure 23 as part of the field demonstration described in Section 3.3.4. This approach involves using an unmanned mobile-host node (delivered via UAV or robot) to deliver radio-frequency (RF) power to rectifying antennas connected to embedded sensor nodes. Operating on transmitted RF energy, the sensors measure the desired response at critical areas of the structure and transmit the signal back to the mobile-host.

In this dissertation, the mobile-agent paradigm has been extended to support a hybrid network configuration, with multiple localized sensor networks within a single structure. This hybrid networking approach would be useful following critical or catastrophic events, where the data from one network could be used by the mobile-agent to identify the next network it should interrogate, enabling the mobile-agent to bypass certain networks and interrogate those likely to have the most pertinent data for emergency response or security personnel. Furthermore, this approach can be used in a combined powering configuration where the sensor node equipped with energy harvesting devices could be supplied supplemental energy by the mobile-agent. If the energy harvesting device provides sufficient power, the mobile-agent can wirelessly trigger the sensor nodes, collect information and provide computational resources, further reducing the

power demand at the sensor node level. This networking approach has contributed to research in the field of distributed sensing for SHM and other applications [48-52].

3.2.2. Embedded Sensor Nodes

As the technology that enables embedded sensing becomes more compact, inexpensive, energy efficient, and computational powerful, researchers in structural health monitoring (SHM) and related fields have been integrating more sophisticated sensing capabilities into structural assets. While some very large structures can support full-sized, permanently installed data acquisition systems, such as the well-known Tsing Ma Bridge in Hong Kong [40], structures designed with little or no carrying capacity beyond their own self-weight, such as a wind turbine rotor blade, may demand a compact, lightweight, embedded system. Each embedded system installation brings specific challenges in terms of communications, data collection, and system power. In terms of power consumption, embedded sensor nodes for SHM generally fall either into the “low-power” or the “wall power” categories. Low-power sensor nodes typically have limited functionality, minimal processing capabilities, and are often intended for use with energy harvesting systems [53, 54]. In this loose definition, wall-power systems may draw 1W or more, far less than a standard data acquisition (DAQ) system or desktop PC, but, except at very low duty cycles, they would be beyond the serviceability of most energy harvesting systems, with the exception of reliable solar power. These systems may have more sophisticated signal conditioning circuitry, onboard processing, and may have the ability to mechanically excite the structure, which is required for active sensing.

Advances in impedance-based methods for SHM [55, 56], the development of sensor diagnostics methods for the piezoelectric transducers that implement them [6, 56, 57], and the availability of low-power integrated circuits (ICs) for impedance measurement, such as the AD5933 from Analog Devices, have combined to unleash a deluge of low-power, impedance-

based sensor nodes on the SHM community. Some of these nodes are listed in Table 5. The wireless impedance device (WID) series of sensor nodes [1, 58, 59] is a prime example low-power, impedance-based wireless sensor nodes (WSNs), with applications to civil infrastructure monitoring [2, 11]. Similar devices have been developed with applications to damage detection in lab tests and on a bridge structure [60]. In addition to impedance measurements, low-power sensor nodes have been applied to fatigue cycle counting [61] and force input estimation [62].

Although the impedance method is an active sensing method, it is limited to detecting highly localized changes in structural behavior. Advances in SHM with active sensing techniques, especially guided wave-based methods, have motivated the development of (necessarily) higher power devices with arbitrary waveform excitation capability. The wireless active sensing platform (WASP) trades low-power operation for greater computation and structural excitation capabilities. Two devices similarly designed for active-sensing SHM, listed in Table 5, are the commercially available IntelliConnector node [22], which has been applied to detect damage in a mock naval structural panel [63], and the SHiMmer active sensing node [64] which has been applied to detect loose bolts in a highway bridge using a sparse sensor array [65].

Active sensing methods for SHM are often restricted to purely empirical implementation, with emphasis placed on numerical damage indices, rather than incorporating data into an appropriate physics-based model. Applications of the impedance method tend to focus on small, local changes, such as loosened bolts or crack formation in specific, predetermined areas, because it is difficult to develop a physical model that correctly reflects these small changes on a local scale. In attempt to address this issue and incorporate existing structural models into the SHM process, researchers have begun implementing multi-scale sensor nodes. The wireless data acquisition (WiDAQ) extension for the WID3 demonstrated the ability to collect low-frequency vibration data for modal analysis in addition to the node's core

impedance function [2]. Some recent work has aimed to extend the iMote2 to multi-scale SHM applications [66, 67], by including an accelerometer connected to spare analog input channel on the iMote2's SHM board, utilizing both measurements in a multi-scale SHM assessment of a test structure. The WASP implements multi-scale sensing functionality on a single platform, using a single 6-channel analog-to-digital converter (ADC) to record passive, low-frequency sensor output or transducer response to simultaneous, high-frequency excitation.

As power requirements and size of electronics decrease, and as wireless communication becomes more advanced, conventional systems for data acquisition are becoming more suitable for SHM applications. Such devices that could be utilized for SHM include the G-Link accelerometer sensor nodes by MicroStrain, and the WLS-9163 Wi-Fi module carrier from National Instruments equipped with an appropriate acquisition module. These devices are still power intensive compared to the low-power sensor nodes described above, and they perform no operations other than data acquisition and telemetry, but they could certainly be integrated into a functional, deployed SHM system.

Table 5: Sensor Nodes in SHM Literature

Node	Power	Purpose	Reference
Imote2 SHM Module	200 mW	Acceleration	[68]
WID 1.5	75 mW	Impedance	[58]
WID 3	75 mW	Impedance	[1]
SHiMmer	1 W	Active Sensing	[69]
MicroStrain G-Link	1 W	Acceleration, Strain	
NI WLS-9163	4.5 W	General	
IntelliConnector	10 W	Active Sensing	[22]
WASP	1 W	Active Sensing, Impedance, General	[4]

3.3. Wireless Impedance Device

3.3.1. Development and Design

The wireless impedance device (WID) was originally developed based on capabilities demonstrated in previous studies of impedance-based structural health monitoring [55]. In the Impedance method, changes in the electrical impedance of a piezoelectric material bonded to a structure are attributable to mechanical changes in the host structure. The theory underpinning impedance-based SHM is described in detail in Section 4.2. Because the impedance method is an inherently local measurement technique requiring no appreciable propagation of a mechanical wave through the structure, it can be implemented with much lower power than the wave-based active sensing techniques typically implemented with the same transducers. The impedance method is uniquely suited for sensor self-diagnostics, the focus of Chapter 4, because of its sensitivity to transducer boundary conditions [6, 57].

The Wireless Impedance Device is a low-power sensor node specifically designed to implement impedance-based SHM [58, 70]. In Figure 14, three generations of WID designs are shown together, including theWID3, which improved on the field utility of the prior versions and enabled the integration of the device into a multi-scale sensing system. Although the impedance measuring function of the WID3 is the same as for prior versions of the node, its unique capabilities include its energy harvesting circuitry and its versatility in implementing various sensor network paradigms for SHM.

In general utility, the WID3 provides increased capabilities over the previous generations, with advanced communication capabilities, increased triggering options, data storage capabilities, as well as multiple powering options coupled with a power-conditioning circuit that permits its use with a variety of energy harvesting sources. Using the 802-15.4-based ZigBee protocol, the WID3 can self-configure into a network with neighboring sensor nodes at

fixed time intervals or in the presence of a mobile-host that physically approaches and interrogates the sensor network. The WID3 has been designed to operate using multiple power options, utilizing onboard storage capability to operate from energy harvested from the environment or RF energy transmission.

Furthermore, the WID3 was designed to function as part of a modular hardware platform that incorporates time-domain sensing capabilities on separate boards. By combining modules, resources such as the telemetry, processing, data storage, and the respective measurement capabilities of each module can be shared, increasing the functionality of the overall sensor node. One such configuration is shown in Figure 14 (right), where the WID3 has been combined with a data acquisition (DAQ) board. This combined modular sensor node, dubbed the WiDAQ, aimed to combine high-frequency impedance measurements and low-frequency passive sensing capabilities in a single package, providing the ability to implement multiple SHM techniques. The WID3 system and its unique capabilities have been presented in several journal publications and conference proceedings, including [2, 12, 13, 59, 71-74].

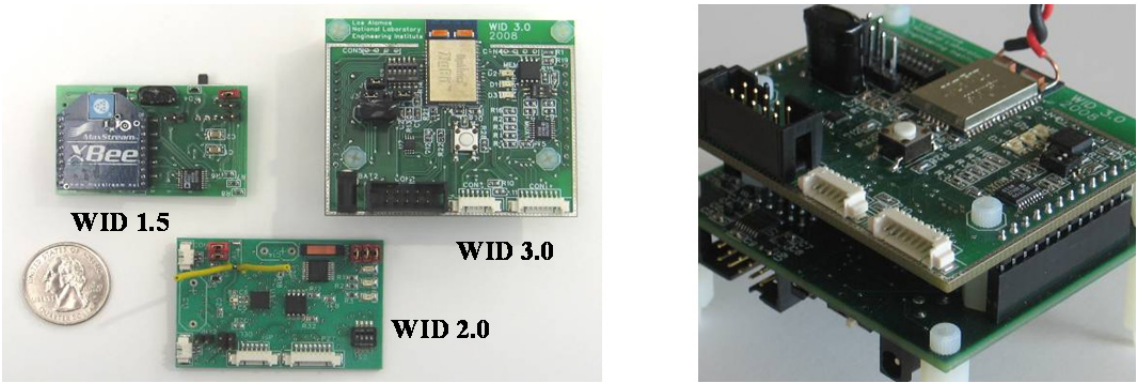

Figure 14: Three generations of wireless impedance devices (shown left) and the combined WID3 / WiDAQ module (shown right)

The major hardware components of the WID3 are shown in Figure 15. The WID3 is controlled by an 8-bit ATmega1281v microcontroller, which controls the primary measurement

device, an Analog Devices AD5933 impedance chip, and the transceiver, an Atmel AT86RF230 802.15.4-compliant radio. The microcontroller and transceiver are packaged together in the Meshnetics ZigBit module. The AT86RF230 has very low energy requirements and low external component counts, making it particularly attractive for an embedded SHM device. The AD5933 impedance chip has many built-in functions that ordinarily require several additional components, including a signal generator, high-speed analog-to-digital converter (ADC), fast Fourier transform (FFT) analyzer, high-speed digital-to-analog converter (DAC), and anti-aliasing filter. While the packaging of all these components in a single chip allows for convenient, low-power impedance measurements, the lack of flexibility precludes the use of the WID3 for other active sensing techniques, such as those requiring controllable excitation waveforms or the use of multiple sensors engaged simultaneously.

The WID3 has also been designed with specific operating modes for field-deployability, and it can be woken from sleep states in several ways depending on the deployment mode. The WID3 includes a low frequency wake-up chip, the ATAK5278, which monitors an inductor antenna for a 125 kHz wake-up signal. This monitoring occurs at very low power (<1μW), but at limited range of only up to 2.5m. The ATAK5278 chip is shown in Figure 15, and the inductor coil antenna is located directly opposite the PCB from it. This wake-up capability would be used for on-demand measurements wirelessly triggered by a mobile base station, which receives the data telemetered by the WID3 on completion of a measurement. The second wake-up option is an internal timer in the ATmega1281v that can wake the WID3 at intervals from on the order of a few seconds (limited primarily by the WID3's start-up time) to a few weeks, permitting an extremely low duty cycle operating mode.

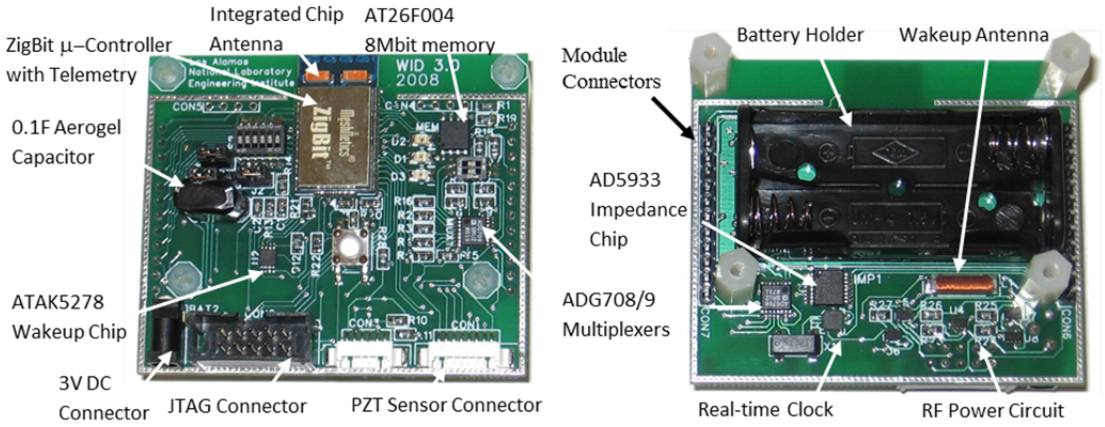

Figure 15: Major components of the WID3

The WID3 has multiple powering options, all of which can also be utilized to communicate to the WID3 the desired behavior on power-up or awakening. From a zero-power state, the WID3 can be initialized by powering it through its 0.1F Aerogel capacitor, controlled by the energy harvesting switch circuit, either through harvested energy or RF transmission. In one mode of operation with RF energy, the WID3 could default to a sleep state on power-up, and by concurrently utilizing the WID3's wake-up chip, it could be instructed to perform context-specific tasks, such as transmitting stored measurements to an inspector's computer or collecting additional, on-demand measurements. From a low-power sleep state maintained by an energy harvester or a small rechargeable battery, the low-frequency trigger or the WID3's internal timer can be utilized to collect on-demand or scheduled measurements, respectively. With these solutions available, the WID could run in low duty cycle operation with additional on-demand measurements indefinitely using an energy harvester and a small local power storage capability.

In order to prevent the charge in the storage capacitor from being drained by attempts at powering the microcontroller, an ultra-low power switch originally developed by Mascarenas et al. [75] was adapted for use with the WID3 [53, 76]. One innovation of the switch developed for

the WID3 was that, in addition to withholding energy from the node until the storage capacitor reached a predetermined voltage level, it would turn off after the capacitor dropped below a lower, predetermined level. This action permitted a pre-charge to be maintained on the storage capacitor, which would increase the effective duty cycle of the sensor node. The diagram of the switch as implemented on the WID3 is shown in Figure 16. Figure 17 shows the response of a free 0.1F capacitor being charged directly with RF energy and the WID3's operational voltage level with the same charging method. Until the capacitor reached its critical voltage, no energy was released to the sensor node. After reaching the critical voltage of 3.6 V, the WID3 powered on, took the measurements, and wirelessly sent the data before the voltage dropped below the pre-defined 2.7V pre-charge level. With the 2.7V pre-charge, the time required to obtain repeat measurements was significantly reduced.

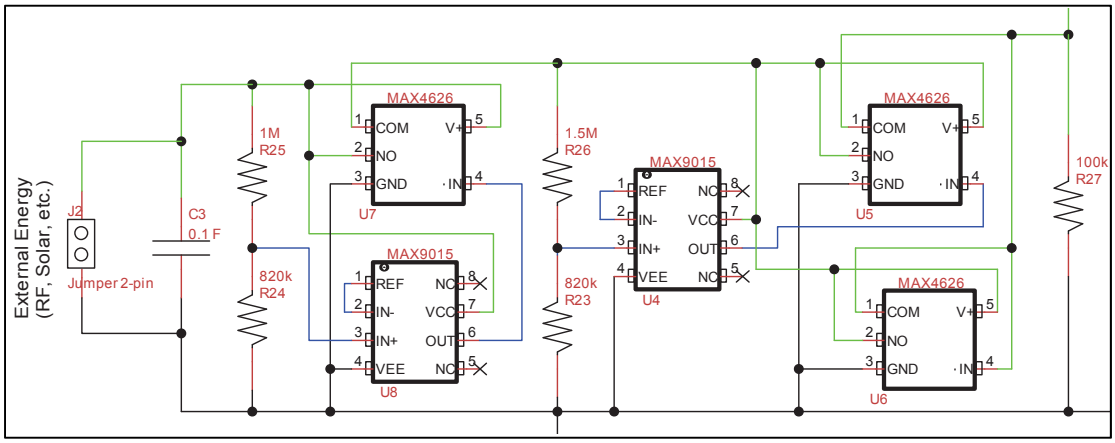

Figure 16: WID3 extremely low-power switch architecture

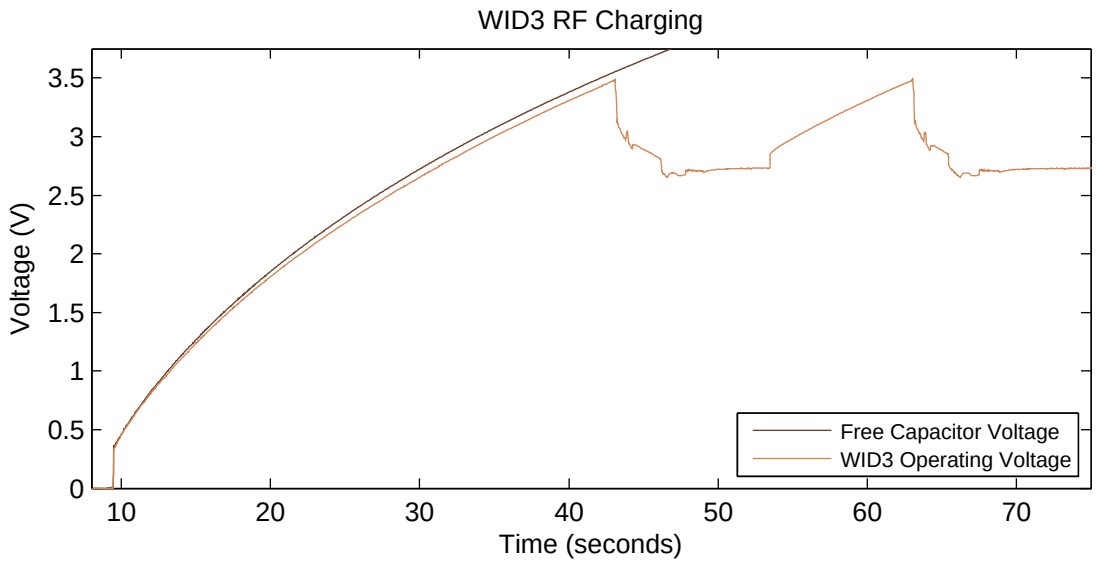

Figure 17: RF energy charging response of a 0.1F capacitor and the WID3 operational response

3.3.2. DAQ Board Hardware and Capabilities

A data acquisition (DAQ) board was developed to extend the capabilities of the WID3 system to collect low frequency measurements from a variety of sensors providing a voltage output, such as accelerometers or strain gauges. The combined modular sensor node, the WiDAQ, is shown in Figure 14 (right). The major components of the DAQ board are shown in Figure 18. The DAQ board is controlled by a dedicated ATmega1281 microcontroller, but it lacks its own telemetry. Having its own microcontroller, the DAQ board could function as a stand-alone device using wired communication, but it is primarily intended to be used in combination with the WID3. The module connectors, indicated both in Figure 15 and Figure 18, provide each module with the ability to share resources, including processing power, data storage, and telemetry.

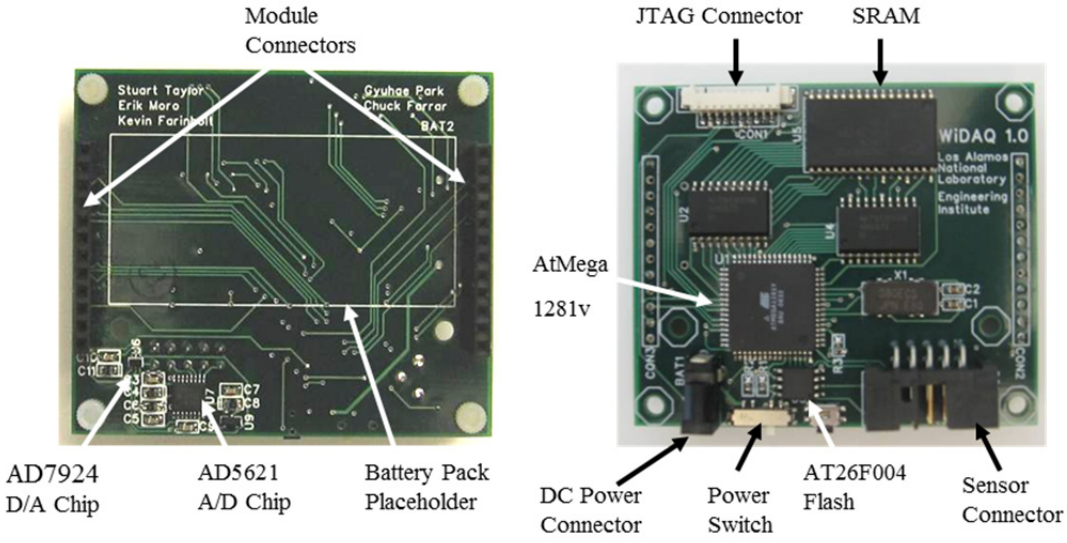

Figure 18: WiDAQ Components

The DAQ board was intended to support both data acquisition and signal generation, so it was equipped with an Analog Devices AD7924 analog-to-digital converter (ADC) and an Analog Devices AD5621 digital-to-analog converter (DAC). Sensor-specific conditioning circuitry was excluded from the WiDAQ, so any specific conditioning requirements, such as ICP™ for accelerometers, was provided on another PCB. The four-channel AD7924 has a 12-bit resolution over a range from zero to 2.5 Volts, and when controlled by the ATmega1281, had a maximum useful sampling rate of 40 kHz. Although the DAQ board was intended for both passive and active sensing, the Analog AD5621 DAC was not used for any active sensing tests because (1) no signal amplification capability was included in the module, and (2) the design did not permit the synchronization of the ADC and DAC at sufficiently high frequencies for active sensing applications. These issues were remedied in the design of the WASP, described in Section 3.4.

3.3.3. WID3 Demonstration: Impedance Measurements

This section presents experimental results for sensor diagnostics using the aluminum plate test platform described in Section 2.2. The raw data collected using the WID3 and the processed results obtained using the instantaneous baseline [56] method for sensor diagnostics implemented in the SHMTools software package [69] with these data are shown in Figure 19 for data collected from seven sensors, two of which were in a debonded condition, and in Figure 20 for data collected from seven sensors, two of which were in a broken condition. In each case, the sensor conditions were correctly identified.

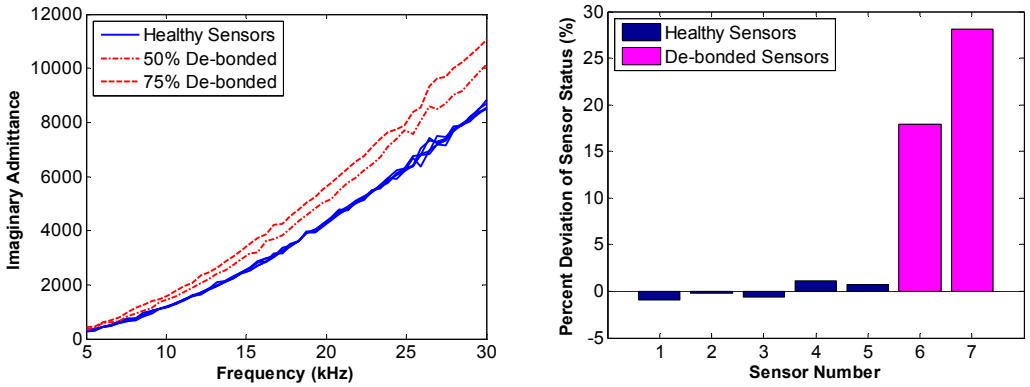

Figure 19: Raw scaled admittance data with two partially debonded sensors collected with the WID3 (left) and auto-classification results from SHMTools (right)

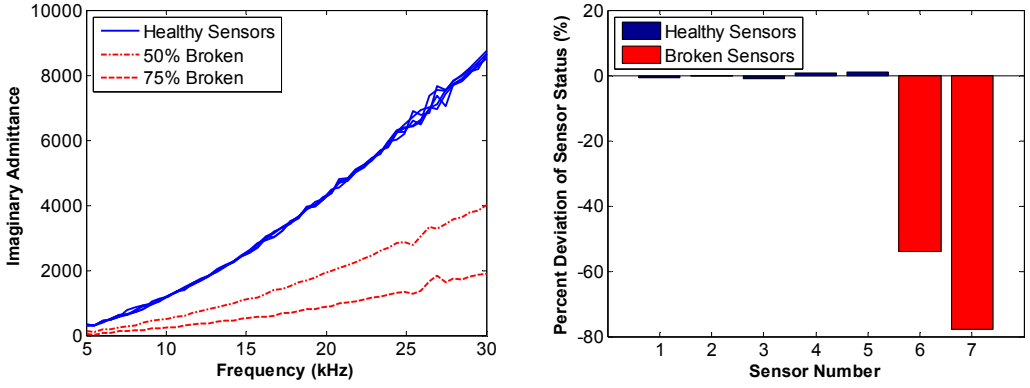

Figure 20: Raw scaled admittance data with two partially broken sensors collected with the WID3 (left) and auto-classification results from SHMTools (right)

3.3.4. WiDAQ Demonstration: Modal Analysis

The WID3/WiDAQ system was used to collect time-domain vibrational data for modal analysis. The experimental setup with the sensor node network and test structure is shown in Figure 21. Two WID3/WiDAQ nodes with ICP conditioning boards were wirelessly networked with a commercially available development board for the microcontroller/ transceiver package. The experimental setup with the sensor network is shown in Figure 21. Four PCB 352A24 accelerometers were mounted on the test structure and connected to Node A, and a PCB 086C03 impact hammer was connected to Node B.

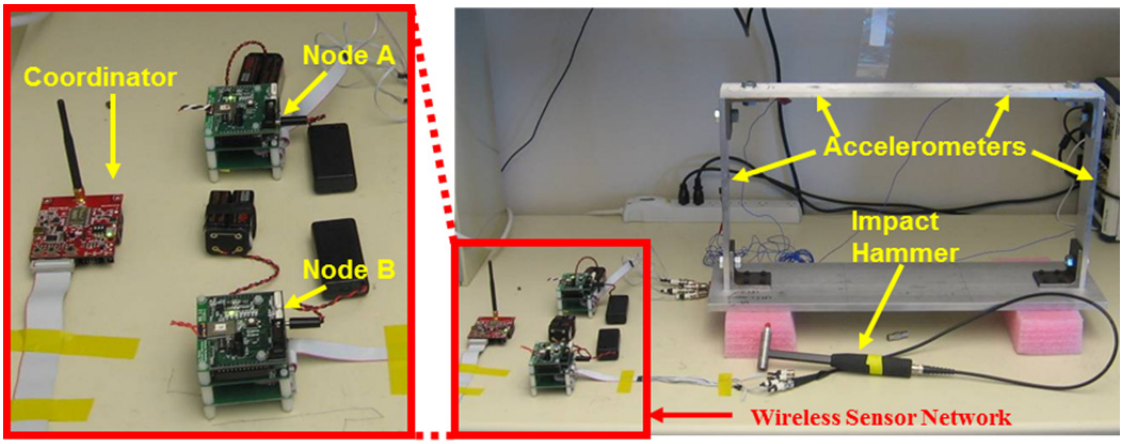

Figure 21: Experimental setup for modal testing using the WiDAQ system

The wireless network implemented in this experiment utilized a “star” topology, in which the coordinator communicated directly with each sensor node. The coordinator was connected to a laptop computer using a serial port. On command, the coordinator broadcasted an instruction to the two sensor nodes to begin recording sensor data simultaneously. The nodes recorded at 969 Hz for just over 4 seconds and stored the results in nonvolatile memory. After completing the measurement, each sensor node transmitted its buffered results to the coordinator, which relayed them to the laptop for analysis. Frequency response functions were

estimated using the recorded data, and the test structure's resonant frequencies and mode shapes were extracted using the rational polynomial curve-fitting method implemented in DIAMOND, a modal analysis software package developed at Los Alamos National Laboratory [77]. The extracted resonant frequencies and mode shapes were compared with those obtained using data collected using a conventional 4-channel Dactron™ data acquisition system. The extracted resonant frequencies using each system and the modal assurance criterion (MAC) between the two sets of extracted mode shapes are shown in Table 6 for the first four modes of vibration.

Table 6: Test structure natural frequencies and MAC values

Mode No.	Measured Frequencies (Hz)		Dactron and WID3/WiDAQ Cross-MAC			
	Dactron	WID3/WiDAQ				
1	71.42	70.94	**0.97**	0.01	0.00	0.15
2	106.02	105.98	0.00	**0.94**	0.68	0.00
3	185.82	185.68	0.01	0.68	**0.98**	0.01
4	287.26	287.27	0.19	0.00	0.00	**0.88**

In this experiment, the correlation between two sets of mode shapes was less than desirable. Some discrepancies between the mode shapes extracted using the traditional data acquisition system and the WiDAQ system can be seen in a line plot of the deformed structure, shown in Figure 22. These discrepancies might be improved by the use of a higher resolution ADC, or they could be the result of discrepancies in the time-synchronization between the two end devices.

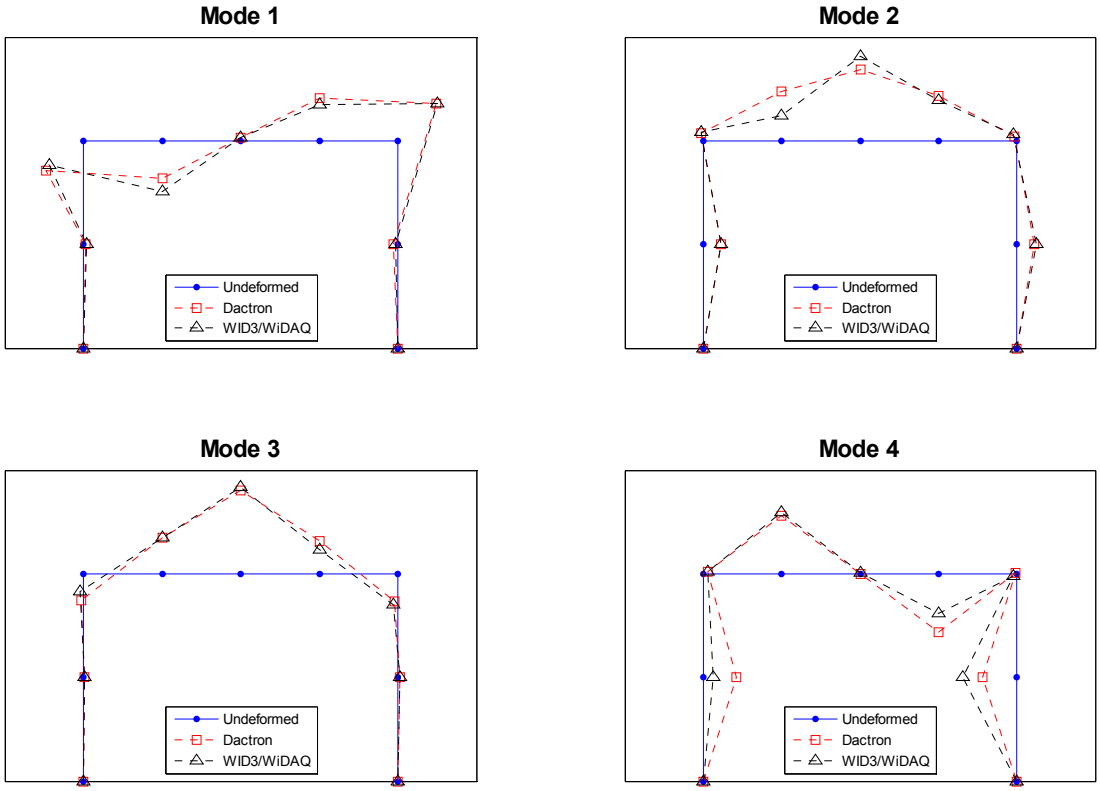

Figure 22: Line plots of the first four mode shapes obtained using the Dactron and WiDAQ systems

3.3.5. WID3 Deployment: Alamosa Canyon Bridge

The WID3 was deployed on the Alamosa Canyon Bridge, an experimental platform described in Section 2.3, for various tasks related to sensor networking and damage detection. Eight sensor nodes were mounted along the longitudinal rails of the bridge. Four sensor nodes installed along the east side of the bridge are shown in Figure 9. The nodes were spaced at intervals of 5 meters. The sensor nodes were mounted on top of the deck for ease of access, and each node was connected to three instrumented washers below the deck that were mounted using 19-mm diameter steel bolts that secured a steel cross member to the outer girder of the bridge. A series of three instrumented washers is visible in Figure 4, with an exploded view of an individual washer clamped between the girder and the steel nut. The tightness of these

components was varied throughout the experiment to test the sensor node's ability to identify the state of each instrumented bolt mounted on the bridge. All the sensor nodes were configured to be wirelessly triggered by the 125 kHz radio signal, which would be initiated by the mobile agent vehicle.

To demonstrate the WID3's triggering capability, a remotely controlled mobile-host approached the sensor node and established a range of 3 m between the RF triggering antenna installed on the side of the vehicle (visible in Figure 23) and the sensor node. On command, a 125 kHz RF wake-up signal was sent to the sensor node, bringing the sensor node out of its sleep status. The WID3 then took measurements from the instrumented washers, locally determined the magnitude of the resonant peak for each sensor, and transmitted the result to the mobile-host vehicle. These data were relayed to a computer, which classified the results to assess the state of each joint. After the mobile-agent made several passes through the network, damage was introduced by loosening one bolt to a finger-tight state for two of the sensor nodes. The mobile-host reported a significant increase in the magnitude of the resonance on the third bolt and correctly identified it as an outlier. Because the change in the location of the resonant peak was so significant, the a 95% confidence rate for an assumed Gaussian distribution of baseline measurements resulted in perfect separation of the baseline healthy data from the loose-bolt data.

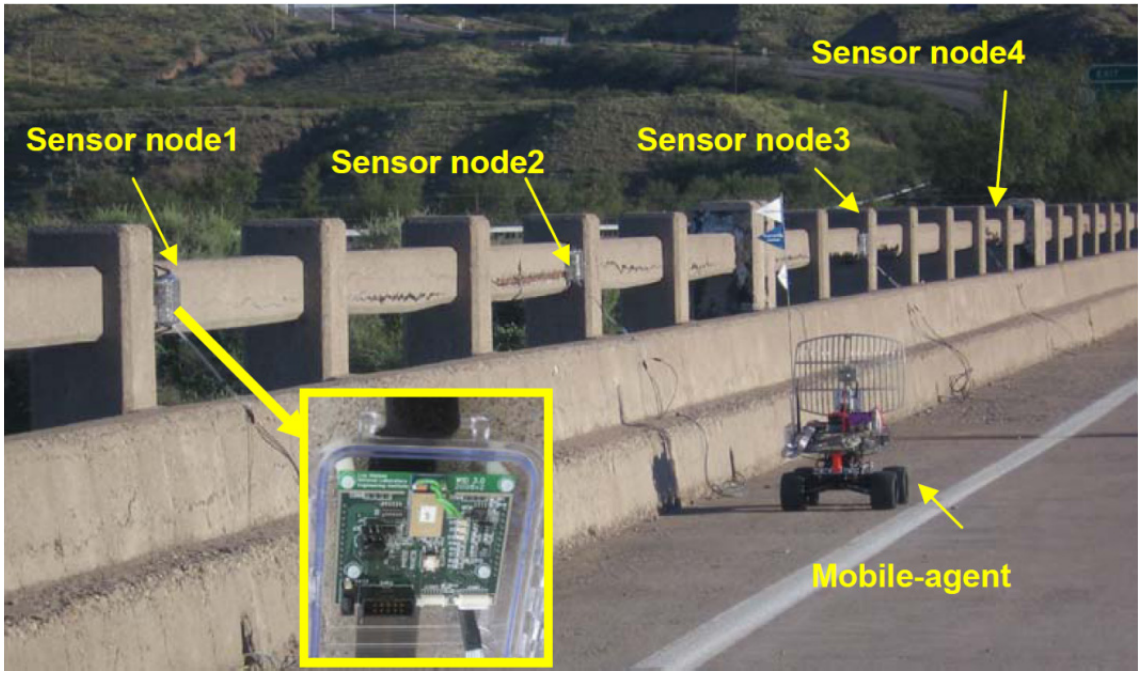

Figure 23: Layout of the field test conducted at the Alamosa Canyon Bridge, NM

3.3.5.1. Hybrid Networking

A simulated permanent installation network test was performed using multiple local networks with a data aggregator present in each network. A visual schematic of the local network is shown in Figure 24 (left). In normal operation, end devices in each network would awaken at regular intervals, perhaps once per day, collect measurements, and transmit the results to an always-on data-aggregating node. Maintaining separate local networks has the advantages with very large structures that additional routers to transmit data over large distances are not required, and that the loss of a single node following a catastrophic event would not destroy the entire network. Three separate local networks were implemented on the bridge, each operating on a different frequency channel. Each coordinator was constantly powered, and the end devices operated in low-power mode, waking at regular intervals to take measurements. The results were transmitted to the data aggregators, which stored the received measurements in non-volatile memory until they were retrieved by the mobile-agent. The experimental set-up for

this field-test is shown in Figure 24 (right). This local network approach was a novel development for SHM applications, as SHM sensors and sensor nodes do not have to be deployed on to the entire structure. Instead, the nodes could be installed on critical areas of a structure, following a targeted, active-sensing SHM strategy. End device sensor nodes does not have to attempt to identify any neighbor nodes or relay the data, as in the case of a hopping networking protocol [43], and the sensors can be more optimally placed on a structure to improve the performance of the SHM process.

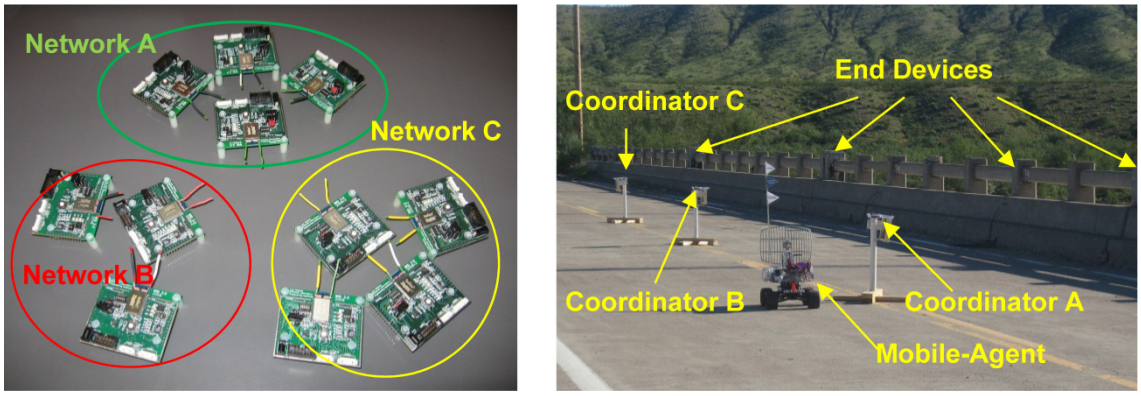

Figure 24: Separate local networks schematic (left); Mobile-agent approaches coordinator A to join network A and retrieve data from network A (right)

3.3.6. Deployment Example: Spaceflight

The WID3 was utilized by a research group at the New Mexico Institute of Mining and Technology for an SHM investigation in low-gravity environments. In this investigation, the WID3 collected impedance measurements as part of an SHM system packaged in a rocket conducting a parabolic maneuver with an apex of 62.5 miles. This effort was reported in [78].

3.4. Wireless Active Sensing Platform

3.4.1. Overview

In attempting to extend the capabilities of the WID3 to include passive data acquisition for acceleration measurements, as well as active sensing capabilities with multiple transducers, it became clear that the low-power, impedance measurement-centered sensor node did not have adequate power or computational capability to be extended into a self-contained sensor node for multi-scale SHM. A new platform was developed, based on a more powerful ARM processor, and intended for operation with a dedicated power supply. The Wireless Active Sensing Platform (WASP) was designed as a multi-scale sensor node to operate in three distinct modes: (1) passive measurements, (2) active sensing, and (3) impedance measurements. The WASP can acquire simultaneous measurements on any of six channels with a bandwidth from DC to 70 kHz, while providing a synchronized excitation output signal on any non-sensing channel. With an innovative digital switching arrangement, each channel can be used to obtain impedance measurements, deliver an excitation signal for structural interrogation, or passively monitor a voltage-output transducer. By appropriately configuring each channel's separate input signal chain, the WASP can easily record low-frequency vibration or strain data. These data could be utilized in concert with a physics-based model of a structure for state and loads estimation, such as that described in Section 6.2. Combining these estimates with active sensing-based estimates of damage location and severity, such as those provided by the methods of Chapter 5, would enable predictions of future structural performance.

The assembled WASP prototype is shown Figure 25. The main processor is an ARM Cortex-M3 processor, seated in an STM3210C evaluation board. Two custom printed circuit boards (PCBs) sit atop the evaluation board: an interface 'daughter' board and a 'mezzanine' board.

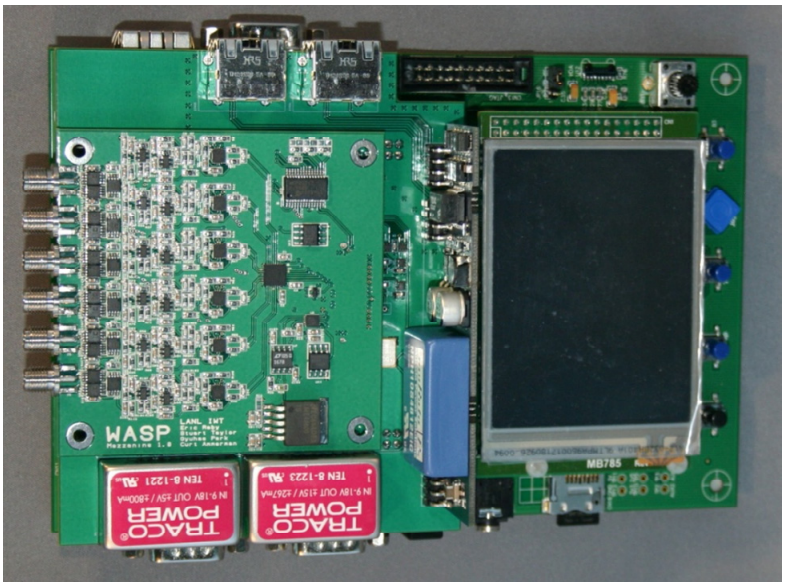

Figure 25: WASP assembled prototype system

The daughter board, shown in Figure 26, provides: (1) physical connectivity for communication between the ARM processor and the analog front end; (2) the WASP's data acquisition clock timing control circuitry; and (3) system power from a Power over Ethernet (PoE) source.

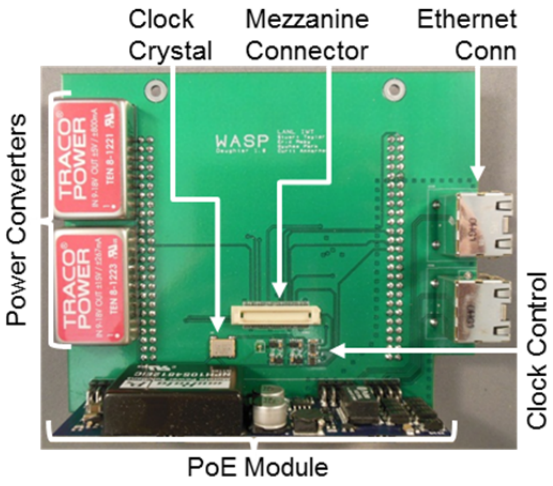

Figure 26: WASP daughter board

The mezzanine board, shown in Figure 27, houses the physical SMA sensor connectors and the WASP's analog front end, which contains: (1) the input signal chains (filter banks) and ADC, (2) the DAC and output signal chain with signal amplification; and (3) the high-current switches and logic control for measurement mode selection. The major components of the WASP detailed below are listed in Table 7.

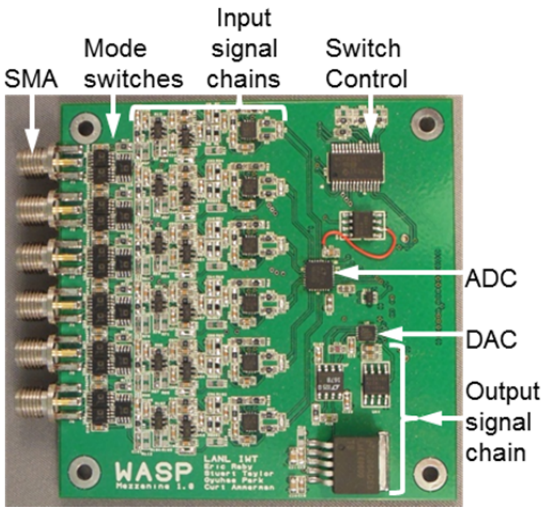

Figure 27: WASP mezzanine board

Table 7: Major components of the WASP

Function	Manufacturer	Part No
Processor development Board	ST Microelectronics	STM3210C-EVAL
PoE Module	Murata	NMPD0112C
Output Switches	Analog Devices	ADG1419
DAC	Linear Technology	LTC2642IDD-16 PBF
Voltage Amplifier	Linear Technology	LT1678CS8#PBF
Current Amplifier	National Semiconductor	LME49600TS-ND
ADC	Linear Technology	LTC2351IUH-14#PBF-ND
Input Amplifier	Linear Technology	LT6233IS6#PBF
Differential ADC Driver	Linear Technology	LT6350CDD#PBF

3.4.2. Development

3.4.2.1. Power and Communication

Both power and communications are delivered to the WASP through an Ethernet cable utilizing the IEEE 802.3af PoE standard. The NMPD0112C PoE module separates 48-Volt AC power from TCP/IP communications and provides a regulated 12V power supply at a maximum of 15W, which is converted to ±15V, ±5V, and ±3V supplies on the Daughter board to power both the Mezzanine board and the STM3210C. The communications lines are routed via a short Ethernet cable to the standard RJ-45 port on the STM3120C board. Commands and data were passed between the WASP and a command PC using a web-based interface. This method enables the implementation of remote or automated data interrogation. Wireless operation is enabled by use of a Wi-Fi bridge, as was implemented in the wind turbine rotor blade flight deployment test described in Section 3.4.6.

3.4.2.2. Seamless Mode Switching

A unique arrangement of software-controlled Analog Devices ADG1419 switches enables any of the six channels to be implemented as a measurement channel, an excitation channel, or an impedance measurement circuit. With a ± 15V power supply, the switches are capable of carrying 215 mA per channel, which is comparable to the current capacity of the output signal chain, described below. The switch configuration, shown schematically in Figure 28, enables each of the 6 channels to be configured for excitation, response measurement, or impedance measurement. The switch configuration for each mode is given in Table 8. In excitation mode, the center pin of the SMA connector is connected to the output signal chain, while in response mode, the center pin connects to the input signal chain. In impedance measurement mode, the output and input signal chains are connected across the SMA connector

through the sensor, with the output signal chain on the center pin, and the input signal chain connected to the SMA connector sheath measuring the voltage across the resistor R_{IMP} to ground.

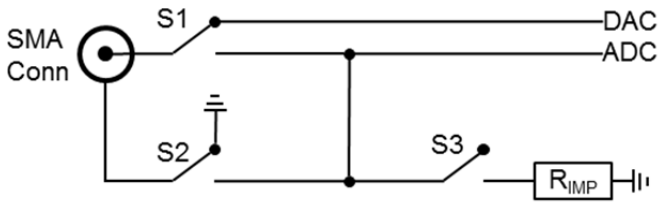

Figure 28: Three-mode switch arrangement for WASP sensor connectors

Table 8: Operational modes for WASP sensor connectors

Channel Mode	Switch Status		
(*as shown in Figure 28)	S1	S2	S3
Excitation*	up	up	up
Response	down	up	up
Impedance	up	down	down

3.4.2.3. Output Signal Chain

The output signal chain, shown schematically in Figure 29, is the path for excitation signals in either active-sensing or impedance measurement mode. The excitation signals are generated from a LTC2642 DAC, which has a 1 μs settling time, about 7 times faster than the WASP's ~140 kHz sampling rate. As a result, the analog signal generated is essentially a stair-step curve, injecting higher frequency content into the excitation signal. In order to mitigate this issue, a single-pole output filter was inserted in the output signal chain prior to amplification. This filter smoothed the output signal significantly, but did not completely eliminate the higher frequency excitation or the potential for aliasing on the response channels. The LT1678 voltage amplifier scales the DAC output to ±15V and feeds the signal to an LME49600TS-ND high-current audio buffer that provides up to 250 mA per rail at ±15V. The output power is sufficient

to implement elastic-wave based SHM methods in metallic structures, but requires additional, external amplification for the thick fiberglass material making up the skin of the CX-100 wind turbine blade on which the WASP was deployed.

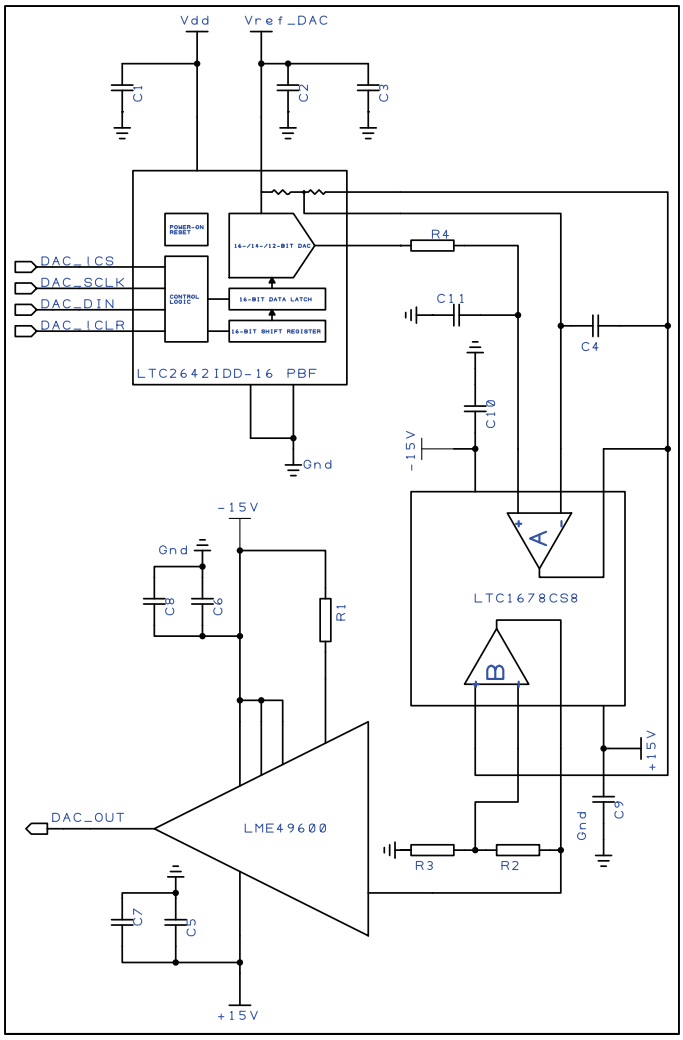

Figure 29: WASP output signal chain

3.4.2.4. Input Signal Chain

The input signal filter chain, shown schematically in Figure 30, is the path for measured signals in either active-sensing measurement mode or impedance measurement mode. Each of the 6 input channels has an individually configurable 5th-order low-pass Bessel filter with

multiple feedback topology, along with two optional single-pole RC filters preceding the first and last Bessel filter stages. These single-pole stages can be implemented as high-pass filters to AC-couple the signal (effectively producing a band pass filter), or as low pass filters to steepen the filter roll-off. Using two resistors, the position could also be implemented as a voltage divider to attenuate the input signal; this implementation is sometimes necessary to avoid saturation of the ADC when collecting low-frequency data with a DC offset. The ability to separately configure each input filter chain enables the WASP to function as a self-contained multi-scale SHM system. Each signal input chain is sampled simultaneously by an LTC2351 ADC at 14 bit resolution over a range of ±1.25 Volts. To achieve simultaneous sampling, the ADC samples and holds all six channels at once, and reads the values into memory during the time between measurements. This process, in conjunction with the output signal synchronization, ultimately limits the WASP's maximum sample rate to ~140 kHz.

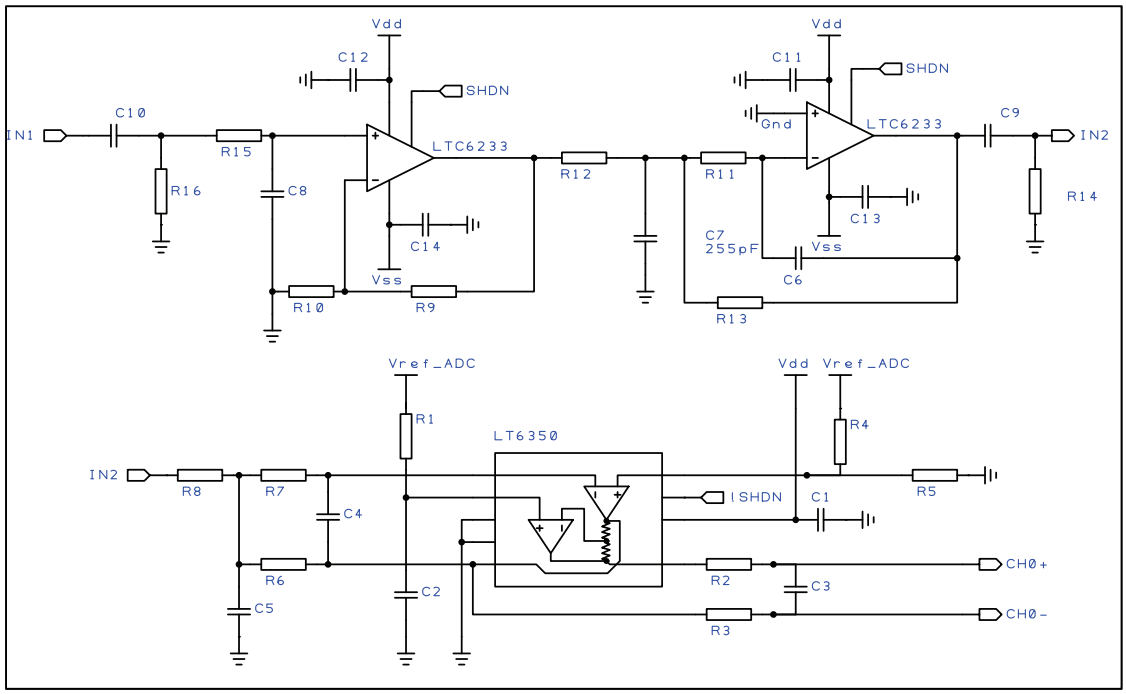

Figure 30: Signal input chain showing fifth-order Bessel filter with multiple feedback topology

3.4.3. Laboratory Demonstration: Impedance Measurements

3.4.3.1. Background

The theory of impedance measurements for SHM and sensor diagnostics is detailed in Chapter 4. However, the practical means of estimating impedance using the WASP is reviewed here. In the simplest case, impedance can be measured by applying Ohm's Law to the circuit shown in Figure 31. With a voltmeter and an ammeter measuring both magnitude and phase, the complex impedance can be measured as

$$Z(s) = \frac{V(s)}{I(s)}, \tag{3.1}$$

where Z is the impedance, V is the voltage, and I is the current. Because it requires a complex current measurement, this method is rarely implemented. The method implemented in commercial devices, including Agilent's 4294A impedance analyzer and Analog Device's AD5933 impedance chip, is the auto-balancing bridge method [79] shown in Figure 32. This method implements an operational amplifier (op-amp) as a current-to-voltage converter to estimate the current through the test object. The impedance measurement circuit implemented on the WASP is that shown in Figure 33. The measurement circuit input voltage is V_{DAC}, which is not measured but assumed to be the DAC command signal ranging over ±15V, and the measurement circuit output voltage is V_{INT}, which enters the WASP's input signal chain. The voltage actually read by the ADC is V_{ADC}. For the purpose of impedance measurements, the WASP's input signal chain and any other effects of its analog front end are modeled generically in the complex impedances Z_1 and Z_2.

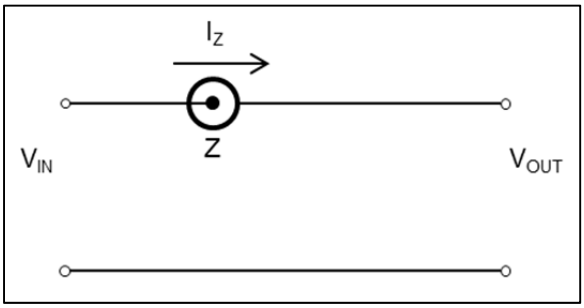

Figure 31: Impedance measurement using Ohm's Law

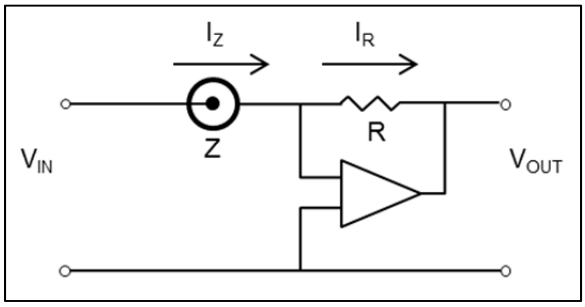

Figure 32: Impedance measurement using an auto-balancing op-amp

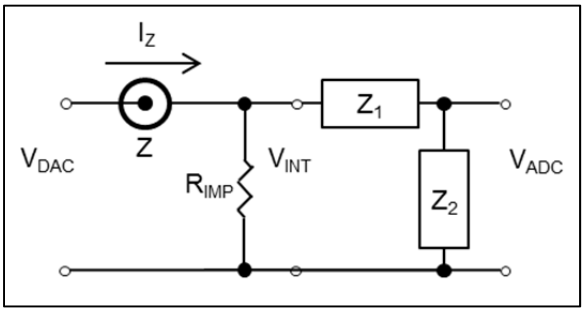

Figure 33: Impedance measurement circuit implemented on the WASP

The transfer function for the left half of the WASP impedance measurement circuit can be estimated using Ohm's and Kirchhoff's laws as

$$\frac{V_{INT}(s)}{V_{DAC}(s)} = \frac{R_{IMP}}{Z(s) + R_{IMP}}, \tag{3.2}$$

where s is the Laplace domain variable. In practice, the complex functions in the Laplace domain will be evaluated on the unit circle by operating on the measurement data with a Fast Fourier Transform (FFT). Each WASP measurement record is 8050 points long, and impedance

data are collected at the maximum sample rate of ~140 kHz using a normally distributed random excitation sequence. Each transfer function estimate was obtained using the H1 autocorrelation method with 1024 FFT points, 50% overlap and a Kaiser-Bessel window with $\beta = 7.85$. As noted in Chapter 4, the quantity of interest in sensor diagnostics for SHM is the admittance, which would be estimated from Eq. (3.2) as

$$Y(\omega) = \left(R_{IMP} \left(\frac{V_{DAC}(\omega)}{V_{INT}(\omega)} - 1 \right) \right)^{-1}, \tag{3.3}$$

where $Y(\omega)$ is the complex admittance of the test object given in Eq. (4.1). In order to estimate V_{INT}, an estimate of the transfer function $\frac{V_{ADC}(\omega)}{V_{INT}(\omega)}$ must be available. In order to obtain this estimate, a 50 Ω terminating resistor was applied to an SMA connector on the WASP, and the response of the total measurement circuit to a broadband, white noise excitation signal was recorded. Noting that $R_{IMP} = 100$, and $Z = 50$, V_{INT} was estimated from Eq. (3.2) as $V_{INT} = \frac{2}{3} V_{DAC}$. Then, the WASP analog front-end transfer function, $TF_{WASP}(\omega)$, can be estimated as

$$TF_{WASP}(\omega) = \frac{V_{ADC}(\omega)}{V_{INT}(\omega)} \approx \frac{3}{2} \left(\frac{V_{ADC}(\omega)}{V_{DAC}(\omega)} \bigg|_{Z=50} \right). \tag{3.4}$$

Combining Eqs. (3.3) and (3.4), the transducer admittance can be estimated as

$$Y(\omega) = \left(R_{IMP} \left(\frac{V_{DAC}(\omega)}{V_{ADC}(\omega)} TF_{WASP}(\omega) - 1 \right) \right)^{-1}. \tag{3.5}$$

3.4.3.2. Demonstration

In order to demonstrate the WASP's general impedance measurement capability, impedance data were collected for the same 50 Ω SMA termination resistor, 100 Ω breadboard

resistor, and 47 nF capacitor. The excitation voltage level was adjusted for each measurement in order to make better use of the dynamic range of the ADC. Component validation results are shown in Figure 34, in which plots of the real and imaginary parts of admittance (conductance and susceptance, respectively) are plotted versus frequency over the full bandwidth of the WASP. The WASP impedance measurement circuit breaks down at very low frequencies (below 2 kHz), but otherwise correctly returns the real admittance values for the 50 Ω and 100 Ω resistors as 0.02 and 0.01 Ω^{-1}, respectively. The measured susceptance for the capacitor increases linearly up to ~30 kHz, and then returns to zero at the top of the WASP's 70 kHz bandwidth; this result is expected because it is not possible to measure both magnitude and phase at the Nyquist limit. The slope of the linear portion of the capacitor susceptance, from 2 kHz to 30 kHz, corresponds to a capacitance of 47.3 nF. These results sufficiently demonstrate the WASP's impedance measurement capability for simple components.

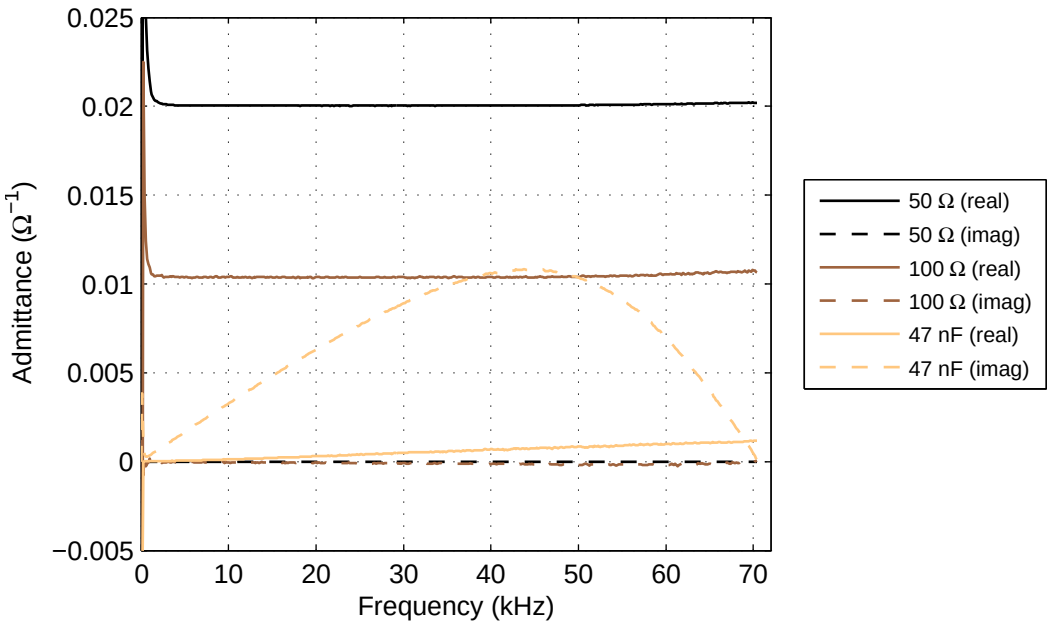

Figure 34: WASP admittance measurements – component validation

Next, the WASP's impedance measurement functionality for sensor diagnostics was demonstrated using the aluminum plate described in Section 2.2. Reference measurements were collected using the Agilent 4294A, and the measured admittance values are plotted for the four functional baseline patches. The real admittance (conductance) is plotted in Figure 35, and the imaginary admittance (susceptance) in Figure 36. There is a constant offset in the imaginary admittance slope between measurements obtained with 4294A and the WASP. This offset might be a result of a temperature change between when the data were collected, or caused by a bias error in estimating the WASP measurement circuit (recall that the circuit was calibrated using a single resistance value); however, because sensor diagnostics are implemented based on changes in measurements, it is only necessary that the WASP's measurement circuit be consistent in order to be effective.

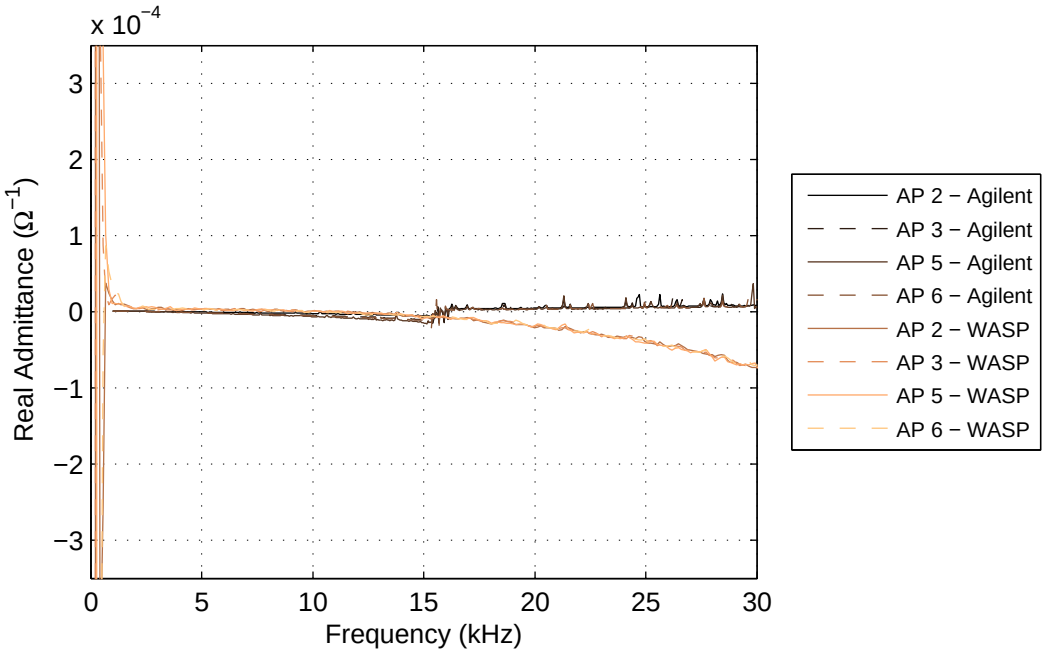

Figure 35: Real admittance comparison – Agilent 4294A and WASP

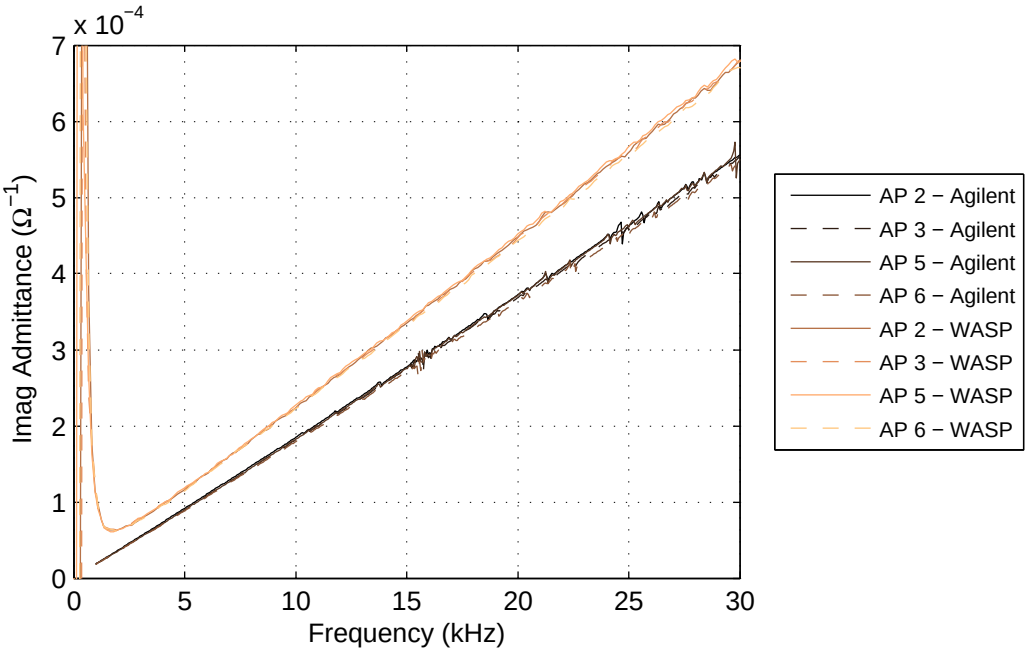

Figure 36: Imaginary admittance comparison – Agilent 4294A and WASP

Data were collected from the debonded and broken patches, and the susceptance slopes were compared with the average susceptance slopes for the healthy patches to determine the relative severity of the defects. The susceptance data are plotted for the debonded and broken patches in Figure 37 and Figure 38, respectively, and the sensor diagnostics results using the WASP are summarized in Table 9. Although the extent of the changes is greater for the broken patches than for the debonded ones, in each case there is a clearly observable trend, indicating the severity of the defect using the admittance measurements obtained with the WASP. These results demonstrate the WASP's ability to perform sensor diagnostics measurements while deployed for active sensing SHM.

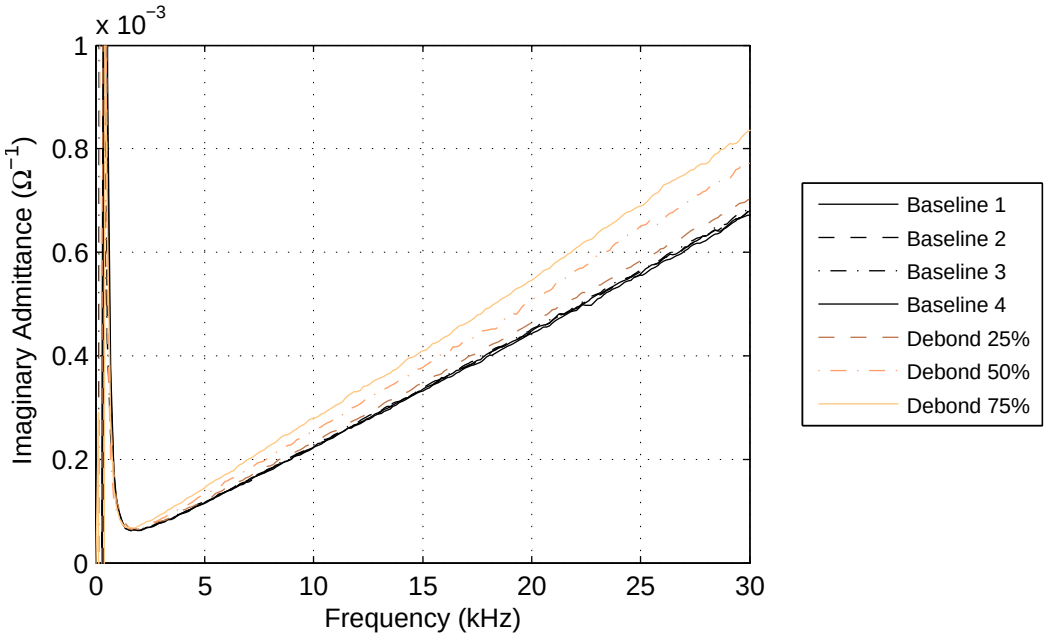

Figure 37: WASP admittance measurements – debonded sensors on aluminum plate

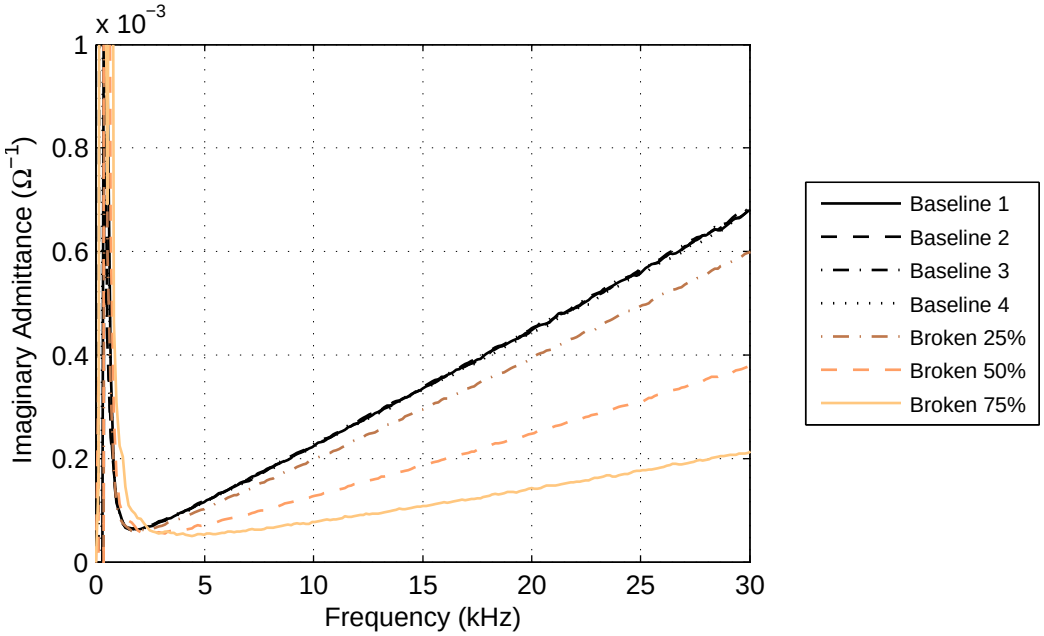

Figure 38: WASP admittance measurements – broken sensors on aluminum plate

Table 9: Sensor diagnostics results

Debonded Sensors		Broken Sensors	
Capacitance (nF)	% Change	Capacitance (nF)	% Change
3.75	3.9%	3.18	-11.7%
4.16	15.5%	2.00	-44.6%
4.46	23.6%	1.08	-70.0%

3.4.4. Deployment Example: Wind Turbine Rotor Blade Fatigue Test

The WASP was deployed on the CX-100 wind turbine rotor blade for the fatigue test described in Section 2.5. In this deployment, the WASP monitored array HP-A3, as listed in Table 2, which had a centrally located patch that the WASP excited with a chirp signal. The chirp signal ranged from 5 kHz to 25 kHz, which was the top of the WASP's bandwidth for this test. Only one actuator was utilized because the thick fiberglass of the rotor blade required external signal amplification in order to overcome signal attenuation in the structure, and a single channel had to be hard-wired through the amplifier. With the long-duration, broadband signal, the WASP effectively excited a diffuse wave field (DWF). The WASP data were processed according to the method presented for DWF data in Section 5.2, and ROC curves were generated using the Normalized Impulse Residual Energy (NIRE) test statistic also described in Section 5.2. To verify the WASP's ability to collect active sensing data for SHM purposes, results are presented here alongside those for the commercially available IntelliConnector that monitored a collocated sensor array, HP-A2 in Table 2, using ultrasonic guided wave (UGW) measurements.

The NRE test statistics for the Metis IntelliConnector are plotted versus test date in Figure 39 (left), and the corresponding ROC curves are shown in Figure 39 (right). The raw test statistics for path 3 are excluded because that patch fractured (although not a result of the structural failure) early in the test. Although the sensor paths on the high-pressure side were not

located near the crack, results with the IntelliConnector system monitoring array LP-A2, detailed in Section 5.3.3.1, show that at these relatively lower frequencies for UGW data (compared to 200 kHz), there is general sensitivity to underlying structural changes in the CX-100 rotor blade that is not dependent on intimate proximity to the developing crack. The results with the Metis IntelliConnector indicate a good ability to detect the incipient damage, with an average AUC (excluding path 3) of 0.986. The NIRE test statistics for the WASP are plotted versus test date in Figure 40 (left), and the corresponding ROC curves are shown in Figure 40 (right). The WASP demonstrates an ability on par with the IntelliConnector to detect the incipient damage, with an average AUC of 0.987.

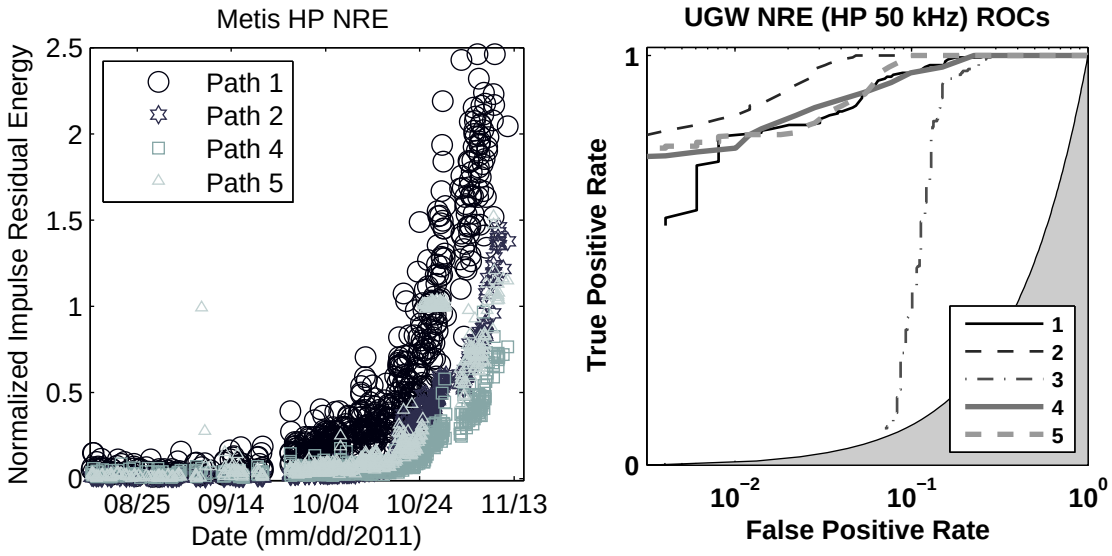

Figure 39: NRE results for IntelliConnector (UGW) data with array HP-A1

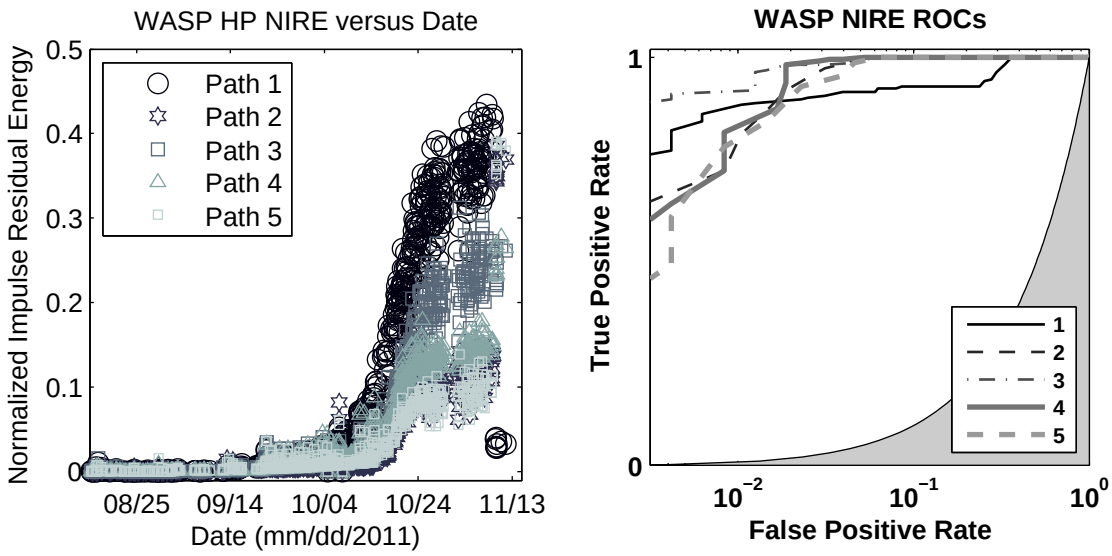

Figure 40: NIRE results for WASP (DWF) data with array HP-A2

3.4.5. Deployment Example: Telescope Drive System

In a data-driven example of low frequency vibration monitoring for SHM, the WASP was deployed to monitor the drive system of a RAPTOR telescope, described in Section 2.4. The WASP collected acceleration measurements using a Rieker B1 DC accelerometer mounted on the motor mount bar in the in-plane direction of the telescope's right ascension axis drive wheel. The Rieker B1 requires a 5V regulated DC power supply, has a 2.5V DC offset, a sensitivity of 129 mV/g, a dynamic range of ±3g, and a bandwidth of 160 Hz. The WASP was configured with a voltage divider to drop the 2.5V-centered signal within range of the ADC, which requires a signal within ±1.25V, and an anti-aliasing filter with a cutoff frequency of 400Hz. The WASP deployment is shown diagrammatically in Figure 41. The telescope control computer has been programmed to command the WASP to record data each time the telescope conducts its homing sequence, which occurs at least once at the beginning of each night. Each acceleration sequence is 8050 points, recorded at 2 kHz. Data are automatically downloaded from the WASP through its web server, and transferred to an off-site PC for further analysis.

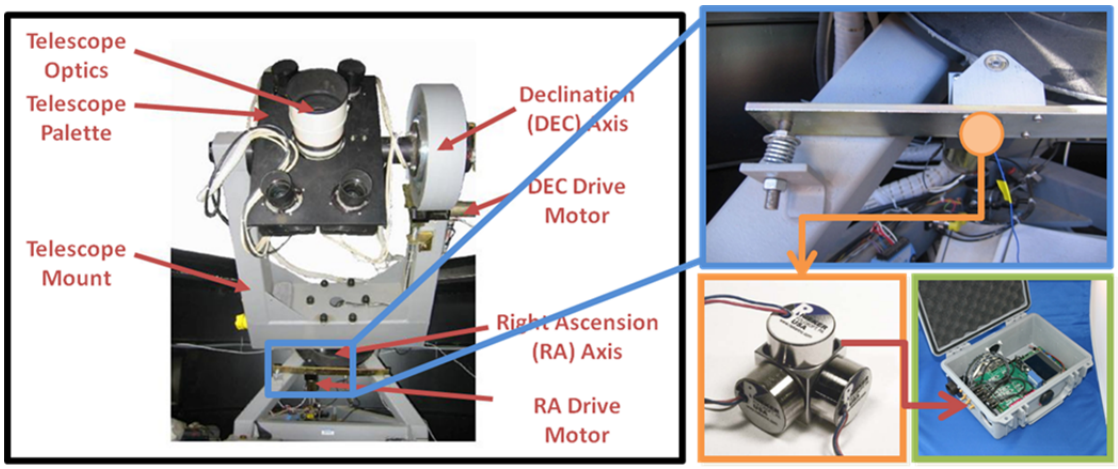

Figure 41: WASP deployment graphical overview

A preliminary study [3] reported the efficacy of outlier classification methods for detecting the onset of capstan wear prior to catastrophic capstan failure. In the telescope drive system, the main drive wheels, which directly contact the capstans, are often marred with slight imperfections in the interface surface. Because these imperfections are unique to each system, there is a unique signature that can be used to train a classification model. As the capstan drives the wheel, these imperfections inject an impulse train through the interface, so that the input to the system can be treated as an impulse train approaching a white noise input. This input assumption allows the recorded acceleration to be modeled as an auto-regressive (AR) process [80]. Modeling the AR model parameters themselves as a multivariate Gaussian distribution, the Mahalanobis squared distance (MSD) can be used as a scalar metric to indicate the "distance" between a set of baseline or training data and a new dataset. The MSD is given as

$$\mathrm{MSD} = \left(\mathbf{x} - \boldsymbol{\mu}\right)^{\mathrm{T}} \boldsymbol{\Sigma}^{-1} \left(\mathbf{x} - \boldsymbol{\mu}\right), \tag{6}$$

where $\mathbf{x}$ in this case is the array of AR model coefficients, and $\boldsymbol{\mu}$ and $\boldsymbol{\Sigma}$ are the mean values and the covariance matrix of the training data set, respectively.

For data collected with the WASP, the power spectral density averaged over approximately six weeks' worth of data is shown in Figure 42. Dividing the total sequence into

1000-point sub-sequences, each sub-sequence was fit to an AR model of order 18, which was determined by inspection of the peaks visible in the PSD estimate. Assigning every second sub-sequence for the first half of the total data sequence as training data, the training data mean and covariance matrices were computed, and the MSD metric was computed for each sub-sequence. These values are plotted versus sub-sequence number for data ranging from 10/12/2012 to 11/23/2012 in Figure 43. The only observed deviation from the historical mean occurred on the night of 11/11/2012 (near sub-sequence number 300 in Figure 43), when the temperature in Los Alamos dropped to nearly -10° C, which was ~10° C colder than the temperatures experienced during the training data gathering. By incorporating some of the data collected at these temperatures into the training data set, the large excursion visible in Figure 43 can be removed, and with the inclusion of a wider range of operating conditions, future observed excursions will be more likely to indicate capstan failure.

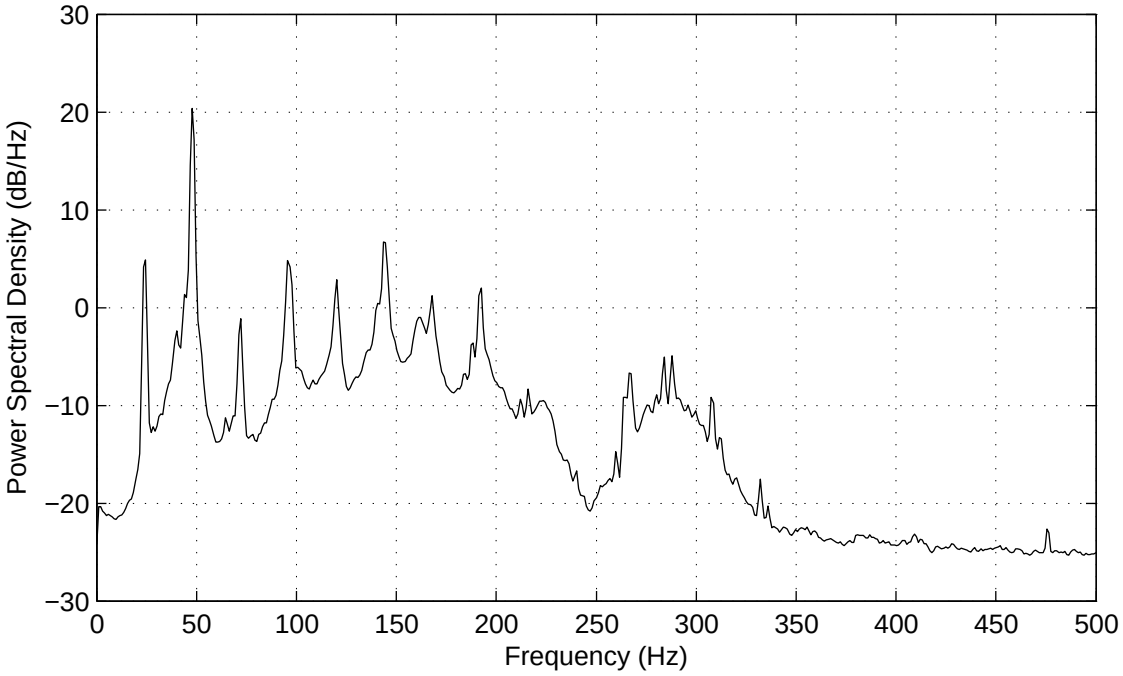

Figure 42: PSD for RAPTOR data from WASP

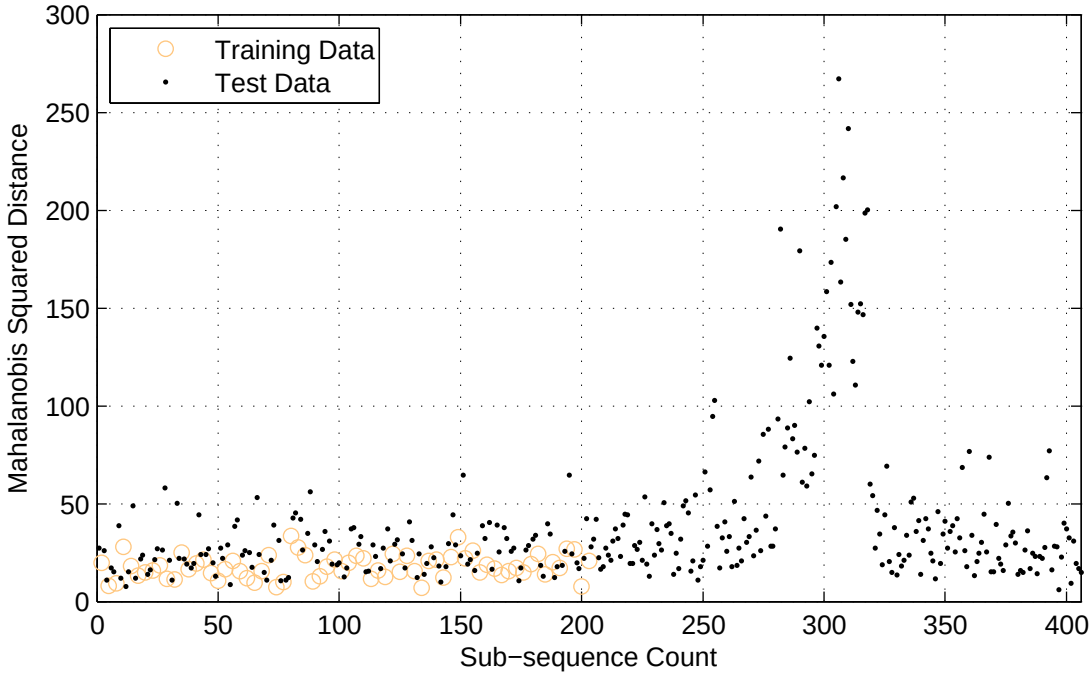

Figure 43: MSD metrics versus sub-sequence number, ranging from 10/12/2012 through 11/19/2012

3.4.6. Wind Turbine Rotor Blade Flight Test

Three WASPs were deployed on a wind turbine rotor blade flight test at the NIST facility described in Section 2.7. In this deployment, the WASPs monitored PZT patches that were embedded inside a CX-100 blade during its manufacture. Also available were data from the accelerometers and fiber optic strain gauges on three blades during the operation of the test. The deployment box for the WASPs, which was mounted to the wind turbine hub, is shown in Figure 44. This weatherproof box included circuitry for power conditioning, lightning protection, and communications. Preliminary data have been successfully retrieved from the sensor arrays embedded in the operational CX-100 blade, but a longer-term deployment of this system would be required in order to assess the ability of the WASP to provide information concerning damage accumulation in operational blades.

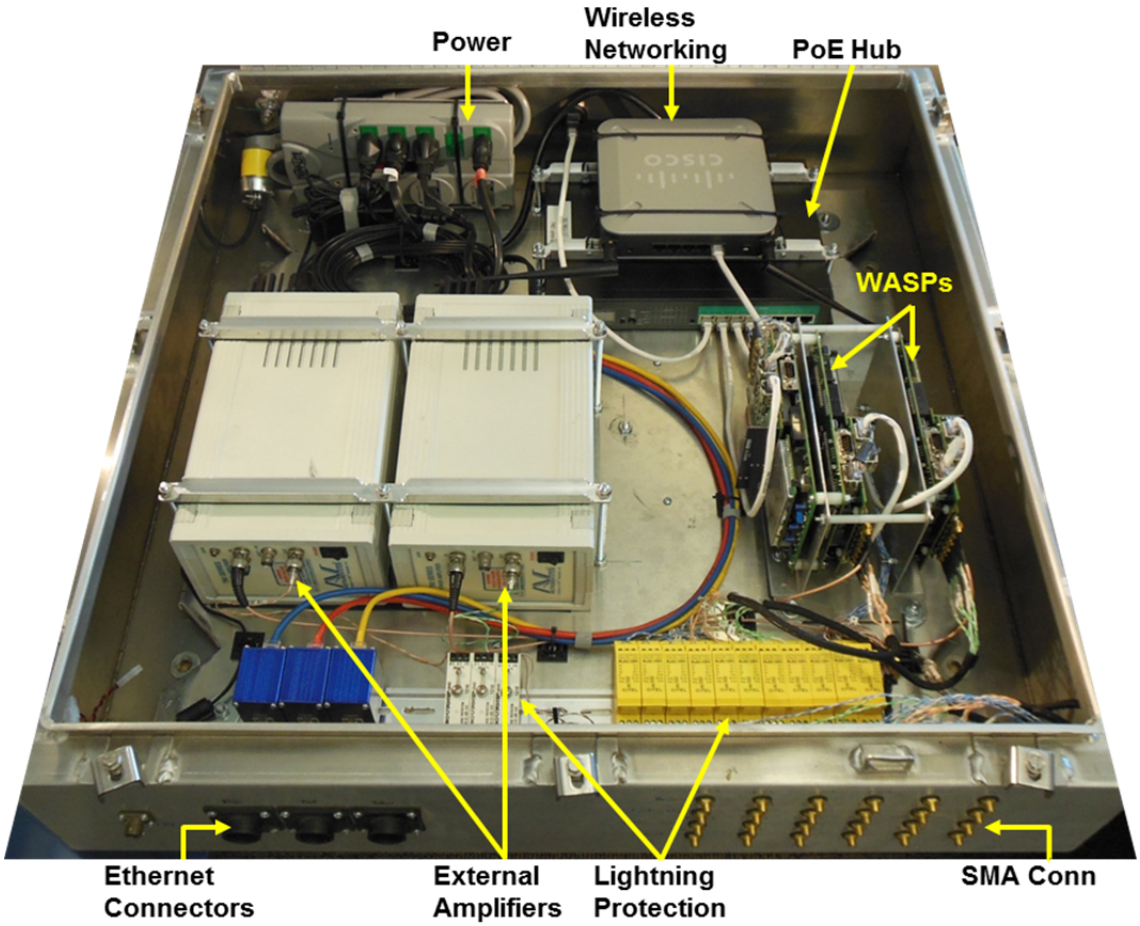

Figure 44: WASP deployment box for the Micon 63/13 wind turbine

3.5. Summary and Acknowledgements

This chapter has described the development and deployment of two embedded sensor nodes for structural health monitoring. The development of the Wireless Impedance Device v3 (WID3) was presented, and its new functionality over previous WID versions was demonstrated. The WID3's most basic capability involves measuring the coupled electromechanical impedance of a structure, capitalizing on the well-established impedance-based structural health monitoring technique to monitor the condition of a structure. The low-power sensor node's capabilities were extended through improved networking capabilities,

increased data storage options, multiple powering options that allow for energy harvesting integration, and increased triggering options that allow for better control of sleep modes, reducing overall power consumption. The node's capabilities were further extended through use of a wireless data acquisition (WiDAQ) module to be capable of collecting low-frequency time-domain data from a variety of sensors. To demonstrate this capability, structural vibration data were collected for modal analysis, and the resulting measured natural frequencies and mode shapes were compared to those measured using a traditional data acquisition system. After successfully verifying the functionality of the WID3 in various laboratory settings, the WID3 was field-tested on an actual structure of significant size and practical importance, demonstrating that the sensor node can efficiently monitor several mechanical response parameters suitable for rapid assessment of structural condition.

The Wireless Active Sensing Platform (WASP), an embedded sensor node uniquely suited to multi-scale structural health monitoring (SHM) applications, was also developed. Its specific features have been described, especially its innovative ability to seamlessly switch between a traditional pitch-catch active sensing mode and impedance measurement mode, which is integral to sensor diagnostics methods for active-sensing SHM. The WASP was demonstrated in three key application areas. First, its ability to perform impedance measurements for piezoelectric sensor diagnostics was demonstrated in comparison to a conventional impedance analyzer. While the absolute estimates of impedance produced using the WASP were not identical to those produced by the impedance analyzer, the relative measurements demonstrated a more-than-sufficient ability to perform sensor diagnostics. Second, its ability to collect active-sensing data for incipient crack detection was demonstrated in comparison to a commercially available module for ultrasonic guided wave measurements. The WASP demonstrated a capability on par with the commercial system in detecting an incipient fatigue crack in a full-scale wind turbine blade. Third, its ability to collect low-

frequency vibration measurements for model-based SHM was demonstrated using acceleration measurements collected from a telescope structure. These measurements will prove useful in an ongoing manner for in situ monitoring of the health of the telescope drive system.

Portions of Section 3.3 have been published in [1] *Smart Structures and Systems,* S. G. Taylor, K. Farinholt, G. Park, M. Todd, and C. Farrar, 2010. The title of this paper is "Multi-scale wireless sensor node for health monitoring of civil infrastructure and mechanical systems." The dissertation author was the primary investigator and author of this paper.

Other portions of Section 3.3 have been published in [2] *Measurement Science and Technology,* S. G. Taylor, K. M. Farinholt, E. B. Flynn, E. Figueiredo, D. L. Mascarenas, E. A. Moro, G. Park, M. D. Todd, and C. R. Farrar, 2009. The title of this paper is "A mobile-agent-based wireless sensing network for structural monitoring applications." The dissertation author was the primary investigator and author of this paper.

Section 3.4 is currently being prepared in part for publication [5]. S. G. Taylor, E. Y. Raby, G. Park, K. M. Farinholt, and M. D. Todd, 2013. The title of this paper is "Active sensing platform: development and deployment." The dissertation author was the primary investigator and author of this paper.

Chapter 4
Sensor Diagnostics for Active Sensing Systems

4.1. Introduction

This chapter presents an overview of sensor diagnostics for active sensing SHM systems employing piezoceramic transducers, as well as experimental results relating to sensor diagnostics from the CX-100 fatigue test described in Section 2.5. Of the 49 piezoceramic transducers employed, the 49 outlasted the expected life of the blade. Of the transducers that did fail in the course of the test, the sensor diagnostics methods presented here were effective in identifying them for replacement and/or data cleansing. Finally, while most sensor diagnostics studies [57, 81] have been performed in a controlled, static environment, some data in this study were collected as the rotor blade underwent cyclic loading. This loading condition motivated the implementation of an additional data normalization step for sensor diagnostics with piezoceramic transducers in operational environments.

Active sensing denotes the use of transducers having both sensing and actuation capability deployed on a structure. The structure is excited using one or more transducers, and its response to that excitation is recorded using the same or other transducers. Piezoelectric materials are well-suited for use in active sensing systems, because their unique properties

enable them to serve both as actuators when excited with a voltage signal, and as sensors when deformed by a mechanical strain wave. The theory supporting the use of piezoelectric materials for active sensing was presented by Liang, et al. [82]. Although many materials exhibit a piezoelectric effect, including ceramics, composites, and polymers, the work in this dissertation is concerned with piezoceramic materials. Much of the theory supporting the use of piezoceramic materials for active sensing has been presented by Park, et al. [83-85] and Bhalla, et al. [86-88]. Impedance measurements as a method for structural health monitoring (SHM) were further developed by Park, et al. [55, 81, 89, 90], and techniques employing impedance measurements specifically for sensor diagnostics were also developed by Park, et al. [56, 57, 91, 92]. While much of the experimental work applying the impedance method for structural health monitoring and sensor diagnostics has been implemented using a conventional network or impedance analyzer, such as the Agilent 4294A [93], several compact, low-power devices (some of which are listed in Section 3.2.2) have also been developed to collect impedance measurements for SHM and sensor diagnostics purposes [1, 59, 60].

Active sensing for SHM is a robust area of research with some very mature methods and applications [94-98]. However, SHM systems often operate in an unsupervised learning mode, which makes systems with failed sensors especially susceptible to false positives. Large excursions of test statistics from historical mean values could be caused either by structural damage or sensor failure. SHM systems in unsupervised learning modes rely on the assumption that the transducers employed are well-bonded and functioning properly. Although data normalization or instantaneous baseline techniques [56, 99] can be implemented to accommodate changing environmental conditions [99], damage to or loss of a transducer requires data cleansing and ultimately sensor replacement. Because physical inspection of sensors is likely no less costly than physical inspection of the structure, it is imperative that a sensor diagnostic capability be included as an integral part of any deployed SHM system.

4.2. Sensor Diagnostics Theory

Sensor diagnostics for piezoelectric transducers utilizes impedance measurements to ascertain the health of the sensor and its bond condition. The impedance method relies on the electro-mechanical nature of piezoelectric transducers, in which the material's electrical response is coupled with its mechanical response. When the material is bonded to a host structure, the electrical response becomes coupled with the structure's mechanical response. One commonly used piezoelectric material in active sensing for SHM is lead zirconate titanate (PZT), a piezoceramic material usually fabricated as thin disc, or patch. A simplified diagram of the coupling between a PZT patch and its host structure is shown in Figure 45. For a PZT patch bonded to a host structure, the measured electrical impedance will be a function of both the patch impedance, Z_a, and the structural impedance, Z_s, in addition to the patch's own electrical impedance. The primary assumptions in utilizing PZT patches for active sensing are: (1) that the patch operates in the d_{3x} mode, such that strains in the planar x direction induce voltages in the out-of-plane 3 direction and vice-versa; (2) that strains in the planar direction are independent of one another; and (3) that a single point at the center of the patch rigidly defines the connection between the patch and the structure [55, 86].

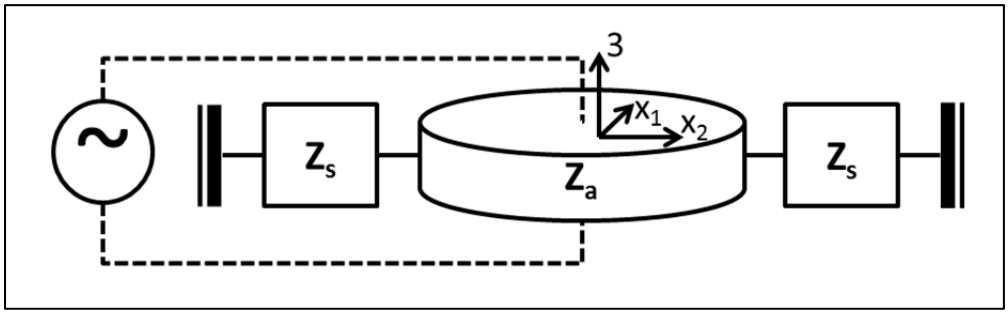

Figure 45: Electro-mechanical coupling diagram for a piezoceramic patch.

The complex electrical admittance of the bonded PZT patch, expressed through Ohm's Law as the ratio of the current flowing through the patch to the applied voltage as a function of frequency, is a function of the total system structural impedance, given as [82]

$$Y(\omega)=\frac{I(\omega)}{V(\omega)}=i\omega a\left(\bar{\varepsilon}_{33}^{\ T}-\frac{Z_s}{Z_s+Z_a}d_{3x}^2\bar{Y}_{xx}^{\ E}\right), \tag{4.1}$$

where i is the imaginary unit, ω is the frequency, a is a geometric constant of the patch, $\bar{\varepsilon}_{33}^{\ T}$ is the complex dielectric constant at zero stress, d_{3x}^2 is the piezoelectric coupling constant in the in-plane (x) direction at zero stress, $\bar{Y}_{xx}^{\ E}$ is the complex Young's modulus of the patch with zero electric field, Z_a is the complex short-circuit mechanical patch impedance and Z_s is the complex structural impedance. All of these terms are complex functions of frequency. They can be written in terms of their real and imaginary components as

$$\begin{aligned} Y(\omega)&=G(\omega)+iB(\omega)\\ \bar{\varepsilon}_{33}^{\ T}&=\varepsilon_{33}^{\ T}(1-\delta i)\\ \bar{Y}_{xx}^{\ E}&=Y_{xx}^{\ E}(1+\eta i)\\ Z_a&=x_a+y_a i\\ Z_s&=x_s+y_s i \end{aligned}, \tag{4.2}$$

where $G(\omega)$ is the conductance, $B(\omega)$ is the susceptance, δ is the dielectric loss factor, η is the mechanical loss factor, and x and y are real and imaginary components of mechanical impedance, respectively. Under the assumptions given above, Eq. (4.1) sets the groundwork for using PZT patches in impedance-based SHM as well as for sensor diagnostics.

The basis of sensor diagnostics methods for PZT patches is to track their capacitive value, which manifests itself in the measured susceptance. For a completely free patch, $Z_s=0$, and the susceptance becomes

$$B_{free}(\omega)=a\varepsilon_{33}^{\ T}\omega\,. \tag{4.3}$$

In the rigidly fixed state, $Z_s \gg Z_a$, and the susceptance becomes

$$B_{fixed}(\omega) = a\left(\varepsilon_{33}^{\ T} - d_{3x}^2 Y_{xx}^{\ E}\right)\omega . \tag{4.4}$$

Equations (4.3) and (4.4) provide the upper and lower bounds, respectively, on the slope of the measured susceptance for a PZT patch. Bonding defects as well as changes in the mechanical or electrical properties of the patch or its host structure can be identified using these measurements. Sensor diagnostics for PZT patches relies on the additional assumption that a, $\varepsilon_{33}^{\ T}$, and $Y_{xx}^{\ E}$ are constant at low frequencies. Then Eqs. (4.3) and (4.4) describe the susceptance of a capacitor, where the entire term pre-multiplying ω is constant, so that

$$B = aK \cdot \omega , \tag{4.5}$$

where $\left(\varepsilon_{33}^{\ T} - d_{3x}^2 Y_{xx}^{\ E}\right) \le K \le \left(\varepsilon_{33}^{\ T}\right)$, and aK can be estimated as the slope of a straight-line fit of the measured susceptance. If the PZT patch becomes debonded, the capacitance will increase, with K approaching $\varepsilon_{33}^{\ T}$. If the patch becomes broken, the then physically smaller patch will have a smaller geometric constant $\hat{a} < a$, and the capacitance will decrease. Because the patch is highly unlikely to increase the fixity of its bond condition [100], a decrease in the measured susceptance slope can almost always be attributed to sensor breakage.

Although in practice, the structural impedance is some time-invariant, complex function of frequency, $Z_s(\omega) = x_s(\omega) + iy_s(\omega)$, at low frequencies (below 30 kHz), it is assumed to be constant, permitting the implementation of sensor diagnostics using the capacitive approximation described above. The behaviors described here are well-established, and they have been demonstrated both in the laboratory and in the field [2, 56, 90, 101]. However, if the structural impedance changes dynamically as a result of operational loading, Eq. (4.1) must be expanded as

$$B(\omega) = a\left({\varepsilon_{33}}^{T} + d_{3x}^{2} {Y_{xx}}^{E} \left(\frac{\eta(x_a y_s - x_s y_a) - (x_a + x_s)x_s - (y_a + y_s)y_s}{(x_a + x_s)^2 + (y_a + y_s)^2} \right) \right) \omega, \qquad (4.6)$$

and that effect must be incorporated into the appropriate terms in Eq. (4.6) in order to properly assess the condition of the sensor.

4.3. Experimental Results

In the CX-100 rotor blade fatigue test experiment, the transducers were tracked using a time-based baseline approach, in which admittance measurements were collected throughout the course of the test, and the slope of the measured susceptance was plotted versus time. Excursions from the established baseline were identified visually, and such excursions would indicate either a broken or a debonding sensor, corresponding to the direction of the change in slope. Impedance measurements were collected using an Agilent 4294A impedance analyzer at roughly weekly intervals. Each measurement contained complex impedance data at 512 frequency lines linearly spaced over a range from 1 kHz to 30 kHz. The HP4294A implements a "sine dwell" measurement approach, in which data are measured at each frequency line in succession, and there is a finite settling time dependent on the measurement frequency itself, that passes between recording data at each frequency line. Each measurement required several seconds to sweep through the frequency range, effectively invoking an assumption that the structure was time invariant during that time.

4.3.1. Sensor Performance

In the ideal case for a group of similarly situated sensors, their measured susceptance values would remain constant, and any deviations from the mean historical value would be tracked by all sensors, so that an instantaneous baseline method [56] could be implemented

either to preclude the need for retaining past baseline measurements, or, in light of a deviation from the historical mean, as a safeguard against concluding that all sensors in the set had failed. Sensor array 1 on the high-pressure side (HP-A1) provides a good example of a healthy sensor set with uniform excursions from its historical mean. The susceptance slopes for each patch in array HP-A1 are plotted versus test date in Figure 46. No sensors in this array failed during the course of the test. On 8/12/2011, as well as on 10/24/2011, there were noticeable deviations from the past values, but because all sensors in the array experienced these changes, it was much more likely that an external factor, such as temperature or loading effects, was driving the change, rather than that all the sensors had failed.

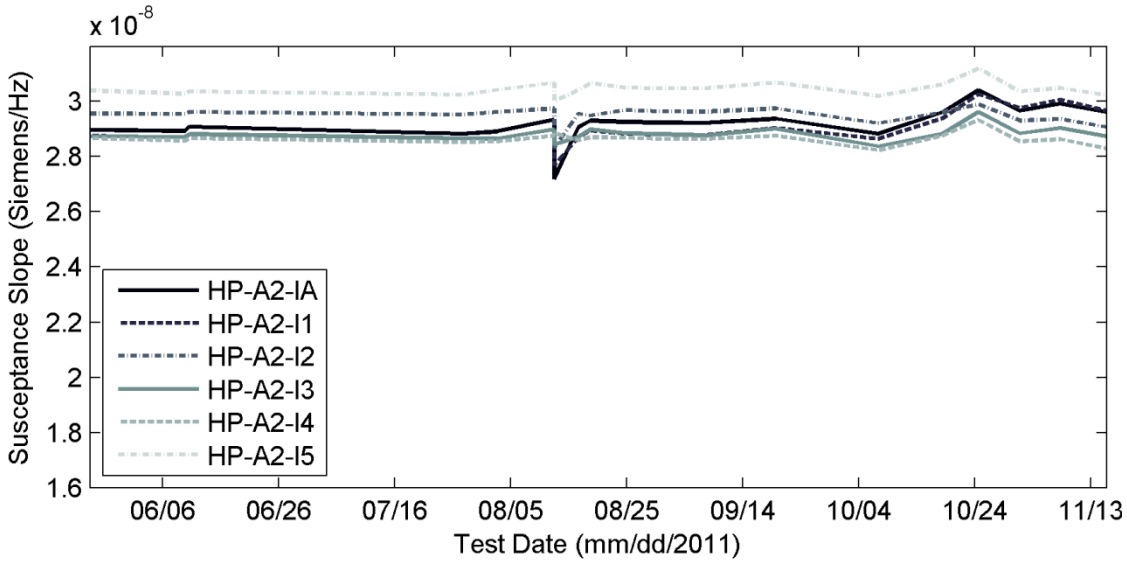

Figure 46: Susceptance slope values versus test date for all patches in array HP-A1

In the course of this fatigue test, a "softening" phenomenon was observed, in which a sensor that appeared well-bonded upon visual inspection would experience an increase in susceptance slope normally indicative of a debonded patch. In the cases where softening was observed, the sensors were located quite near the incipient crack, and it is likely that the local stiffness began to decline as the crack formed, causing a decrease in the structural impedance,

and a corresponding increase in the susceptance slope. Patch LP-A1-I3, which sat quite near the forming crack, is a good example of this phenomenon. The susceptance slopes for the patches in array LP-A1 are plotted versus test date in Figure 47. The susceptance slopes for Patch LP-A1-IA and LP-A1-I0 through LP-A1–I2 track each other through the end of the test, while that for Patch LP-A1-I3 increases dramatically prior to the catastrophic failure of the blade, when the crack surfaced and simultaneously broke the patch.

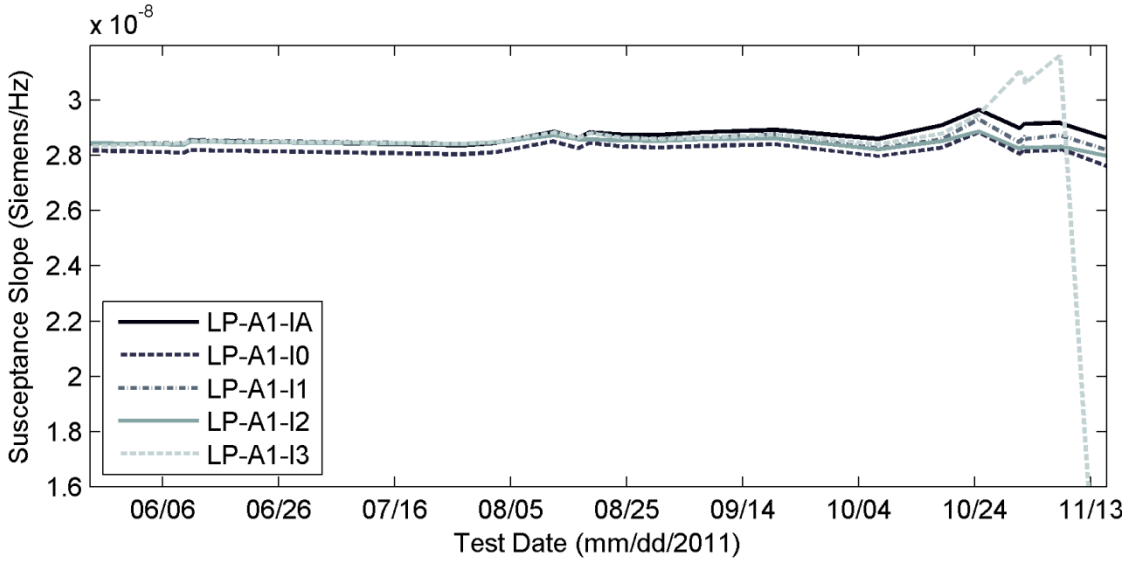

Figure 47: Susceptance slope values versus test date for several patches in array LP-A1

As described in Section 2.5.2 and indicated in Figure 10, a total of 11 sensors failed during the test. Most of these sensors were located near the catastrophic crack, and their susceptance slopes are plotted versus test date in Figure 48 and Figure 49. The susceptance slopes for failed sensors in other locations are plotted in Figure 50. For many of these sensors, the failures are preceded by increases in susceptance slope, reflecting the softening boundary condition described above. This phenomenon points to an overlap between sensor diagnostics and structural damage detection; while the increased susceptance slopes might have been interpreted as indicating a debonded sensor, they were actually harbingers of incipient structural

damage. In this case, the development of structural damage may first have caused the susceptance slope to increase as its boundary condition softened, and then the increasing surface strain caused by the crack propagation fractured the patch itself.

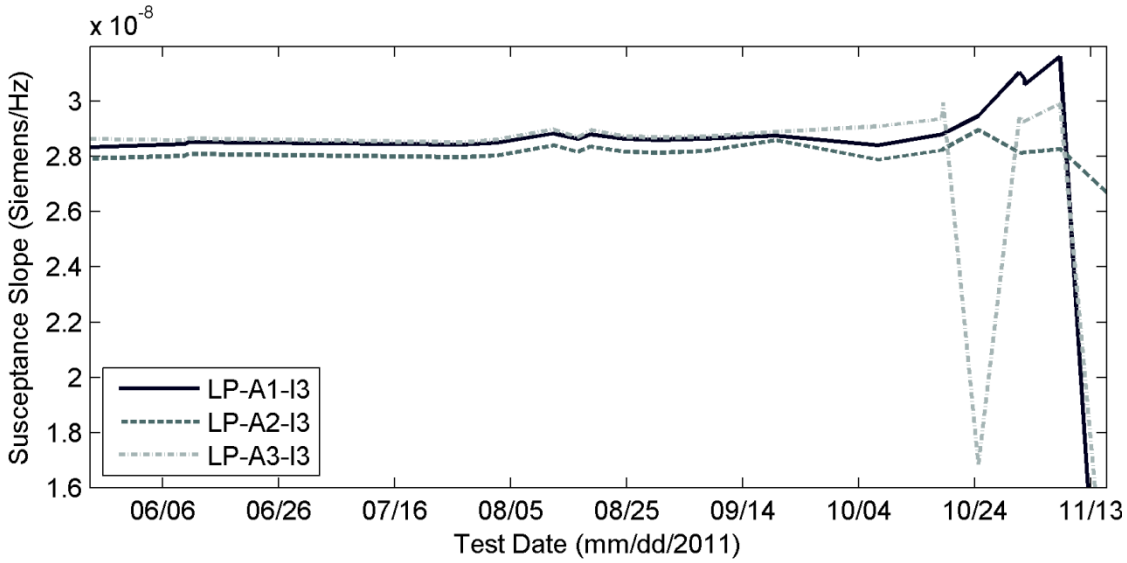

Figure 48: Susceptance slope values versus test date for patches at array location LP-I3

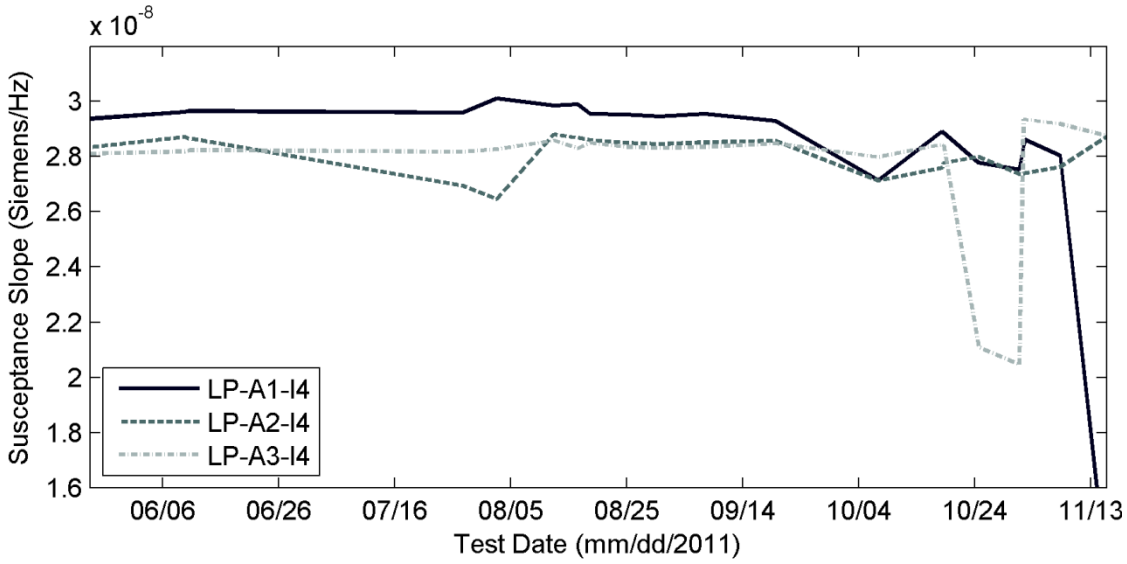

Figure 49: Susceptance slope values versus test date for patches at array location LP-I4

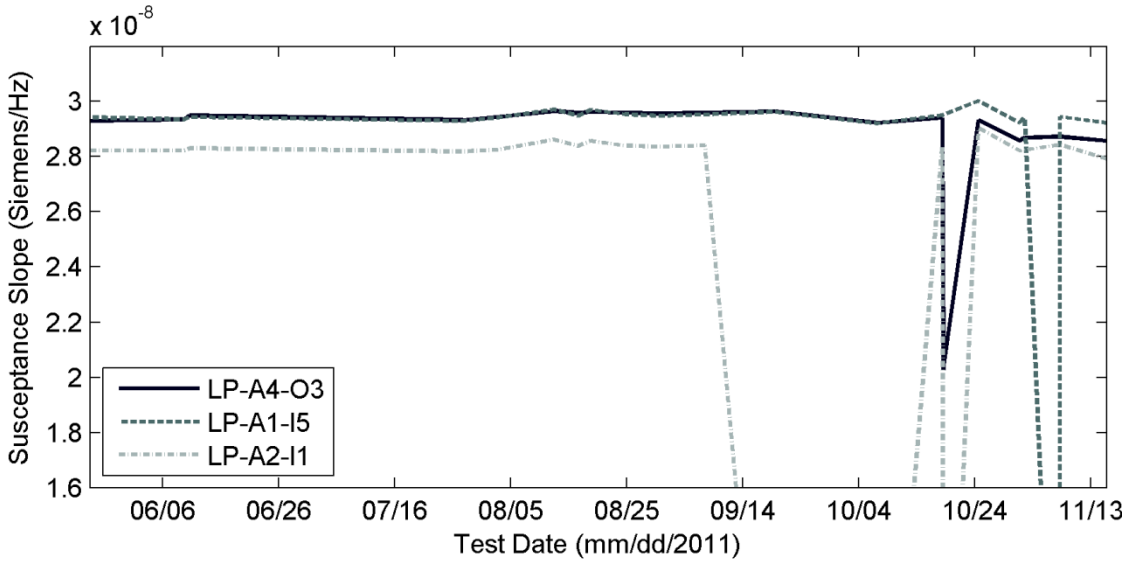

Figure 50: Susceptance slope values versus test date for failed sensors at locations other than LP-I3 and LP-I4

4.3.2. Data Cleansing

Patch LP-A4-O3 exhibited a significant decrease in its susceptance slope for measurements taken on 10/18/2011. The drop in slope was visually observable in the plot shown in Figure 50. Because the drop was severe, and the other patches in that array exhibited no such drop, the patch was deemed broken and was replaced on 10/24/2011. The measured susceptance slope for the new patch was similar to that for the previous patch. After replacing the patch, a new set of baseline measurements were collected, both for sensor diagnostics and SHM purposes. As noted in Section 2.5.3, at this point in the fatigue test progression the rotor blade was already in an incipient damage state, and while the further change from incipient to catastrophic damage would be detectable using baselines collected with the new patch, it was not possible to use this sensor location to detect the incipient damage state. In analyzing the available data in an attempt to detect the incipient damage, or to assess the detection performance of various methods or sensor paths, data both from the broken patch and its replacement must be cleansed from the overall dataset.

Consider the Impulse Correlation Coefficient Complement (ICCC) test statistic, described in Section 5.2.3. This test statistic is plotted versus test date in Figure 51 for three patches in array LP-A4, including LP-A4-O3, which was determined on 10/18/2011 to have fractured. After fracturing, patch LP-A4-O3 exhibited a step change in the computed ICCC test statistic. Without available sensor diagnostics information, such a step change in a test statistic value might be interpreted as indicating a step change in the condition of the structure, warranting possibly costly action. In a detection performance assessment, this particular sensor path might be erroneously interpreted to have near perfect detection performance. However, because the sensor was identified as broken, data from that sensor could simply be excluded from the analysis. If this situation had arisen while the structure was still in operation and also still considered healthy, the patch could be replaced, and the new baseline data gathered after its installation would be useful for detecting future structural changes.

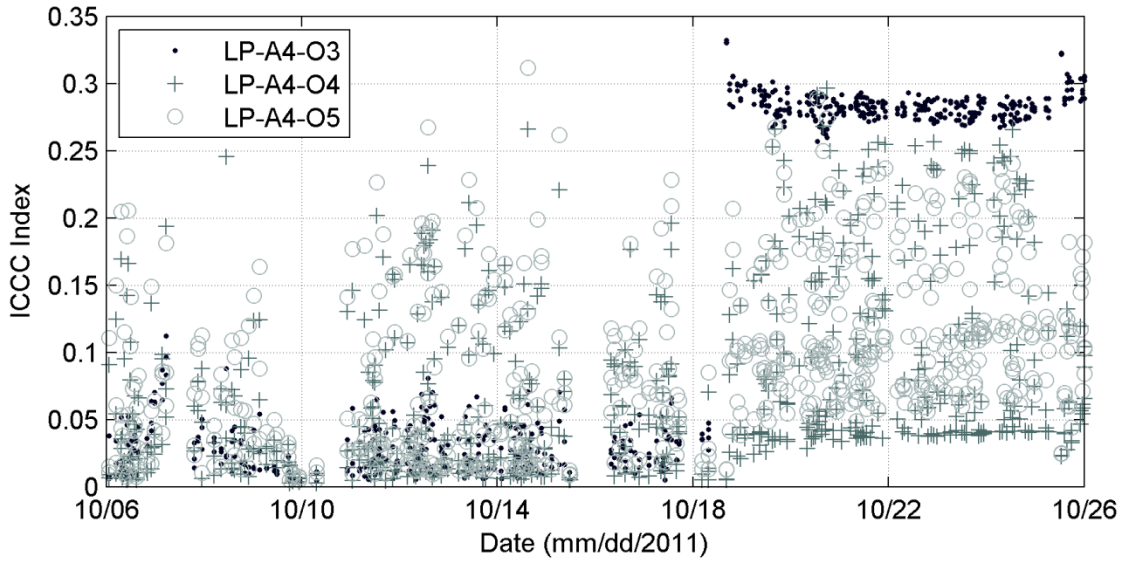

Figure 51: ICCC test statistic versus test date for three patches in array LP-A4

4.3.3. Nonstationary Structural Impedance

In the course of this study, some impedance measurements were collected while the rotor blade was undergoing cyclic loading, subjecting the surface on which the patches were mounted to a strain field that varied in time. This time-varying strain field directly resulted in a time-varying structural impedance. Because of the frequency-stepping method implemented with the HP4294A, the measured impedance appeared to be a nonlinear function of frequency, dependent on the ratio of the "admittance frequency lines per second" sampling rate to the "cycles per second" rate of the blade's motion, resulting an "admittance frequency lines per cycle" frequency space.

The "cycles per second" rate of the blade's motion can be fairly simply established with kinematic measurements. Throughout the course of the fatigue test, strain data were collected at various locations on the surface of the rotor blade, and acceleration data were collected in the flapwise and edgewise directions at the rotor blade tip. These data were partly used for the feedback control system driving the excitation of the blade, and they were also saved as part of the record of the fatigue test. The common data collection practice was to retain only the data points corresponding to the maxima and minima of the displacement input, which effectively assumes that the input contained only a single fundamental frequency. However, some isolated strain and acceleration sequences were collected at a sampling rate of 120 Hz. Although the target excitation was a pure sinusoid at the rotor blade's first resonance, an estimate of the power spectral density (PSD) for the input excitation revealed the presence of several harmonics, and, unfortunately, two aliased peaks. For a time-series dataset collected near the start of the test on 08/16/2011, the normalized power spectral density (PSD) estimates of the input excitation (recorded in inches) and the strain (recorded in percent microstrain) at a point 1.35 m from the root on the blade's high-pressure side are shown in Figure 52. The PSDs were

estimated from a 56200-point sequence at 120 Hz, using Welch's method of averaged periodograms with a Hann window, 4096-point blocks and 50% overlap. Note the harmonics of the fundamental frequency, near 1.8 Hz, which are also reflected in the strain response. The other two peaks are most likely harmonics of the fundamental frequency above 60 Hz, which have been aliased back into the measured spectrum. There is a strong response at the fundamental frequency and its first harmonic, and also at the fourth harmonic, near 9 Hz. The stronger response at 9 Hz is likely the result of the harmonic excitation falling near the rotor blade's second flapwise bending mode at 9.23 Hz.

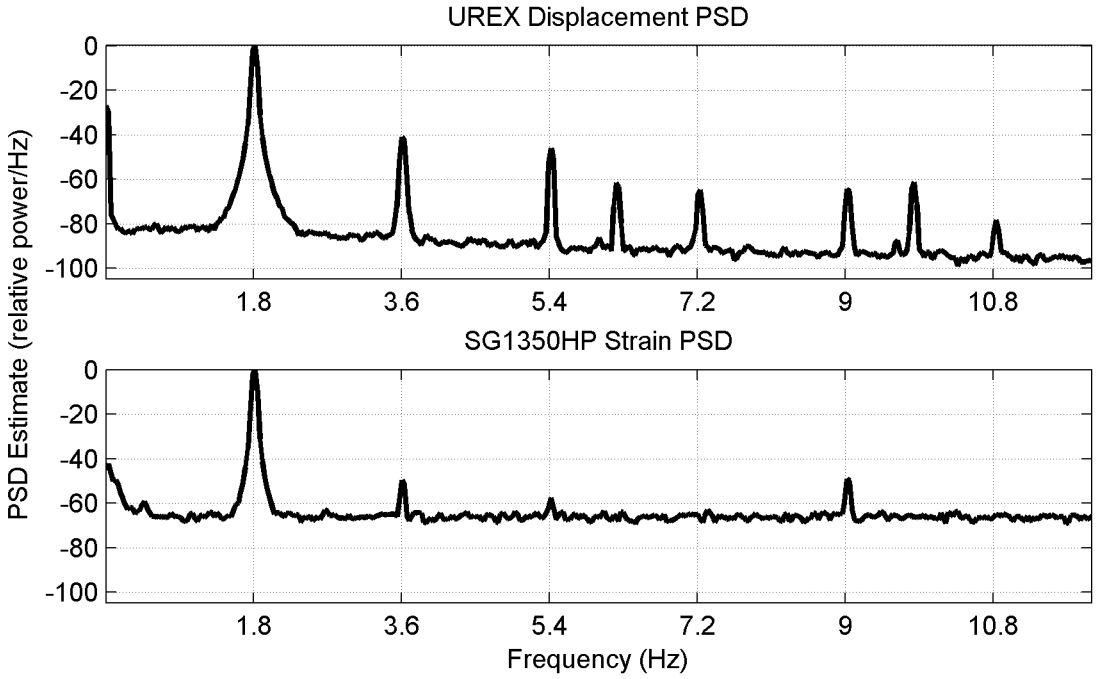

Figure 52: Displacement excitation (top) and strain response (bottom) PSD estimates

An example of admittance measurement behavior under cyclic loading is shown for patch HP-A1-L3 in Figure 53. The raw susceptance data have been plotted versus measurement frequency for two separate sets of impedance measurements taken on 10/24/2011 and 10/31/2011. The data collected on 10/24/2011 reflect the cyclic excitation with a fundamental

frequency of 1.793 Hz. The susceptance data are shown again in Figure 54 with the linear trend removed. Although there is some drift, note the flat, smooth nature of the measurement taken with the rotor blade in a quiescent state, compared to the harmonic oscillations in the measurement collected under cyclic loading.

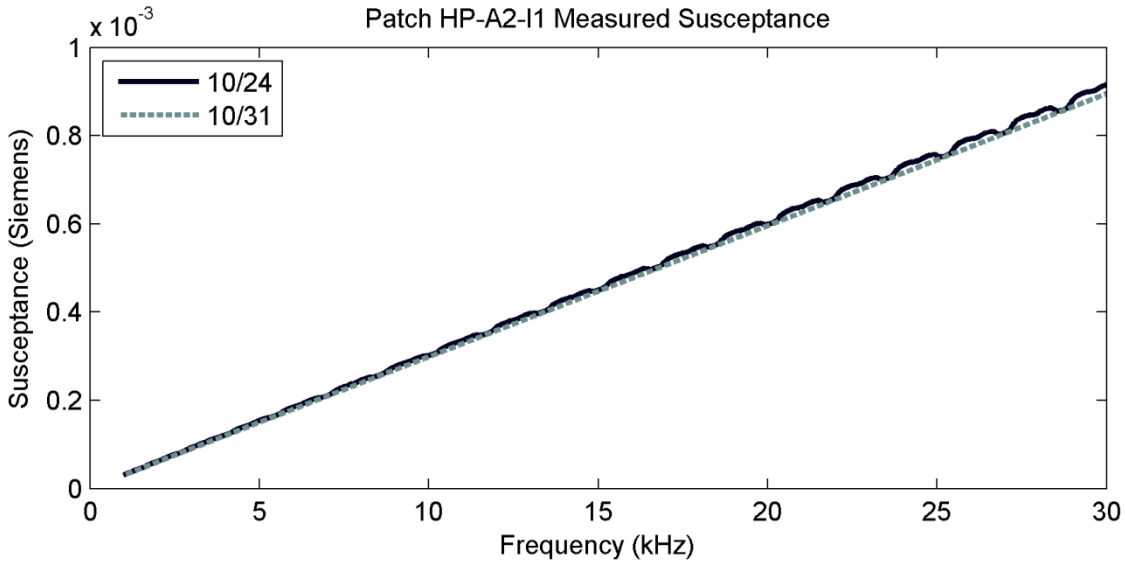

Figure 53: Measured susceptance for patch HP-A2-I1 with and without cyclic loading

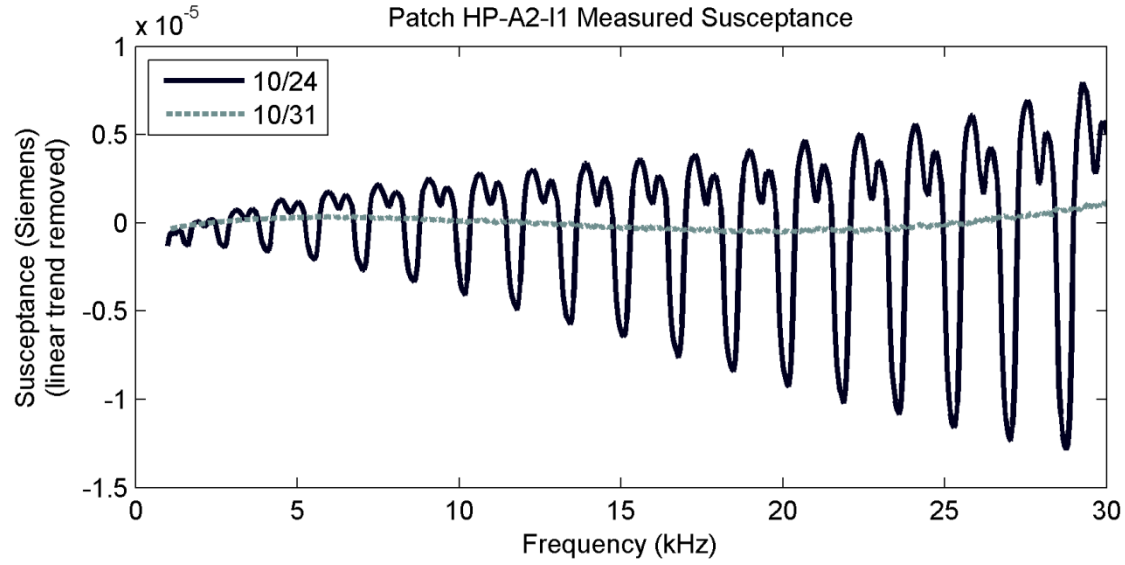

Figure 54: Susceptance curves for patch HP-A2-I1 with and without cyclic loading

For the impedance measurement method implemented in this test, the time lapse between collecting impedance data at each frequency line was not constant at very low frequencies. For the 512-point sequence with its linear trend removed, where each sample is related to impedance data collected at a particular frequency line, a PSD estimate was computed in normalized "cycles per frequency line" space. Computing several such estimates using a short-time 64^{th}-order Yule-Walker estimator operating on 128-point blocks with 120 overlap points, a spectrogram image was generated, which is shown in Figure 55. The spectrogram image has been normalized so that the largest value is 0 dB, and lighter colors represent larger values. Assuming the UREX loading frequency was constant in time, it is apparent from Figure 55 that over the course of the impedance measurement the time lapse between frequency lines decreased as the admittance measurement frequency increased, and then became constant for admittance measurement frequencies above 20 kHz. In this measurement region, the rotor blade would undergo one fatigue cycle in slightly more than the time required to collect 30 data points, so the apparent fatigue loading frequency, in the normalized admittance measurement frequency space (fatigue cycles per admittance frequency line), was about 1 cycle per 30 frequency lines. For the region where the time lapse between admittance measurement frequency lines was constant, a PSD estimate was computed by taking the mean across the columns of the spectrogram. This PSD estimate is shown in Figure 56.

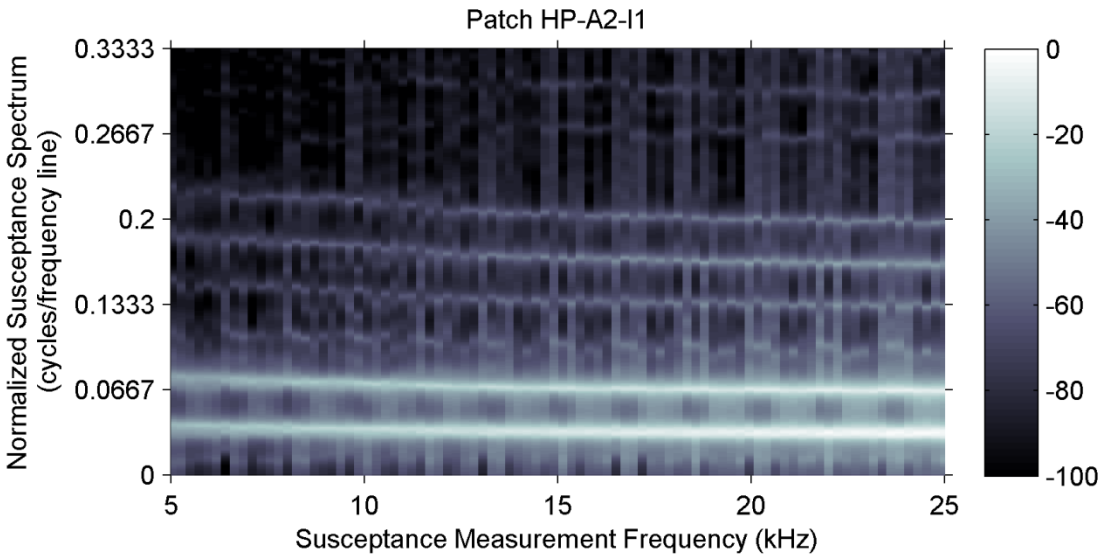

Figure 55: Susceptance spectrogram for nonstationary impedance measurement

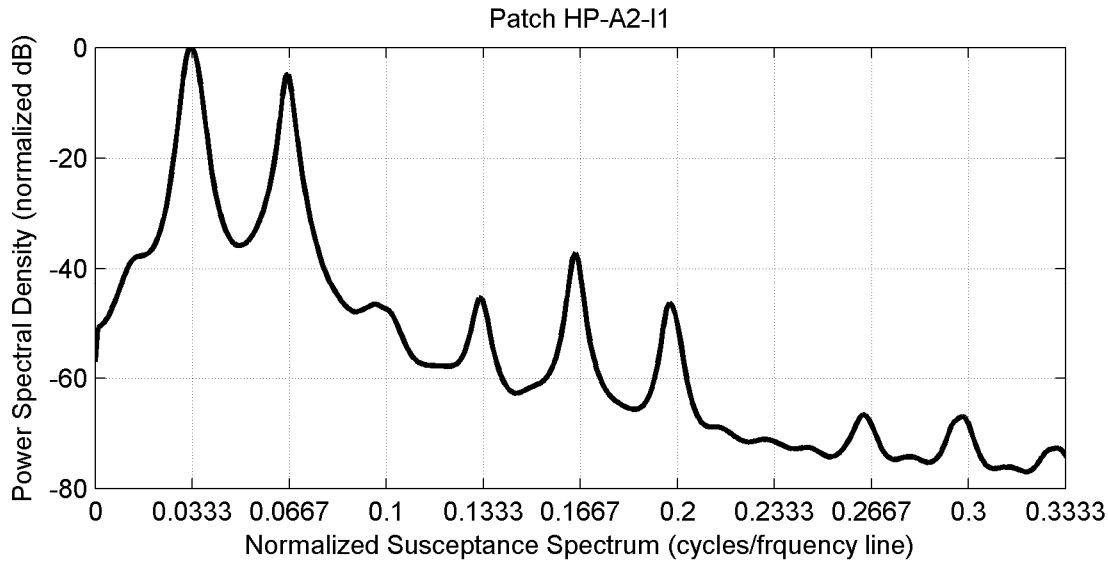

Figure 56: Susceptance power spectral density for nonstationary impedance measurement

In order to account for the effect of this nonstationarity, its functional form must be incorporated into an expression for the susceptance, which is expressed in Eq. (4.6). Noting from [86] that changes in the local stiffness manifest in the imaginary part of the structural impedance, Eq. (4.6) can be rewritten with $y_s = y_s + A\cos\left(\Omega\omega + \Phi\right)$, modeling this component

of structural impedance as a harmonic oscillation about a nonzero mean. Inserting this expression in to Eq. (4.6) gives an expression for the susceptance as

$$B(\omega) = \frac{a\omega \begin{pmatrix} \varepsilon x_a^2 + \left(-d^2 Y + \varepsilon\right) x_s^2 - d^2 Y \eta x_s y_a \\ -\left(A\cos\left(\Omega\omega + \Phi\right) + y_a + y_s\right)\left(-\varepsilon y_a + \left(d^2 Y - \varepsilon\right)\left(A\cos\left(\Omega\omega + \Phi\right) + y_s\right)\right) \\ +x_a\left(\left(-d^2 Y + 2\varepsilon\right) x_s + d^2 Y \eta\left(A\cos\left(\Omega\omega + \Phi\right) + y_s\right)\right) \end{pmatrix}}{\left(x_a + x_s\right)^2 + \left(y_a + y_s + A\cos\left(\Omega\omega + \Phi\right)\right)^2}. \quad (4.7)$$

While Eq. (4.7) might be appropriate for use in determining the individual components of mechanical impedance for the patch and the structure under these loading conditions, it is not necessary simply to normalize the admittance measurement and remove the effect of the nonstationary behavior. Noting from Figure 53 that the measured susceptance is dominated by the linear capacitive behavior, the numerator in (4.7) can be approximated by a linear expression with arbitrary constants, so that

$$B(\omega) = \frac{c_1 + c_2\omega}{\left(x_a + x_s\right)^2 + \left(y_a + y_s + A\cos\left(\Omega\omega + \Phi\right)\right)^2}. \quad (4.8)$$

Noting also that the nonstationarity has been accounted for in the cosine term, the remaining parameters in the denominator can be combined in arbitrary constants $c_3 = x_a + x_s$ and $c_4 = y_a + y_s$, so that an empirical expression for the measured susceptance can be written as

$$B(\omega) = \frac{c_1 + c_2\omega}{c_3^2 + \left(c_4 + A\cos\left(\Omega\omega + \Phi\right)\right)^2}, \quad (4.9)$$

where the c_n are constants relatable to the parameters in Eq. (4.2), Ω is the cyclic loading frequency in cycles per admittance measurement frequency line space, and Φ is an arbitrary, constant phase angle fixed by the timing between the cyclic loading and the start of the impedance measurement. Although the experimental PSD in Figure 56 does reveal the presence

of higher harmonics, the expression given in Eq. (4.9) would capture the first two dominant frequencies.

An example implementing the normalization model of Eq. (4.9) is shown in Figure 57 for patch HP-A2-I1, where plotted together are the measured data taken with the rotor blade undergoing cyclic loading, the fitted and normalized curves for that data, and measured data taken with the rotor blade in a static condition. This plot demonstrates the ability to normalize susceptance measurements in the presence of a dynamic strain field so that the measurements can still be compared among different tests, reducing the likelihood that incorrect conclusions concerning the sensor condition would be drawn based on susceptance slope values artificially inflated by host structure dynamics. Figure 58 shows the corresponding locations of the measured susceptance slope and the normalized slope relative to a histogram of the sample population of slopes for all the healthy sensors in the fatigue test. The sample mean was 2.90×10^{-8} Siemens/Hz and the standard deviation was 7.38×10^{-10} Siemens/Hz. The measured susceptance slope is just over two standard deviations above the mean at 3.06×10^{-8} Siemens/Hz while the normalized susceptance slope is well within the expected range of slopes, at 2.99×10^{-8} Siemens/Hz.

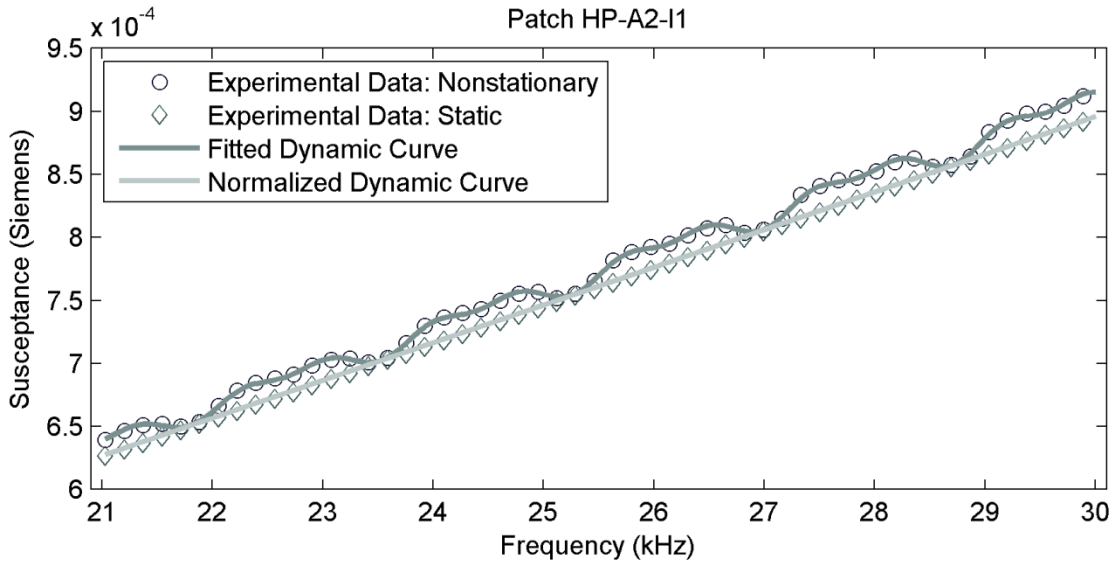

Figure 57: Dynamic and static experimental data shown with fitted dynamic data and normalized curve

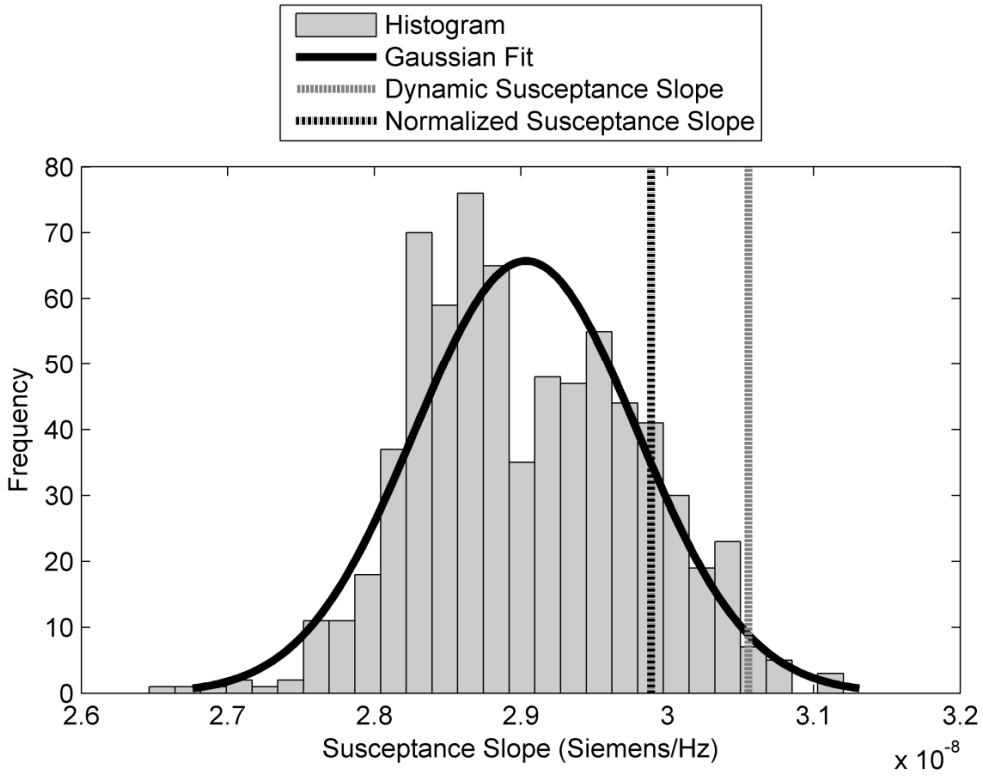

Figure 58: Histogram and Normal fitted curve for all healthy sensor susceptance slopes; vertical lines indicate measured and normalized slopes for data collected from sensor HP-A2-I1 on 10/24/2011

In some cases involving cyclic structural loading, partially fractured patches exhibited a crack-breathing phenomenon, in which the susceptance slope value oscillated between a "healthy" level and a "broken" level. Patch LP-A3-I3 was clearly observed on 10/24/2011 to be fractured, and the change in its slope can be seen in Figure 48. Its raw susceptance measurements are plotted in Figure 59 for data collected on 10/18/2011, when the patch was still healthy, and on 10/24/2011, when the patch had fractured. Although this patch would still be identified as broken using the slope fitted to the bilinear curve that was measured, this measurement provides a clear indication of the effect that cyclic loading has on the patches and their measured impedance.

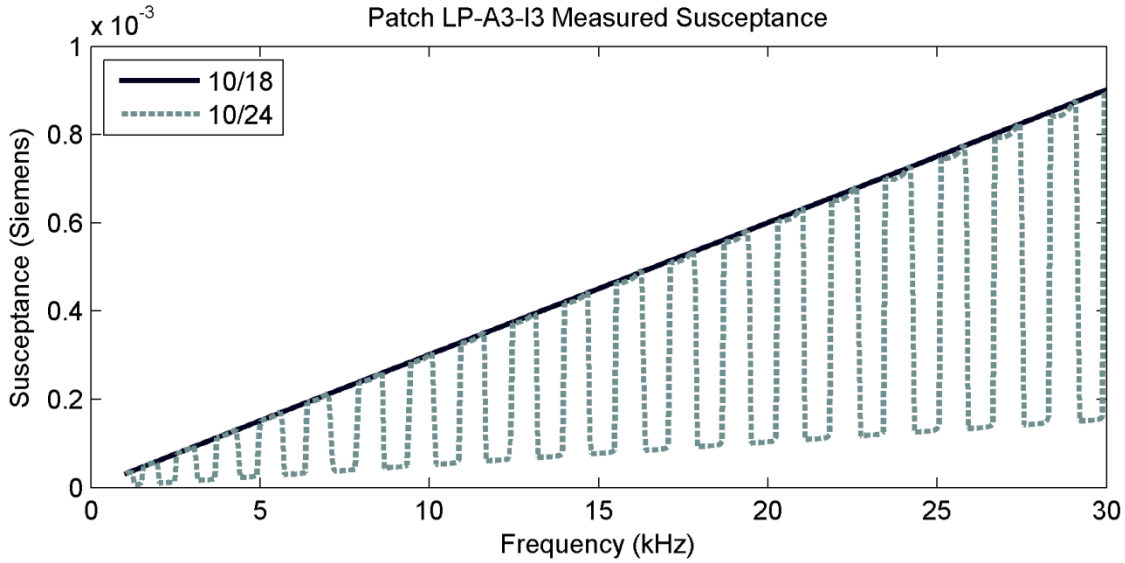

Figure 59: Example of bilinear behavior with breathing crack

4.4. Summary and Acknowledgements

This chapter has presented an overview of impedance-based sensor diagnostics for piezoceramic transducers used in active sensing applications for SHM. A case study was presented in which 49 transducers were used to monitor the health of a wind turbine rotor blade

subjected to fatigue loading until failure. The transducers proved effective in their longevity and ability to perform within the SHM system until after the blade began to fail. For those sensors that did fail, the sensor diagnostics procedures implemented were effective in identifying them. In some cases where the susceptance slope increased, which would ordinarily indicate a debonded sensor, the fiberglass material to which the transducer was affixed seems to have softened. In this case, the increased susceptance slope would be an indication of incipient structural damage, rather than sensor failure. Furthermore, data taken under dynamic loading, which is often necessary for *in situ* operation of an SHM system, exhibited a clearly measureable impact on the susceptance values. An empirical model was proposed as a tool to normalize these measurements in order to enable comparison among measurements taken in other loading conditions.

Chapter 4, in part, has been recommended for publication in [6] *Smart Materials and Structures*, S. G. Taylor, G. Park, K. M. Farinholt, and M. D. Todd, 2012. The title of this paper is "Diagnostics for piezoelectric transducers under cyclic loads deployed for structural health monitoring applications." The dissertation author was the primary investigator and author of this paper.

Chapter 5
SHM with Active Sensing Systems

5.1. Introduction

A variety of data acquisition and analysis methods have been applied to the problem of fatiguing wind turbine rotor blades, and the CX-100 rotor blade has been a specimen of particular popularity [7, 15, 20, 102-108]. The experiment considered in this example was the CX-100 rotor blade fatigue test described in Section 2.5. Focusing on a comparison between ultrasonic guided wave (UGW) measurements and diffuse wave field measurements (DWF), data from sensor arrays LP-A1, LP-A2, and LP-A4 are presented; these sensor arrays are described in detail in 2.5.2 and summarized in Table 2. This study showed that UGW data at relatively high frequencies for fiberglass structures, at 200 kHz and above, provided excellent detection performance for sensor arrays along the rotor blade's carbon fiber spar cap, taking advantage of its architecture to implement a very low-density array capable of detecting incipient damage. However, diffuse wave data using excitation signals limited to 40 kHz displayed the greatest overall sensitivity to the incipient crack formation, with damage localization capability enabled by heightened sensitivity for sensor paths near the crack. In all

cases, energy methods outperform correlation methods, confirming previous results indicating that an energy detector is often the optimal detector for guided wave applications [94, 109].

5.2. Background for Active-sensing SHM

5.2.1. Ultrasonic Guided Wave Processing

In SHM applications for ultrasonic guided waves (UGWs), a short-time, narrow-band wave packet $\mathbf{x}_i$ is used to excite the structure, and the measured response $\mathbf{y}_i$, usually at another location, contains the structure's multipath response to that excitation. The subscript i refers to the i^{th} measurement over a particular SHM campaign, and the signals are shown in bold face to indicate that they are discrete signals (*i.e.*, $\mathbf{x}_i = \mathrm{x}_i[k]$, where k is the signal array index). If the underlying structure changes, the properties of the propagation paths for a given wave packet will also change, resulting in a change in the measured response. In practice, each measured response is match-filtered with the excitation signal, producing the filtered response $\tilde{\mathbf{y}}_i$. This process increases the apparent signal-to-noise ratio, but also suppresses any nonlinear frequency-shifting effects that may be inherent to the structure. For each filtered signal $\tilde{\mathbf{y}}_i$, a residual $\mathbf{r}_i$ is computed using an optimal baseline subtraction method [99], taking the difference between the filtered waveform $\tilde{\mathbf{y}}_i$ and the baseline filtered waveform $\tilde{\mathbf{y}}_j$ that minimizes the residual's norm. The subscript j refers to the particular past measurement in the SHM campaign that minimizes the i^{th} residual.

If the structure remains unchanged, and the baseline data sufficiently span the structure's environmental operating space, the residual will be noise, albeit generally not normally distributed, with an expectation of zero. If the structure has changed, that change

would manifest itself as a deterministic signal embedded in the noise, detectable as a measureable increase in the residual energy. Because relative phase information is often impossible to determine using the sparse arrays typically implemented in UGWSHM applications, a residual envelope $\mathbf{v}_i$ can be computed, with no significant loss of information, as the amplitude of the analytic signal of the residual $\mathbf{r}_i$ [110]. For use in normalization, the baseline signal envelope $\mathbf{w}_j$ is similarly computed from each filtered baseline signal $\tilde{\mathbf{y}}_j$. Any of these signals could be used to compute various test statistics for detection purposes.

5.2.2. Diffuse Wave Field Processing

In diffuse wave field (DWF) measurements, a broadband signal is used to excite the structure for a long time relative to the wave's travel time from the actuator to the sensor. Each measurement pair is then a particular representation of the DWF. The measured signals are colored noise, with the specific coloration being a function of the underlying structural properties of the DWF. Unless identical excitation sequences are used for subsequent tests, any two measurements would be largely uncorrelated because of the complex, random nature of the DWF. Therefore, traditional baseline subtraction as implemented for guided waves would not produce meaningful results due to unacceptable signal-to-noise ratios.

In order to implement similar test statistics as for UGW signals, the "local" impulse response $\boldsymbol{\psi}_i$ was first estimated for each DWF measurement $\mathbf{y}_i$. Rather than match-filtering the response signal with the excitation, the frequency response function (FRF) was estimated for each input-output pair $(\mathbf{x}_i, \mathbf{y}_i)$, and the time-domain impulse response function (IRF) was estimated from that FRF by taking its symmetric inverse Fast Fourier Transform (iFFT). In a true diffuse field, this IRF will be an estimate of the pulse-echo response for the measurement transducer [111]. Although these measurements can be obtained directly, estimating them in the

manner presented here permits the use of less sophisticated data acquisition hardware, and also allows the structure to be excited with more energy for each measurement, effectively collecting more information in a single record.

Each estimated impulse response $\boldsymbol{\psi}_i$ can be processed in the same manner as for UGW signals to obtain a corresponding impulse residual $\boldsymbol{\rho}_i$, a residual impulse envelope signal $\boldsymbol{\upsilon}_i$, and an appropriate baseline impulse envelope signal $\boldsymbol{\omega}_j$. These signals can then be used in the same manner as the UGW signals to compute test statistics for detection purposes. Although the impulse residual signal is not narrow-band as UGW signals are, its expectation in the absence of structural changes is still zero, and changes in the underlying structure are detectable using test statistics computed with these signals.

5.2.3. Test Statistics

A variety of test statistics can be computed using the processed waveforms described above. There are two classes of test statistics commonly applied in structural health monitoring, and here, the simplest version of each is implemented. The first class of test statistic aims to detect the presence of a signal in noise, under the assumption that its presence would be indicative of structural change. The simplest of these is an energy detector, cast in [110] as the energy in a residual signal normalized by the energy in a baseline signal, and listed in Table 10 as the normalized residual energy (NRE) test statistic. The analogous test statistic using the IRFs estimated from the DWF data is listed as the normalized impulse residual energy (NIRE) test statistic. Other energy-based detectors not utilized here include the normalized maximum residual, used by Croxford, et al. [99], and the normalized maximum amplitude, used by Michaels, et al. [96]. The second class aims to detect the degree to which a measurement is unlike previous measurements. To that end, the correlation coefficient complement (CCC) is

utilized, which ranges from 0 to 1 with values increasing for signals that are less correlated with previous ones. The analogous test statistic using the IRFs estimated from the DWF data is listed as the impulse correlation coefficient complement (ICCC). Computing the correlation coefficient requires the signal mean μ and the standard deviation σ; subscripts on these quantities in Table 10 indicate the signal from which they were calculated.

Table 10: Test Statistics implemented for CX-100 fatigue crack detection

Name	Expression	Reference
Normalized Residual Energy (NRE)	$NRE = \frac{\sum_{k=1}^{N}\left(\mathrm{v}_i[k]\right)^2}{\sum_{k=1}^{N}\left(\mathrm{w}_j[k]\right)^2}$	Kay [110]
Normalized Impulse Residual Energy (NIRE)	$NIRE = \frac{\sum_{k=1}^{N}\left(\upsilon_i[k]\right)^2}{\sum_{k=1}^{N}\left(\omega_j[k]\right)^2}$	[7]
Correlation Coefficient Complement (CCC)	$CCC = 1 - \sum_{k=1}^{N}\frac{\left(\tilde{\mathrm{y}}_i[k]-\mu_{\tilde{\mathrm{y}}_i}\right)\left(\tilde{\mathrm{y}}_j[k]-\mu_{\tilde{\mathrm{y}}_j}\right)}{\sigma_{\tilde{\mathrm{y}}_i}\sigma_{\tilde{\mathrm{y}}_j}}$	Yinghui and Michaels [112]
Impulse Correlation Coefficient Complement (ICCC)	$ICCC = 1 - \sum_{k=1}^{N}\frac{\left(\psi_i[k]-\mu_{\psi_i}\right)\left(\psi_j[k]-\mu_{\psi_j}\right)}{\sigma_{\psi_i}\sigma_{\psi_j}}$	[7]

5.2.4. Receiver Operating Characteristic Curves

In detection theory [110], a basic problem formulation is one in which a signal may or may not be present in noise, and a hypothesis test is applied to determine the presence or absence of the signal. A test statistic derived from a measured signal, usually a scalar, is formulated such that a positive detection results when the test statistic exceeds a given threshold, disproving the null hypothesis that the signal is absent. If the distribution of the test statistic is known, the performance of the detector can be evaluated analytically by computing,

over a range of threshold values, the probability that the test statistic will exceed the threshold when the signal is present (a true positive) and when the signal is not present (a false positive). The true positive rate is plotted versus the false positive rate in a receiver operating characteristic (ROC) curve. The area under the curve (AUC) is an indicator of a given detector's performance, where a value of 1 would indicate perfect detection, a value of 0.5 would be equivalent to a random guess, and a value of 0 would imply that all the decisions were wrong. If the distribution of the test statistic is not known, ROC curves can still be produced in a data-driven manner from experimental results. As long as the truth of the signal's presence or absence is known, the true positive rate and the false positive rate can be computed for each case (signal present or absent) over the range of threshold values as the ratio of the number of tests for which the test statistic exceeds the threshold to the total number of tests in each respective case. The approach utilized in this dissertation is to produce a scalar test statistic for each dataset, from which data-driven ROC curves are generated for each sensor path in order to evaluate the performance of each hardware and test statistic combination.

5.3. Experimental Results

5.3.1. Representative Signals

Example filtered signals from two different test dates, along with their respective baseline and residual signals, are shown in Figure 60 for UGW data collected with an excitation signal at 200 kHz. In computing the test statistics for the UGW data, only the first arrival was used, so the plots include only the first 0.15 milliseconds (ms) of the time record, which was captured at 10 MHz. In the healthy case, with data collected on 09/02/2011, the new waveform is similar its corresponding baseline, resulting in a residual signal relatively close to zero. For

the post-incipient damage case, with data collected on 10/24/2011, the new waveform actually has a larger amplitude than its corresponding baseline. Although this result is not consistent with the notion that the presence of a crack would attenuate the signal, it does support the theory that the spar cap acted as a waveguide for the 200 kHz excitation; as the growing crack caused spar cap to become more free, there may have been less attenuation of the UGW signals. However this difference is still detectable as an increase in the energy of the residual waveform.

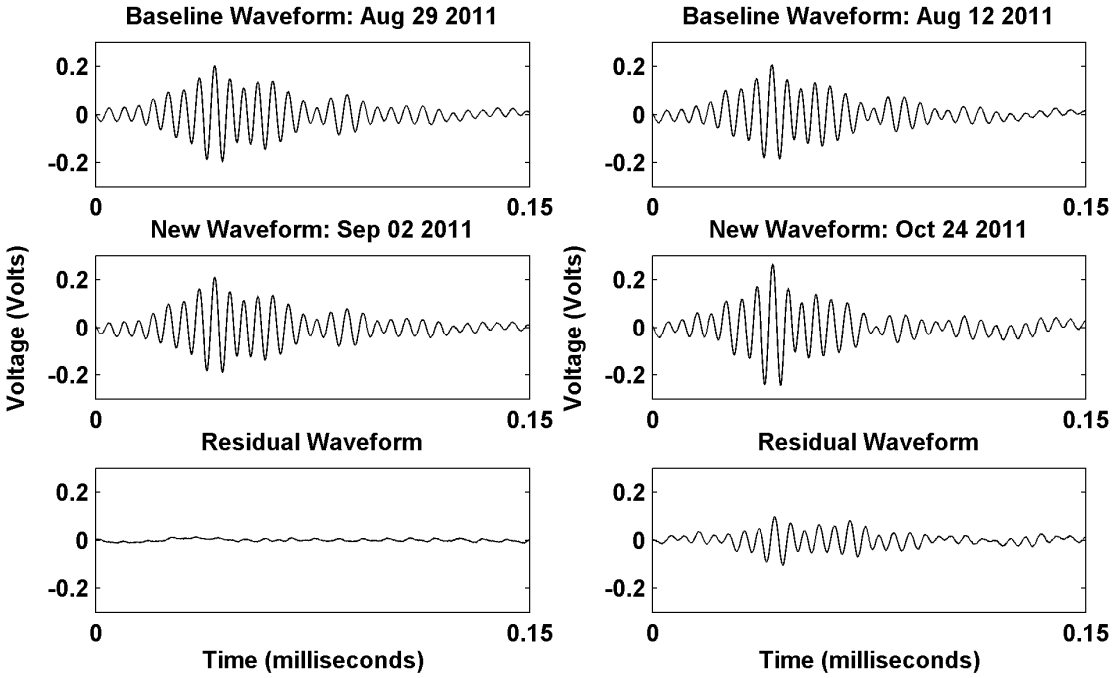

Figure 60: Sample signals for UGS measurements: healthy (left) and damaged (right)

Example signals are shown for DWF data using the same dates for the new waveforms in Figure 61. The frequency response function (FRF) was estimated for each sensor path using the H1 autocorrelation estimate, which is the ratio of the cross power spectrum of the output and input with the auto power spectrum of the input. The power spectra were computed using Welch's method of averaged Periodograms with a Hamming window, 1024 FFT points, and 50% overlap. The time-domain impulse response function (IRF) was estimated from that FRF

by computing its symmetric inverse Fast Fourier Transform (iFFT). The originally measured signals had 16384 points sampled at 96 kHz, for a duration of 170.67 ms. Because the FRFs used to estimate the IRF signals were computed with 1024-point overlapping blocks, the IRF estimates represent a duration of 10.67 ms. In order to capture the IRF dynamics, only the first 2.67 ms were retained (analogous to retaining only the first arrival for UGW data). Sample signals of the IRFs and residuals are shown in Figure 61 for a healthy and post-incipient damage case. In the healthy case, with data collected on 09/02/2011, the IRF is similar its corresponding baseline, resulting in a residual signal close to zero. For the post-incipient damage case, with data collected on 10/24/2011, the IRF is attenuated compared to its baseline, which is consistent with the physically intuitive notion that the presence of a crack would cause elastic wave attenuation. This difference is detectable as an increase in the energy of the residual waveform.

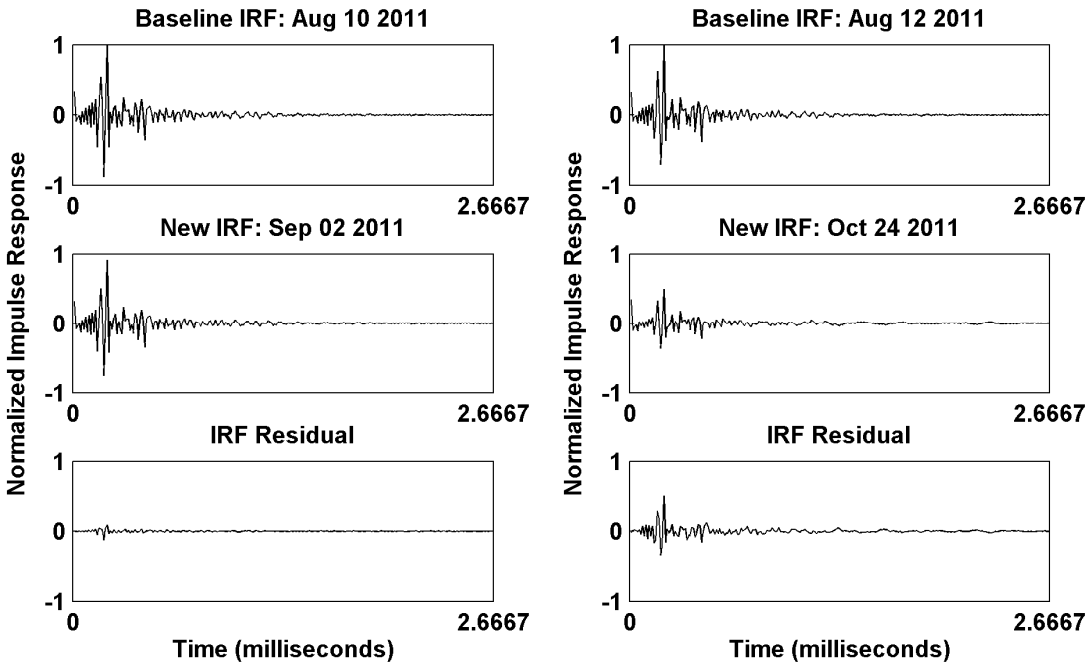

Figure 61: Sample signals for IRF estimates using DWF data: healthy (left) and damaged (right)

5.3.2. Incipient Crack Detection

5.3.2.1. Overview

The aim of this chapter is to compare the relative crack detection performance for different data collection and analysis methods. In order to assess detector performance, receiver operating characteristic (ROC) curves should be produced from experimental results, but this method requires that the truth of the structure's state to be known. In the case of incipient damage, the truth was unknown; so the desire is to determine from the experimental data both when the crack became detectable as well as the relative detection performance of the various approaches. A definition of truth (in terms of the detectability of the crack) is proposed as the one that maximizes the average detection performance over all methods considered. In many detection or classification applications, this problem might be intractable because of the large number of possible definitions of truth; however, because the data are perfectly separable in time (that is, the rotor blade was healthy until a certain date and damaged for all dates thereafter), the number of possible classification assignments is reduced to a number of demarcation time points no greater than the total number of datasets. Furthermore, under a binary classification assumption, one of these dates necessarily provides the true classification assignment. Then, the true demarcation date can be estimated as that which maximizes ROC performance, defined as the AUC for the associated ROC curve.

5.3.2.2. Approach

Each measurement time point was taken in turn as the "true" demarcation point. In each case, all measurements collected up to and including that point were taken to have come from the rotor blade in the pristine state, and all measurements collected after that point were taken to have come from the rotor blade in the damaged state. For each demarcation time point, the ROC

curves were computed for all sensor paths and transmission frequencies. As an example, the histograms for the NRE test statistic are shown for sensor path 3 at 50 kHz excitation in Figure 62 (left). The distribution shown has contributions from two overlapping distributions, and the selection of the demarcation point defines to which distribution each instance of the test statistic belongs. Choosing a demarcation date roughly as the halfway point in terms of UGW data collected, corresponding to 10/07/2011, results in histograms for the two distribution as shown in Figure 62 (right), where each distribution has been normalized to represent total unity area. Having selected the demarcation date, an ROC curve can be constructed as described above. Although the actual curve is not shown, for this example, the AUC is 0.9262. This process is applied for all sensor paths at each excitation frequency over all possible demarcation dates. The resulting AUC values can be plotted versus demarcation date to enable the selection of the demarcation date yielding the greatest detection performance. This data is then the most likely date on which the incipient structural damage appeared.

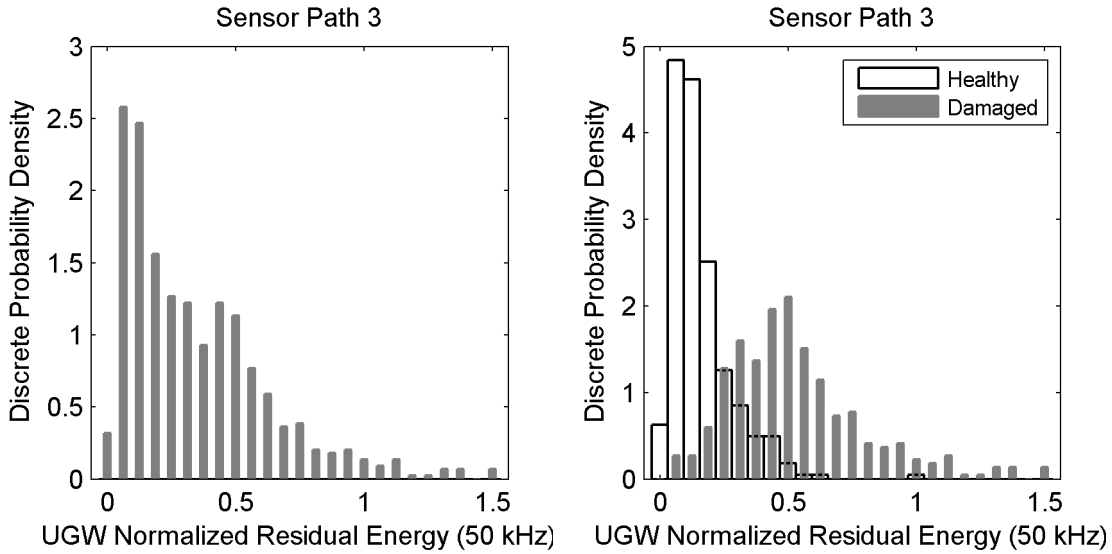

Figure 62: Histograms for the UGW test statistic with 50 kHz excitation along sensor path 3: all test statistic instances (left); test statistics divided according to a demarcation date of 10/07/2011 (right)

5.3.2.3. Results

The AUC values are plotted versus demarcation date for path 1 in Figure 63. The flat results for both paths 1 and 3 are indicative of a steady change in the test statistic over the period for which the AUC plot is flat. This would be visible in the raw test statistic plot, and would suggest the use of an external sensor pair along the spar cap as a gauge of damage progression. The AUC values are plotted versus demarcation date for path 2 in Figure 64. The performance drops off steadily with increasing frequency, and the peak location generally increases in time with increasing frequency. The performance drop is a reflection of the significant signal attenuation for path 2, and the increasing demarcation date indicates that for poorer signal quality, the damage had to become more severe in order to be detected. The AUC values are plotted versus demarcation date for path 3 in Figure 65. With the exception of the 50 kHz data, the results are similar to those for path 1. However, note also that for 75 kHz and 100 kHz, the flat portion begins on 10/04 and extends through 10/24, indicating an even longer period of change detectable along path 3 at low frequencies. The AUC values are plotted versus demarcation date for path 4 in Figure 66. Path 4 was quite near the crack, and this is reflected in the stronger concavity of the AUC curves. Also, as the excitation frequency increased, the date at which the incipient crack became detectable moved back: the incipient crack was detectable earlier with path 4 at higher frequencies than for most path/frequency pairs. Path 4 also exhibited a strong second peak in early November, when the crack surfaced. The AUC values are plotted versus demarcation date for path 5 in Figure 67. Path 5 displayed similar degrading performance with increasing frequency as path 2; with the peak shifting slightly forward until after 200 kHz, where the sharp peak indicates a step-change behavior in the test statistic. At higher frequencies with path 5, the only notable peaks occur in November.

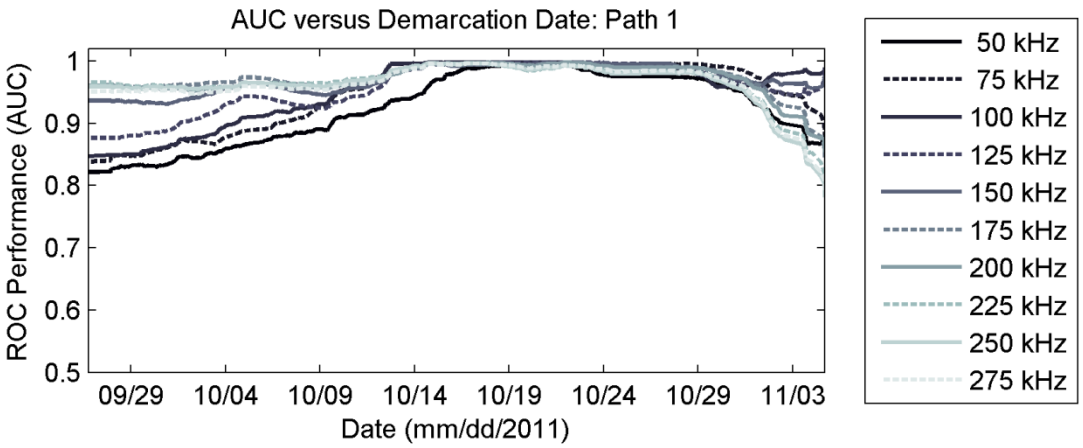

Figure 63: UGW NRE Performance versus demarcation date for path 1 at various frequencies

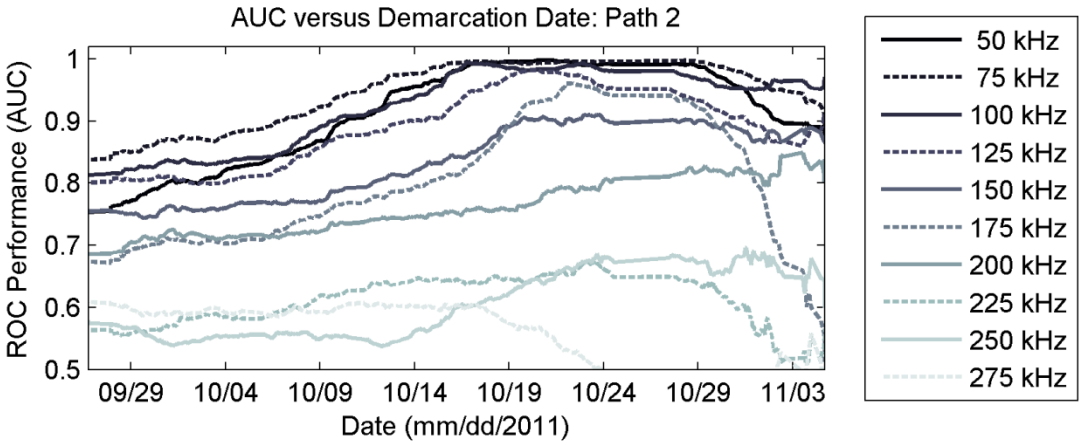

Figure 64: UGW NRE Performance versus demarcation date for path 2 at various frequencies

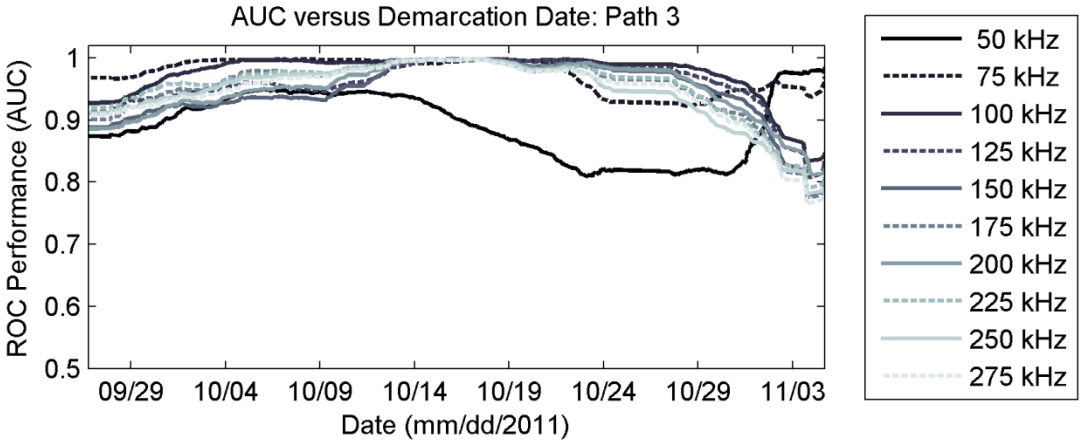

Figure 65: UGW NRE Performance versus demarcation date for path 3 at various frequencies

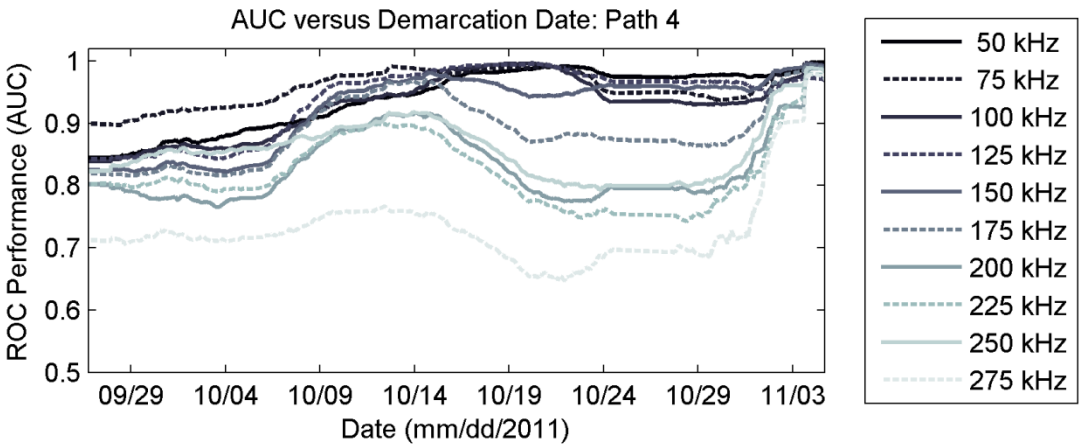

Figure 66: UGW NRE Performance versus demarcation date for path 4 at various frequencies

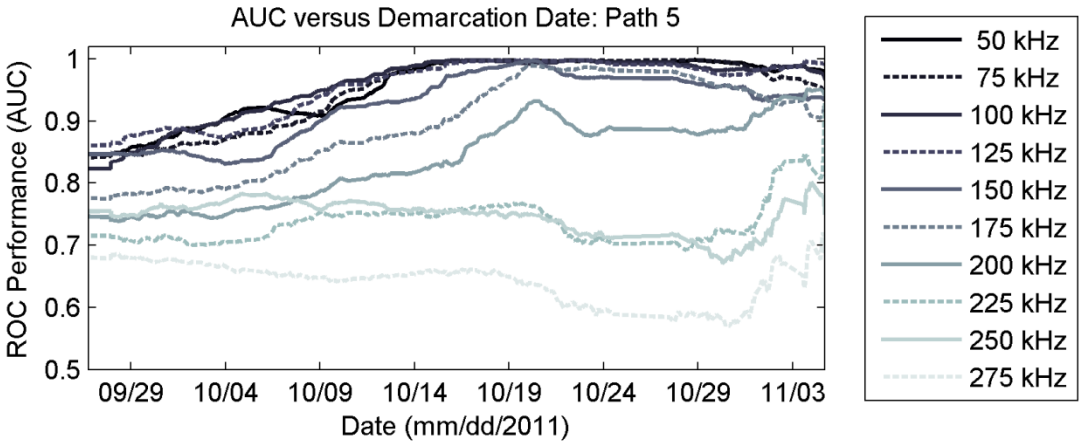

Figure 67: UGW NRE Performance versus demarcation date for path 5 at various frequencies

These results indicate that there are specific strengths and weaknesses of given paths and excitation frequencies, but a direct comparison of their performance requires a consistent definition of incipient damage, which in this case is the demarcation date used to generate the ROC curves used to compare performance. To that end, the prominent performance curve peaks from 50 path/frequency pairs plotted above were extracted and used to generate a histogram to show the distribution of demarcation dates. Because the physical rotor blade exhibited two distinct changes in time, first with the appearance of the incipient damage, and second with the surfacing of the catastrophic crack, two peaks were extracted from each AUC versus date curve.

The histogram is shown in Figure 68. It exhibits a strongly bimodal distribution, with one peak near 10/21/2011, and another near 11/08/2011. Choosing the date as 10/21/2011 would correspond to assessing performance in incipient crack detection, while choosing the date as 11/08/2011 would correspond to assessing performance in catastrophic crack detection. While it may not be useful to apply this type of SHM system to catastrophic crack detection, it is useful to note which methods are better performers in the different areas.

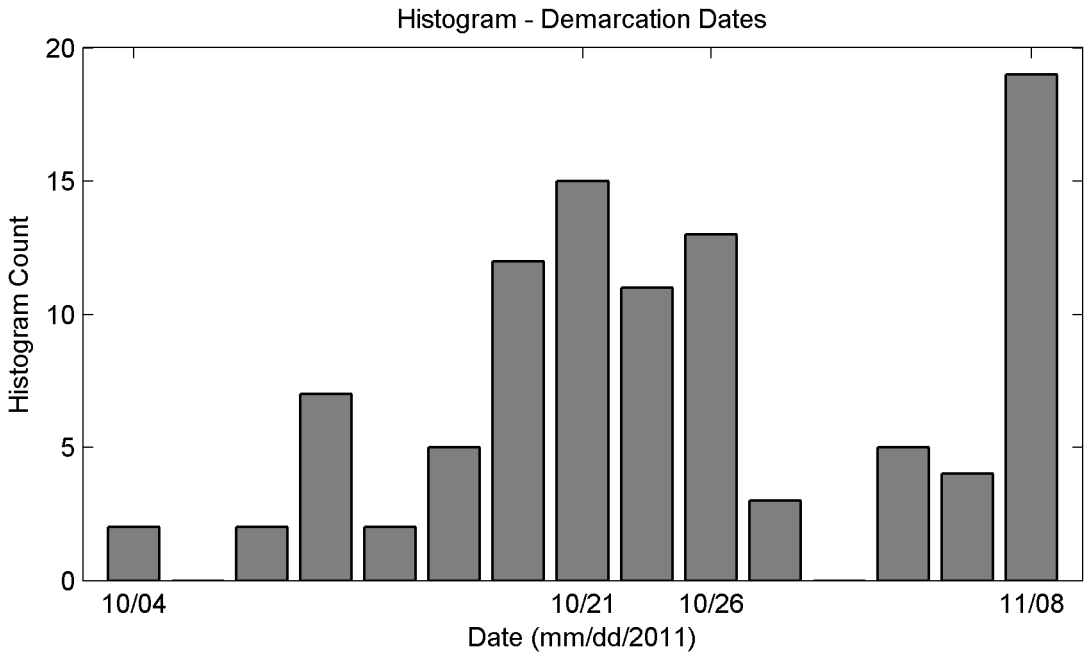

Figure 68: Histogram of most likely demarcation dates

5.3.3. Detector Performance Assessment

This section presents a detailed performance comparison between UGW and DWF data using the test statistics listed in Table 11. The results presented build on the arguments from the previous section, assigning 10/21/2011 as the "true" demarcation date. For each dataset, the data were divided into 'healthy' and 'damaged' groups, and histograms and ROC curves were generated for each hardware, test statistic, and sensor path combination described in Section

2.5.2. The histograms were normalized so that they represent discrete probability density functions (PDFs) with total probability of unity. While the shape of an ROC curve is informative in assessing the detection performance of a given test statistic, the AUC is a useful metric to describe the test statistic's basic detection performance in the hypothesis test. The AUC values for each test statistic are tabulated in Table 11. Along with the individual AUC values, three average values of interest are also tabulated: the overall average, A(all); the average between the two paths that lay nearest the fatigue crack, A(crack); and the average between the two paths that lay along the carbon fiber spar cap A(spar). The histograms and ROC curves corresponding to each AUC value included in Table 11 are plotted in subsequent figures.

Table 11: AUC values for dataset and test statistic pairs

	Inner Array Configuration						Outer Array Configuration Diffuse Waves (LP-A4)		
	Guided Waves (LP-A2)				Diffuse Waves (LP-A1)				
	50 kHz		200 kHz						
Path	NRE	CCC	NRE	CCC	NIRE	ICCC	Path	NIRE	ICCC
1	0.98	0.97	1.00	0.99	0.94	0.79	1	0.80	0.80
2	0.98	0.97	0.75	0.76	0.95	0.94	2	0.86	0.84
3	0.90	0.90	1.00	1.00	0.98	0.95	3	0.95	0.95
4	0.97	0.98	0.89	0.86	0.99	0.91	4	0.81	0.81
5	1.00	0.99	0.83	0.82	0.91	0.74	5	0.91	0.87
							6	0.88	0.89
A (all)	0.97	0.96	0.89	0.88	0.95	0.86	A (all)	0.85	0.84
A (crack)	0.94	0.94	0.94	0.93	0.98	0.93	A (crack)	0.86	0.84
A(spar)	0.94	0.93	1.00	0.99	0.96	0.87	A(spar)	0.80	0.81

5.3.3.1. Ultrasonic Guided Waves

The histograms for the NRE test statistic using 50 kHz guided waves are shown in Figure 69, with the corresponding ROC curves shown in Figure 71 (left). The shaded area in the

ROC plots indicates the random guess line; any curves that fall within that area would have an AUC of less than 0.5 and perform worse than a random binary guess. The data provide good classification performance, with an A(all) of 0.97. Curiously, path 5 had the greatest performance, but this path was far from the crack and did not lie along the spar cap. The histograms for the CCC test statistic using 50 kHz guided waves are shown in Figure 70, with the corresponding ROC curves shown in Figure 71 (right). The results for the CCC are nearly identical to those for the NRE, but with a slight performance drop.

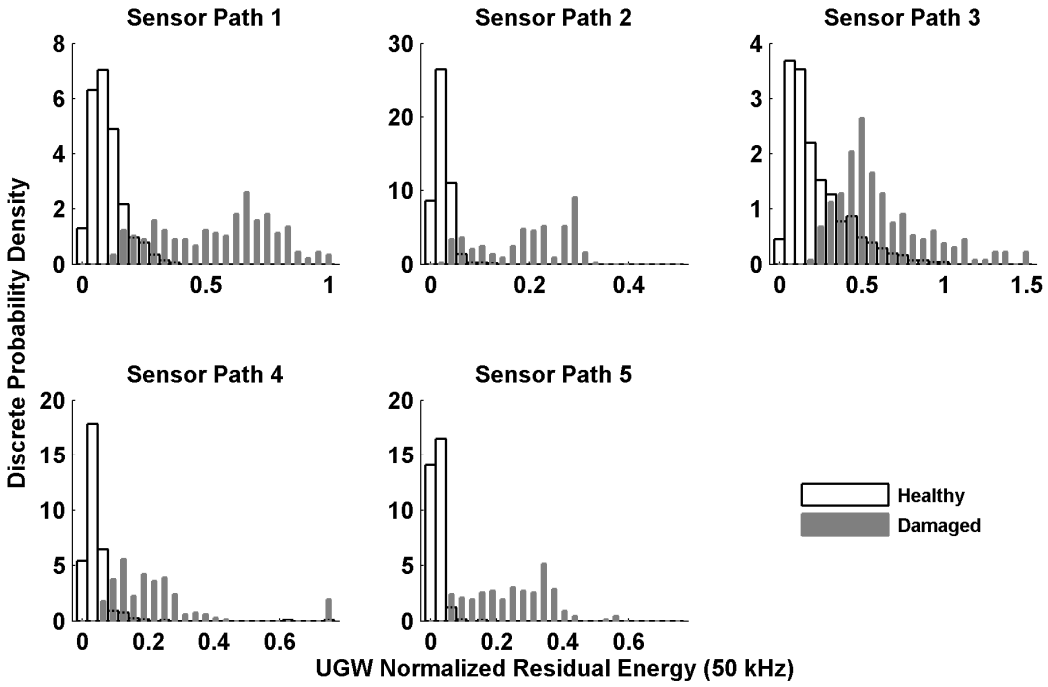

Figure 69: Test statistics for NRE using guided wave data at 50 kHz

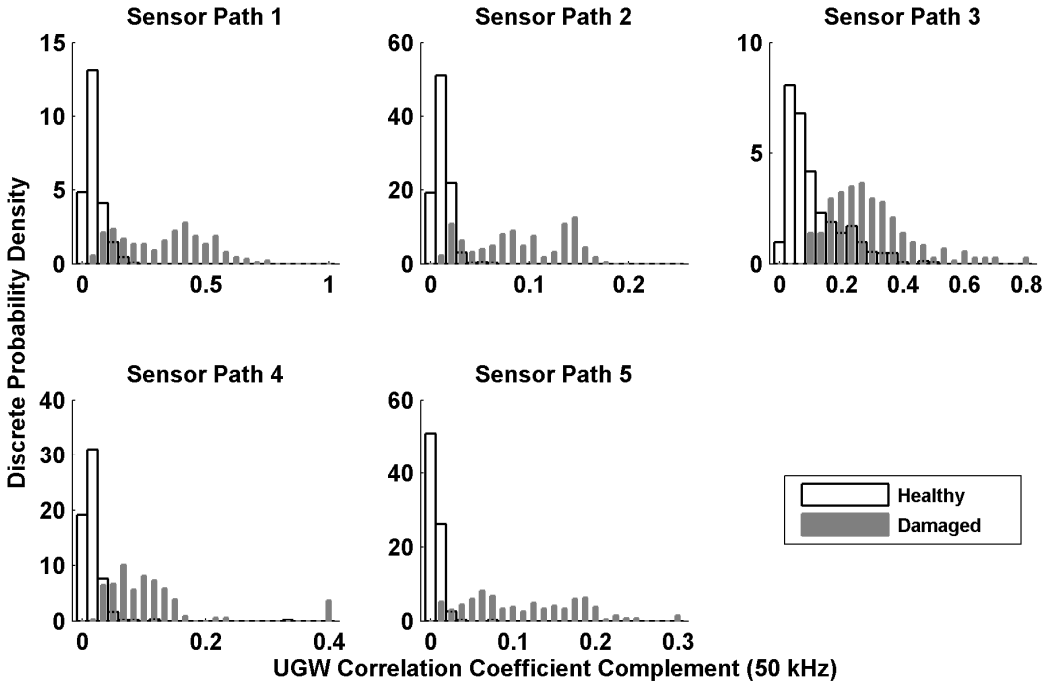

Figure 70: Test statistics for CCC using guided wave data at 50 kHz

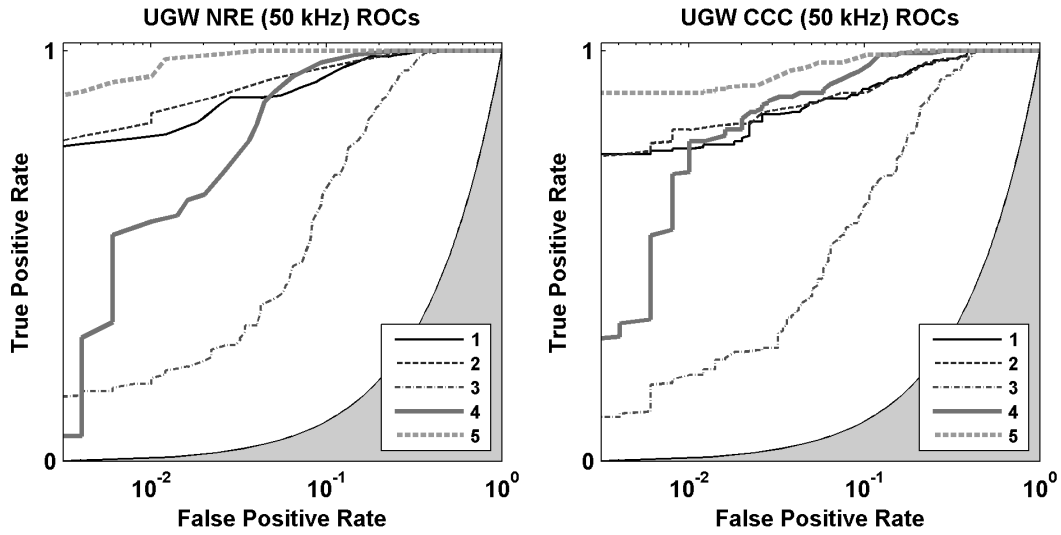

Figure 71: ROC curves for 50 kHz guided wave data at 50 kHz: NRE (left); CCC (right)

The histograms for the NRE test statistic using 200 kHz guided waves are shown in Figure 72, with the corresponding ROC curves shown in Figure 74 (left). The overall classification performance was worse than for the 50 kHz data, with an A(all) of 0.89. This low

average AUC was largely brought down by the poor performance of path 2, which lay entirely off of the spar cap and away from the crack. The best performance for 200 kHz guided waves was with paths 1 and 3, which lay along the spar cap, and produced an A(spar) of 0.996. The carbon fiber spar cap likely acted as a wave guide for the 200 kHz excitation, enabling the communication of changes in the underlying structure along its length. The histograms for the CCC test statistic using 200 kHz guided waves are shown in Figure 73, with the corresponding ROC curves shown in Figure 74 (right). The results for the CCC test statistic were substantially similar to those for the NRE, but with a slight drop in performance.

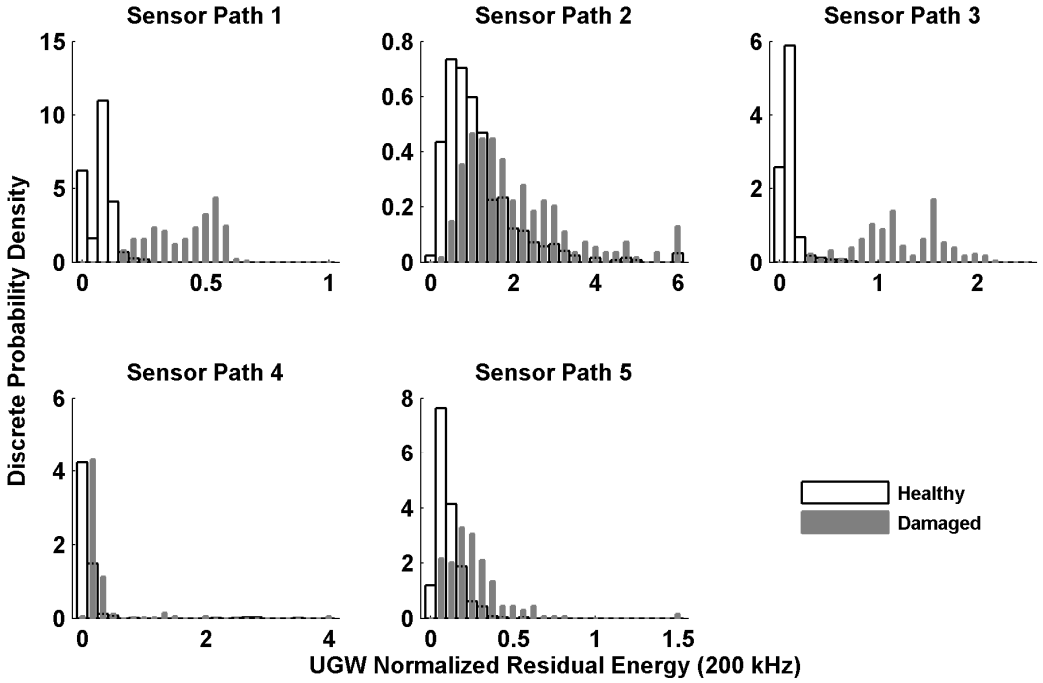

Figure 72: Test statistics for NRE using guided wave data at 200 kHz

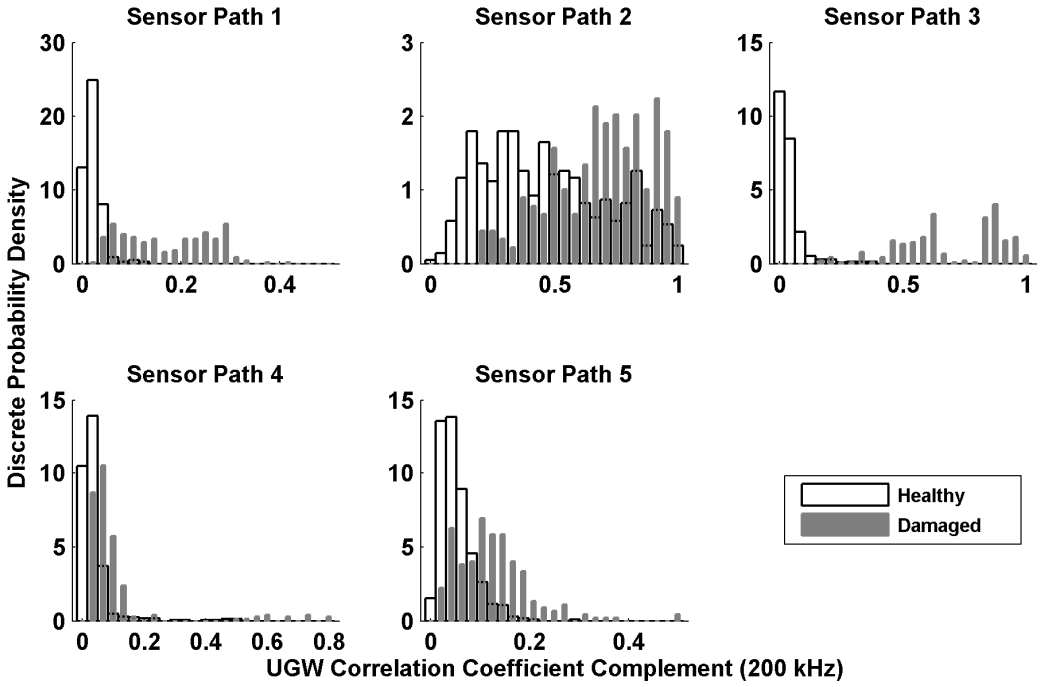

Figure 73: Test statistics for CCC using guided wave data at 200 kHz

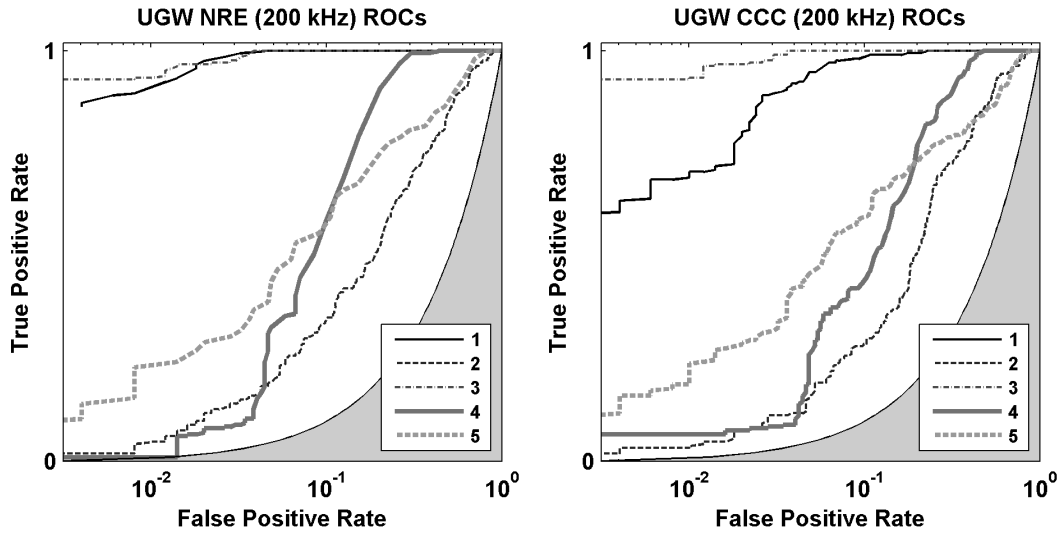

Figure 74: ROC curves for guided wave data at 200 kHz: NRE (left); CCC (right)

5.3.3.2. Diffuse Wave Field Measurements

The histograms for the NIRE test statistic using DWF data from the LP-A1 "inner array" are shown in Figure 75, with the corresponding ROC curves in Figure 77 (left). The data

for all paths represent good classification performance, with an average AUC, A(all), of 0.95. The method also showed excellent sensitivity in terms of performance near the crack location, with an A(crack) of 0.98. The histograms for the ICCC test statistic using the inner DWF sensor array data are shown in Figure 76, with the corresponding ROC curves in Figure 77 (right). The ICCC classification performance was poor by comparison, with an A(all) of 0.86, and the heightened sensitivity to the crack location was eroded, with A(crack) of only 0.93, compared to 0.98 for the NIRE using the same data.

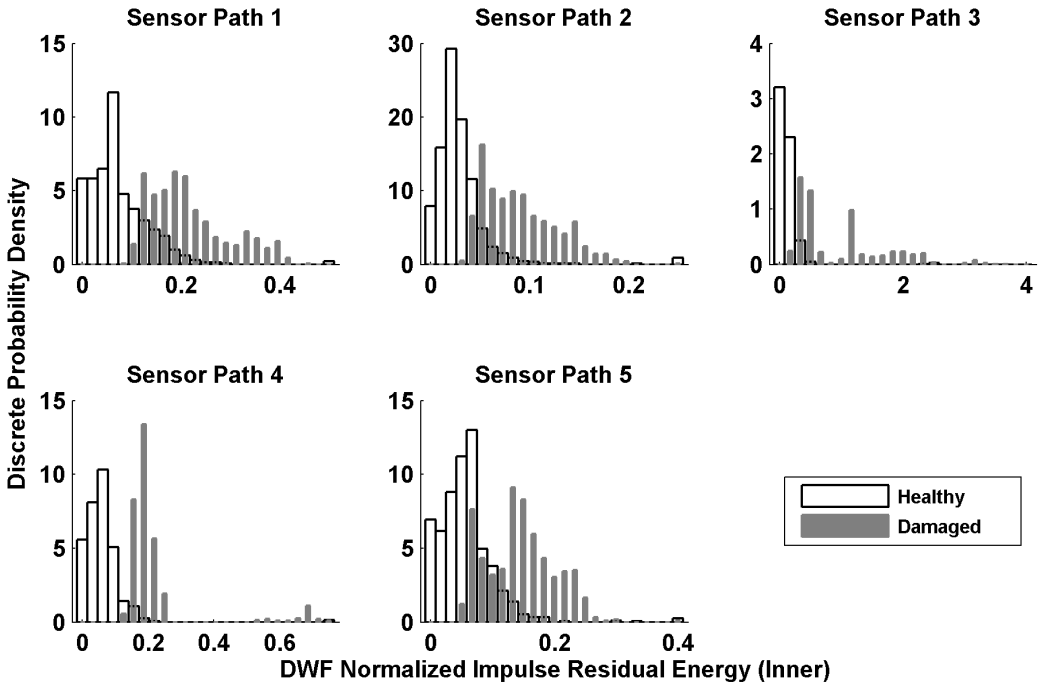

Figure 75: Test statistics for NIRE using DWF data from the inner sensor array

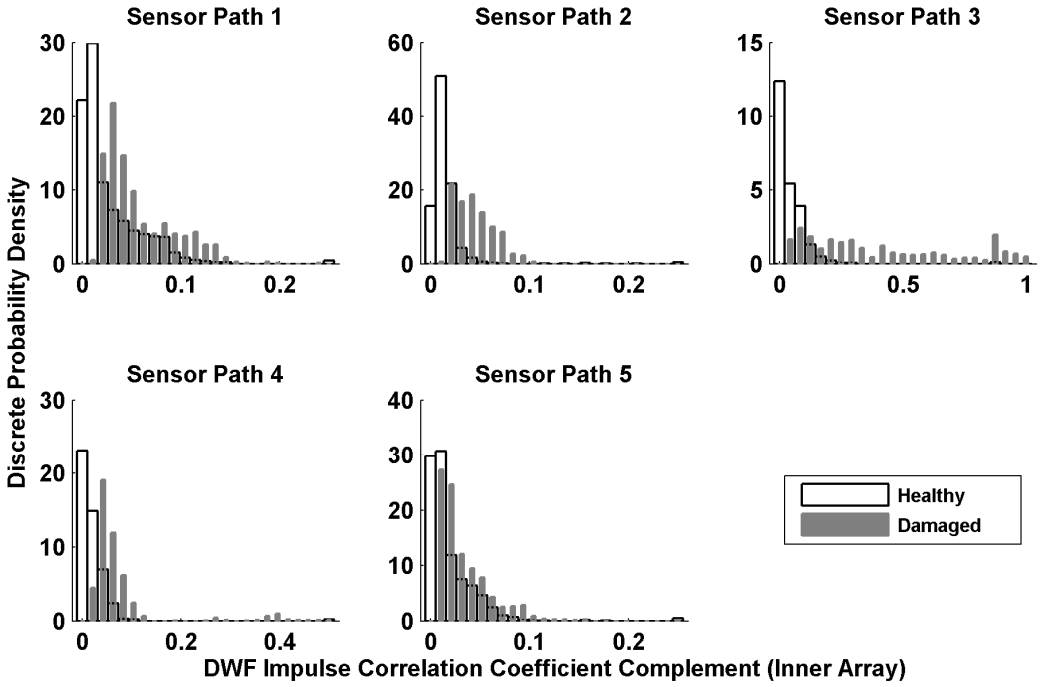

Figure 76: Test statistics for ICCC using DWF data from the inner sensor array

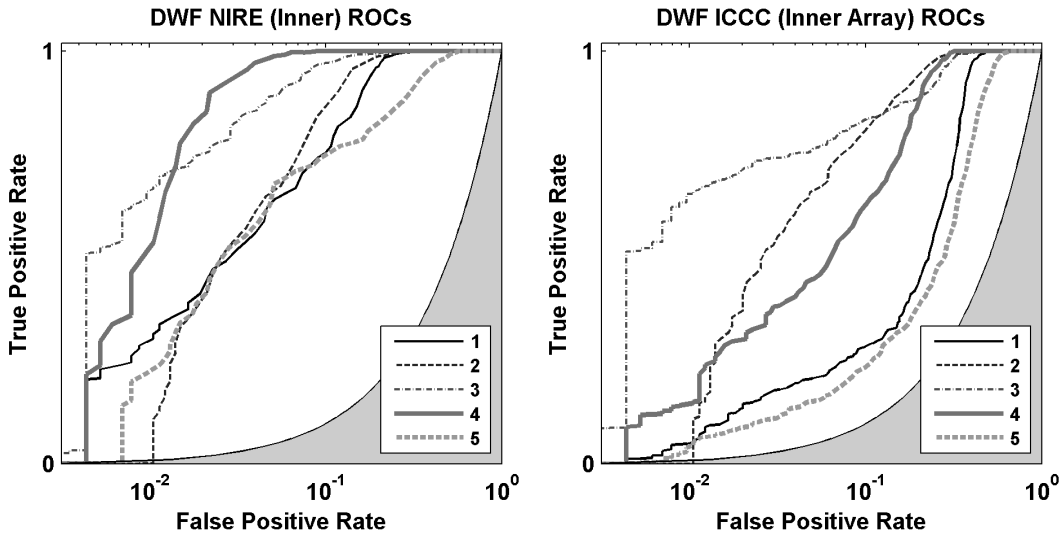

Figure 77: ROC curves for DWF data from the inner sensor array: NIRE (left); ICCC (right)

The histograms for the NIRE test statistic using the outer DWF sensor array data are shown in Figure 78, with the corresponding ROC curves shown in Figure 80 (left). Unfortunately, the data for path 3 were tainted, because the sensor for that path was discovered

to be broken on 10/18/11. Although it was replaced, the sensor fractured at approximately the same time as the incipient structural damage appeared, so the new baseline data would not have been useful for detecting the change due to incipient crack development. Excluding path 3, the other paths provide poor classification performance, with an A(all) of 0.85. Furthermore, with this larger array, there was negligible sensitivity for paths that crossed or were in the vicinity of the crack; with an average A(crack) of 0.86. The histograms for the ICCC test statistic using the outer DWF sensor array data are shown in Figure 79, with the corresponding ROC curves shown in Figure 80 (right). The results for the ICCC are similar to those for the NIRE, again with a slight drop in performance.

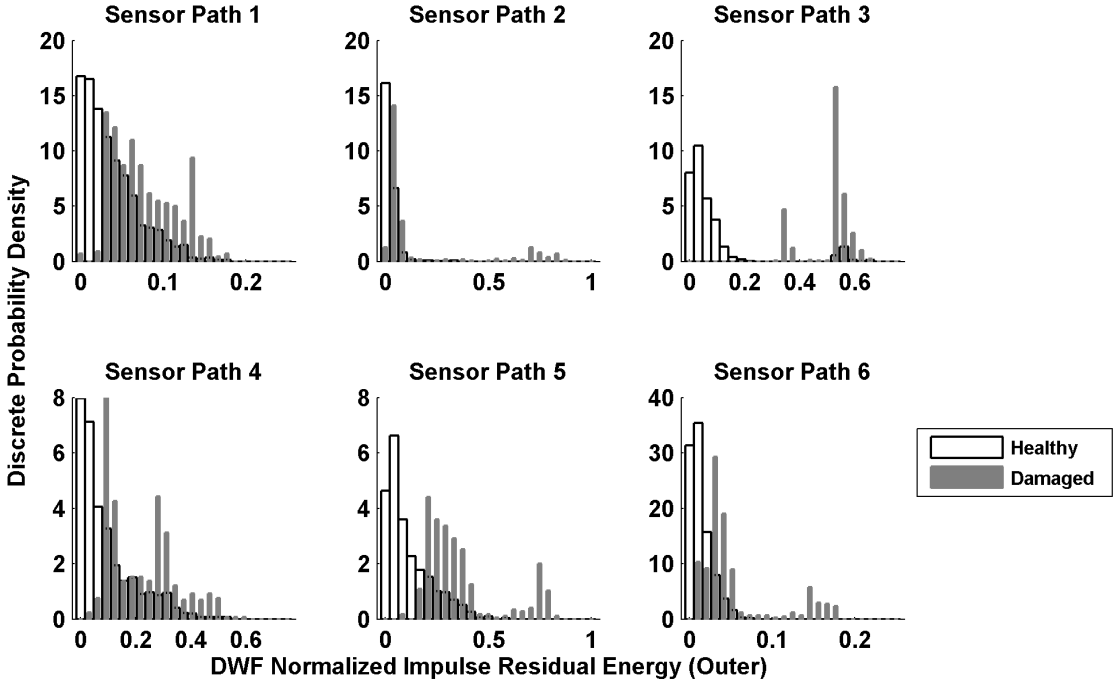

Figure 78: Test statistics for NIRE using DWF data from the outer sensor array

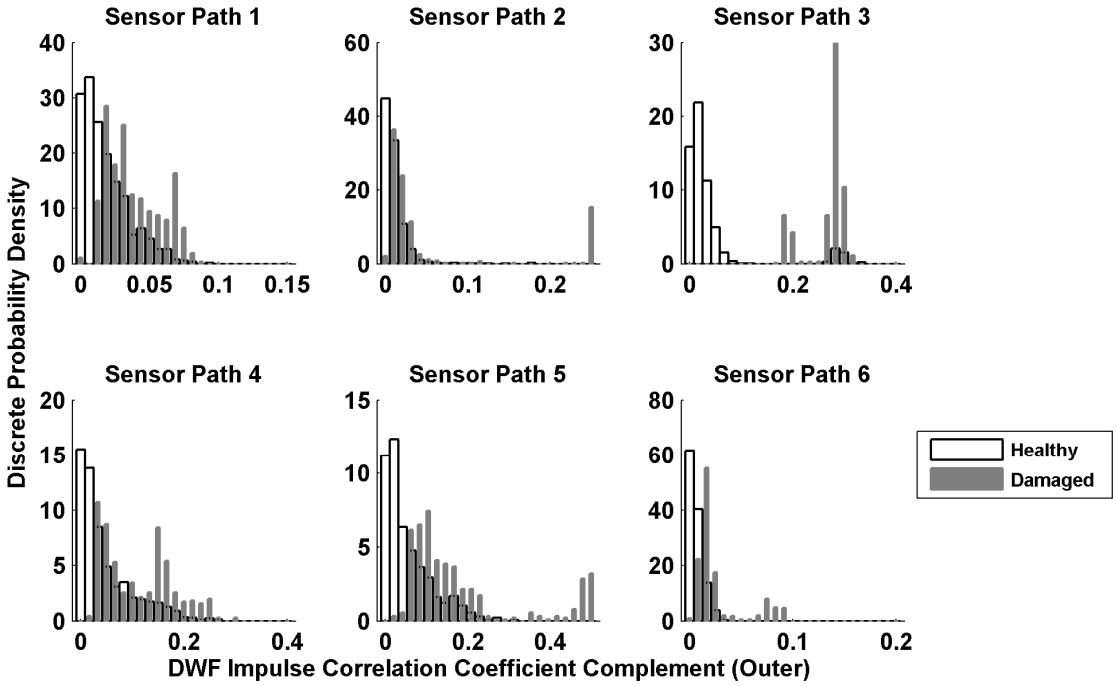

Figure 79: Test statistics for ICCC using DWF data from the outer sensor array

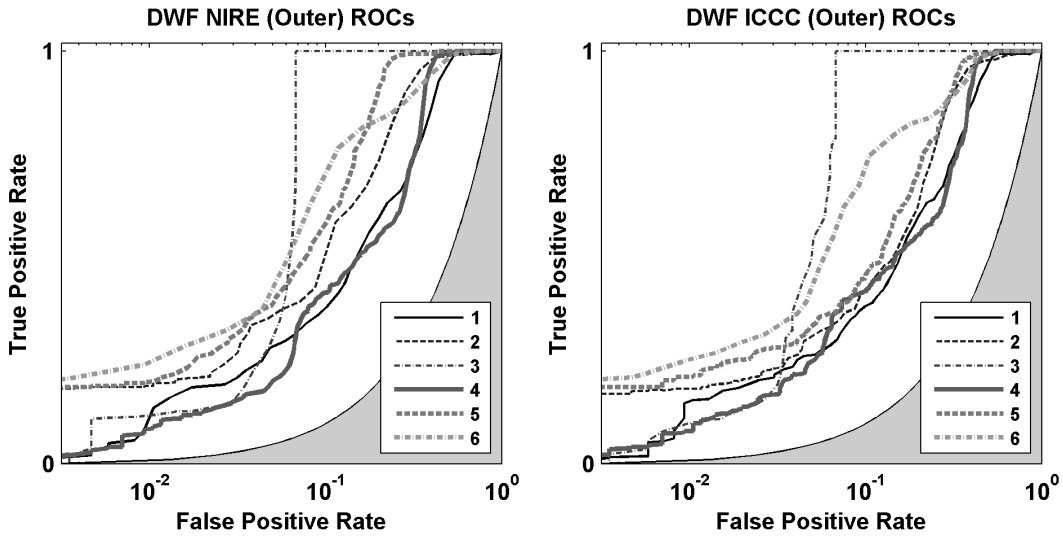

Figure 80: ROC curves for DWF data from the outer sensor array: NIRE (left); ICCC (right)

5.4. Summary and Acknowledgements

The goal of this work presented in this chapter was to identify an approach to achieve better performance in fatigue crack detection for composite structures with fiberglass shells, especially wind turbine rotor blades. Extensive data were collected using different acquisition systems and analyzed using different signal processing approaches and test statistics in order to compare incipient crack detection performance. In the acquisition hardware domain, ultrasonic guided waves were compared with diffuse wave field measurement methods; in the detector domain, energy methods were compared with correlation methods.

The guided wave data at 200 kHz produced comparable detection performance for both the energy and the correlation methods. At this frequency, detection performance was best along the spar cap, indicating that for this structure, an extremely low-density array (as little as one actuator/sensor pair) might be sufficient to detect incipient cracks that cross the spar cap. While the 50 kHz guided wave data provided good detection performance, the better performing paths lay neither near the crack nor along the spar cap. The diffuse wave data displayed the greatest overall sensitivity using the smaller inner array with the energy-based test statistic, with even heightened sensitivity for sensor paths near the crack. This heightened sensitivity is likely the result of the IRF estimate used for the DWF data being an estimate of the pulse-echo response for the measurement transducer, which could be expected to be more sensitive to structural changes in its vicinity. Similar to the 50 kHz UGW data, the diffuse wave data with excitation signal content only up to 40 kHz did not seem affected by the presence or absence of the spar cap along a given sensor path. The larger outer array performed generally poorly compared to the more compact inner array, possibly owing to wave attenuation over the required travel distance in the fiberglass structure.

In all cases, the energy-based detector outperformed the correlation-based detector, and in some cases, applying the correlation-based detector resulted in serious drops in performance otherwise available with the same data. Furthermore, for this structure, broadband excitation, even at low frequencies compared to traditional guided wave applications, produces detection results more sensitive to damage location, while the higher frequency excitation relies on the structure's architecture (i.e. the carbon-fiber spar cap) to detect underlying structural changes. Although this reliance may increase overall sensitivity, it does so at the expense of localization. This trade-off, suggesting the importance of differentiating detection from localization objectives when designing a detector, has been observed previously [94].

Portions of Chapter 5 have been accepted in part by [7] *Structural Health Monitoring,* S. G. Taylor, G. Park, K. M. Farinholt, and M. D. Todd, 2012. The title of this paper is "Fatigue crack detection performance comparison in a composite wind turbine rotor blade." The dissertation author was the primary investigator and author of this paper.

Other portions of Chapter 5 are intended in part for submission to [8] *Journal of Intelligent Material Systems and Structures,* S. G. Taylor, K. M. Farinholt, G. Park, C. R. Farrar, M. D. Todd, and J.-R. Lee, 2013. The title of this paper is "Incipient crack detection in composite wind turbine blades." The dissertation author was the primary investigator and author of this paper.

Chapter 6
State and Loads Estimation

6.1. Introduction

In a multi-scale sensing system for SHM, state and loads estimates provide the ability to evaluate operational structural performance. While active sensing systems and damage detection methods can provide information concerning the condition of the structure, effective structural prognostics require a structural model that will respond in the same way as the structure to current and future loads. A multi-scale SHM system combines these approaches to incorporate the effects of detected structural changes into a physics-based model, and then couples that model with physical measurements to estimate how the structure responds to its environment in its current state. Because parameters related to common performance requirements such as deflections or reaction loads are not easily directly measureable, state estimation methods must be employed to enable the utilization of easily measureable kinematic quantities, such as acceleration, for structural performance assessment.

Techniques to obtain state and loads estimates have been the subject of active research for the past several decades, and there is a huge body of literature that addresses this topic. This section presents a list, which is by no means exhaustive, of representative works in the area of

state and loads estimation. One of the more popular approaches to state estimation is the Kalman filter [113], which minimizes the error covariance given estimates of system input and measurement noise variances. However, many other approaches have been proposed for such estimation given measurements and a model of a structure. Moraal and Grizzle [114] presented observer designs for discrete-time, nonlinear systems, including a discussion of the Newton method and its relationship to the extended Kalman filter. Bartlett [115] applied a regression technique to estimate forces in a helicopter rotor hub using operational acceleration measurements and a model of the relationship among accelerations at multiple locations on the airframe. Doyle [116] proposed a method to reconstruct an impact force on a bilateral beam using a wave guide model. Liu, et al. [117] applied a Kalman filter to the problem of simultaneous displacement and input force estimation for a cantilever plate with a known input location. Citing the ineffectiveness of linear, steady-state tools for shaft torque estimation, Goedtel et al. [118] abandoned physical modeling and trained an artificial neural network to approximate key nonlinear relationships in induction motor performance.

Wind turbine flexible members have been a recent application of state and loads estimation. For a class systems with linear state matrices and nonlinear, state-dependent inputs, Ha et al. [119] proposed a method for simultaneous state and input estimation, which Fritzen et al. [120] applied to estimation of state and loads on a laboratory-scale model of a tripod-supported wind turbine tower. White, et al. [35, 36] proposed a power expansion method to estimate wind turbine rotor blade operational deflection using a tip-mounted triaxial accelerometer and accounting for the rotation between the tip of the blade and the assumed direction of centripetal acceleration. Hernandez, et al. [62] developed a modal-based iterative method analogous to Rayleigh's method for use with distributed embedded sensing and computing to estimate the wind load input to a wind turbine tower.

This chapter develops and implements a Kalman-based observer for state estimation using *NLBeam*, a finite element code recently developed at LANL. *NLBeam* is a research code implementing a geometrically nonlinear, generalized Timoshenko beam theory. Geometrically exact beam methods have developed primarily from the work of Reissner [121, 122], and have been notably extended by Simo and Vu Quoc [123] and Jelenic and Crisfield [124, 125]. Recently, versions of this theory have been applied to model helicopter rotor blades [126] and wind turbine blades [127-129]. The theory supports geometric nonlinearities by maintaining a fixed inertial reference frame related through an orthogonal transformation to an initial beam configuration reference frame. The initial beam configuration displacement field is directed along the centroid line of the beam, and the deformed configuration reference frame is related to the fixed inertial frame and the initial beam configuration reference frame through cascading orthogonal transformations. Because no small angle assumptions are used in these transformations, the representation of the deformed beam is geometrically nonlinear. This theory is generally applicable to slender, composite, beam-like structures, and it is well-suited to modeling the CX-100 blade described in earlier chapters [129]. Coupling the model-based state estimation approach presented here with techniques for uncertainty propagation would produce PDFs of state estimates that could be fed into probabilistic decision models.

6.2. Observer For State Estimation

6.2.1. Overview

State observers for physical systems, usually referred to as “plants,” are ordinarily employed to enable the implementation of full state feedback control, measurements from the plant and a reference model to estimate, or “observe” the state of the plant. A basic review of

state-space control and state observers can be found in [130]. The state is defined here as the position and velocity at a set of discrete DOFs. In these cases, the ideal control signal would be calculated given the state of the plant, but the state is often not measureable or is otherwise inaccessible. State observers are implemented to recover an estimate of the system state using a reference model and available measurements. Some observers (e.g. the Kalman filter) can be considered optimal in certain ways for linear systems given certain assumptions required by the method. Observers can also be approached as a pole-placement problem [131], in which the designer must balance performance with rejection of noise or other disturbances in choosing the placement of the closed-loop observer system poles.

State observers are most commonly developed for implementation on systems in a state-space representation. A linear, time-invariant (LTI) system can be expressed in state space as

$$\begin{aligned} \dot{\underline{x}}(t) &= \mathbf{A}\underline{x}(t) + \mathbf{B}\underline{u}(t) \\ \underline{y}(t) &= \mathbf{C}\underline{x}(t) + \mathbf{D}\underline{u}(t) \end{aligned}, \tag{6.1}$$

where $\mathbf{A}$ is the system state matrix, $\underline{x}(t)$ is the time-varying state vector, $\mathbf{B}$ is the input influence matrix, $\underline{u}(t)$ is the time-varying system input vector, $\mathbf{C}$ is the output influence matrix, $\underline{y}(t)$ is the time-varying system output vector, and $\mathbf{D}$ is the feed forward matrix. Boldface indicates matrix quantities, underlines indicate vector quantities, and the overdot represents differentiation with respect to time. Henceforth, the time-dependency of the state, input and output vectors will be assumed in the notation. Consider a state observer with a reference model being identical to the plant, having observer gain $\mathbf{K}_e$. The system representing the error is then

$$\left(\dot{\underline{x}} - \dot{\hat{\underline{x}}}\right) = \left(\mathbf{A} - \mathbf{K}_e\mathbf{C}\right)\left(\underline{x} - \hat{\underline{x}}\right), \tag{6.2}$$

where the hats indicate quantities relating to the reference model. The dynamics of the error vector are determined by the poles of the error state matrix $\left(\mathbf{A}-\mathbf{K}_e\mathbf{C}\right)$. If the error state matrix is stable, the error will tend to zero regardless of the system initial conditions, but the speed of the observer response may not be fast enough for effective control. If the pair $\left(\mathbf{A},\mathbf{C}\right)$ is observable, then $\mathbf{K}_e$ can be chosen to arbitrarily place the poles of the error state matrix and ensure that the state estimate will be a reasonably real-time estimate of the true state [130]. If the plant is exactly represented by the reference model, and when there is white noise with known variance present in the input and/or the output signals, the Kalman filter provides an estimate of the state that minimizes the covariance of the state estimation error, balancing between reliance on the measurement and the prediction. However, the reference model is inevitably an inexact representation of the plant; consider a reference model

$$\begin{aligned}\dot{\underline{\hat{x}}} &= \widehat{\mathbf{A}}\underline{\hat{x}}+\widehat{\mathbf{B}}\underline{\hat{u}}\\ \underline{\hat{y}} &= \mathbf{C}\underline{\hat{x}}+\mathbf{D}\underline{\hat{u}}\end{aligned}, \tag{6.3}$$

where $\widehat{\mathbf{A}}=\mathbf{A}+\Delta\mathbf{A}$ and $\widehat{\mathbf{B}}=\mathbf{B}+\Delta\mathbf{B}$. In this formulation, it is still assumed that the output influence and feed forward matrices are known and identical for both the plant and the reference models. Then the corresponding error system is

$$\left(\dot{\underline{x}}-\dot{\underline{\hat{x}}}\right)=\left(\mathbf{A}-\mathbf{K}_e\mathbf{C}\right)\left(\underline{x}-\underline{\hat{x}}\right)-\left(\Delta\mathbf{A}\underline{\hat{x}}+\Delta\mathbf{B}\underline{u}\right). \tag{6.4}$$

Note that any claims of optimality or stability that could be made for the choice of $\mathbf{K}_e$ in Eq. (6.2) are jeopardized by the disturbance terms $\Delta\mathbf{A}$ and $\Delta\mathbf{B}$ in Eq. (6.4). For a linear plant, the observer design would become a pole-placement problem, with the pole locations chosen to balance maintaining stability and with achieving desired performance. For a nonlinear plant, the disturbance terms effectively become functions of time, and some form of adaptive observer is required.

6.2.2. Newton Raphson Observer Derivation

Here, an observer is presented that is intended to provide state estimates for nonlinear systems. This observer adjusts the force input to a reference model using the system Jacobian to eliminate the measureable model output error in an iterative Newton-Raphson scheme by finding the root of an error expression in terms of the input force correction. Rather than updating the state estimate directly, this implementation permits the model to filter the observer correction through its own force input structure. However, the efficacy of this observer is still predicated on an assumption that the reference model is "close enough" to the system being observed that, in driving the output error to zero, the state estimate error will also be driven toward zero. For nonlinear systems, which are in general not fully observable, there is no guarantee that eliminating the output error will eliminate the state estimation error.

A block diagram for a discrete system with a force correction observer is shown in Figure 81, in which the Z^{-1} blocks refer to a discrete integration step. The plant has an input $\underline{u}_n$ combined with an unmeasured disturbance $\underline{w}_n$, an inaccessible state $\underline{x}_n$, and an output $\underline{y}_n$ combined with measurement noise $\underline{v}_n$. The reference model has an accessible state $\hat{\underline{x}}_n$ and an output $\hat{\underline{y}}_n$. The subscript n corresponds to the n^{th} time point in a temporally discretized representation. Assuming full state measurements (i.e. $\mathbf{C} = \mathbf{I}$ and $\mathbf{D} = \mathbf{0}$), and neglecting $\Delta\underline{u}_n$, the state vectors $\underline{x}_n$ and $\hat{\underline{x}}_n$ can be written as functions of the system input $\underline{u}_n$ so that error signal is

$$\underline{e}_n = \underline{x}(\underline{u}_n) - \hat{\underline{x}}(\underline{u}_n). \tag{6.5}$$

For nonzero $\Delta\mathbf{A}$ and $\Delta\mathbf{B}$, $\underline{e}_n$ will be nonzero in general. An updating scheme is proposed whereby the input $\underline{u}_n$ to the reference model is modified as $\hat{\underline{u}}_n = \underline{u}_n + \Delta\underline{u}_n$ with the goal of driving an updated error signal to zero; this updated error is given by

$$\hat{\underline{e}}_n = \underline{x}\left(\underline{u}_n\right) - \hat{\underline{x}}\left(\hat{\underline{u}}_n\right). \tag{6.6}$$

The goal of driving the updated error to zero is equivalent to finding the root of the right hand side (RHS) of Eq. (6.6), thereby identifying an input perturbation $\Delta\underline{u}_n$ that eliminates the output error. Expanding the reference model state in the vicinity of the actual input $\underline{u}_n$ with a Taylor series allows Eq. (6.6) to be written as

$$\hat{\underline{e}}_n = \underline{x}\left(\underline{u}_n\right) - \left(\hat{\underline{x}}\left(\underline{u}_n\right) + \frac{\partial \hat{\underline{x}}\left(\underline{u}_n\right)}{\partial \underline{u}} \Delta\underline{u}_n + \text{H.O.T.} \right). \tag{6.7}$$

Neglecting higher-order terms (H.O.T.), setting $\hat{\underline{e}}_n = \underline{0}$, and substituting Eq. (6.5) into (6.7) yields an expression for $\Delta\underline{u}_n$ as

$$\underline{e}_n \approx \left[\frac{\partial \hat{\underline{x}}\left(\underline{u}_n\right)}{\partial \underline{u}} \right] \Delta\underline{u}_n. \tag{6.8}$$

Consider the application of this result to an LTI reference model for the observer. The discrete-time model can be expressed in state-space as

$$\begin{aligned} \hat{\underline{x}}_n &= \widehat{\mathbf{A}}_{n-1}\hat{\underline{x}}_{n-1} + \widehat{\mathbf{B}}_{n-1}\underline{u}_n \\ \hat{\underline{y}}_n &= \mathbf{C}\hat{\underline{x}}_n + \mathbf{D}\underline{u}_n \end{aligned}, \tag{6.9}$$

where the subscripts $n-1$ on the reference model state matrix $\widehat{\mathbf{A}}$ and the reference model input influence matrix $\widehat{\mathbf{B}}$ indicates that the matrices have been implemented in a discrete formulation according to some time integration scheme. For an LTI system, the matrices will be constant for all n; for a nonlinear system, the subscripts indicate the operating point about which the matrices would be linearized. Given this representation, the result in Eq. (6.8) takes the form

$$\underline{e}_n = \left[\frac{\partial \hat{\underline{x}}}{\partial \underline{u}} \left(\hat{\mathbf{A}}_{n-1} \hat{\underline{x}}_{n-1} + \hat{\mathbf{B}}_{n-1} \underline{u}_n \right) \right] \Delta \underline{u}_n , \tag{6.10}$$

so that the force correction is simply

$$\Delta \underline{u}_n = \left[\hat{\mathbf{B}}_{n-1} \right]^{-1} \underline{e}_n . \tag{6.11}$$

Equation (6.11) is an exact root in $\Delta \underline{u}_n$ for Eq. (6.8) for a linear plant and linear reference model with full state measurements. For system outputs other than full state measurements (i.e. $\mathbf{C} \neq \mathbf{I}$ and $\mathbf{D} \neq \mathbf{0}$), Eq. (6.8) must be expressed in terms of the system output as

$$\underline{e}_n \approx \left[\frac{\partial}{\partial \underline{u}} \left(\mathbf{C} \left[\hat{\mathbf{A}}_{n-1} \hat{\underline{x}}_{n-1} + \hat{\mathbf{B}}_{n-1} \underline{u}_n \right] \right) \right] \Delta \underline{u}_n , \tag{6.12}$$

so that the force correction becomes

$$\Delta \underline{u}_n = \left[\mathbf{C} \hat{\mathbf{B}}_{n-1} \right]^{-1} \underline{e}_n . \tag{6.13}$$

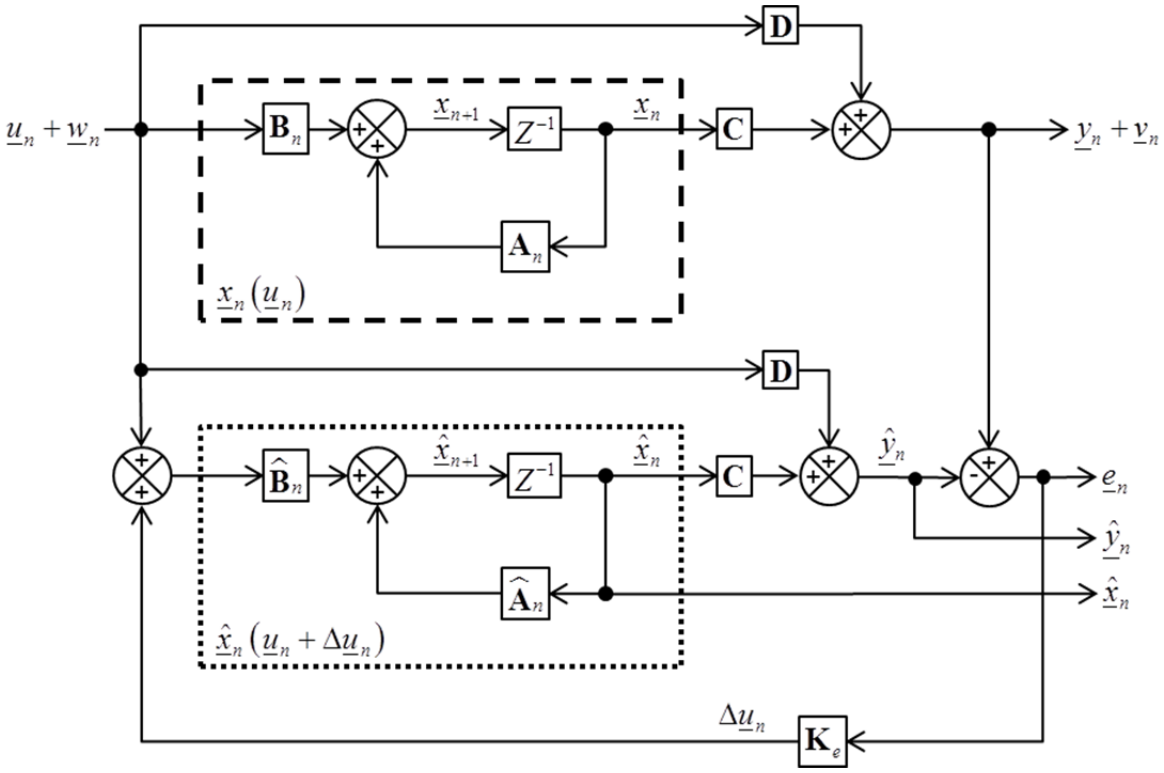

Figure 81: Block diagram of a general observer for a discrete system

For nonlinear models, Eq. (6.8) is not exact, but only provides the Newton-Raphson step for successive iterative corrections to the perturbed input; multiple iterations would be required to drive the updated error to zero at the conclusion of every time step. Defining (for brevity) $\underline{x}_n = \underline{x}(\underline{u}_n)$ and $\hat{\underline{x}}_{n,k} = \hat{\underline{x}}(\hat{\underline{u}}_{n,k})$, and then expressing the updated error at the k^{th} and the $(k+1)^{th}$ iterations of the observer for the n^{th} time step as $\hat{\underline{e}}_{n,k} = \underline{x}_n - \hat{\underline{x}}_{n,k}$ and $\hat{\underline{e}}_{n,k+1} = \underline{x}_n - \hat{\underline{x}}_{n,k+1}$, respectively, enables an expression for the change in error over the $(k+1)^{th}$ iteration as

$$\begin{aligned} \hat{\underline{e}}_{n,k+1} - \hat{\underline{e}}_{n,k} &= \left(\underline{x}_n - \hat{\underline{x}}_{n,k+1}\right) - \left(\underline{x}_n - \hat{\underline{x}}_{n,k}\right) \\ &= \hat{\underline{x}}_{n,k} - \hat{\underline{x}}_{n,k+1} \end{aligned} . \tag{6.14}$$

Similar to the procedure followed for the linear case, the model output is expressed as a first-order Taylor series approximation at the n^{th} time step in the vicinity of the k^{th} estimate for the updated input force, as

$$\underline{\hat{x}}_{n,k+1} \approx \underline{\hat{x}}_{n,k} + \frac{\partial \underline{\hat{x}}_{n,k}}{\partial \underline{u}} \Delta \underline{\hat{u}}_{n,k}, \tag{6.15}$$

where $\underline{\hat{u}}_{n,k+1} = \underline{\hat{u}}_{n,k} + \Delta \underline{\hat{u}}_{n,k}$. Substituting this approximation of the model state into the error expression of Eq. (6.14) yields

$$\begin{aligned} \underline{\hat{e}}_{n,k+1} - \underline{\hat{e}}_{n,k} &= \underline{\hat{x}}_{n,k} - \left(\underline{\hat{x}}_{n,k} + \frac{\partial \underline{\hat{x}}_{n,k}}{\partial \underline{u}} \Delta \underline{\hat{u}}_{n,k} \right) \\ &= -\frac{\partial \underline{\hat{x}}_{n,k}}{\partial \underline{u}} \Delta \underline{\hat{u}}_{n,k} \end{aligned}. \tag{6.16}$$

Setting $\underline{\hat{e}}_{n,k+1} = \underline{0}$ and solving Eq. (6.16) for $\Delta \underline{\hat{u}}$, the Newton-Raphson correction to the perturbed input array is

$$\Delta \underline{\hat{u}}_{n,k} = \left[\frac{\partial \underline{\hat{x}}_{n,k}}{\partial \underline{u}} \right]^{-1} \underline{\hat{e}}_{n,k}, \tag{6.17}$$

which, for a single iteration, is equivalent to the expression in Eq. (6.8).

For the case of a general, nonlinear reference model, consider a finite element discretization of the equations of motion (EOM), for which the spatially discrete form can be expressed as

$$\underline{\hat{R}}(\underline{x}, \underline{\dot{x}}, \underline{\ddot{x}}) = \underline{0}, \tag{6.18}$$

and they are satisfied through a nonlinear solution scheme at every time step to within some tolerance. This is the solution approach adopted in the *NLBeam* code. The discrete finite element equations of motion expressed in Eq. (6.18) as an array of nodal residuals can be expressed in a temporally discrete fashion by taking into account the discrete time integration

scheme relating velocity and acceleration to changes in displacement over a time step and the velocity and acceleration at the previous time step. With this formulation, Eq. (6.18) becomes

$$\underline{\hat{R}}_n\left(\underline{x}_n;\left\{\underline{x}_{n-1},\underline{\dot{x}}_{n-1},\underline{\ddot{x}}_{n-1}\right\}\right)=\underline{0}\,, \tag{6.19}$$

where the nodal residual vector $\underline{\hat{R}}_n$ is conveniently decomposed into contributions from internal stresses ($\underline{\hat{R}}_n^{int}$), inertial forces ($\underline{\hat{R}}_n^{dyn}$), and external forces ($\underline{\hat{R}}_n^{ext}$) as

$$\underline{\hat{R}}\left(\underline{x}_n;\left\{\underline{x}_{n-1},\underline{\dot{x}}_{n-1},\underline{\ddot{x}}_{n-1}\right\}\right)=\underline{\hat{R}}_n^{ext}-\underline{\hat{R}}_n^{int}+\underline{\hat{R}}_n^{dyn}=\underline{0}\,. \tag{6.20}$$

In this representation, internal stresses are expressed as a resultant vector with units of force, and the external force corresponds to the model inputs (i.e. $\underline{\hat{R}}^{ext}=\underline{u}$), so the equations of motion are satisfied when

$$\underline{u}_n=\underline{\hat{R}}_n^{int}+\underline{\hat{R}}_n^{dyn}\,. \tag{6.21}$$

Differentiating Eq. (6.21) with respect to $\underline{\hat{x}}$ simply gives

$$\left[\frac{\partial \underline{u}_n}{\partial \underline{\hat{x}}}\right]=\left[\frac{\partial \underline{\hat{R}}_{n,k}^{int}}{\partial \underline{\hat{x}}}\right]+\left[\frac{\partial \underline{\hat{R}}_{n,k}^{dyn}}{\partial \underline{\hat{x}}}\right]. \tag{6.22}$$

The partial derivatives on the RHS of Eq. (6.22) are computed and used by *NLBeam* to solve the nonlinear equations of motion at every time step. They are the tangent stiffness and inertial matrices, respectively, where $\mathbf{K}_{n,k}^{int}=\left.\frac{\partial \underline{\hat{R}}_{n,k}^{int}}{\partial \underline{\hat{x}}}\right|_{\underline{\hat{x}}_{n,k}}$ and $\mathbf{K}_{n,k}^{dyn}=\left.\frac{\partial \underline{\hat{R}}_{n,k}^{dyn}}{\partial \underline{\hat{x}}}\right|_{\underline{\hat{x}}_{n,k}}$. Adopting this notation, and substituting Eq. (6.22) into Eq. (6.17), and noting that $\left[\frac{\partial \underline{\hat{x}}}{\partial \underline{u}}\right]^{-1}=\left[\frac{\partial \underline{u}}{\partial \underline{\hat{x}}}\right]$, the k^{th} correction to the input perturbation at the n^{th} time step is

$$\begin{aligned}\Delta\underline{\hat{u}}_{n,k}&=\left(\mathbf{K}_{n,k}^{int}+\mathbf{K}_{n,k}^{dyn}\right)\underline{\hat{e}}_{n,k}\\&=\mathbb{K}_{n,k}\,\underline{\hat{e}}_{n,k}\end{aligned}\,, \tag{6.23}$$

where $\mathbb{K} = \mathbf{K}^{int} + \mathbf{K}^{dyn}$ is the combined sum of the tangent stiffness and inertial matrices, dubbed the "full Jacobian," which is the form in which these matrices are made available in *NLBeam*. Equation (6.23) provides the update force for displacement measurements. If only a subset of the DOFs is measured, then only the corresponding columns of the full Jacobian would be used in computing the force correction. However, acceleration measurements are much more easily obtained experimentally than displacement measurements, so the observer should be adapted for acceleration outputs. Expressing the measured error vector in terms of the translational accelerations at the k^{th} and the $(k+1)^{th}$ iterations,

$$\underline{\hat{e}}_{n,k+1} - \underline{\hat{e}}_{n,k} = \underline{\ddot{\hat{x}}}^{(t)}_{n,k} - \underline{\ddot{\hat{x}}}^{(t)}_{n,k+1}. \tag{6.24}$$

The superscript (t) indicates that only translational DOFs are utilized in computing the error vector. Following the same procedure as for the displacement measurement case, $\underline{\ddot{\hat{x}}}^{(t)}_{n,k+1}$ can be expressed as a first-order Taylor series expanded about $\underline{\hat{u}}_n$. Simplifying and setting $\underline{\hat{e}}_{n,k+1} = 0$ Eq. (6.24) becomes

$$\underline{\hat{e}}_{n,k} = \left(\frac{\partial \underline{\ddot{\hat{x}}}^{(t)}_{n,k}}{\partial \underline{u}} \left(\underline{u}_{n,k} \right) \right) \Delta \underline{\hat{u}}_{n,k}. \tag{6.25}$$

Solving Eq. (6.25) for $\Delta \underline{\hat{u}}_{n,k}$ requires inverting the expression in the parentheses; by the chain rule,

$$\frac{\partial \underline{\ddot{\hat{x}}}^{(t)}_{n,k}}{\partial \underline{u}} = \frac{\partial \underline{\ddot{\hat{x}}}^{(t)}_{n,k}}{\partial \underline{\hat{x}}^{(t)}_{n,k}} \frac{\partial \underline{\hat{x}}^{(t)}_{n,k}}{\partial \underline{u}}. \tag{6.26}$$

From the Newmark time integration scheme implemented in *NLBeam*, $\frac{\partial \underline{\ddot{\hat{x}}}}{\partial \underline{\hat{x}}} = \frac{1}{\beta \Delta t^2} \mathbf{I}$ (where β is a parameter of the integration scheme). Then, following the arguments preceding Eq. (6.23), the solution to Eq. (6.25) is

$$\begin{aligned}\Delta\hat{\underline{u}}_{n,k} &= \beta\Delta t^2\left(\left(\mathbf{K}_{n,k}^{int}\right)^{(t)}+\left(\mathbf{K}_{n,k}^{dyn}\right)^{(t)}\right)\hat{\underline{e}}_{n,k} \\ &= \beta\Delta t^2\mathbb{K}_{n,k}^{(t)}\hat{\underline{e}}_{n,k}\end{aligned}, \tag{6.27}$$

where the superscript (t) indicates that only the columns of the full Jacobian corresponding to translational DOFs are employed in computing the force correction. If only a subset of accelerations is measured, then the columns of the full Jacobian would be limited to that subset.

6.2.3. Relationship Between the N-R Observer and the Kalman Filter

Consider the well-known Kalman filter, written in predictor-corrector form for state-space systems as

$$\begin{aligned}&1.\quad \hat{\underline{x}}_n^- = \widehat{\mathbf{A}}_{n-1}\hat{\underline{x}}_{n-1}+\widehat{\mathbf{B}}_{n-1}\underline{u}_n \\ &2.\quad \mathbf{P}^-{}_n = \widehat{\mathbf{A}}_{n-1}\mathbf{P}_{n-1}\widehat{\mathbf{A}}_{n-1}{}^{\mathrm{T}}+\mathbf{Q}_{n-1} \\ &3.\quad \mathbf{L}_n = \mathbf{P}^-{}_n\mathbf{C}^{\mathrm{T}}\left[\mathbf{C}\mathbf{P}^-{}_n\mathbf{C}^{\mathrm{T}}+\mathbf{R}_n\right]^{-1}, \\ &4.\quad \hat{\underline{x}}_n = \hat{\underline{x}}_n^- + \mathbf{L}_n\left(\underline{y}_n-\mathbf{C}\hat{\underline{x}}_n^-\right) \\ &5.\quad \mathbf{P}_n = \left(\mathbf{I}-\mathbf{L}_n\mathbf{C}\right)\mathbf{P}^-{}_n\end{aligned} \tag{6.28}$$

where the superscript "$-$" indicates a predicted, or "uncorrected" quantity, $\mathbf{Q}_n = \mathrm{E}\left[\underline{w}_n\underline{w}_n^{\mathrm{T}}\right]$ is the covariance of the input disturbance $\underline{w}_n$, and $\mathbf{R}_n = \mathrm{E}\left[\underline{v}_n\underline{v}_n^{\mathrm{T}}\right]$ is the covariance of the measurement noise $\underline{v}_n$. Consider the case in which there is no noise on the measurement channels, and there is Gaussian, IID noise on the measurement channels, so that $\mathbf{R}_n = \mathbf{0}$ and $\mathbf{Q}_n = \sigma_w\widehat{\mathbf{B}}_{n-1}\widehat{\mathbf{B}}_{n-1}^{\mathrm{T}}$, where σ_w is the input disturbance standard deviation. Then, in the first step, with $\mathbf{P}_0 = \mathbf{0}$ for assumed zero initial conditions, steps 3 and 4 of Eq. (6.28) give

$$\Delta\hat{\underline{x}}_n = \sigma_w\widehat{\mathbf{B}}_{n-1}\widehat{\mathbf{B}}_{n-1}^{\mathrm{T}}\mathbf{C}^{\mathrm{T}}(\sigma_w\mathbf{C}\widehat{\mathbf{B}}_{n-1}\widehat{\mathbf{B}}_{n-1}^{\mathrm{T}}\mathbf{C}^{\mathrm{T}})^{-1}\underline{e}_n, \tag{6.29}$$

where $\Delta\hat{\underline{x}}_n - \hat{\underline{x}}_n - \hat{\underline{x}}_n^-$ and $\underline{e}_n = \underline{y}_n - \mathbf{C}\hat{\underline{x}}_n$, as in Eq. (6.5). Then, noting from Eq. (6.9) that, for fixed $\hat{\underline{x}}_{n-1}$, $\Delta\hat{\underline{x}}_n = \widehat{\mathbf{B}}_{n-1}\Delta\underline{u}_n$. Then Eq. (6.29) can be rewritten as

$$\begin{aligned}\Delta\underline{u}_n &= \sigma_w \hat{\mathbf{B}}_{n-1}^{\mathrm{T}}\mathbf{C}^{\mathrm{T}}\left(\sigma_w \mathbf{C}\hat{\mathbf{B}}_{n-1}\hat{\mathbf{B}}_{n-1}^{\mathrm{T}}\mathbf{C}^{\mathrm{T}}\right)^{-1}\underline{e}_n \\ &= \left(\mathbf{C}\hat{\mathbf{B}}_{n-1}\right)^{\mathrm{T}}\left(\mathbf{C}\hat{\mathbf{B}}_{n-1}\right)^{-\mathrm{T}}\left(\mathbf{C}\hat{\mathbf{B}}_{n-1}\right)^{-1}\underline{e}_n\,, \\ &= \left(\mathbf{C}\hat{\mathbf{B}}_{n-1}\right)^{-1}\underline{e}_n\end{aligned} \tag{6.30}$$

which is identically the result in Eq. (6.13), so it is apparent that the N-R observer reduces to the Kalman filter under the assumption that there is no noise on the measurement channels. Although in some applications, such as the operational monitoring of wind turbine rotor blades in mind here, the noise on the measurement channels may be small in comparison to unmeasured input disturbances, the measurement noise will not be negligible. That noise will have the potential to produce accumulating error, which the N-R observer should be implemented with a mechanism to avoid.

The Kalman filter process given in Eq. (6.28) minimizes the covariance of the observer error given white noise on the input and output channels, but without knowledge of the noise/disturbance variances, and given that the unmeasured input is generally not white noise, the values σ_w and σ_v simply become parameters in the observer implementation. Beginning with the first line Eq. (6.30), but admitting an a Gaussian, IID measurement error with variance σ_v, the force correction can be written as

$$\Delta\underline{u} = \sigma_w\left(\mathbf{C}\hat{\mathbf{B}}_{n-1}^{\mathrm{T}}\right)\left(\sigma_w \mathbf{C}\hat{\mathbf{B}}_{n-1}\hat{\mathbf{B}}_{n-1}^{\mathrm{T}}\mathbf{C}^{\mathrm{T}} + \mathbf{R}\right)^{-1}\underline{e}_n\,. \tag{6.31}$$

Functionally equating $\left(\mathbf{C}\mathbf{B}_{n-1}\right)^{-1}$ from the linear case to $\mathbb{K}_n$ from the *NLBeam* implementation, the update rule for a Kalman-like N-R observer becomes

$$\Delta\underline{u}_n = \sigma_w \mathbb{K}_n^{-1}\left(\sigma_w \mathbb{K}_n^{-2} + \sigma_v \mathbf{I}\right)^{-1}\underline{e}_n\,. \tag{6.32}$$

Rather than explicitly computing the inverse of the full Jacobian at each time step, $\Delta \underline{u}_n$ can be obtained as the solution to the linear system

$$\left(\mathbf{I} + \frac{\sigma_v}{\sigma_w} \mathbb{K}_n^{\,2} \right) \Delta \underline{u}_n = \mathbb{K}_n \underline{e}_n \,. \tag{6.33}$$

The RHS of Eq. (6.33) is the one-step equivalent of the RHS of Eq. (6.23), and if the measurement noise is assumed to be zero, Eq. (6.33) collapses to (6.23) for $k = 1$. In the case of acceleration measurements, the force correction would be computed from

$$\left(\mathbf{I} + \frac{\sigma_v}{\sigma_w} \left(\mathbb{K}_n^{(t)} \right)^2 \right) \Delta \underline{u}_n = \beta \Delta t^2 \mathbb{K}_n^{(t)} \underline{e}_n \,. \tag{6.34}$$

As the parameter σ_v increases, corresponding to an assumed increase in the measurement noise, the term premultiplying $\Delta \underline{u}_n$ increases, so the force correction necessarily decreases for constant error $\underline{e}_n$. As such, the ratio σ_v / σ_w and the number of iterations become tuning parameters that define the extent to which the observer output conforms to the available measurements.

6.3. Numerical Examples

6.3.1. *NLBeam* Plant with LTI SDOF Reference Model

The N-R observer was implemented with numerical simulation "measurements" using the formulation given in Eqs. (6.33) and (6.34). In the first example, measurements from a simulated *NLBeam* plant were used with an LTI SDOF model of the beam. The SDOF representation of the beam was modeled as a spring and a mass, with the natural frequency adjusted to equal that of the first mode of the *NLBeam* plant model. For the *NLBeam* plant modeled as described in Section 2.6.1, the input was a sinusoidal base displacement at 3.9673

Hz. This frequency was originally chosen because it is the nearest bin-centered sinusoid to 4 Hz for a sampling frequency of 1250 Hz and a record length of 8192 points. For small amplitude base excitation, the numerical model's first resonance was at 3.745 Hz, and the excitation frequency was chosen to be sufficiently close to the beam's first resonance that large amplitude motion could be obtained without inducing an unstable response. Because the excitation and resonant frequencies were within two bins of each other, the bin-centeredness of the excitation was intended to ease the frequency-domain separation of the excitation from the first resonance of the beam. This selection would aid in the exploration of the "beating" phenomenon that also results from the proximity of the excitation frequency to a resonant frequency of the plant. For these numerical studies, the excitation consisted of 8192 points of the above-mentioned sinusoid (from 0 to 6.5528 seconds), followed by nothing for the remainder of an 8-second record. The beam was allowed to free-decay following the end of the excitation period, so that damping differences between the plant and the reference models could be seen more clearly, and so that the observers' performance in the absence of excitation could be observed.

Using the *NLBeam* plant and an SDOF reference model permits a direct comparison of the N-R observer with the linear Kalman filter. In the case of the N-R observer, the performance is a function of the ratio σ_v/σ_w, while for the Kalman filter, the performance is a function of σ_v and σ_w separately. For the sake of comparison, the input disturbance parameter was fixed at $\sigma_w = 1\times10^{-3}$ and the ratio σ_v/σ_w was varied. The observer results are shown for the $\sigma_v/\sigma_w = 0$ case in Figure 82. In this case, the Kalman filter and the N-R observer are identical. In Figure 82a, the acceleration outputs are plotted together for the plant model, the reference model, the Kalman filter output, and the N-R observer output. In Figure 82b, the tip displacement is plotted for the same models. These plots show that, on the scale presented, the outputs of both observers overlay the plant output exactly. Note that there are transient events at 0 and 6.5528

seconds. These transient events are a result of the numerical damping implemented in the Newmark time integration scheme, and they occur following the abrupt changes in the simulated loading that correspond to the start and end of the excitation. In Figure 82c, the displacement error envelopes are plotted in order to present more clearly the observers' state estimation performance. Each envelope is obtained as the magnitude of the error analytic signal, computed using the Hilbert transform. This presentation is chosen over the raw error signal so that several error signal envelopes can be plotted together without confusion. With the SDOF model tuned to the first resonance of the *NLBeam* model, the prediction error is on the order of 1 cm, or about 50% of the maximum true displacement. The prediction error coincidentally drops close to zero at the "neck" of the "beat" near 4.3 seconds. The Kalman filter and the Newton-Raphson observer errors are identical, with a mean error of 0.22 mm, and a peak error of 1.42 cm when tracking the transient event at 6.5528 seconds.

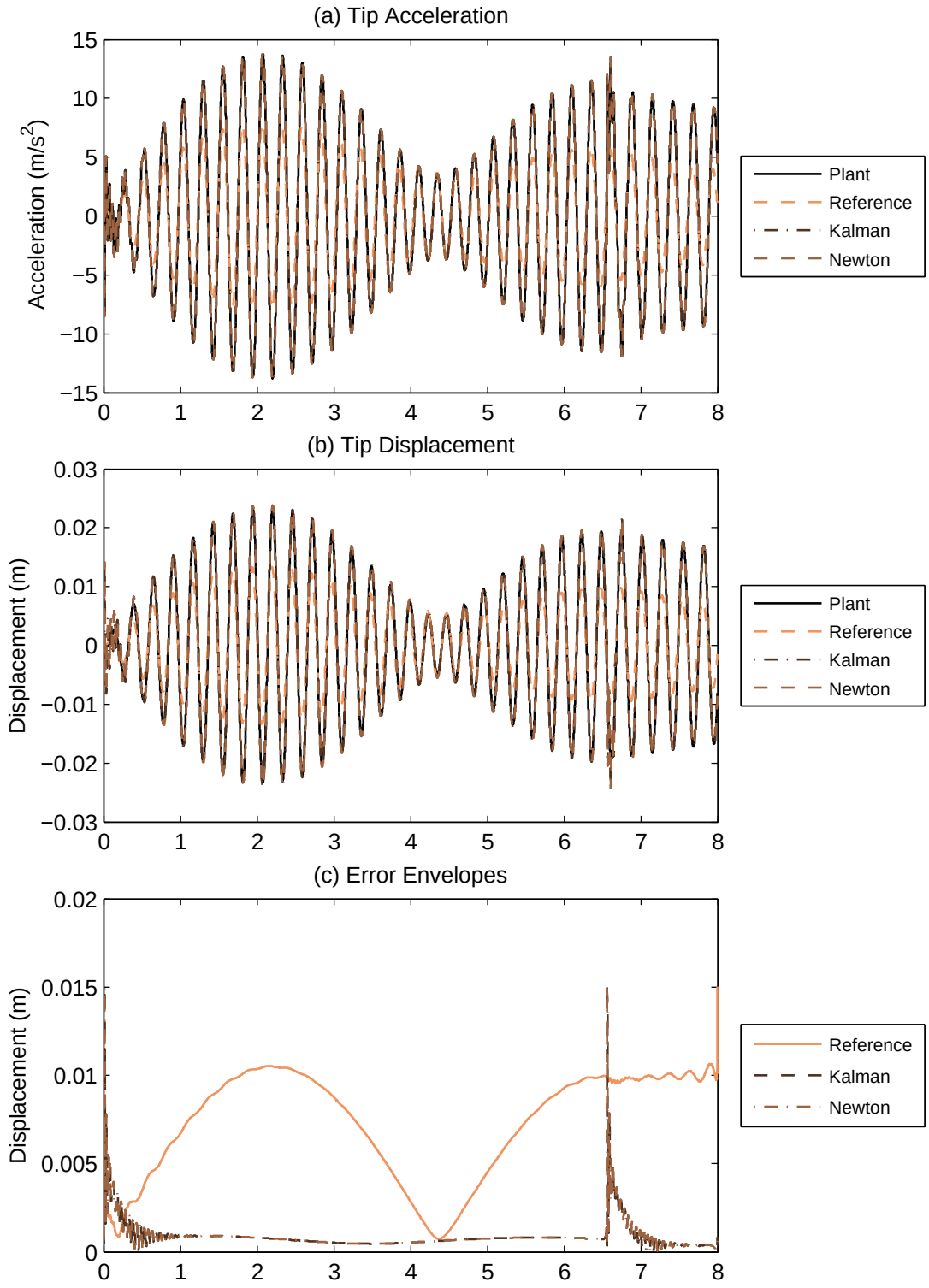

Figure 82: Observer results for *NLBeam* plant and SDOF reference model, with $\sigma_w = 1\times10^{-3}$ and $\sigma_v/\sigma_w = 0$

The maximum and mean errors with both the Kalman filter and the N-R observer are plotted for $\sigma_w = 1\times10^{-3}$ in Figure 83 versus σ_v/σ_w ranging over several orders of magnitude. The Kalman filter has a simple error structure, with the maximum equal to that for the $\sigma_v/\sigma_w = 0$ case, a minimum near the $\sigma_v/\sigma_w = 1$ case, and as the measurement error grows, the Kalman filter output approaches the pure prediction output. The N-R observer error behavior is more complex, although it does have the same behavior as the Kalman filter at extreme values of σ_v/σ_w. The multiple peaks are a result of the non-optimal algorithm's poor tracking of the transient effects from the Newmark integration scheme, but there is a minimum error for the N-R observer on the same order as that for the Kalman filter; this result demonstrates that the N-R observer performance is dependent on the parameter σ_v/σ_w, and that better results can be obtained by its proper selection.

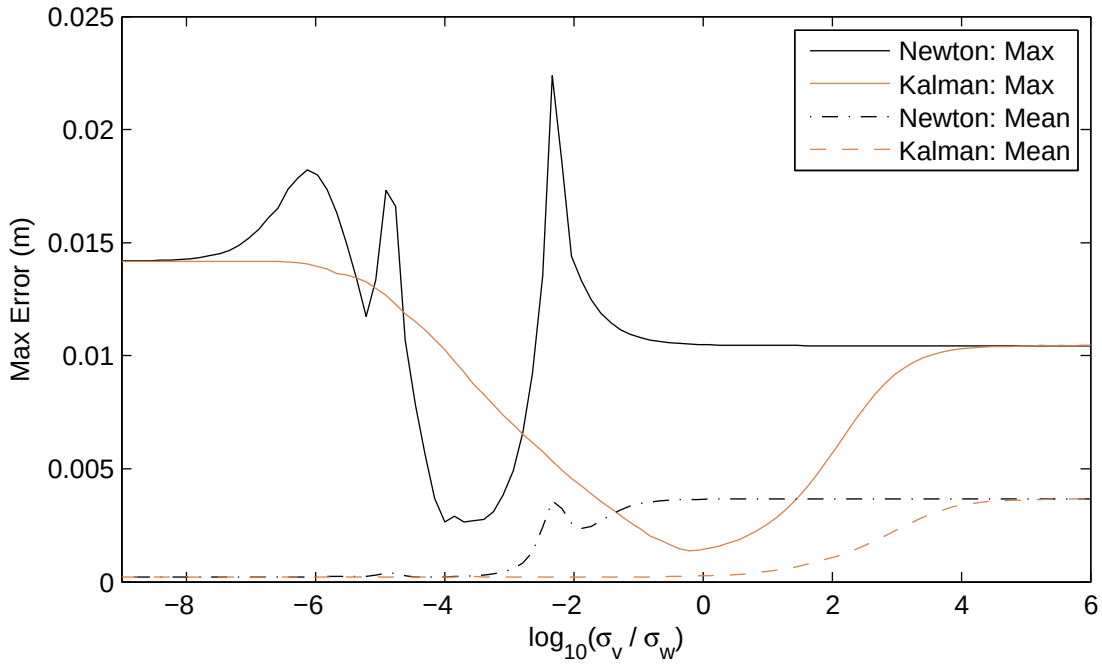

Figure 83: Maximum and mean displacement error versus σ_v/σ_w for $\sigma_w = 1\times10^{-3}$

The observer results for the $\sigma_v/\sigma_w = 1\times10^{-4}$ case, near the minimum error case for the N-R observer, are shown in Figure 84. The transient spike for the Kalman filter is somewhat diminished, at 1 cm, and the spike for the N-R observer has dropped to 2.6mm. The observer results for $\sigma_v/\sigma_w = 1$ case, near the minimum error case for the Kalman filter, are shown in Figure 85. The transient spike for the Kalman filter is greatly diminished, at 1.4mm, while the N-R observer output simply tracks the prediction. This result is expected, noting from Figure 83 that the N-R observer error has leveled out by the $\sigma_v/\sigma_w = 1$ case. The observer results for the $\sigma_v/\sigma_w = 1\times10^{3}$ case are shown in Figure 86. This noise level is almost unrealistically large, forcing both observers to rely heavily on the prediction. In this case, the N-R observer error simply tracks that for the prediction, while the Kalman filter error tends toward the same level, although it is still able to slowly reduce the prediction error in the absence of any external excitation.

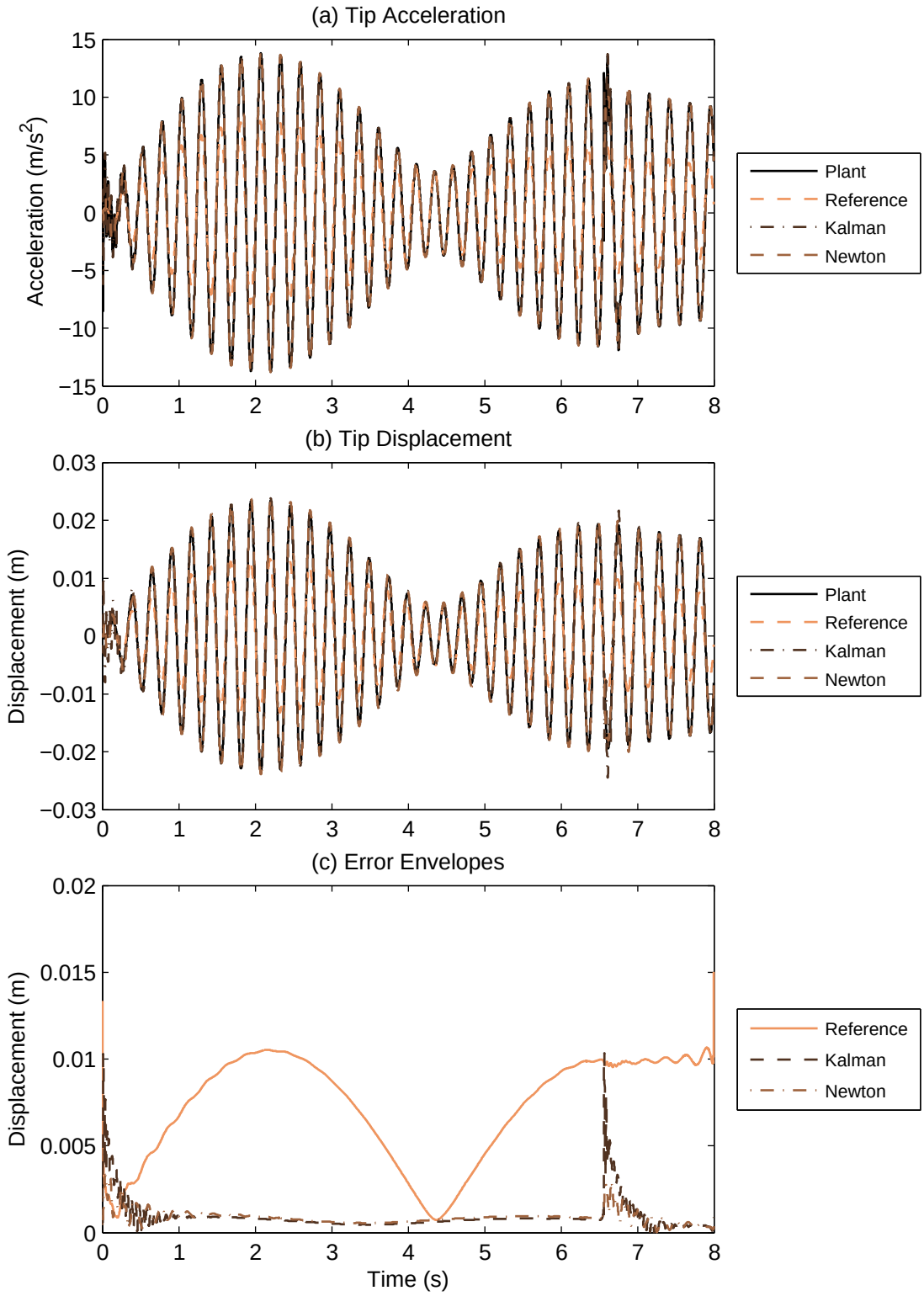

Figure 84: Observer results for *NLBeam* plant and SDOF reference model, with $\sigma_w = 1\times10^{-3}$ and $\sigma_v/\sigma_w = 1\times10^{-4}$

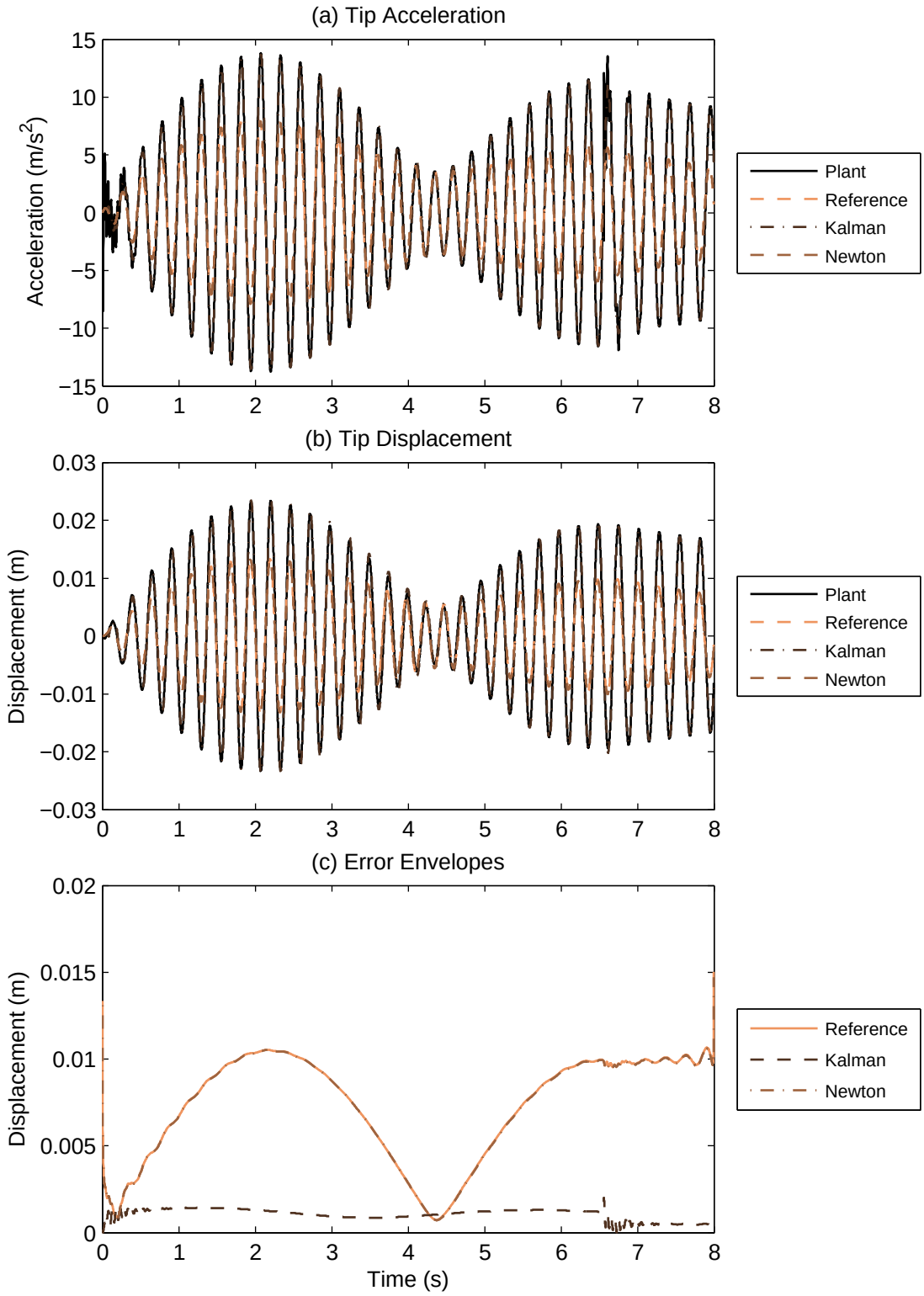

Figure 85: Observer results for *NLBeam* plant and SDOF reference model, with $\sigma_w = 1\times10^{-3}$ and $\sigma_v/\sigma_w = 1$

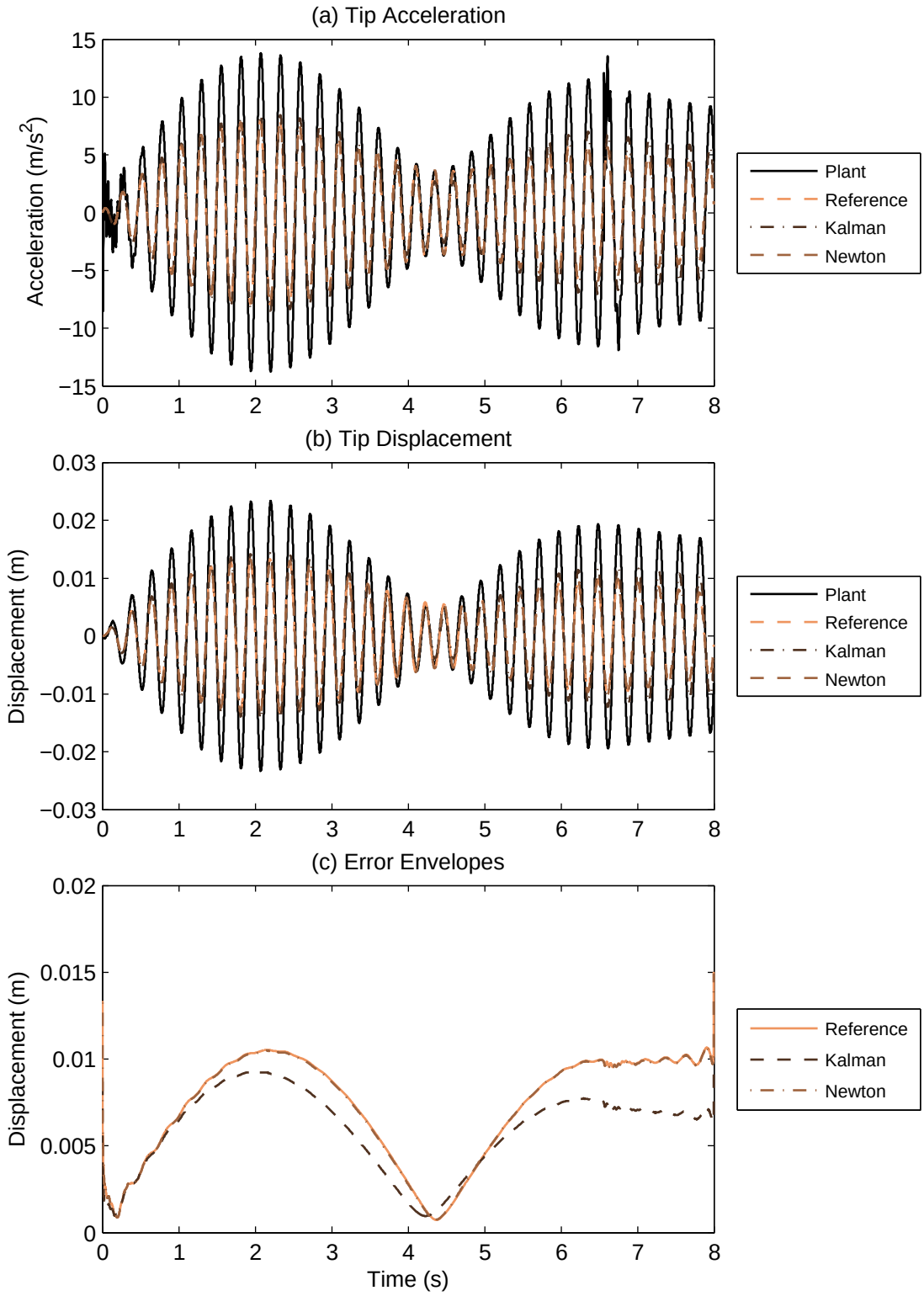

Figure 86: Observer results for *NLBeam* plant and SDOF reference model, with $\sigma_w = 1\times10^{-3}$ and $\sigma_v/\sigma_w = 1\times10^{3}$

6.3.2. *NLBeam* Plant with *NLBeam* Reference Model

The *NLBeam* reference model was a perturbed version of the plant model described above. The perturbation was introduced by reducing the number of elements from 10 to 2 and decreasing the numerical damping in the simulation by choosing $\alpha = 0.25$, so that, from Eq. (2.3), $\beta = 0.390625$ and $\gamma = 0.75$. The observer results for two cases are plotted in Figure 87. The first case was a verification step for the nonlinear implementation of the Newton-Raphson observer in which a full-field displacement measurement (including translations and rotations) was utilized to compute the force correction using Eq. (6.23) at each iteration. Because the reference model had only five nodes and the plant model had 21 nodes, the measurements were a subset of the available outputs from the plant model, corresponding to the DOFs of the reference model. This case is referred to as "N-R All-Disp" in Figure 87. In the second case, referred to as "N-R Tip Acc," only the tip acceleration in the x-direction was utilized, and the force correction at each iteration was computed using Eq. (6.27). For the full-field measurement verification case, four iterations of the Newton-Raphson update step were used at each time step, while for the tip acceleration measurement case, eight iterations were used. Although a better practice would be to define a convergence criterion to determine the number of iterations required, these iteration counts were determined to be sufficient for the examples considered.

The N-R observer results for the *NLBeam* reference model are shown in Figure 87. In Figure 87a-b, the output tip acceleration and observed tip displacement are plotted for the plant model, the reference model, the NR All Disp case, and the NR X-Tip Acc case. The prediction error envelopes for the five reference model nodes are plotted in in Figure 87c. The error for Node 1 was zero, because that node was driven by the same displacement boundary condition for the plant and the reference models. The errors at the other nodes were on the order of 0.5 cm, compared to the ~2 cm displacement at the tip of the beam. The error envelopes at each

node for the NR All-Disp case are shown in Figure 87d; the errors in this case were on the order of the machine precision. This result is expected, because using all measurements, Eq. (6.23) is the unique solution to Eq. (6.16) that drives the error signal toward zero at each iteration. The error envelopes at each node for the NR Tip-Acc case are shown in Figure 87e. With the exception of Node 1, which was identical for the plant and the reference model, the observer errors are well above machine precision. The error signals are about two orders of magnitude below the reference model prediction errors, with an overall observer error of less than 1%. The transient events at the start and the end of the excitation signal are still present as was for the SDOF reference model, but their impact on the maximum error is significantly diminished in comparison to the SDOF reference model.

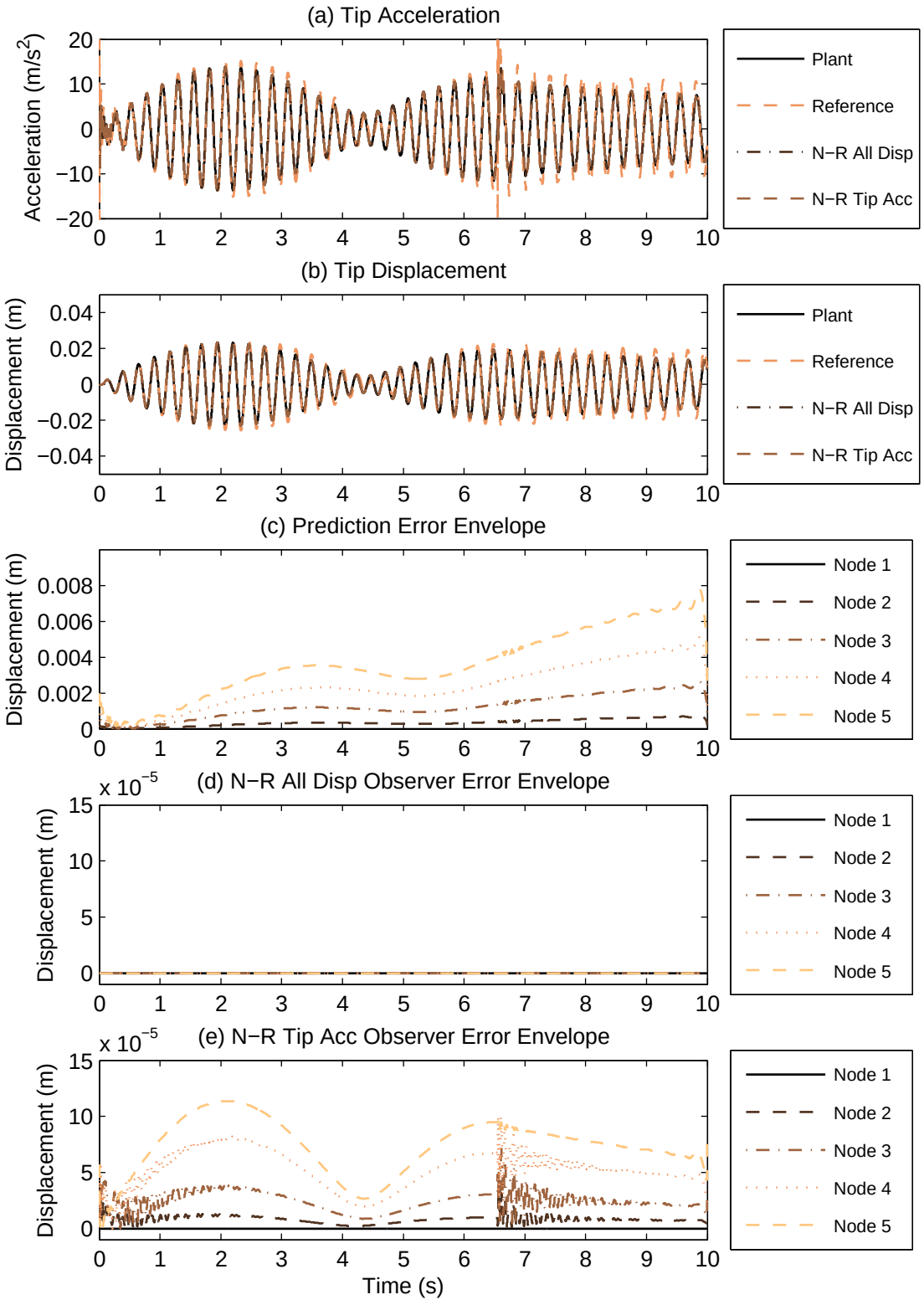

Figure 87: Newton-Raphson observer results for *NLBeam* plant and *NLBeam* reference model

6.4. Experimental Example

The N-R observer was implemented using experimental data from the plant described in Section 2.6.3, applying Eq. (6.34) to the 10-element version of the *NLBeam* model used for the plant in the previous example. The base on which the beam was mounted was excited using a broken shaker, which made input estimation somewhat challenging. Rather than prescribing an input, the reference model was left unexcited, and the N-R observer applied the necessary force to drive the model toward the measured acceleration response. The acceleration measurements in the X-direction at the tip and the base, high-pass filtered to remove any DC measurement error, were provided to the N-R observer. The X-direction acceleration at the midpoint of the beam was retained for validation purposes. Results are presented for two values of the σ_v/σ_w parameters: 0, which assumes no measurement noise, and 0.1. In each case, 8 iterations of the N-R observer were implemented, which was sufficient for the observer to converge.

For $\sigma_v/\sigma_w = 0$, the acceleration values are plotted in Figure 88 for approximately the first second a 30-second record, and the corresponding acceleration error over the full record is plotted in Figure 90. For $\sigma_v/\sigma_w = 0.1$, the acceleration values are plotted in Figure 89 for approximately the first second a 30-second record, and the corresponding acceleration error over the full record is plotted in Figure 91. Note that, for the $\sigma_v/\sigma_w = 0.1$ case, the observed acceleration does not perfectly track the measurement for the tip or the base, for which data were provided to the observer, although their error levels are lower than that for the midpoint. Furthermore, the observed acceleration error at the midpoint is noticeably greater for the $\sigma_v/\sigma_w = 0.1$ case, with an RMS error of 1.1 m/s^2, than for the $\sigma_v/\sigma_w = 0$ case, with an RMS error of 0.60 m/s^2.

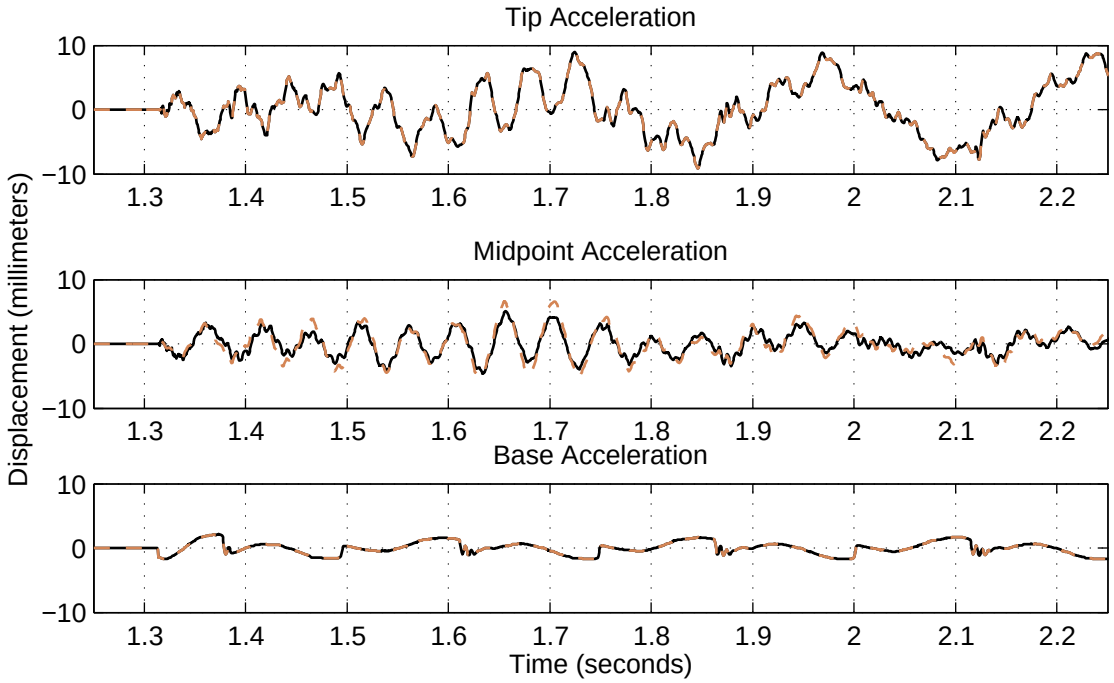

Figure 88: Measured acceleration (solid black) with observer estimates (dashed orange) for $\sigma_v/\sigma_w = 0$

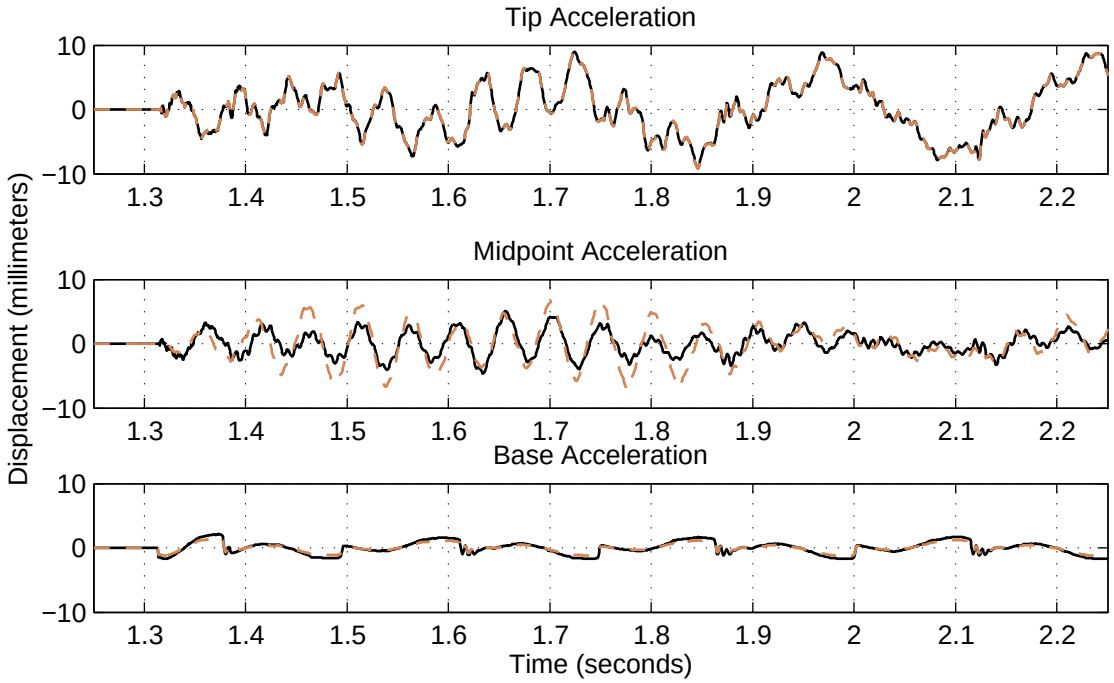

Figure 89: Measured acceleration (solid black) with observer estimates (dashed orange) for $\sigma_v/\sigma_w = 0.1$

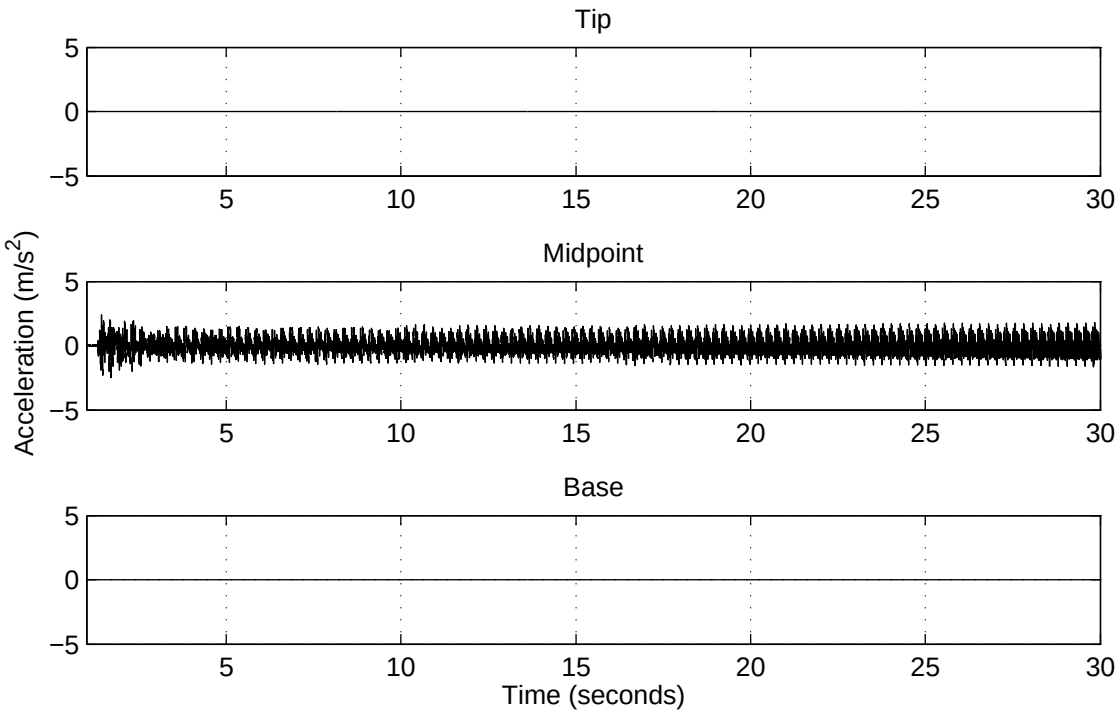

Figure 90: Acceleration observer error for $\sigma_v/\sigma_w = 0$

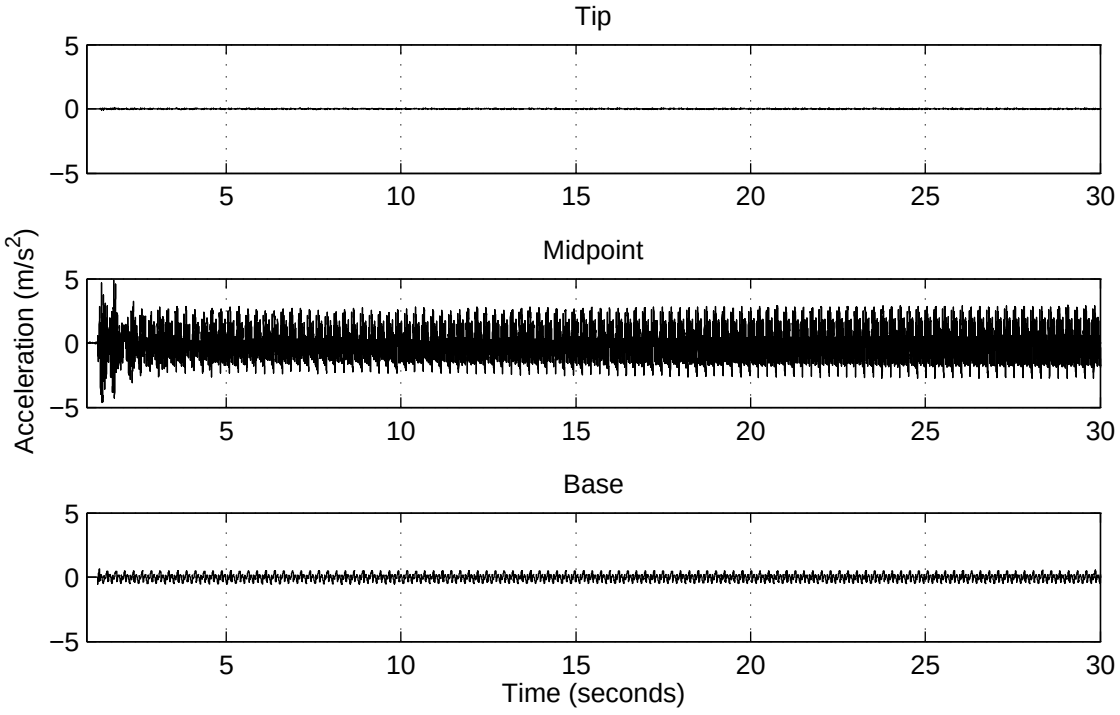

Figure 91: Acceleration observer error for $\sigma_v/\sigma_w = 0.1$

The observed displacements in the X-direction at three points on the beam (tip, midpoint, and base) are plotted together for the $\sigma_v/\sigma_w = 0$ case in Figure 92. Although the observed midpoint acceleration error was lower for the $\sigma_v/\sigma_w = 0$ case, the observed displacements demonstrate a peculiar tendency to drift apart. This is actually a result of over-conforming to noise in the acceleration measurements, and ultimately causes unrealistic estimates of strain. The observed displacements at the three points are plotted together for the $\sigma_v/\sigma_w = 0.1$ case in Figure 93. The displacement observations are not centered on zero, but instead "drift" in unison. Although the experiment did not drift, because the large shaker that excited it was fixed, the base to which the beam was mounted was free to move in the X-direction on low-friction linear rails. As a result, the reference model was not constrained in the X-direction. However, because the drift in the $\sigma_v/\sigma_w = 0.1$ case is effectively quasi-static rigid body motion, it does not affect estimates of strains or bending curvature. In order to make a direct comparison to the measured displacement, the observed displacement can be high-pass filtered to remove the rigid body motion. This high-pass filtered signal is shown in Figure 94.

The observed displacements for the $\sigma_v/\sigma_w = 0.1$ case are plotted along with the displacements measured with the high-speed camera in Figure 95. As noted in Section 2.6.3, the camera resolution was 1.9 mm per pixel, so the displacement measurements are highly quantized. The displacement observations closely align with what can be gleaned from the camera measurements; however, note the spectral richness of the observation compared to the highly quantized measurement. It is possible that the estimate is able to provide a fuller and more accurate measure of the displacement than the camera; however, because the higher-frequency motion is below the quantization level of the camera, it would only be possible to validate the displacement measurements below a very low frequency level.

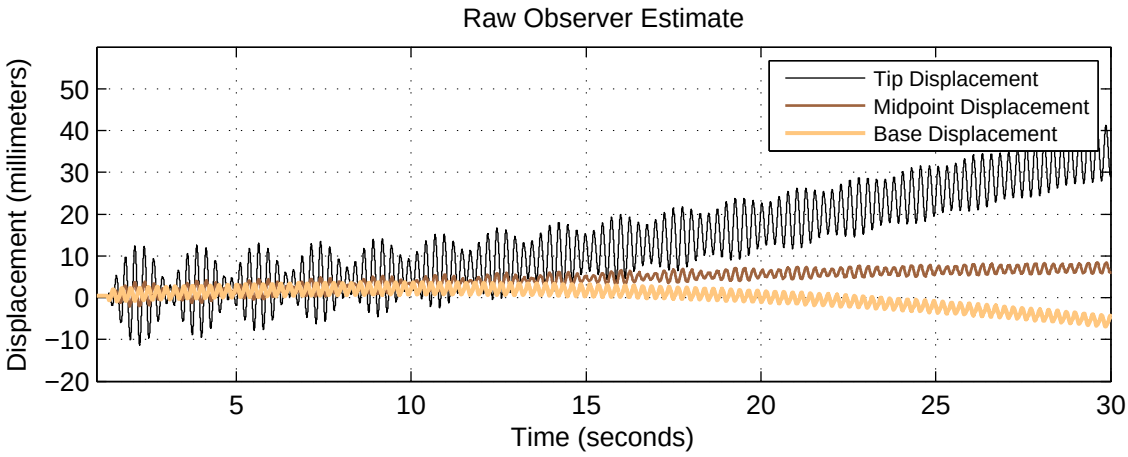

Figure 92: Displacement observations for $\sigma_v/\sigma_w = 0$

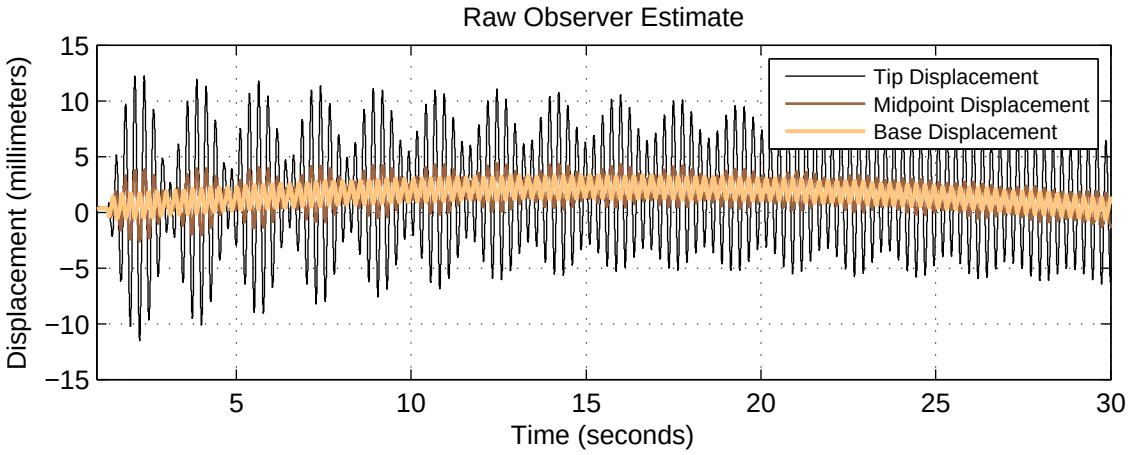

Figure 93: Displacement observations for $\sigma_v/\sigma_w = 0.1$

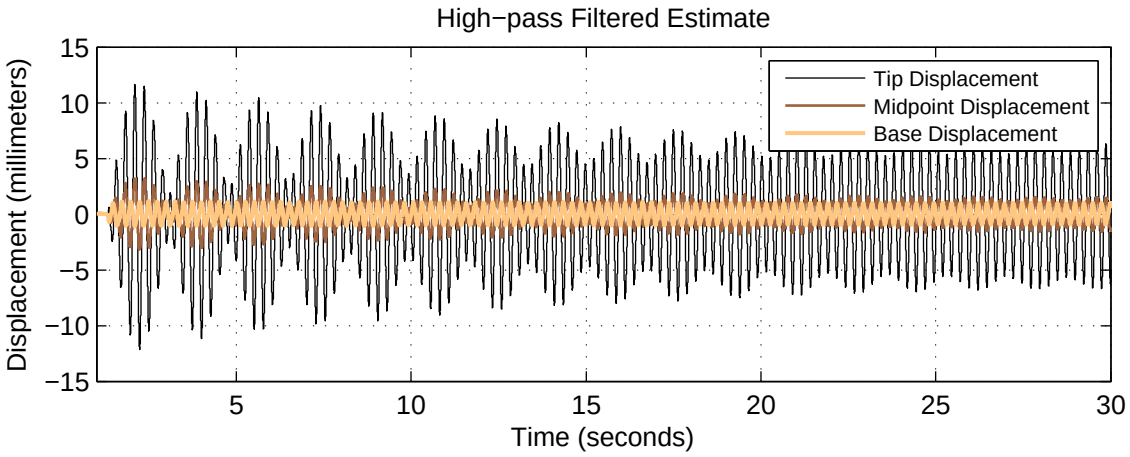

Figure 94: AC-filtered displacement observations for $\sigma_v/\sigma_w = 0.1$

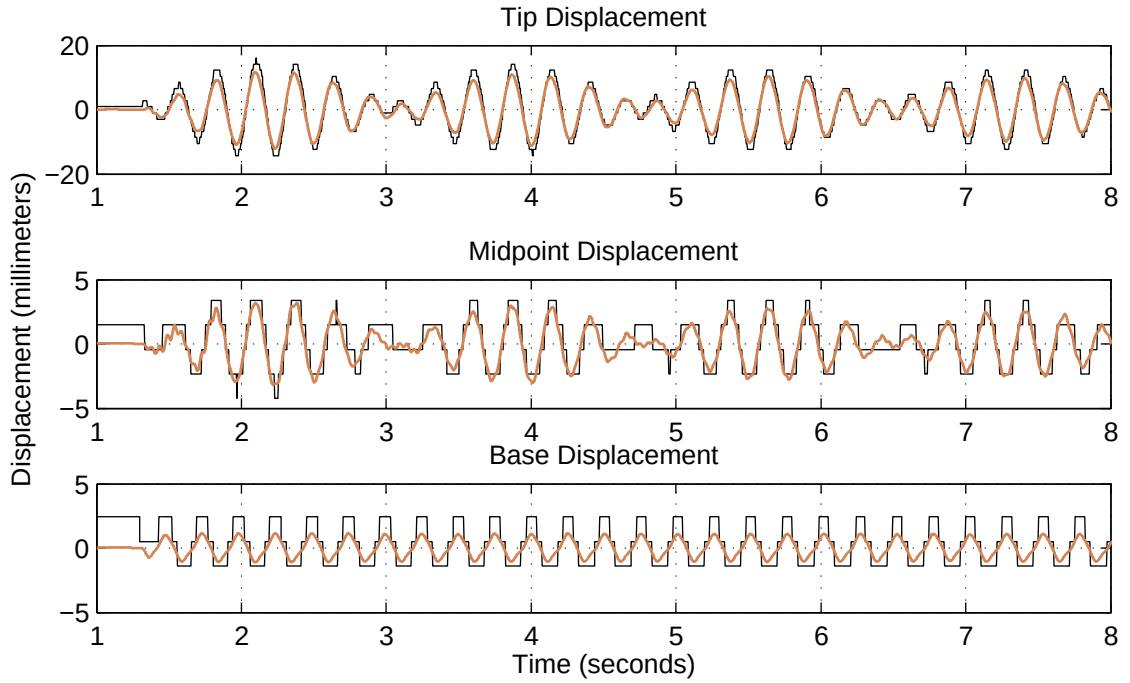

Figure 95: Measured displacement (black) with observer estimates (orange) for $\sigma_v/\sigma_w = 0.1$

The strain estimates for the $\sigma_v/\sigma_w = 0$ case are plotted in Figure 96. The effect of the divergent displacement estimates can be clearly seen in the unstable growth of the axial strain and the continuous divergence of the bending curvature, as the observer attempts to stretch the beam to conform to the accumulating measurement error. The three strain and bending

curvature estimates for the $\sigma_v/\sigma_w = 0.1$ case are plotted in Figure 97. The strain estimates for the $\sigma_v/\sigma_w = 0.1$ case appear stable, and the values are reasonable (e.g. a linear static calculation of axial strain in the root element due to the weight of the beam above it gives 2.9×10^{-7}, which is within 10% of the mean axial strain indicated in Figure 96). However, the observed strain and curvature values cannot be validated because no such measurements are available from the experiment.

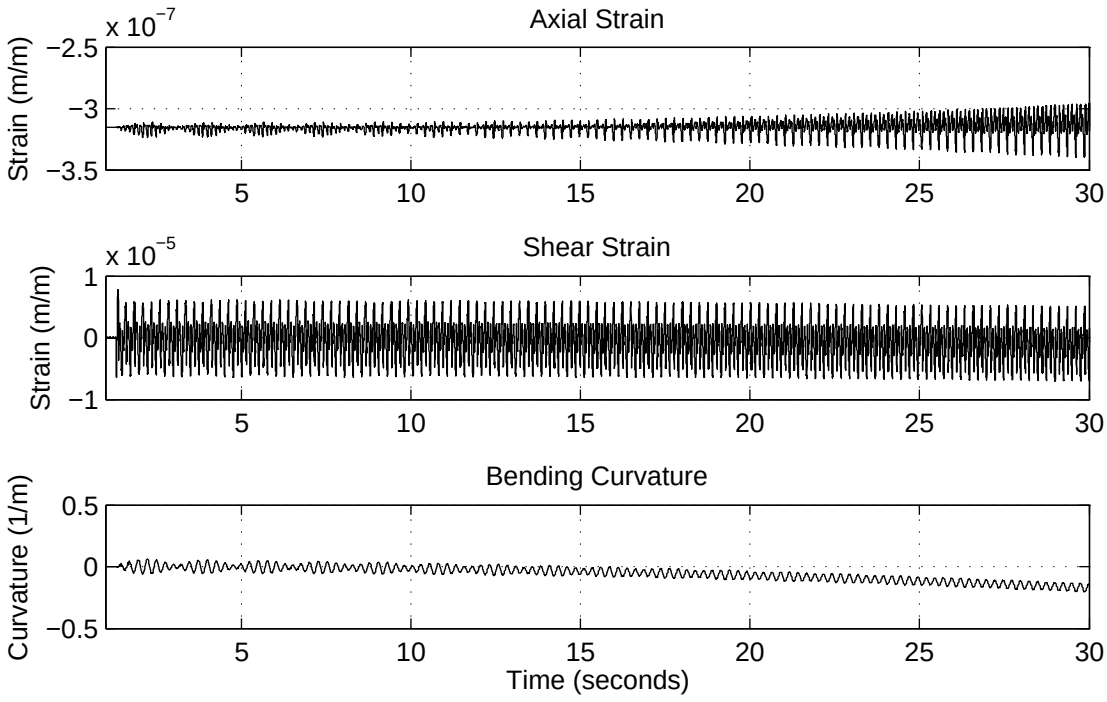

Figure 96: Observed strains and curvature for the root element with $\sigma_v/\sigma_w = 0$

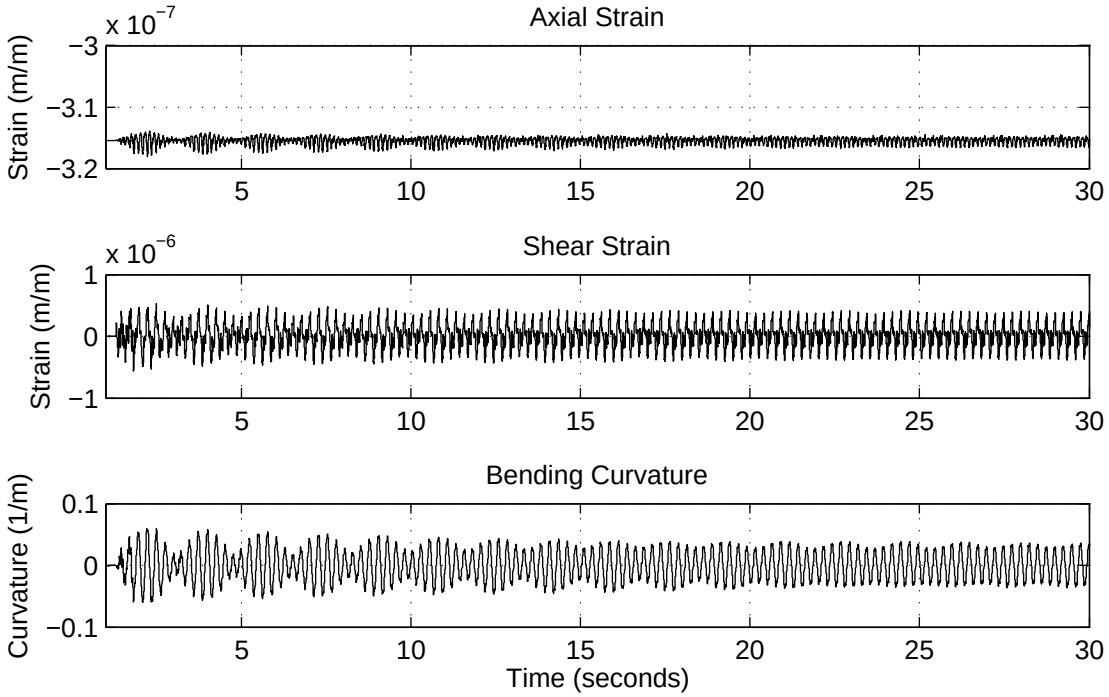

Figure 97: Observed strains and curvature for the root element with $\sigma_v / \sigma_w = 0.1$

6.5. Summary and Acknowledgements

In this chapter, a Newton-Raphson force correction observer has been introduced and demonstrated for a linear and nonlinear numerical example. The observer was implemented in a numerical example using a geometrically nonlinear beam code developed for modeling of wind turbine blades. The observer is designed to take advantage of the availability of the full system Jacobian matrices from the *NLBeam* solver at each time step. The form of the Newton-Raphson observer was verified using synthesized full-field displacement measurement data from an *NLBeam* plant model and a perturbed version of the same *NLBeam* model as the reference model. The Newton-Raphson observer was further tested using a single acceleration measurement to observe displacement at the reference model nodes, demonstrating the

numerical ability of the observer to generate a state estimate given acceleration measurements at a subset of nodes.

The relationship between the proposed Newton-Raphson observer and the linear Kalman filter was derived, and they were shown to be identical for an assumed zero measurement noise case. A modified version of the Newton-Raphson observer was developed to accommodate the presence of measurement noise. Applications of this modified version to experimental data from a vertically cantilevered beam showed that, while the assumed zero-noise case produced unstable estimates due to accumulating error, the modified, Kalman-like Newton-Raphson observer produced stable predictions of strain and bending curvature using measured acceleration, with displacement observations that corresponded well to displacement measurements collected using a high-speed, low-resolution camera.

Portions of Chapter 6 have been submitted in part to [9] *IMAC XXXI: A Conference and Exposition on Structural Dynamics*, S. G. Taylor, D. J. Luscher, and M. D. Todd, 2013. The title of this paper is "State estimate of wind turbine blades using geometrically exact beam theory." The dissertation author was the primary investigator and author of this paper.

Other portions of Chapter 6 are currently being prepared for publication [10]. S. G. Taylor, D. J. Luscher, and M. D. Todd, 2013. The title of this paper is "Nonlinear state observer for structural monitoring of wind turbine rotor blades." The dissertation author was the primary investigator and author of this paper.

Chapter 7
Conclusions and Proposals for Future Work

7.1. Overview

This dissertation has contributed in key areas among the underpinnings of an overarching probabilistic decision framework for structural health monitoring. The contribution areas are: (1) embedded sensor development and deployment; (2) sensor diagnostics for active-sensing methods; (3) an assessment of incipient damage detection performance for large-scale composite structures; and (4) the development and application of a state observer, demonstrated in the specific case of a geometrically nonlinear beam model.

Embedded sensor nodes tailored to the unique requirements of SHM were developed, with focus on robust communication and multi-scale sensing capability. Two embedded sensing platforms for SHM were developed. The WID3 is a low-power device designed for embedded sensor networking and impedance-based SHM. The WASP is a platform with greater power requirements, but one that is uniquely suited for SHM deployment, with integrated measurement capabilities for capturing relatively low-frequency structural kinematic quantities and implementing ultrasonic active sensing methods, as well as seamless support for impedance-based sensor diagnostics. This system was demonstrated in a long-term fatigue test

of a 9-m wind turbine rotor blade, and also deployed on a 20-m rotor diameter wind turbine. The fatigue test permitted a detailed assessment of piezoelectric sensor performance in terms of failure modes, longevity, and the utility of sensor diagnostics methods. Piezoelectric transducer behavior under cyclic loading as it relates to sensor diagnostics was explored, and novel data normalization steps necessary for consistent sensor evaluation were proposed. This fatigue test also provided the backdrop for the performance assessment of various active sensing-based hardware and data analysis approaches in their ability to detect crack formation in its incipient state in the composite rotor blade structure. Finally, a state observer for application with nonlinear finite element models was developed and validated in a bench-top experiment using a geometrically nonlinear beam model. This observer formulation would provide the ability to map easily measureable kinematic quantities, such as acceleration, to less accessible quantities, such as deflections and reaction loads, which are directly relatable to structural performance requirements.

7.2. Embedded Sensing

In the area of embedded sensing, two sensor nodes were developed for SHM applications. The development of the Wireless Impedance Device v3 (WID3) was presented, and its new functionality over previous WID versions was detailed. The WID3's most basic capability involves measuring the coupled electromechanical impedance of a structure, capitalizing on the well-established impedance-based structural health monitoring technique to monitor the condition of a structure. The low-power sensor node's capabilities were extended through improved networking capabilities, increased data storage options, multiple powering options that allow for energy harvesting integration, and increased triggering options that allow for better control of sleep modes, reducing overall power consumption. The node's capabilities

were further extended through use of a wireless data acquisition (WiDAQ) module to be capable of collecting low-frequency time-domain data from a variety of sensors. To demonstrate this capability, structural vibration data were collected for modal analysis, and the resulting measured natural frequencies and mode shapes were compared to those measured using a traditional data acquisition system. After successfully verifying the functionality of the WID3 in various laboratory settings, the WID3 was field-tested on the Alamosa Canyon Bridge, a structure of significant size and representative of practical importance, demonstrating that the sensor node can efficiently monitor several mechanical response parameters suitable for rapid assessment of structural condition.

The Wireless Active Sensing Platform (WASP), an embedded sensor node uniquely suited to multi-scale structural health monitoring (SHM) applications, was also developed. Its specific features were detailed, especially its innovative ability to seamlessly switch between a traditional pitch-catch active sensing mode and impedance measurement mode, which is integral to sensor diagnostics methods for active-sensing SHM. The WASP was demonstrated in three key application areas. First, its ability to perform impedance measurements for piezoelectric sensor diagnostics was demonstrated in comparison to a conventional impedance analyzer. While the absolute estimates of impedance produced using the WASP were not identical to those produced by the impedance analyzer, the relative measurements demonstrated a more-than-sufficient ability to perform sensor diagnostics. Second, its ability to collect active-sensing data for incipient crack detection was demonstrated in comparison to a commercially available module for ultrasonic guided wave measurements. The WASP demonstrated a capability on par with the commercial system in detecting incipient crack development in a full-scale wind turbine rotor blade fatigue test. Third, its ability to collect low-frequency vibration measurements for model-based SHM was demonstrated using acceleration measurements collected from a telescope drive system.

Among the WASP's notable shortcomings and opportunities for further development are: (1) its output signal amplification chain for active sensing; (2) its ability to be remotely reprogrammed or updated; and (3) its bulky size. A major shortcoming of the WASP was its output signal chain's ability to sufficiently excite the thick fiberglass of the CX-100 rotor blade. Although the current amplifier utilized in the WASP dramatically increased its power output capability beyond, say, the AD5933 utilized in the WID, and it would be capable of implementing guided wave methods for SHM in a metallic plate-like structure, the signal attenuation in the fiberglass was severe, and external amplification was required. Future versions of the WASP should significantly increase the output signal power capability. This would require not only more powerful amplification circuitry, but also careful consideration of the signal isolation required to prevent cross-talk across the switches that enable any of the channels to be inputs or outputs; feeding a powerful signal back into the ADC, even with 60 dB attenuation (the cross-talk specification for the ADG1419 switches used), would corrupt measurements. The WASP would benefit greatly in deployed applications from an ability to be remotely reprogrammed. In its current implementation, changes to the WASP's behavior, web interface, available excitation waveforms, or even its IP address require a firmware flash operation. Obviously, if the WASP were embedded in a spinning wind turbine rotor blade, accessing the device to physically re-flash its firmware would be difficult, although upgrades and improvements could be being developed constantly. As such, future versions should incorporate an over-the-air type reprogramming capability. Finally, the WASP's large size may be an impediment to its deployment. The WASP's major innovations, including its signal chains and switching circuitry, are on PCBs designed to interface with a commercially available development board for the ARM processor that controls the system. Future versions of the WASP should incorporate the processor, communications, power delivery, storage, and the like in a dedicated, compact base board, rather than relying on the bulky prototype platform.

7.3. Sensor Diagnostics

In the area of sensor diagnostics, a detailed overview of impedance-based sensor diagnostics for piezoceramic transducers used in active sensing applications for SHM was presented. A case study from a long-term, large-scale test was presented in which 49 transducers were used to monitor the health of a wind turbine rotor blade subjected to fatigue loading until failure. The transducers proved effective in their longevity and ability to perform within the SHM system until the blade itself began to fail. For those sensors that did fail, the sensor diagnostics procedures implemented were effective in identifying them. Some peculiar behaviors were observed, which might not have been present in a smaller-scale or bench-top test. In some cases where the susceptance slope increased, which would ordinarily indicate a debonded sensor, the fiberglass material to which the transducer was affixed seems to have softened. In this case, an increased susceptance slope would be an indication of incipient structural damage, rather than sensor failure. Furthermore, data taken under dynamic loading, which is often necessary for *in situ* operation of an SHM system, exhibited a clearly measureable impact on the susceptance values. It was observed that the low-frequency behavior of the host structure had a significant impact on the measurements obtained using this high-frequency technique, which previously had been thought to be immune to low-frequency interference. A normalization method was proposed for data collected from a structure under operational conditions that induce time-varying strain fields at the transducer locations, and its utility as a normalization step to enable comparison among measurements taken in multiple loading conditions was demonstrated.

These peculiar behaviors should be explored in more detail and with intentional experiments aimed at characterizing them. In the case of the softening effect, smaller coupons of fiberglass material should be instrumented and purposefully loaded to weaken the material,

and the corresponding effect on PZT patches bonded to the material surface should be measured. In this type of smaller-scale experimental campaign, the effect of the material softening could be distinguished from simple patch debonding. In the case of the nonstationary impedance measurements, a thorough examination of the effects of low-frequency vibration on impedance measurements should be undertaken. It is clear that, with the constant excitation at the rotor blade's fundamental frequency, and with the "sine sweep" measurement method implemented by the impedance analyzer, that there was an effect on the measurement that would impact the decision process in determining the health of the sensor. This effect should be explored for other measurement methods, such as a broadband excitation, and for other nonstationary structural behaviors, such as turbulent distributed loading in the case of the wind turbine blade.

7.4. Incipient Damage Detection Performance

The goal of this portion of the dissertation was to identify an approach to achieve better performance in incipient crack detection for the CX-100 rotor blade under cyclic loading. The CX-100 is a representative composite wind turbine rotor blade structure, having a balsa wood frame and a fiberglass shell. Extensive data were collected using different acquisition systems and analyzed using different signal processing approaches and test statistics in order to compare incipient crack detection performance. In the acquisition hardware domain, ultrasonic guided waves were compared with diffuse wave field measurement methods; in the detector domain, energy methods were compared with correlation methods.

The guided wave data at 200 kHz produced good detection results for both test statistics. At this frequency, detection performance was best along the rotor blade's spar cap, indicating that for this structure, an extremely low-density array (as little as one actuator/sensor

pair) might be sufficient to detect incipient cracks that cross the spar cap. While the 50 kHz guided wave data provided good detection performance, the better performing paths lay neither near the crack nor along the spar cap. The diffuse wave data demonstrated a lack of sensitivity over long transmission distances, with lower sensitivity for the larger outer array than the smaller inner array. The high-frequency, narrow-band excitation showed increased sensitivity based on the rotor blade's structure, rather than the crack location, while the lower-frequency, broadband excitation produced detection results more sensitive to the damage location. This trade-off suggests the importance of differentiating detection from localization objectives when designing a detector.

The lessons learned in this fatigue test should be applied to a real-world situation, in which natural loads are permitted to excite a structure and slowly degrade and damage it over time. Alternatively, a compromise experimental campaign could be constructed in which a blade seeded with certain types of damage would be put in operation and monitored while it moved through an accelerated life cycle. This sort of SHM system deployment would require a long-term commitment and a next-generation embedded sensing system with the remote interface capabilities described above.

7.5. State Observer

A state observer based on a Newton-Raphson iterative force correction scheme was introduced and demonstrated for both linear and nonlinear numerical examples, as well as on a bench-top experiment with inherently noisy, real-world data. The observer was implemented using a geometrically nonlinear beam code, *NLBeam*, developed for modeling of wind turbine blades, and it is designed to take advantage of the availability of the full system Jacobian matrices at each time step from the nonlinear solver. The form of the Newton-Raphson observer

was verified numerically using synthesized full-field displacement measurement data from a simulated plant model and a perturbed version of the same model as the observer reference model. The Newton-Raphson observer was further tested using a single acceleration time history to infer displacement time histories at the reference model nodes, demonstrating the ability to generate a state estimate given acceleration measurements at a subset of DOFs. The relationship between the proposed Newton-Raphson observer and the linear Kalman filter was derived, and they were shown to be identical in the case with of zero measurement noise. A modified version of the Newton-Raphson observer was developed to accommodate the presence of measurement noise. Applications of this modified version to experimental data from a vertically cantilevered beam showed that, while the assumed zero-noise case produced unstable estimates due to accumulating error, the modified, Kalman-like Newton-Raphson observer produced stable predictions of strain and bending curvature using measured acceleration, with displacement observations that corresponded well to displacement measurements collected using a high-speed, low-resolution camera.

There are significant improvements and further developments that should take place in the implementation of this observer. A future experiment could be devised with three key improvements: (1) constrain the base on which the beam was cantilevered using a stiff spring in order to eliminate drift in both the experimental setup and the numerical models; (2) use a higher resolution camera in order to validate higher-frequency displacement behavior, which tend to have smaller motion; and (3) collect surface strain data on the beam as a secondary means of validating the model output with the observer implementation. This third step would validate the model and observer combination for estimating the in-service reaction forces, which are important in evaluating overall wind turbine structural performance. Furthermore, although the development and bench-top demonstration of the state observer designed for application with the nonlinear beam code is a necessary step in obtaining state estimates for

structural performance prediction, the application must be extended to the large, flexible, composite structures for which the code was developed. In parallel with the work presented in this dissertation, others have developed models of the CX-100 blade in *NLBeam*, but these models have not been validated against any operational data. Some such data exists from the WASP's flight deployment at the LIST facility. A natural progression of these works would be to apply the observer to the CX-100 blade model using measured, in-flight acceleration data, and verify it against strain data collected using the fiber Bragg grating array. Finally, the observer output should be tested in a numerical analysis-of-variance campaign to determine the sensitivity of the model and the observer implementation to noise on various inputs, and to enable to production of state estimates in the form of probability density functions for implementation with risk-based probabilistic decision models.

References

[1] S. G. Taylor*, et al.*, "Multi-scale wireless sensor node for health monitoring of civil infrastructure and mechanical systems," *Smart Structures and Systems,* vol. 6, pp. 661-673, 2010.

[2] S. G. Taylor*, et al.*, "A mobile-agent-based wireless sensing network for structural monitoring applications," *Measurement Science and Technology,* p. 045201, 2009.

[3] C. J. Stull*, et al.*, "Real-Time Condition Assessment of RAPTOR Telescope Systems," *Journal of Structural Engineering,* vol. 1, p. 426, 2012.

[4] S. G. Taylor*, et al.*, "Embedded sensor node deployment to monitor telescope drive system components," in *SPIE Smart Structures/NDE*, San Diego, California, USA, 2012, pp. 83430C-6.

[5] S. G. Taylor*, et al.*, "Active sensing platform: development and deployment," *Sensors Journal, IEEE,* in review 2012.

[6] S. G. Taylor*, et al.*, "Diagnostics for piezoelectric transducers under cyclic loads deployed for structural health monitoring applications," *Smart Materials and Structures,* accepted 11-Dec 2012.

[7] S. G. Taylor*, et al.*, "Fatigue crack detection performance comparison in a composite wind turbine rotor blade," *Structural Health Monitoring,* accepted 12-Nov. 2012.

[8] S. G. Taylor*, et al.*, "Incipient crack detection in composite wind turbine blades," *Journal of Intelligent Material Systems and Structures,* in progress 2013.

[9] S. G. Taylor*, et al.*, "State estimate of wind turbine blades using geometrically exact beam theory," in *IMAC XXXI: A Conference and Exposition on Structural Dynamics*, Garden Grove, CA, 2013.

[10] S. G. Taylor*, et al.*, "Nonlinear state observer for structural monitoring of wind turbine rotor blades," in progress 2013.

[11] S. G. Taylor*, et al.*, "Integrated wireless powering and data interrogation for civil infrastructure monitoring," presented at the Bridge Maintenance, Safety, Management and Life-Cycle Optimization, Philadelphia, PA, 2010.

[12] S. G. Taylor*, et al.*, "Impedance-based Wireless Sensor Node for SHM, Sensor Diagnostics, and Low-frequency Vibration Data Acquisition," in *7th International Workshop on Structural Health Monitoring*, Stanford, CA, 2009, pp. 831-838.

[13] S. G. Taylor*, et al.*, "Multi-scale wireless sensor node for impedance-based SHM and long-term civil infrastructure modeling," presented at the Bridge Maintenance, Safety, Management and Life-Cycle Optimization, Philadelphia, PA, 2010.

[14] C. R. Farrar and K. Worden, "An introduction to structural health monitoring," *Philosophical Transactions of the Royal Society A: Mathematical, Physical and Engineering Sciences,* vol. 365, pp. 303-315, February 15, 2007 2007.

[15] K. Deines*, et al.*, "Modal Analysis and SHM Investigation of CX-100 Wind Turbine Blade," in *Rotating Machinery, Structural Health Monitoring, Shock and Vibration*. vol. 5, T. Proulx, Ed.: Springer New York, 2011, pp. 413-438.

[16] (08-13-2012). *APC International piezoelectric material properties*. Available: http://www.americanpiezo.com/apc-materials/piezoelectric-properties.html

[17] R. R. White, "Concepts," in *The Los Alamos Thinking Telescope Project*: Los Alamos National Laboratory, 2006.

[18] W. T. Vestrand*, et al.*, "RAPTOR: Closed-Loop monitoring of the night sky and the earliest optical detection of GRB 021211," *Astronomische Nachrichten,* vol. 325, pp. 549–52, 2004.

[19] D. Berry, "Design of 9-Meter Carbon-Fiberglass Prototype Blades: CX-100 and TX-100," Sandia National Laboratories, Albuquerque, NM SAND2007-0201, 2007.

[20] S. G. Taylor*, et al.*, "Full-scale fatigue tests of CX-100 wind turbine blades. Part II: analysis," in *SPIE Smart Structures/NDE*, San Diego, California, 2012, pp. 83430Q-10.

[21] K. M. Farinholt*, et al.*, "Full-scale fatigue tests of CX-100 wind turbine blades. Part I: testing," in *SPIE Smart Structures/NDE*, San Diego, California, 2012, pp. 83430P-8.

[22] S. S. Kessler*, et al.*, "A Cable-Free Digital Sensor-Bus for Structural Health Monitoring of Large Area Composite Structures," presented at the Annual Conference of the Prognostics and Health Management Society, 2009.

[23] A. V. Oppenheim*, et al.*, *Discrete-time signal processing* vol. 2: Prentice hall Englewood Cliffs, NJ:, 1989.

[24] S. G. Taylor, *et al.*, "Wind turbine blade fatigue tests: lessons learned and application to SHM system development," in *European Workshop on Structural Health Monitoring*, Dresden Germany, 2012.

[25] S. G. Taylor, *et al.*, "Incipient Crack Detection in Composite Wind Turbine Blades," presented at the Advances in Structural Health Management and Composite Structures, Jeonju, Korea, 2012.

[26] N. Dervilis, *et al.*, "Novelty detection applied to vibration data from a CX-100 wind turbine blade under fatigue loading," presented at the Modern Practice in Stress and Vibration Analysis, Glasgow, UK, 2012.

[27] T. Belytschko and T. J. R. Hughes, *Computational methods for transient analysis* vol. 1: North-Holland, 1983.

[28] P. L. Jones, *et al.*, "LIST/BMI Turbines: Instrumentation and Infrastructure," SAND2001-1642, 2001.

[29] H. J. Sutherland, *et al.*, "Update of the Long-Term Inflow and Structural Test Program," in *ASME Wind Energy Symposium*, 2004.

[30] H. J. Sutherland, "Analysis of the Structural and Inflow Data from the LIST Turbine," *Transactions-American Society of Mechanical Engineers Journal of Solar Energy Engineering,* vol. 124, pp. 432-445, 2002.

[31] H. J. Sutherland, "Inflow and the Fatigue of the LIST Wind Turbine," in *2002 ASME Wind Energy Symposium*, 2002, pp. 427-437.

[32] H. J. Sutherland, "Preliminary analysis of the structural and inflow data from the LIST turbine," in *2001 ASME Wind Energy Symposium*, 2001, pp. 173-183.

[33] H. J. Sutherland, *et al.*, "The Long-Term Inflow and Structural Test Program," in *2001 ASME Wind Energy Symposium*, 2001, pp. 162-172.

[34] H. J. Sutherland, *et al.*, "The Long-Term Inflow and Structural Test Program," in *Wind Energy*, 2001.

[35] J. White and D. Adams, "Inertial measurements monitor wind turbines in action."

[36] J. R. White, *et al.*, "Operational load estimation of a smart wind turbine rotor blade," San Diego, CA, USA, 2009, pp. 72952D-12.

[37] J. R. White, *et al.*, "Theoretical analysis of acceleration measurements in a model of an operating wind turbine," San Diego, CA, USA, 2010, pp. 76431F-10.

[38] J. R. White, *et al.*, "Modal Analysis of CX-100 Rotor Blade and Micon 65/13 Wind Turbine," in *Structural Dynamics and Renewable Energy, Volume 1*. vol. 10, T. Proulx, Ed.: Springer New York, 2011, pp. 15-27.

[39] C. R. Farrar, *et al.*, "Sensor network paradigms for structural health monitoring," *Structural Control and Health Monitoring,* vol. 13, pp. 210-225, 2006.

[40] Y.-Q. Ni, *et al.*, "Simulation studies of damage location in Tsing Ma Bridge deck," pp. 312-323, 2000.

[41] J. P. Lynch and K. J. Loh, "A Summary Review of Wireless Sensors and Sensor Networks for Structural Health Monitoring," *Shock & Vibration Digest,* vol. 38, pp. 91-128, 2006.

[42] Y. Jia, *et al.*, "Design and characterization of a passive wireless strain sensor," *Measurement Science and Technology,* vol. 17, p. 2869, 2006.

[43] C. Farrar, *et al.*, "Sensor network paradigms for structural health monitoring," *Structural Control and Health Monitoring,* vol. 13, pp. 210-225, 2006.

[44] A. T. Zimmerman, *et al.*, "Automated Modal Parameter Estimation by Parallel Processing within Wireless Monitoring Systems," *Journal of Infrastructure Systems,* vol. 14, pp. 102-113, Mar 2008.

[45] G. Park, *et al.*, "Energy Harvesting for Structural Health Monitoring Sensor Networks," *Journal of Infrastructure Systems,* vol. 14, pp. 64-79, 2008/03/01 2008.

[46] D. D. L. Mascarenas, *et al.*, "Demonstration of a roving-host wireless sensor network for rapid assessment monitoring of structural health," San Diego, California, USA, 2008, pp. 69330K-11.

[47] M. D. Todd, et al., "A Different Approach to Sensor Networking for SHM: Remote Powering and Interrogation with Unmanned Arial Vehicles," in *6th International Workshop on Structural Health Monitoring*, Stanford, CA, 2007.

[48] H. Okada, *et al.*, "Wireless sensor system for detection of avian influenza outbreak farms at an early stage," in *Sensors, 2009 IEEE*, 2009, pp. 1374-1377.

[49] C.-B. Yun and J. Min, "Smart sensing, monitoring, and damage detection for civil infrastructures," *KSCE Journal of Civil Engineering,* vol. 15, pp. 1-14, 2011.

[50] S. Yuan, *et al.*, "Mobile Multi-Agent Evaluation Method for Wireless Sensor Networks-Based Large-Scale Structural Health Monitoring," *International Journal of Distributed Sensor Networks,* vol. 2012, p. 15, 2012.

[51] B. Pearre and T. X. Brown, "Model-Free Trajectory Optimisation for Unmanned Aircraft Serving as Data Ferries for Widespread Sensors," *Remote Sensing,* vol. 4, pp. 2971-3005, 2012.

[52] Y. BAO, *et al.*, "A Mobile Wireless Sensor-Based Structural Health Monitoring Technique," presented at the Workshop on Civil Structural Health Monitoring, Berlin, Germany, 2012.

[53] K. M. Farinholt, *et al.*, "Wireless energy transmission to supplement energy harvesters in sensor network applications," in *SPIE Smart Structures/NDE*, San Diego, CA, 2010, p. 764505.

[54] S. R. Anton, *et al.*, "Multi-source energy harvesting for wind turbine structural health monitoring node," presented at the Advances in Structural Health Management and Composite Structures, Jeonju, Korea, 2012.

[55] G. Park, *et al.*, "Overview of Piezoelectric Impedance-Based Health Monitoring and Path Forward," *Shock & Vibration Digest,* vol. 35, pp. 451-463, 2003.

[56] T. G. Overly, *et al.*, "Piezoelectric Active-Sensor Diagnostics and Validation Using Instantaneous Baseline Data," *Sensors Journal, IEEE,* vol. 9, pp. 1414-1421, 2009.

[57] G. Park, *et al.*, "Piezoelectric Active Sensor Self-Diagnostics Using Electrical Admittance Measurements," *Journal of Vibration and Acoustics,* vol. 128, pp. 469-476, 2006.

[58] D. L. Mascarenas, *et al.*, "Development of an impedance-based wireless sensor node for structural health monitoring," *Smart Materials and Structures,* p. 2137, 2007.

[59] K. M. Farinholt, *et al.*, "Recent advances in impedance-based wireless sensor nodes," presented at the ASME Conference on Smart materials, Adaptive Structures and Intelligent Systems, Ellicott City, MD, 2008.

[60] J. Min, *et al.*, "Development of multi-functional wireless impedance sensor nodes for structural health monitoring," 2010, p. 764728.

[61] S. O'Connor, *et al.*, "Fatigue Life Monitoring of Metallic Structures by Decentralized Rainflow Counting Embedded In a Wireless Sensor Network," in *ASME 2010 Conference on Smart Materials, Adaptive Structures and Intelligent Systems*, Philadelphia, Pennsylvania, USA.

[62] A. V. Hernandez, *et al.*, "A Framework for Embedded Load Estimation from Structural Response of Wind Turbines," *Rotating Machinery, Structural Health Monitoring, Shock and Vibration, Volume 5,* pp. 295-305, 2011.

[63] S. S. Kessler, *et al.*, "Hybrid Coherent/Incoherent Beam Forming Diagnostic Approach to Naval Assets," in *International Workshop on Structural Health Monitoring*, Dresden, Germany, 2012.

[64] D. Musiani, *et al.*, "Active sensing platform for wireless structural health monitoring," presented at the Proceedings of the 6th international conference on Information processing in sensor networks, Cambridge, Massachusetts, USA, 2007.

[65] E. B. Flynn, "A Bayesian Experimental Design Approach to Structural Health Monitoring with Application to Ultrasonic Guided Waves," Doctor of Philosophy, Structural Engineering, University of California, San Diego, La Jolla, CA, 2010.

[66] D.-D. Ho, *et al.*, "Multiscale Acceleration-Dynamic Strain-Impedance Sensor System for Structural Health Monitoring," *International Journal of Distributed Sensor Networks,* vol. 2012, p. 17, 2012.

[67] J.-H. Park, *et al.*, "Multi-scale hybrid sensor nodes for acceleration-impedance monitoring for steel structural connections," in *SPIE Smart Structures/NDE*, San Diego, CA, 2011, pp. 79810E-79810E.

[68] J. A. Rice and J. B. F. Spencer, "Structural health monitoring sensor development for the Imote2 platform," 2008, p. 693234.

[69] E. B. Flynn, *et al.*, "SHMTools: a new embeddable software package for SHM applications," in *SPIE Smart Structures/NDE*, San Diego, CA, 2010, p. 764717.

[70] T. G. S. Overly, *et al.*, "Development of an extremely compact impedance-based wireless sensing device," *Smart Materials and Structures,* p. 065011, 2008.

[71] S. G. Taylor, *et al.*, "Application of a Wireless Sensor Node to Health Monitoring of Operational Wind Turbine Blades," presented at the International Modal Analysis Conference, Jacksonville, FL, 2010.

[72] S. G. Taylor, *et al.*, "A Mobile-Agent Based Wireless Sensing Network for SHM – Field Study at the Alamosa Canyon Bridge," in *7th International Workshop on Structural Health Monitoring*, Stanford, CA, 2009, pp. 1731-1738.

[73] M. F. Kevin, *et al.*, "New Generation of Impedance-based Wireless Active-Sensor Node," in *Fourth European Workshop on Structural Health Monitoring*, Cracow, Poland, 2008.

[74] S. G. Taylor, *et al.*, "Wireless impedance device for electromechanical impedance sensing and low-frequency vibration data acquisition," in *SPIE Smart Structures/NDE*, San Diego, CA, USA, 2009, pp. 729228-12.

[75] D. L. Mascarenas, *et al.*, "Experimental studies of using wireless energy transmission for powering embedded sensor nodes," *Journal of Sound and Vibration,* vol. 329, pp. 2421-2433, 2010.

[76] S. G. Taylor, *et al.*, "Energy harvesting and wireless energy transmission for powering SHM sensor nodes," presented at the Bridge Maintenance, Safety, Management and Life-Cycle Optimization, Philadelphia, PA, 2010.

[77] S. W. Doebling, *et al.*, "DIAMOND: A graphical interface toolbox for comparative modal analysis and damage identification," in *International Conference on Recent Advances in Structural Dynamics*, Southampton, UK, 1997.

[78] W. Reiser, *et al.*, "Design, development, and assembly of sub-orbital space flight structural health monitoring experiment," in *SPIE Smart Structues/NDE*, 2012, pp. 83481J-83481J.

[79] "Agilent Impedance Measurement Handbook," Agilent Technologies, Inc. 5950-3000, 2009.

[80] J. Markel, "Digital inverse filtering-a new tool for formant trajectory estimation," *Audio and Electroacoustics, IEEE Transactions on,* vol. 20, pp. 129-137, 1972.

[81] P. Gyuhae*, et al.*, "Performance assessment and validation of piezoelectric active-sensors in structural health monitoring," *Smart Materials and Structures,* vol. 15, p. 1673, 2006.

[82] C. Liang*, et al.*, "Coupled Electro-Mechanical Analysis of Adaptive Material Systems -- Determination of the Actuator Power Consumption and System Energy Transfer," *Journal of Intelligent Material Systems and Structures,* vol. 5, pp. 12-20, Jan. 1994.

[83] G. Park*, et al.*, "Removing effects of temperature changes from piezoelectric impedance-based qualitative health monitoring," 1998, pp. 103-114.

[84] G. Park*, et al.*, "Impedance-based health monitoring technique for massive structures and high-temperature structures," 1999, pp. 461-469.

[85] G. Park*, et al.*, "Impedance-based health monitoring of civil structural components," *Journal of Infrastructure Systems,* vol. 6, p. 153, 2000.

[86] S. Bhalla and C. K. Soh, "Structural impedance based damage diagnosis by piezo-transducers," *Earthquake Engineering & Structural Dynamics,* vol. 32, pp. 1897-1916, 2003.

[87] S. Bhalla and C. K. Soh, "High frequency piezoelectric signatures for diagnosis of seismic/blast induced structural damages," *NDT & E International,* vol. 37, pp. 23-33, 2004.

[88] S. Bhalla*, et al.*, "Wave propagation approach for NDE using surface bonded piezoceramics," *NDT & E International,* vol. 38, pp. 143-150, 2005.

[89] G. Park and D. J. Inman, "Structural health monitoring using piezoelectric impedance measurements," *Philosophical Transactions A: Mathematical, Physical and Engineering Sciences,* vol. 365, pp. 373-392, 2007.

[90] M. K. O'Brien*, et al.*, "An efficient signal processing tool for impedance-based structural health monitoring," in *SPIE Smart Structures/NDE*, San Diego, CA, USA, 2009, pp. 72951K-9.

[91] T. G. S. Overly*, et al.*, "Development of signal processing tools and hardware for piezoelectric sensor diagnostic processes," 2007, p. 653018.

[92] S. Park*, et al.*, "Sensor Self-diagnosis Using a Modified Impedance Model for Active Sensing-based Structural Health Monitoring," *Structural Health Monitoring,* vol. 8, pp. 71-82, January 1, 2009 2009.

[93] *4294A*. Available: www.agilent.com

[94] E. B. Flynn*, et al.*, "Maximum-likelihood estimation of damage location in guided-wave structural health monitoring," *Proceedings of the Royal Society A: Mathematical, Physical and Engineering Science,* vol. 467, pp. 2575-2596, 2011.

[95] E. B. Flynn and M. D. Todd, "A Bayesian approach to optimal sensor placement for structural health monitoring with application to active sensing," *Mechanical Systems and Signal Processing,* vol. 24, pp. 891-903, 2010.

[96] J. E. Michaels*, et al.*, "A comparison of feature-based classifiers for ultrasonic structural health monitoring," in *SPIE Smart Stuctures/NDE*, San Diego, CA, 2004, pp. 363-374.

[97] J. E. Michaels and T. E. Michaels, "Detection of structural damage from the local temporal coherence of diffuse ultrasonic signals," *Ultrasonics, Ferroelectrics and Frequency Control, IEEE Transactions on,* vol. 52, pp. 1769-1782, 2005.

[98] A. J. Croxford*, et al.*, "Strategies for guided-wave structural health monitoring," *Proceedings of the Royal Society A: Mathematical, Physical and Engineering Science,* vol. 463, pp. 2961-2981, 2007.

[99] A. J. Croxford*, et al.*, "Efficient temperature compensation strategies for guided wave structural health monitoring," *Ultrasonics,* vol. 50, pp. 517-528, 2010.

[100] S. Carnot, "Reflections on the Motive Power of Fire and on Machines Fitted to develop that Power. Reprinted in: Mendoza, E.(ed).(1960)," *Reflections on the motive power of fire by Sadi Carnot and other papers on the Second Law of Thermodynamics by E. Clapeyron and R,* 1824.

[101] G. Park*, et al.*, "A wireless active-sensor node for impedance-based structural health monitoring," presented at the US-Korea Smart Structures Technology for Steel Structures, Seoul, Korea, 2006.

[102] M. Rumsey*, et al.*, "Experimental Results of Structural Health Monitoring of Wind Turbine Blades," in *46th AIAA Aerospace Sciences Meeting and Exhibit*, 2008.

[103] M. A. Rumsey and J. A. Paquette, "Structural health monitoring of wind turbine blades," in *SPIE Smart Structures/NDE*, San Diego, California, USA, 2008, pp. 69330E-15.

[104] S. J. Dyas*, et al.*, "Structural health monitoring of wind turbine blades under fatigue loads," in *IMAC XXX*, Jacksonville, FL, 2012.

[105] G. Park*, et al.*, "Piezoelectric active sensing techniques for damage detection on wind turbine blades," 2011, p. 79790K.

[106] G. Park*, et al.*, "SHM of Wind Turbine Blades Using Piezoelectric Active-Sensors," in *Fifth European Workshop on Structural Health Monitoring*, Sorrento, Italy, 2010, pp. 321-326.

[107] S. G. Taylor*, et al.*, "Incipient Crack Detection in Composite Wind Turbine Blades," presented at the Advances in Structural Health Management and Composite Structures, Jeonju, Korea, 2012.

[108] S. G. Taylor*, et al.*, "Structural health monitoring of research-scale wind turbine blades," in *Asia-Pacific Workshop on Structural Health Monitoring*, Melbourne, Australia, 2012.

[109] C. Haynes and M. Todd, "Bayesian probabilistic modeling for damage assessment in a bolted frame," in *SPIE Smart Structures/NDE*, San Diego, CA, 2012, p. 83480D.

[110] S. M. Kay, *Fundamentals of Statistical Signal Processing* vol. 2. Upper Saddle River, NJ: Prentice-Hall PTR, 1998.

[111] O. I. Lobkis and R. L. Weaver, "On the emergence of the Green's function in the correlations of a diffuse field," *The Journal of the Acoustical Society of America,* vol. 110, pp. 3011-3017, 2001.

[112] L. Yinghui and J. E. Michaels, "Feature Extraction and Sensor Fusion for Ultrasonic Structural Health Monitoring Under Changing Environmental Conditions," *IEEE Sensors Journal,* vol. 9, pp. 1462-1471, 2009.

[113] R. E. Kalman, "A new approach to linear filtering and prediction problems," *Journal of basic Engineering,* vol. 82, pp. 35-45, 1960.

[114] P. E. Moraal and J. W. Grizzle, "Observer design for nonlinear systems with discrete-time measurements," *Automatic Control, IEEE Transactions on,* vol. 40, pp. 395-404, 1995.

[115] J. F. D. Bartlett and W. G. Flannelly, "Model Verification of Force Determination for Measuring Vibratory Loads," *Journal of the American Helicopter Society,* vol. 24, pp. 10-18, 1979.

[116] J. Doyle, "Force identification from dynamic responses of a bimaterial beam," *Experimental Mechanics,* vol. 33, pp. 64-69, 1993.

[117] J.-J. Liu*, et al.*, "Input force estimation of a cantilever plate by using a system identification technique," *Computer Methods in Applied Mechanics and Engineering,* vol. 190, pp. 1309-1322, 2000.

[118] A. Goedtel*, et al.*, "Load torque identification in induction motor using neural networks technique," *Electric Power Systems Research,* vol. 77, pp. 35-45, 2007.

[119] Q. P. Ha and H. Trinh, "State and input simultaneous estimation for a class of nonlinear systems," *Automatica,* vol. 40, pp. 1779-1785, 2004.

[120] C. Fritzen*, et al.*, "Structural health monitoring of offshore wind energy plants," in *4th European Conference on Structural Health Monitoring*, Cracow, Poland, 2008, pp. 3-20.

[121] E. Reissner, "On one-dimensional finite-strain beam theory: The plane problem," *Zeitschrift für Angewandte Mathematik und Physik (ZAMP),* vol. 23, pp. 795-804, 1972.

[122] E. Reissner, "On finite deformations of space-curved beams," *Zeitschrift für Angewandte Mathematik und Physik (ZAMP),* vol. 32, pp. 734-744, 1981.

[123] J. C. Simo and L. Vu-Quoc, "A three-dimensional finite-strain rod model. part II: Computational aspects," *Computer Methods in Applied Mechanics and Engineering,* vol. 58, pp. 79-116, 1986.

[124] G. Jelenic and M. A. Crisfield, "Geometrically exact 3D beam theory: implementation of a strain-invariant finite element for statics and dynamics," *Computer Methods in Applied Mechanics and Engineering,* vol. 171, pp. 141-171, 1999.

[125] M. A. Crisfield and G. Jelenic, "Objectivity of Strain Measures in the Geometrically Exact Three-Dimensional Beam Theory and Its Finite-Element Implementation," *Proceedings: Mathematical, Physical and Engineering Sciences,* vol. 455, pp. 1125-1147, 1999.

[126] H. K. Lee*, et al.*, "Helicopter Rotor Load Prediction Using a Geometrically Exact Beam with Multicomponent Model," *Journal of Aircraft,* vol. 47, pp. 1382-1390, 2010.

[127] D. H. Hodges and W. Yu, "A rigorous, engineer-friendly approach for modelling realistic, composite rotor blades," *Wind Energy,* vol. 10, pp. 179-193, 2007.

[128] D. J. Luscher and G. Ellis, "Part II: Plant-scale aeroelastically-coupled wind turbine resonse from geometrically exact beam theory," in *Intelligent Wind Turbine LDRD Mid-Project Review*, Los Alamos National Laboratory, 2011.

[129] K. Van Buren*, et al.*, "Developing Simplified Models for Wind Turbine Blades," in *53rd AIAA/ASME/ASCE/AHS/ASC Structures, Structural Dynamics and Materials Conference*, 2012.

[130] K. Ogata, *Modern control engineering*, 4 ed.: Prentice Hall, 2002.

[131] A. J. Laub and M. Wette, "Algorithms and software for pole assignment and observers," Lawrence Livermore National Laboratory UCRL-15646, 1984.